Laboratoire de Constructions Hydrauliques
Ecole Polytechnique Fédérale de Lausanne

Communication 15

Effects of obstacles and jets on reservoir sedimentation due to turbidity currents

Christoph Oehy

Editeur : Prof. Dr A. Schleiss

Lausanne, 2003

Communications du Laboratoire de constructions hydrauliques
Ecole Polytechnique Fédérale de Lausanne
Editeur: Prof. Dr A. Schleiss

Preface

The growing demand of water and food all over the world can be satisfied in arid regions only by artificial reservoirs, which supply water for drinking and irrigation. Unfortunately, all reservoirs are endangered by sedimentation and without effective measures their sustainability is questioned. Beside the loss of life storage also the proper functioning of outlet structures such as intakes and bottom outlets can be affected by deposits of sediments. In narrow reservoirs with rather steep bottom slopes, as present in alpine regions, turbidity currents are often the main process in the reservoir sedimentation. The highly sediment-laden density current not only transports the sediments along the thalweg to the dam but also erodes already deposited fine sediments. Technical measures to influence and govern turbidity currents are therefore very important in view of a sustainable reservoir sedimentation management.

By means of systematic, physical experiments and numerical simulations, as described in the present communication, Dr. Christoph Oehy filled up a considerable gap towards a better scientific understanding of the effects of obstacles, screens, water jets and bubble curtains on the reservoir sedimentation by turbidity currents. With an innovative measurement device, based on the electrical resistance of the deposited sediment layer, the spatial and temporal evolution of the deposits could be measured with high accuracy. Vertical velocity profiles and the front velocities allowed gathering further valuable data for the verification of the numerical model.

The three-dimensional, numerical model was based on the flow solver CFX-4.4 and enhanced by adding user routines, which allowed taking into account the settling of the sediments as well as their erosion and sedimentation at the bottom. For the first time the fractional suspended-sediment transport and the effects of stratification in the turbulence model were considered in this context. The effects of obstacles, screens and water jets on the turbidity currents were quantified in terms of their efficiency to retain the sediments. Generally, the comparison of the numerical simulations with the measured velocity profiles, front velocities and evolution of deposits showed good agreement. Therefore, the numerical model can be applied with confidence for prototype problems as the case study on the Lake of Grimsel revealed.

Based on the results of the experimental and numerical study, Dr. Christoph Oehy gives valuable recommendations for possible applica-

tions of the investigated measures to control reservoir sedimentation due to turbidity currents in alpine reservoirs.

We would like to thank Dr. Daniel Gessler of Colorado State University and Dr. Johannes Bühler from IHW at ETH Zürich, which gave significant support and guidance during their stay as academic guests at LCH. Finally, we thank the Fund for Projects and Studies of the Swiss Electricity Utilities (PSEL) and the Swiss Committee on Dams for their financial support to the project.

Prof. Dr. Anton J. Schleiss

Préface

La demande croissante en eau et en nourriture, au niveau mondial, ne peut être satisfaite dans les régions arides que par des réservoirs artificiels. Malheureusement, ces retenues sont souvent soumises au phénomène de l'alluvionnement et, sans mesures efficaces, leur durabilité peut être remise en question. Outre la réduction du volume de stockage, le fonctionnement des ouvrages annexes tels que prise d'eau et vidange de fond peut être compromis par les dépôts de sédiments. Dans des retenues étroites où la pente de fond est raide comme c'est souvent le cas dans les régions alpines, les courants de turbidité sont souvent le principal vecteur d'alluvionnement. Le courant de densité, chargé de sédiments en suspension, ne transporte pas seulement les particules solides le long du thalweg, mais il érode également des sédiments fins déjà déposés. Des mesures techniques pour influencer et maîtriser les courants de turbidité sont donc indispensables en vue d'une gestion durable de l'alluvionnement.

A l'aide d'essais physiques et de simulations numériques systématiques, décrits dans cette communication, Dr Christoph Oehy a contribué à une meilleure compréhension scientifique des effets d'obstacles, de grilles en géotextiles, de jets d'eau et d'écrans d'air sur l'alluvionnement par courants de turbidité. Grâce à un dispositif de mesure novateur, basé sur la résistance électrique de la couche de sédiments déposés, l'évolution spatio-temporelle des dépôts a été enregistrée avec une haute précision au cours des essais physiques. De plus, la mesure de profils de vitesse verticaux et de la vitesse du front a permis d'obtenir des données complémentaires très utiles pour la vérification du modèle numérique.

Le modèle tri-dimensionel a été basé sur le solveur CFX-4.4, dans lequel des routines supplémentaires ont été intégrées pour tenir compte de la sédimentation des particules, de l'érosion et de la déposition sur le fond. Dans ce contexte, et pour la première fois, le transport fractionnel de sédiments et l'effet de la stratification sur le modèle de turbulence ont été considérés. Les effets d'obstacles, de grilles en géotextiles et de jets d'eau sur le courant de turbidité ont été quantifiés en terme d'efficacité de rétention des sédiments. De plus, la comparaison entre simulations numériques et profils de vitesse, vitesses de front et évolution des dépôts mesurés a montré une bonne correspondance, de sorte que le modèle numérique peut actuellement être utilisé avec confiance

dans des situations réelles. Cela a d'ailleurs déjà été le cas pour l'étude du lac de Grimsel.

Sur la base des résultats de l'étude expérimentale et numérique, Dr Christoph Oehy donne des recommandations précieuses pour l'application possible des mesures investiguées pour la maîtrise de l'alluvionnement des retenues alpines par courants de turbidité.

Nous aimerions remercier Dr Daniel Gessler du Colorado State University et Dr Johannes Bühler de l'IHW de l'EPF Zurich pour leur soutien et les discussions fructueuses lors de leurs visites comme hôtes académiques au LCH. Finalement, nous remercions le fonds pour projets et études de l'Economie électrique (PSEL) et le Comité suisse des barrages pour leur soutien financier à ce projet.

Prof. Dr Anton Schleiss

Vorwort

Die weltweit zunehmende Nachfrage nach Wasser und Nahrung kann in ariden Gebieten oft nur durch Stauseen, welche Wasser für die Trinkwasserversorgung und die Bewässerung zur Verfügung stellen, befriedigt werden. Leider sind alle Stauseen der Verlandung unterworfen und ohne wirksamen Massnahmen ist deren nachhaltige Nutzung in Frage gestellt. Nebst dem Verlust an Speichervolumen, wird oft auch der Betrieb der Auslassorgane, wie Wasserfassung und Grundablass, durch Sedimentablagerungen beeinträchtigt. In engen Stauseen mit eher steilen Sohlenneigungen, wie in alpinen Gebieten vorhanden, wird die Problematik der Verlandung in der Nähe der Auslassorgane durch Trübeströme verschärft. Die stark sedimentbeladenen Dichteströme transportieren nicht nur Sedimente entlang dem Talweg, sondern können auch bereits im Stausee abgelagerte Sedimente erodieren. Technische Massnahmen um Trübeströme zu beeinflussen und zu beherrschen sind deshalb von grosser Wichtigkeit um eine nachhaltige Stauraumbewirtschaftung zu gewährleisten.

Mit Hilfe hydraulischer Modellversuche und numerischer Simulationen, wie in der vorliegenden Mitteilung beschrieben, hat Dr. Christoph Oehy einen bedeutendend Beitrag zu einem besseren, wissenschaftlichen Verständnis der Wirkungen von Hindernissen, Geotextilgitter, Wasserstrahlen und Luftblasenschleier auf die Stauraumverlandung durch Trübeströme geleistet. Mit einer innovativen Messvorrichtung, basierend auf der elektrischen Widerstandsmessung der abgelagerten Sedimentschicht, konnte die räumliche und zeitliche Entwicklung der Ablagerungen in den Modellversuchen mit hoher Genauigkeit gemessen werden. Vertikale Geschwindigkeitsprofile und die Frontgeschwindigkeit lieferten weitere wichtige Daten um die numerischen Simulationen zu überprüfen.

Das drei-dimensionale, numerische Modell wurde basierend auf dem Strömungsberechnungsprogram CFX-4.4 entwickelt und durch zusätzliche Routinen ergänzt, welche das Absetzen der Sedimente, sowie deren Erosion und Ablagerung am Boden berücksichtigen. Erstmals wurden auch der fraktionelle Sedimenttransport und die Wirkung der Dichtestratifizierung in diesem Zusammenhang betrachtet. Die Wirkungen von Hindernissen, Geotextilgitter und Wasserstrahlen auf Trübeströme wurden mittels derer Sedimentrückhalteffizienz quantifiziert. Im Allgemeinen stimmten die Resultate der numerischen Simulationen gut mit den im Versuchskanal gemessenen Geschwindigkeitsprofilen, Frontgeschwindigkeiten und Ablagerungen überein. Das nu-

merische Modell kann, wie das vorgestellte Fallbeispiel des Grimselsees zeigt, zuverlässige Resultate bei praktischen Fragestellungen liefern.

Basierend auf den Ergebnissen der experimentellen und numerischen Untersuchungen, gibt Dr. Christoph Oehy schliesslich wertvolle Empfehlungen für mögliche Anwendungen der untersuchten Massnahmen mit dem Ziel Stauraumverlandungen durch Trübeströme in alpinen Stauseen zu beherrschen.

Wir danken Dr. Daniel Gessler von der Colorado State University und Dr. Johannes Bühler vom IHW der ETH Zürich für Ihre hilfreiche Unterstützung während Ihrem Aufenthalt als akademische Gäste am LCH. Abschliessend danken wir dem Projekt- und Studienfonds der Elektrizitätswirtschaft (PSEL) und dem Schweizer Talsperrenkomitee für die finanzielle Unterstüzung des Forschungsprojekts.

Prof. Dr. Anton Schleiss

Table of Contents

Abstract

Effects of obstacles and jets on reservoir sedimentation due to turbidity currents

Reservoir sedimentation is a subject of major importance in many Alpine reservoirs and is often related to the phenomenon of sediment transport by means of turbidity currents. These density currents with a high suspended-sediment concentration follow the thalweg of the lake to the deepest area, normally near the dam, where the sediments settle down. They can cover the bottom outlet, affect the operation of the power intake and reduce the storage capacity of the reservoir. To control the sedimentation within the reservoir, the effects of obstacles, screens, water jets and bubble curtains on the turbidity current were investigated with physical experiments and numerical simulations.

The experimental investigations were carried out in a flume of 7.1 m long, 27.2 cm wide and 90.0 cm high. The tested measures consisted of a continuously-fed turbidity current, flowing

- over an obstacle;
- through two types of vertical screens made of different geotextiles;
- across vertical jets issuing from a multiport diffuser;
- across inclined jets issuing from a multiport diffuser at 45°upstream; and
- across a bubble curtain.

For each series, experiments on horizontal and inclined slopes of 4.64% were done. To measure the deposits a new device, based on the electrical resistance measurement of the deposited sediment layer, was developed. This method allowed measuring of the spatial and temporal evolution of the deposits with an accuracy in the order of 0.15 mm. Furthermore, vertical velocity profiles were measured with an ultrasonic velocity profiler (UVP), and the front velocities were determined from video recordings.

To further investigate the effects of obstacles, screens, and water jets, a three-dimensional numerical model, based on the flow solver CFX-4.4, was developed. In this program, interfaces were added to take into account the settling of the sediments, their erosion and sedimentation at the bed, the fractional suspended-sediment transport and the effect of stratification in the turbulence model. The numerical simulations were compared with good agreement to the physical experiments and the blocking efficiency of the different configurations was computed.

From the physical experiments and numerical simulations, some recommendations, given as rules of thumb, were determined to propose possible applications of the investigated measures to control reservoir sedimentation due to turbidity currents.

In a case study in Lake Grimsel, the possibility of influencing the turbidity current with submerged dams was evaluated with the numerical model. The results showed, that due to the blocking effect of the dam, the sediments can efficiently be retained and sediment deposits in the area of the intake and bottom outlet structures can be prevented.

Résumé

Effets d'obstacles et de jets sur l'alluvionnement des retenues par courants de turbidité

L'alluvionnement est un thème d'importance majeure dans nombreuses retenues alpines. Il est souvent associé au processus de transport sédimentaire par courants de turbidité. Ces courants, à hautes concentrations de sédiments en suspension, suivent le fond du lac jusqu'aux zones les plus profondes, situées habituellement à proximité du barrage, où ils se déposent. Ils peuvent ainsi recouvrir la vidange de fond, perturber l'exploitation de la prise d'eau usinière et réduire la capacité de stockage de la retenue. Afin de contrôler l'alluvionnement à l'intérieur d'une retenue, les effets d'un obstacle, d'une grille, de jets d'eau, et d'un écran d'air ont été étudiés par expérimentation physique et simulation numérique.

Les études expérimentales ont été effectuées dans un canal de 7.1 m de long, 27.2 cm de large et 90.0 cm de haut. Les configurations testées concernent un courant de turbidité passant

- par dessus un obstacle;
- à travers deux types de grilles verticales en géotextiles;
- à travers des jets verticaux sortant d'un diffuseur multi-ports;
- à travers des jets inclinés à 45°sortant d'un diffuseur multi-ports; et
- à travers un écran d'air.

Pour chaque série d'essais, des expériences sur fond horizontal et incliné de 4.64% ont été faites. Pour mesurer les dépôts, un appareil original, basé sur la mesure de la résistance électrique de la couche de sédiments déposés, a été développé. Cette méthode de mesure a permis de suivre l'évolution temporelle et spatiale des dépôts avec une précision de l'ordre de 0.15 mm. De plus, des mesures de profils verticaux de vitesse par ultrasons (Ultrasonic Velocity Profiler – UVP) ainsi que de la vitesse du front du courant de turbidité par traitement d'enregistrement digital ont été réalisées.

Pour étudier les effets d'un obstacle, d'une grille et d'un jet d'eau de manière plus approfondie, un modèle numérique tri-dimensionel basé sur le programme CFX-4.4 a été développé. Des routines ont été implémentées pour tenir compte de la sédimentation des particules, de leur érosion et déposition au fond, du transport fractionnel des sédiments, ainsi que de l'effet de la stratification dans le modèle de turbulence. Les simulations numériques ont

été comparées avec les essais expérimentaux et l'efficacité des différentes configurations a été déterminés.

Sur la base des essais physiques et des simulations numériques, des règles de première approximation ont été définies dans le but de concrétiser les possibilités d'application des différentes mesures étudiées.

Comme étude de cas, l'influence des digues submergées sur le courant de turbidité dans la géométrie tri-dimensionnelle de la retenue de Grimsel a été évaluée. Les résultats ont montré, que, par l'effet de la digue, les sédiments pouvaient être retenus, évitant ainsi que des dépôts ne se forment à proximité de la vidange de fond et de la prise d'eau.

Zusammenfassung

Wirkungen von Hindernissen und Strahlen auf die Stauraumverlandung durch Trübeströme

Stauraumverlandung ist ein wichtiges Problem in Alpinen Stauseen und ist oft mit dem Phänomen des Sedimenttransports durch Trübeströme verbunden. Diese Dichteströmung mit hohen Schwebstoffkonzentrationen folgt dem Talweg des Stausees bis in die tiefsten Zonen, normalerweise in der Nähe der Staumauer, wo sich die Sedimente ablagern. Dabei können sie den Grundablass zudecken oder den Betrieb der Triebwasserfassung beeinträchtigen. Um diesen Verlandungsprozess innerhalb des Stausees zu kontrollieren wurden die Wirkungen von Hindernissen, Gitter, Wasserstrahlen und Blasenschleier auf den Trübestrom mit physikalischen Versuchen und numerischen Simulationen untersucht.

Die physikalischen Versuche wurden in einem Kanal von 7.1 m Länge, 27.2 cm Breite und 90.0 cm Höhe durchgeführt. Die getesteten Massnahmen bestanden aus einem Trübestrom fliessend

- über ein Hindernis;
- durch zwei vertikale Gitter aus verschiedenen Geotextilien;
- über vertikale Wasserstrahlen aus einem Diffusor;
- über 45°-stromaufwärtsgerichtete Wasserstrahlen aus einem Diffusor; und
- durch einen Blasenschleier.

Für jede Konfiguration wurden Versuche mit horizontaler und 4.64%-geneigter Sohle gemacht. Um die Ablagerungen zu messen wurde ein neues Gerät entwickelt, dass auf dem Prinzip der Widerstandsmessung der abgelagerten Sedimentschicht beruht. Diese Messmethode erlaubte es, die zeitliche und räumliche Entwicklung der Ablagerungen mit einer Genauigkeit von rund 0.15 mm zu erfassen. Zusätzlich wurden vertikale Geschwindigkeitsprofile mit einem Ultraschall-Geschwindigkeits-Profiler (UVP) und die Frontgeschwindigkeit mit Videoaufnahmen ermittelt.

Um die Wirkungen von Hindernissen, Gitter, und Wasserstrahlen weiter zu untersuchen, wurde ein drei-dimensionales, numerisches Model, basierend auf dem Strömungsberechnungsprogramm CFX-4.4, entwickelt. Dabei wurde das Programm mit zusätzlichen Modulen ergänzt, die das Absetzen der Sedimente, deren Erosion und Ablagerung am Boden, den fraktionellen Sedimenttransport und den Effekt der Dichteschichtung im Turbulenzmodell berücksichtigen. Die numerischen Simulationen wurden mit den physikalischen

Versuchen verglichen und die Effizienz der verschiedenen Massnahmen bestimmt.

Aufgrund der physikalischen Versuche und der numerischen Berechnungen, wurden Empfehlungen in Form von Faustregeln bestimmt, um mögliche Anwendungen der untersuchten Massnahmen aufzuzeigen.

In einer Fallstudie im Grimselstausee, wurde mit dem numerischen Modell die Möglichkeit der Beeinflussung eines Trübestroms mit versenkten Dämmen untersucht. Die Resultate zeigten, dass durch den Rückhalteffekt des Damms, die Sedimente effizient zurückgehalten werden können, und keine Ablagerungen in der Nähe des Grundablasses und der Triebwasserfassung entstehen.

List of Symbols

Roman Symbols

$\overline{c_s' w'}$	Reynolds flux of sediment
A	Cross-sectional area
a	Reference level for equilibrium concentration
A_j	Total jet area
a_j	Slot width of jet
a_v	Distance of virtual origin of electrical field lines
B	Buoyancy flux
b	Reference level for pick-up and settling rate
B_0	Initial buoyancy flux per unit width
B_b	Buoyancy flux of bubble curtain
b_b	Buoyancy flux per unit width of bubble curtain
B_i	Body force vector
$B_{i\ \mathrm{buoy}}$	Buoyancy force vector
$B_{i\ \mathrm{rot}}$	Rotational force term
b_{j0}	Buoyancy flux of jet per unit width
c	Velocity of sound in the fluid, ($\cong$1480 m/s)
c_s'	Fluctuation of volumetric sediment concentration
C_1	Constant in deposition calibration curve in Eq. (3.16)
C_2	Constant in deposition calibration curve in Eq. (3.16)
C_3	Constant in deposition calibration curve in Eq. (3.16)
C_μ	Constant in k-ε model, ($= 0.09$)
c_μ^0	Constant in buoyancy-extension to the k-ε model, (=0.5562)
C_c	Flow-contraction coefficient
C_s	Average volumetric sediment concentration

c_s	Local volumetric sediment concentration
$C_{1\varepsilon}$	Constant in k-ε model, $(= 1.44)$
$C_{2\varepsilon}$	Constant in k-ε model, $(= 1.92)$
$C_{3\varepsilon}$	Constant in k-ε model
C_{D*}	Bed friction coefficient
c_{s1}	Concentration in near-bed cell
$c_{sb\star}$	Equilibrium concentration close to the bed at distance $z = a$
c_{sb}	Local volumetric sediment concentration close to the bed
c_{si}	Concentration of size fraction i
D	Dissipation length scale
d	Particle diameter
$D_\star$	Particle size parameter
d_a	Arithmetic mean diameter
d_b	Sediment layer thickness
d_g	Geometric mean diameter
D_s	Characteristic sediment size
d_s	Settling-velocity weighted mean diameter
d_v	Particle-volume weighted mean diameter
d_{16}	Diameter with 16% finer by weight
d_{50}	Median particle diameter
d_{84}	Diameter with 84% finer by weight
d_{90}	Diameter with 90% finer by weight
$D_{\max}$	Maximum distance of UVP
E	Roughness parameter
E_s	Entrainment coefficient of sediments
E_w	Entrainment coefficient of ambient fluid
F	Force
f	Ratio of flow area at vena contracta to screen area, $(= C_c\, p_g)$
f_0	Emitted ultrasound frequency
f_1	Stability function acting on eddy viscosity in Eq. (5.15)
f_2	Stability function acting on eddy diffusivity in Eq. (5.15)
f_D	Doppler frequency shift
F_i	Resistance force to flow in porous region

f_{prf}	Pulse repetition frequency of UVP
Fr_d	Densimetric Froude number
Fr_{d1}	Densimetric Froude number in section 1
Fr_{d2}	Densimetric Froude number in section 2
Fr_{d3}	Densimetric Froude number in section 3
G	Buoyancy production
g	Acceleration due to gravity
g'	Reduced gravitational acceleration
g'_0	Initial reduced gravitational acceleration
g'_2	Reduced gravitational acceleration in section 2
g'_3	Reduced gravitational acceleration in section 3
g'_{j0}	Initial reduced gravitational acceleration of jet
g_i	Gravity vector, $= [0, 0, -9.81\ \mathrm{m/s^2}]$
H	Water depth
h	Average height of the current
h_0	Initial current height
h_1	Height in section 1
h_2	Height in section 2
h_3	Height in section 3
h_c	Critical height of the current
H_f	Height of turbidity current front
h_f	Height of the nose of the turbidity current
H_j	Dimensionless jump height
H_m	Dimensionless obstacle height
H_p	Ratio of heights down- and upstream of screen
h_t	Height of turbidity current at which $u \equiv 0$
h_w	Water depth at sliding gate
h_{max}	Height of maximum velocity
H_{mc}	Critical dimensionless obstacle height
h_m	Obstacle height
i_T	Turbulence intensity
K	Mean kinetic energy of turbulence
k	Turbulent kinetic energy

k_{in}	Inlet value of k
k_1	Turbulent kinetic energy at first grid point
k_s	Equivalent roughness height
k_s^+	Dimensionless equivalent roughness height
l_1	Constant in Eq. (2.1)
l_2	Constant in Eq. (2.3)
l_M	Jet-crossflow length scale
m_b	Sediment mass per unit area
m_{j0x}	Initial momentum of jet in x direction per unit width
M_{j0x}^+	Additional momentum of jet in x direction
M_{j0z}	Initial momentum of jet in z direction
m_{j0z}	Initial momentum of jet in z direction per unit width
M_{j0z}^+	Additional momentum of jet in z direction
M_{j0}	Momentum of jet
m_{j0}	Initial momentum of jet per unit width
N	Total number of cells
n	Form factor
N_{xi}	Number of cells in longitudinal direction
N_{zi}	Number of cells in vertical direction
P	Shear production
p	Pressure
p'	Modified pressure
p_g	Geometric porosity of screen
Q_0	Initial discharge
q_0	Initial discharge per unit width
Q_b	Discharge of bubble curtain
q_b	Discharge of bubble curtain per unit width
q_c	Critical discharge per unit width
Q_p	Peak discharge
q_s	Sediment flux passing an obstacle, screen or jet
Q_{j0}	Jet discharge
q_{j0}	Jet discharge per unit width
q_{s0}	Sediment flux passing without an obstacle, screen or jet

R	Submerged specific density of the sediment
r	Radius of electrode
R_0	Resistance of water at reference temperature T_{ref}
r_0	Constant in Eq. (2.27)
R_1	Constant resistance in Wheatstone bridge circuit
R_2	Constant resistance in Wheatstone bridge circuit
R_{layer}	Resistance of sediment layer
R_{water}	Resistance of water
R_{mi}	Measured resistance over electrode i
R_m	Measured resistance
Re	Reynolds number
Re_p	Particle Reynolds number
Ri	Global Richardson number
S	Bottom slope
s	Velocity projection in the beam axis of UVP
S_Φ	Source or sink term for scalar Φ
S_c	Source or sink term for volumetric sediment concentration
S_D	Sediment deposition term
S_E	Sediment erosion term
T	Temperature
t	Time
T_0	Temperature of inflowing fluid
$T_\star$	Non-dimensional excess bed-shear stress
T_a	Temperature of ambient fluid
t_p	Time to peak
T_{ref}	Reference temperature
U	Average velocity of the current
u	Local velocity component in x direction
U_{in}	Inlet velocity
U_0	Initial velocity
U_1	Average velocity in section 1
U_2	Average velocity in section 2
u_2	Local velocity upstream of the screen

U_3	Average velocity in section 3
$u_\star$	Shear velocity
U_a	Velocity of the ambient fluid
U_c	Critical velocity of the current
u_c	Velocity at vena contracta
U_f	Velocity of the front
U_i	Velocity vector, $= [u, v, w]$
U_j	Jump velocity
U_T	Velocity tangential to the wall
U_W	Voltage applied across Wheatstone bridge circuit
u_{*b}	Shear velocity
$U_{\max}$	Maximum detectable velocity of UVP
U_{res}	Velocity resolution of UVP
$u_{\star cr}$	Critical shear velocity at incipient motion
$U_{f1\text{calc}}$	Computed front velocity upstream of obstacle, screen or jet
$U_{f1\text{meas}}$	Measured front velocity upstream of obstacle, screen or jet
$U_{f2\text{calc}}$	Computed front velocity downstream of obstacle, screen or jet
$U_{f2\text{meas}}$	Measured front velocity downstream of obstacle, screen or jet
$U_{fb\text{calc}}$	Computed propagation speed of reflected bore
$U_{fb\text{meas}}$	Measured propagation speed of reflected bore
U_{j0z}	Initial velocity of jet in z direction
U_{j0}	Initial velocity of jet
U_{max}	Maximum velocity of current
U_{mi}	Measured output voltage over electrode i
v	Local velocity component in y direction
v_{ss}	Settling velocity
w	Local velocity component in z direction
w'	Fluctuation of vertical velocity
W_h	Entrainment velocity
x	Longitudinal coordinate
x_i	Cartesian coordinates, $= [x, y, z]$
x_m	Position of maximum height of obstacle
x_s	Distance along the UVP measurement axis

y	Lateral coordinate
z	Vertical coordinate
z_0^+	Dimensionless viscous sub-layer thickness
z_1	z coordinate of cell center close to the bottom
z_1^+	Dimensionless distance parameter
Z_u	Dimensionless parameter in Eq. (2.23)

Greek Symbols

α	Angle of bottom slope
$\alpha_{\min}$	Constant in Eq. (5.17)
α_c	Constant in Eq. (5.17)
α_K	Dimensionless constant in Eq. (2.25)
α_N	Non-dimensional parameter for stratification and shear
α_p	Linear resistance force coefficient
α_T	Temperature coefficient of resistance
β	Volume porosity
β_p	Non-linear resistance force coefficient
δF	Incremental force
ΔH	Local head loss
Δp	Pressure difference
Δq	Injected flow discharge per unit width
δq	Incremental discharge per unit width
Δx	Thickness of porous region
δz	Incremental height
δz_c	Incremental height at vena contracta
$\Delta\psi$	Roughness function of k_s^+
$\Delta\rho$	Density excess
Δ_i	Percentage of sediment material falling in the ith size fraction of the frequency histogram
δ_{ij}	Kronecker delta
ε	Turbulent dissipation rate
ε_{in}	Inlet value of ε
ε_1	Turbulent dissipation rate at first grid point

ε_s	Diffusion coefficient
ϵ_0	Mean rate of turbulent kinetic energy dissipation
η	Proportion of passing sediment fluxes
γ	Angle of electrical field lines
Γ_{eff}	Effective diffusivity
Γ_T	Turbulent or eddy diffusivity
κ	Von Karman constant, ($\cong 0.41$)
λ_C	Concentration scale
λ_f	Friction coefficient
λ_h	Length scale
λ_t	Time scale
λ_U	Velocity scale
λ_w	Wall function coefficient
μ	Dynamic molecular viscosity
μ_{eff}	Effective viscosity
μ_T	Turbulent or eddy viscosity
ν	Kinematic viscosity of water
Ω	Angular velocity of earth rotation, =[0, 0, 0.0000075 rad/s]
Φ	Scalar
ϕ	Angle of inclination of UVP transducer
ψ	Additive constant in wall law, ($\cong 5.3$)
ρ	Density of fluid
ρ_a	Density of the ambient fluid
ρ_s	Density of sediment particles
ρ_t	Bulk density of turbidity current
ρ_w	Density of water
ρ_{el}	Resistivity of sediment layer
ρ_{j0}	Density of fluid in jet
σ_ε	Turbulent Prandtl number of ε
σ_Φ	Turbulent Prandtl number of Φ
σ_g	Geometric standard deviation of particle size distribution
σ_k	Turbulent Prandtl number of k
τ_w	Wall shear stress vector

τ_{ij}	Turbulent stress tensor
θ	Jet exit angle
$\tilde{\alpha}_N$	Modified non-dimensional parameter for stratification and shear
ξ	Latitude
ξ_{Re}	Loss coefficient

1 Introduction

1.1 Reservoir Sedimentation Due to Turbidity Currents

In most natural river reaches sediment inflow and outflow are approximately balanced. Dam construction dramatically alters this balance, creating an artificial lake or reservoir characterized by extremely low flow velocities and efficient sediment trapping. Over the years as the sediments accumulate, the reservoir looses its storage capacity. Declining storage reduces and eventually eliminates the capacity for flow regulation and with it all water supply, energy and flood control benefits (Graf, 1984; International Comittee on Large Dams (ICOLD), 1989). Within the reservoir, the sediment can enter intakes and greatly accelerate abrasion of hydraulic machinery, thereby decreasing its efficiency and increasing maintenance costs (Varma et al., 2000; Krause and Grein, 1993). Sediment accumulations can generate a risk of blockage of intake and bottom outlet structures or damage gates which are not designed for sediment passage (Boillat and Delley, 1992; Schleiss et al., 1996).

There are no accurate data on the rates of reservoir sedimentation worldwide, but it is commonly accepted that about 1–2% of the worldwide storage capacity is lost annually (Jacobsen, 1999). A detailed collection of sedimentation rates in regions all over the world can be found in Batuca and Jordaan (2000). The volumes of water-storage capacity lost due to reservoir sedimentation and the volumes of installed water-storage capacity in the world are presented in Fig. 1.1. The graph shows the evolution over the last century, and the predicted future development. To obtain values for the sedimentation rates in Switzerland, Beyer Portner (1998) conducted an analysis of sedimentation data from 14 reservoirs. The work showed that on average in Switzerland only about 0.2% of the storage capacity is lost annually due to reservoir sedimentation. The evolution in Switzerland of the water-storage volumes lost due to reservoir sedimentation, and that of the installed water-storage capacity over the last century with the estimated future development are also presented in the same Fig. 1.1. The lower sedimentation rate in Switzerland is due to the geologic characteristics, mainly rocky mountains, of the catchment areas at high altitudes.

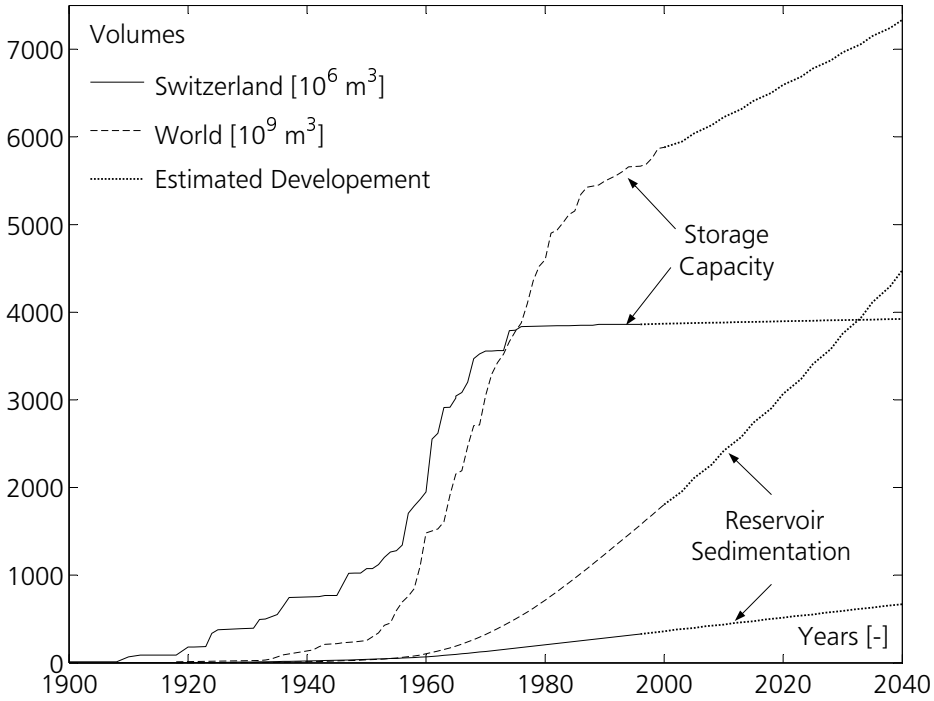

Figure 1.1: Development and estimated evolution of installed water-storage capacity and volumes lost due to reservoir sedimentation in the world (dashed line) and in Switzerland (solid line) (after Oehy et al. (2000)).

Nevertheless, sedimentation is also a subject of major importance in Alpine reservoirs and is mainly due to turbidity currents. The sediment discharge of the inflowing rivers is usually significant during flood events and consists mainly (80 to 90%) of suspended materials finer than fine sands (Alam, 1999; Sinniger et al., 1999). When the turbid water flows into stagnant and less dense water of the reservoir, the inflow displaces the ambient water until it reaches a balance of forces, at which point the denser water plunges beneath the free surface. This point is referred to as plunge point (see Fig. 1.2). In a narrow reservoir the plunging flow will form a line across the width of the reservoir; the surface water will be turbid up to this line and clear beyond it. However, when a sediment-laden flow discharges into a wide reservoir, the turbid surface water extends into the reservoir as an irregular tongue-shaped current which can shift from one side to the other (see also Fig. 1.3). Generally, the plunge line is located at the downstream limit of the zone of delta deposition, but its location is not fixed, being determined by pool level, discharge, suspended sediment concentration, and reservoir geometry. The plunging flow establishes a weak countercurrent in the overlying clear water just downstream of the plunge line, causing clear surface water to travel towards it. Since the turbid and the clear flows converge along the plunge line, floating debris carried by the flood

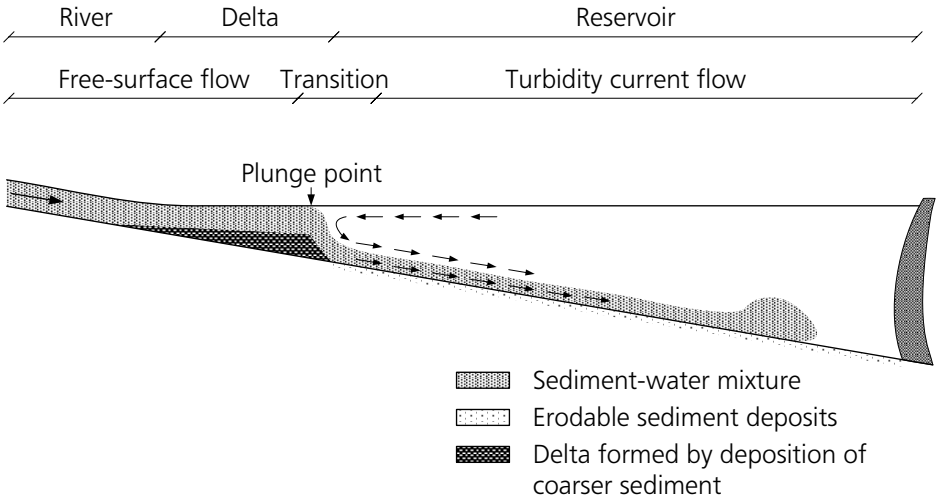

Figure 1.2: Sediment-laden river inflow entering a reservoir, which plunges and induces a turbidity current that transports the incoming suspended load and any eroded sediments on the way to an area near the dam, where the sediment accumulation may cover bottom outlet and intake structures.

typically accumulate in the region of the plunging flow. The phenomenon of plunging density currents has been extensively investigated in the field (Hebbert et al., 1979; Ford and Johnson, 1983; Cao, 1992) and in the laboratory (Singh and Shah, 1971; Hauenstein and Dracos, 1984; Akiyama and Stefan, 1984; Akiyama and Stefan, 1986; Lee and Yu, 1997) to determine the water depth at which plunging occurs. Recently, plunging has been investigated numerically by Bournet et al. (1999). The plunge phenomenon can be defined as the transition from a homogeneous open channel flow to stratified, entraining underflow.

This gravity-induced movement of one fluid under another fluid, caused by density differences between the two fluids, is commonly referred to as density or gravity current. Other gravity currents in the environment are cold fronts, cold water cascading in lakes, avalanches, duststorms, or lava flows. A well illustrated general review on gravity currents in the environment and in the laboratory is given by Simpson (1997). Gravity currents caused primarily or entirely by the presence of sediment in the turbid water flowing as a bottom current beneath an overlaying layer of clear water are called turbidity currents. When a lake is stratified, and the density of turbid water is not large enough, it can plunge to the top of the thermocline and travel on top of the colder bottom water as an interflow (Lavelli et al., 2002). A general review of the methods commonly used in the analysis of the various flow regimes occurring when density currents enter lakes and reservoirs is presented by Alavian et al. (1992).

When a turbidity current is initiated, it typically contains a wide range of

Figure 1.3: Sediment-laden Rhone River plunging into Lake Geneva and inducing a turbidity current (Ch. Oehy).

suspended particle sizes, including the particle sizes that cannot be maintained in suspension by the turbulence within the current, but not yet settled out of suspension. Settling of larger particles reduces the density difference, and the gravitational force which maintain the flow, causing the velocity to decrease, and the current to disintegrate. Therefore, turbidity currents induced by small floods or snowmelt seldom reach the dam. This process also causes a longitudinal reduction in the grain size of the suspended solids carried by the current and deposited along the bottom of the reservoir.

To travel long distances, the velocity of a turbidity current must be sufficient to exert a shear stress on the bed capable of eroding additional sediments, and to generate a sufficient turbulence intensity to maintain these sediments in suspension, thereby maintaining its driving force. On steep bed slopes, the density and velocity of the current may even increase along its path due to sediment erosion. As the bed shear stress increases further, more sediment is entrained and a self-reinforcing cycle is created which allows the development of an auto-sustaining turbidity current that can gradually reach high speeds. Only the availability of sediments for entrainment at the bottom, the reservoir geometry or eventually the damping of turbulence at high sediment concentrations will limit the growth of such a gravity-driven flow.

When the turbidity current reaches a barrier such as the dam, its kinetic energy is converted into potential energy as the current rises up against the face of the dam and subsequently falls back down, initiating the formation of a muddy layer. After some time the fine sediment deposits can cover the bottom outlets and power intakes, both of which are often located near or

at the dam. Therefore, the reservoir sediment not only reduces water-storage capacity, but it also increases the risks of blockage of bottom outlets and of sediment entrainment into the waterway systems of hydropower schemes.

The earliest records of turbidity current flows in a reservoir were made in 1919 at Elephant Bute Reservoir on the Rio Grande in the United States, where the inflow suspended-sediment concentration was 72 g/l (2.7% by volume). Similar observations were made 1921 to 1935 by Lane and Koelzer (1943). Data collected during the measuring campaigns on sedimentation and turbidity currents in Lake Mead, created by the Hoover Dam, conducted by the U.S. Bureau of Reclamation from 1935 to 1936 were reported by Grover and Howard (1938) and later by Howard (1953). Turbidity currents in Lake Mead travelled for distances of 129 km to reach the dam. In China, systematic measurements of turbidity currents were made in Guanting Reservoir in the 1960's and at the Luijiaxia Reservoir in the 1970's, both on the Yellow River. Theoretical and experimental investigations on turbidity currents started only later. Bell (1942) has carried out extensive experimental work in flumes and has emphasized the importance of turbidity currents in sedimentation of reservoirs. During the 1950's and later, aware of reservoir sedimentation problems created by turbidity currents in Algeria and France, experimental and theoretical studies of turbidity currents were undertaken in France (Nizéry et al., 1953; Thévenin, 1960). Pyrkin and Samolyubov (1978) showed that a bottom density current exists in the Nurek Reservoir and that the bottom current transports the bulk of suspended sediments in the reservoir. Graf (1983) mentioned that a proper knowledge of the hydraulic behavior of density currents throughout the reservoir might be useful to the determination of the loss of storage capacity as a result of settling out of the suspended matter. In Switzerland, Bezinge and Aeschlimann (1989) measured turbidity currents with velocities up to 0.5 m/s created by pump storage operation. Fan (1986) and Fan and Morris (1992a) described patterns of sediment deposition and erosion on field measurements and density current data for reservoirs in China. Chikita (1990) presented field measurements of river-induced turbidity currents in the Hokkaido Reservoir in Japan. In order to clarify the flow mechanism of river-induced turbidity currents in Alpine reservoirs, field observations of turbidity currents were carried out in the Luzzone Reservoir and its main inflow river (Sinniger et al., 1994; De Cesare, 1998; De Cesare et al., 2001). The in-situ observations confirmed that turbidity currents are the main transport medium for the incoming fine suspended sediments and that they largely contribute to the redistribution of the sediments within the reservoir by entraining sediment particles, and carrying them to the deepest areas of the reservoir. A review of case studies dealing with reservoir sedimentation due to turbidity currents is also given by Morris and Fan (1998).

1.2 Measures Against Reservoir Sedimentation

Recent books on the state of the art of dealing with reservoir sedimentation are presented by Morris and Fan (1998), Batuca and Jordaan (2000) and by the International Comittee on Large Dams (ICOLD) (1996). A number of case studies for the removal of deposited sediments and compensation of reservoir silting are also described in detail. Here, the known measures are shortly summarized and the reader is referred to the literature for detailed information and guidelines. As shown in Fig. 1.4, the measures against reservoir sedimentation can be classified in three major groups depending on the location where they are applied (Schleiss and Oehy, 2002).

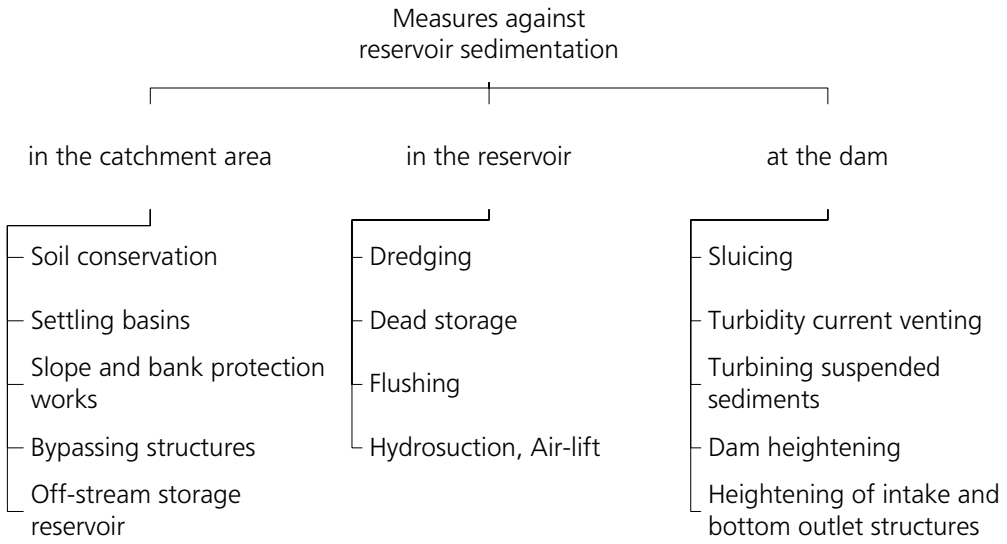

Figure 1.4: Inventory of known measures against reservoir sedimentation.

A reduction of sediment yield by soil conservation in the catchment area can be very effective, and can solve the reservoir sedimentation problem in a sustainable way. Where the climatic conditions allow vegetation practices, the soil can be protected from erosion by afforestation or vegetation screens. However, these measures are very complex and often related to other agricultural techniques. In catchment areas without vegetation, as for example the high Alpine catchment areas, erosion protection can only be achieved with engineering measures such as gully control, as well as slope and bank protection works on rivers.

Settling basins are often constructed in the catchment area to limit gully erosion. The small size dams trap only the coarser sediment particles and the sediment load quickly builds up again downstream. Therefore, this measure seldom has a major impact on the sediment yield. The construction of such debris trap dams in the upper catchment areas may be a solution; but without

proper regular maintenance, these will fill up by bed load transport very quickly and in the long term they serve no purpose. A further problem with upstream sediment trap dams is finding a place for continuous, long-term disposal of the incoming sediments, which accumulate indefinitely. Often the settling basins are also too small to significantly affect the sediment yield into the reservoir. This led to the idea of catching the sediment-laden current upstream of the reservoir and releasing it downstream, by means of bypass tunnels.

It is well known that the sediment yield is closely related to the characteristics of the catchment area. Reservoirs which have a small catchment area or which are off-stream may be supplied by waterways systems from neighboring catchment areas with the condition that the intake structures of the waterways system have sediment traps. For rivers transporting large volumes of coarse materials, from cobbles to coarse sands, it is possible to extract the materials regularly or continuously from the delta near the upstream end of the reservoir. Such extracted materials can often be used as construction materials.

The most common method to conserve the storage capacity is to oversize reservoirs, i.e. to keep some of the volume available for sedimentation. In case this volume is not available for reservoir operation, it is called dead storage.

Sediment flushing of reservoirs is a technique whereby previously accumulated and deposited sediments in a reservoir are hydraulically eroded and removed by accelerated flows created when the bottom outlets of the dam are opened and the reservoir water level is drawn down. Flushing will prove more effective, when the head on the sluice is low, the sluice is wide, the discharge available is large, the duration of flushing is long, and the bottom slope is steep. Quantitative criteria for assessing the feasibility of flushing sediments from reservoirs are developed by Atkinson (1998). The flushing method is often associated with a host of adverse environmental impacts. Generally, flushing operations must be conducted with the aim of limiting the impact on the downstream reaches of the river (Office fédéral de l'environnement, des forêts et du paysage (OFEFP), 1994). Moreover, legal requirements may restrict or prohibit the practice of removing solids from surface waters and reintroducing them into the flow at a later time (Suter, 1998; Boillat and Pougatsch, 2000).

Hydrosuction removal systems remove deposited sediments by using the available energy head due to the difference between water levels upstream and downstream of a dam. Hotchkiss and Huang (1995) describe the design of such a system and presented some field tests. The main problem with a gravity suction system is that the approach flow velocities drop very quickly as the radial distance from the suction point increases, and beyond a short distance sediments are no longer entrained into the suction pipe. To be efficient, the suction end of the pipe would have to be repositioned almost continuously. But

with a long pipe length and high sediment volume, the head loss may increase dramatically, choking the pipeline (Alam, 1999). A special suction system was presented by Jacobsen (1998) and consists of a slotted pipe which is laid on the reservoir bottom. The sediments are then evacuated by suction either through the bottom outlets or over the spillway. Huwiler (2002) presented some preliminary tests for a new approach for resuspension of fine sediments by an air-lift system and evacuating the sediments within an acceptable range of concentration through the intake structures.

While a partial or full drawdown of the reservoir water level is required for most hydraulic removal techniques, a lesser amount of water is lost in mechanical removals by dredging. Generally, this measure is only cost effective for localized sediment removal operations (Scheuerlein, 1992).

In areas with abundant runoff the sediment can be kept in suspension and released through the sluices in the dam by fully or partially drawing down the water level during the entire flood season (Shen, 2000). This method is called sluicing. A special case of sluicing is initiated by opening a bottom outlet near or in the dam during periods of high inflow without significantly drawing down the water level. The heavy sediment suspension then flows down along the thalweg as a turbidity current, therefore this method is also often referred to as turbidity current venting. Operation rules for the reservoir control require a knowledge of the behavior of turbidity currents in order to open the bottom sluices at the right moment, and to reduce water loss during the operation (Graf, 1983; Fan and Morris, 1992b; Rémini, 2000). An early application of this method, where submerged dykes were used to concentrate the turbidity current in a narrow channel, was presented by Schaad (1979).

The sediment-laden water is usually released through bottom outlets, sluice gates or bypass tunnels. An ideal solution is to use it for power generation. Recent developments in turbine coating allow much higher sediment concentrations without significant increase in abrasion damage. Specially designed turbines could be installed to allow the passage of the fine sediments within controlled concentration ranges (Grein and Schachenmann, 1992; Grein and Krause, 1994).

The heightening of a dam is one of the alternatives for compensating for the loss of reservoir capacity due to sedimentation. Although it might be cost effective in the short term, dam heightening does not provide a long term solution of the sedimentation problem. Construction of new dams to solve the sedimentation problem leads to the same problems. Furthermore, suitable dam sites are becoming scarcer.

Finally, with the heightening of the intake and bottom outlet structures the dead storage volume is increased and sediment entrainment into the intakes can be prevented for a certain period.

1.3 Scope and Organization of the Present Study

As presented in Section 1.1, reservoir sedimentation is a problem in reservoirs all over the world. It is well known that especially in Alpine reservoirs, turbidity currents largely contribute to the transport and redistribution of fine sediments inside the reservoir by entraining particles on their way and bringing them to the deeper part of the reservoir. Many measures against reservoir sedimentation are presently used, as described in Section 1.2. In Alpine reservoirs, a common method is certainly the flushing through the bottom outlet, but without completely drawing down the water level this method is only effective in the proximity of the outlet structure. Recently, some cost intensive heightening works of intake and bottom outlet structures were also necessary to overcome the sediment accumulation in the deepest area.

The purpose of the present work is to study new measures which have a retarding effect on the turbidity currents in order to control the sedimentation within Alpine reservoirs. For example, submerged dams or groynes could be introduced to stop the turbidity current upstream of the affected structures or to divert it and favor deposition in areas of the reservoir, which are not significant for operation purposes, but easily accessible for dredging. Similar effects may be obtained by floating permeable screens which retain some sediment-laden fluid and diminish the driving force of the turbidity current. Finally, external energy could be injected by means of water jets or bubble curtains to dilute the turbidity current and eventually stop it. In the case of bubble curtains, the fine sediments could be maintained in suspension to prevent their sedimentation and favor their evacuation through the intake structures. The concentrations of the suspended sediment particles should be kept within an acceptable range to prevent damage to the hydromechanical equipments. At present, the constructive measures mentioned above are rarely used, primarily due to a lack of knowledge on their performance and cost. An investigation is therefore carried out to analyze their efficiency and their governing parameters by means of physical experiments and numerical simulations.

In Chapter 2, the main physical characteristics of a turbidity current flow are presented, and the literature on effects of obstacles and screens on stratified flows is analyzed. The work on water jets, and bubble curtains in crossflows and stratified environments is reviewed as well.

The experimental installation and the measuring instrumentation are described in Chapter 3. The instrumentation includes a device which was developed to measure the evolution of the deposition during the various experiments.

Chapter 4 presents the results of the experiments with continuously-fed

turbidity currents and with a turbidity current flowing over an obstacle, or through a screen. Furthermore, experiments of a turbidity current flowing through vertical or inclined multiple jets are presented and one experiment with a turbidity current flowing through a bubble curtain is discussed. Finally, conclusions on the physical experiments are drawn.

To further investigate and simulate the effects of obstacles, screens, and water jets, a three-dimensional numerical model, based on the commercial flow solver CFX-4.4, was developed by adding interfaces to take into account the erosion and sedimentation at the bed, fractional suspended sediment transport and the effect of stratification in the turbulence model. The model as well as the user routines which were added to simulate the different experiments are described in Chapter 5.

The experimental results and numerical simulations are compared in Chapter 6. Special attention is paid on the deposition patterns. The efficiency of sediment retention by the different measures allowed conclusions on their performance.

In Chapter 7, the validated numerical model is applied to simulate turbidity currents within the complex topography of Lake Grimsel in Switzerland. The effect of submerged dams on the turbidity current and the sedimentation is investigated.

In Chapter 8, recommendations for possible applications are given and some concluding remarks on the results of the present study are made. Finally, a summary and ideas for further work are provided in Chapter 9.

2 Literature Review and Theoretical Background

2.1 Description of Turbidity Currents

A turbidity current consists of a front or head advancing into the ambient fluid, being followed by the body as illustrated in Fig. 2.1. The driving force for the front is essentially the pressure gradient due to the density difference between the front and the ambient fluid ahead of it. This flow is unsteady and the head grows at it advances. The driving force for the body is the gravitational force of the heavier fluid. The flow in the body is often considered as being steady.

Experimental studies carried out by Middleton (1966) and Altinakar et al. (1990) have shown that the turbidity current head has a well defined shape but a rather complicated internal structure. The front has a height, H_f, at its highest point and a nose which is situated at a small distance, h_f, above the bed. For sufficiently high head Reynolds numbers (>1000), Altinakar et al. (1990) found that the dimensionless nose height h_f/H_f is approximately equal to 0.14.

Various theoretical and experimental relationships have been proposed for the velocity of the turbidity current front, U_f. Using various experiments from turbidity currents – but also from density currents – for a large range of slopes and roughness, a simple and useful relationship was proposed by Middleton (1966), such as

$$U_f = l_1 \sqrt{g' H_f} \tag{2.1}$$

where l_1 is a constant and g' is the reduced gravitational acceleration expressed as

$$g' = g\left(\frac{\rho_t - \rho_a}{\rho_a}\right) = g\frac{\Delta\rho}{\rho_a} = g\,C_s\left(\frac{\rho_s - \rho_w}{\rho_w}\right) \tag{2.2}$$

where g is the acceleration due to gravity, ρ_t is the bulk density of the turbidity current, ρ_a the one of the ambient fluid, C_s the average volumetric sediment concentration with ρ_s being the density of sediment particles and ρ_w the density of water. $\Delta\rho$ is the density excess, which in the case of a turbidity current can range from $\Delta\rho \cong 20$ to 130 g/l.

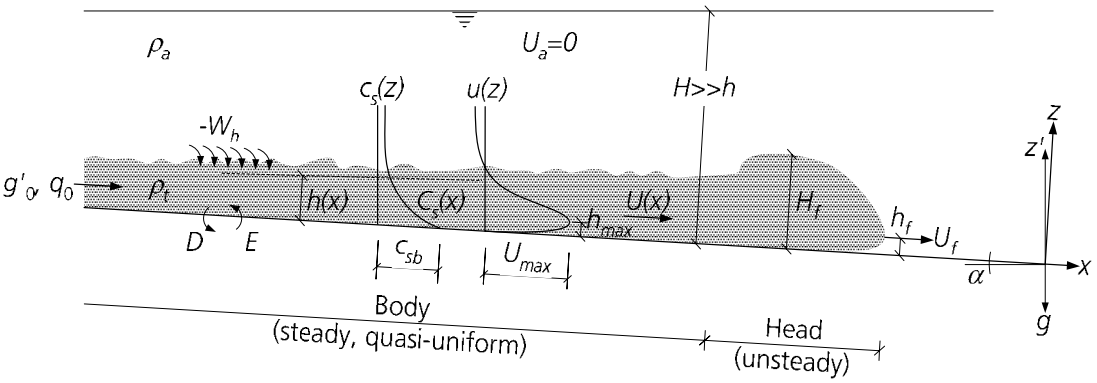

Figure 2.1: Turbidity current flowing down a slope.

The average velocity of the body, U always remains larger than the one of the front, $U > U_f$. This inequality grows as the angle of bottom slope, α, increases. In order to maintain flow continuity, the height of the front will, therefore, always be larger than the one of the body, $H_f > h$. Furthermore, it has been observed by Altinakar (1988), that the velocity of the front, U_f, remains more or less constant and independent of the distance covered by the turbidity current. This implies that the reduced gravity compensates the frictional force. However, for turbidity currents over small slope angles, $\alpha \leqslant 0.5°$, and for depositing ones, the front of the current decelerates slightly. The height of the front, H_f, increases with the distance covered; this is attributed to the entrainment of the ambient fluid.

Following Britter and Linden (1980), the dimensional analysis leads to the following expression for the front velocity,

$$U_f = l_2 B_0^{1/3} \tag{2.3}$$

where l_2 is a constant depending on the slope and the Reynolds number, and B_0 the initial buoyancy flux per unit width is defined as

$$B_0 = g'_0 h_0 U_0 = g'_0 q_0 \tag{2.4}$$

where q_0 is the initial discharge of the current per unit width, g'_0 is the initial reduced gravitational acceleration, h_0 is the initial height, and U_0 the initial velocity of the current.

When the flow is highly turbulent, the dependence of U_f on the Reynolds number can be ignored. As for the constant l_2 in Eq. (2.3), Britter and Linden (1980) obtained experimentally a constant value of 1.5 ± 0.2 for slopes greater than $5° \leqslant \alpha \leqslant 90°$. For slopes less than $\alpha < 5°$, Altinakar et al. (1990), found values varying linearly from 0.7 to 1.5. Choi and Garcia (1995) proposed $l_2 = 1.0$ based on numerical experiments and laboratory data of Altinakar et al. (1990). Furthermore, Altinakar et al. (1990) emphasizes that the relative submergence ratio, between the height of the current and the total water depth h/H is an important parameter in experiments with small slopes.

Cao (1992) presented field measurements of the front velocity of turbidity currents in Chinese Reservoirs. The following formula similar to Eq. (2.3) was proposed

$$U_f = B^{1/3} \left(\frac{8}{\lambda_f} S \right)^{1/3} \tag{2.5}$$

where B is the buoyancy flux, λ_f is a friction coefficient found to be between 0.05 and 0.22, $S = \tan\alpha$ is the bottom slope.

In the body, the interface between the turbidity current and the ambient fluid is usually not easy to distinguish. Therefore, a height, h, and a velocity, U, as shown in Fig. 2.1 are given by integral scales proposed by Ellison and Turner (1959) as

$$Uh = \int_0^\infty u \, \mathrm{d}z = \int_0^{h_t} u \, \mathrm{d}z = q \tag{2.6}$$

and

$$U^2 h = \int_0^\infty u^2 \, \mathrm{d}z = \int_0^{h_t} u^2 \, \mathrm{d}z \tag{2.7}$$

where $u(z)$ is the local velocity, h_t is the height where the velocity, u, is zero. The vertical variation of the volumetric sediment concentration, $c_s(z)$, is a gradual one, notably at the interface and the average concentration, C_s, is defined by

$$C_s U h = \int_0^\infty (u c_s) \, \mathrm{d}z = \int_0^{h_t} (u c_s) \, \mathrm{d}z \tag{2.8}$$

When the integration is performed up to the zero velocity level ($u(h_t)$=0), the entrainment rate includes the influence of the drag of the water above the gravity current. When integration is performed up to the zero concentration level ($c_s(h_t)$=0), only interfacial mixing is taken into account. At low concentrations, the levels of zero velocity and zero concentration nearly coincide, both ways of integration then give nearly the same results (Van Kessel and Kranenburg, 1996).

Altinakar et al. (1996) compared the body of a turbidity current to a wall jet. Two regions can be distinguished: the wall and the jet region. The height, h_{max}, where the maximum velocity, $u = U_{max}$, is measured, separates these regions:

- in the wall region, $z < h_{max}$, turbulence is created at the wall (bottom); entrainment of sediments can take place;

- in the (free) jet region, $z > h_{max}$, turbulence is created by friction and by entrainment of the ambient fluid.

Experimentally Altinakar et al. (1996) found that

$$\frac{h_{max}}{h} \approx 0.3; \quad \frac{U_{max}}{U} \approx 1.3; \quad \frac{h_t}{h} \approx 1.3 \tag{2.9}$$

Turbidity currents differ from the simple conservative density underflows studied by Ellison and Turner (1959) in that the source of the buoyancy difference, i.e. the suspended sediment, is not conserved; suspended sediment is free to exchange with bed sediment by means of bed erosion and deposition. This additional degree of freedom allows for self-acceleration via the entrainment of bed sediment.

In a simple model, the flow in the body of the turbidity current can be considered as two-dimensional and plane, the flow, being turbulent and incompressible. The height, h, the velocity, U, and the concentration, C_s, are average values, defined by the integral scales in Eqs. (2.6)–(2.8). The current moves in the longitudinal direction, x, over a bottom slope, S, under a deep layer, $H \gg h$, of ambient stagnant fluid ($U_a \equiv 0$) the density ρ_a, of which is slightly smaller than the density of the turbidity current, $\rho_a < \rho_t$.

The theory of unidirectional steady gravity flows with entrainment was developed by Ellison and Turner (1959). Parker et al. (1986) extended the model to describe the flow of turbidity currents, and used first a conventional three-equation model, based upon the conservation of momentum, fluid mass and mass of sediment. The conservation of mean momentum implies that,

$$\frac{\mathrm{d}}{\mathrm{d}t}\left(Uh\right) + \frac{\mathrm{d}}{\mathrm{d}x}\left(U^2 h\right) = -\frac{1}{2}Rg\frac{\mathrm{d}}{\mathrm{d}x}\left(C_s h^2\right) + gRC_s hS - u_{*b}^2 \tag{2.10}$$

where t is time, $R = (\rho_s/\rho_w) - 1$ is the submerged specific density of the sediment, and u_{*b} is the shear velocity.

The second and third equations conserve fluid (mixture of water/sediment) and sediment, respectively,

$$\frac{\mathrm{d}h}{\mathrm{d}t} + \frac{\mathrm{d}}{\mathrm{d}x}\left(Uh\right) = W_h \tag{2.11}$$

where W_h is the entrainment velocity of the ambient fluid into the current often assumed to be proportional to the velocity of the turbidity current, U, such that Eq. (2.11) becomes after Turner (1973)

$$\frac{\mathrm{d}h}{\mathrm{d}t} + \frac{\mathrm{d}}{\mathrm{d}x}\left(Uh\right) = E_w U \tag{2.12}$$

where the constant of proportionality, E_w, is the entrainment coefficient of ambient fluid, which in turn depends upon the global Richardson number, Ri, or the densimetric Froude number, Fr_D, defined as

$$Ri = \frac{g' h \cos\alpha}{U^2} = \frac{1}{Fr_d^2} \tag{2.13}$$

This non-dimensional number represents the ratio of inertia to reduced gravity forces. Furthermore, a distinction can be made between subcritical flow, where $Ri > 1$ or $Fr_d < 1$, and supercritical flow, where $Ri < 1$ or $Fr_d > 1$ (Turner, 1973).

The conservation equation for the sediment is

$$\frac{\mathrm{d}}{\mathrm{d}t}(C_s h) + \frac{\mathrm{d}}{\mathrm{d}x}(C_s U h) = S_E - S_D \tag{2.14}$$

where S_E is the sediment erosion and S_D the sediment deposition term.

The description of these erosion and deposition terms follows the ideas of Parker et al. (1986) with the closure relations proposed by Garcia and Parker (1993). The equation of continuity for the solid phase in a steady two-dimensional case approximates the equation of diffusion of granular material.

$$\frac{\partial(uc_s)}{\partial x} + \frac{\partial(wc_s)}{\partial z} = v_{ss}\frac{\partial c_s}{\partial z} + \varepsilon_s \frac{\partial^2 c_s}{\partial z^2} \tag{2.15}$$

where u and w are the horizontal, vertical velocity, v_{ss} is the settling velocity and ε_s is the diffusion coefficient of granular material. The diffusion term can be expressed by Elder's relation:

$$\varepsilon_s \frac{\partial^2 c_s}{\partial z^2} \cong -\frac{\partial}{\partial z}\left(\overline{c_s' w'}\right) \tag{2.16}$$

where $\overline{c_s' w'}$ is the vertical Reynolds flux of the sediments, with w' being the fluctuation of the vertical velocity and c_s' being the fluctuation of the volumetric sediment concentration.

In order to obtain the sediment mass exchanges at the bottom, Eq. (2.15) can be integrated vertically over the entire height, $0 < z < h_\mathrm{t}$, of the turbidity current and evaluated at a level $z = b$ close to the bottom

$$\frac{\partial}{\partial x}\int_0^{h_t}(uc_s)\,\mathrm{d}z = -v_{ss}c_s\,|_{z=b} + \overline{c_s' w'}\,|_{z=b} \tag{2.17}$$

Parker et al. (1987) further proposed that

$$S_E = \overline{c_s' w'}\,|_{z=b} = v_{ss}E_s \tag{2.18}$$

where $v_{ss}E_s$ represents the erosion of sediments per unit area, with E_s as the entrainment coefficient of sediments from the bed, and that

$$S_D = -v_{ss}c_s\,|_{z=b} = -v_{ss}c_{sb} \tag{2.19}$$

where $v_{ss}c_{sb}$ represents the deposition of sediments per unit area on the bed and c_{sb} is the local volumetric sediment concentration close to the bed at a

distance of $b \cong 0.05\, h_t$. The conservation equation for the sediment is therefore

$$\frac{\mathrm{d}}{\mathrm{d}t}\left(C_s h\right) + \frac{\mathrm{d}}{\mathrm{d}x}\left(C_s U h\right) = v_{ss}\left(E_s - c_{sb}\right) \tag{2.20}$$

This three-equation model was solved numerically with the result that, under certain initial conditions, the flow accelerates strongly and consumes more turbulent energy than is available form the flow. This led to introducing a fourth equation in which the turbulence production rate is specifically dealt with through the conservation of the mean value of kinetic energy of turbulence,

$$\begin{aligned} &\frac{\mathrm{d}}{\mathrm{d}t}\left(K h\right) + \frac{\mathrm{d}}{\mathrm{d}x}\left(K U h\right) = u_{*b}^2 U + \frac{1}{2} U^3 E_w - \epsilon_0 h \\ &- RgC_s h v_{ss} - \frac{1}{2} RgChE_w - \frac{1}{2} Rgh v_{ss}\left(E_s - c_{sb}\right) \end{aligned} \tag{2.21}$$

where, K is the mean kinetic energy of turbulence computed in the same manner as the mean concentration in Eq. (2.8), and ϵ_0 the mean rate of turbulent kinetic energy dissipation due to viscosity.

In Eqs. (2.10), (2.12), (2.20), and (2.21) it is still necessary to specify the entrainment parameters, E_w, E_s, and the friction velocity, u_{*b}. These parameters are given with empirical relations.

Many experiments (notably in the laboratory) with different types of density and turbidity currents for large Reynolds numbers have been carried out and the entrainment coefficient, E_w, was related to the global Richardson number, Ri by the following empirical relationship proposed by Parker et al. (1987)

$$E_w = 0.075\left(1 + 718 Ri^{2.4}\right)^{-0.5} \tag{2.22}$$

If $Ri \to 0$, $E_w \cong 0.075$ such a value is obtained for a non-buoyant jet. If $Ri \simeq 1$, $E_w \simeq 0.003$ such a value is obtained if the entrainment of ambient fluid is negligible, notably for $Ri > 1$, when the flow is subcritical at weak slopes of the bed.

The equation of continuity for the solid phase, Eq. (2.20), requires a value for the entrainment coefficient of the sediments, E_s. The experiments, performed in open-channel flows with sediment transport (Akiyama and Stefan, 1985), and in flows of turbidity currents (Parker et al., 1987; Garcia, 1989), show that the following empirical relation, proposed by Garcia and Parker (1993), can be used.

$$E_s = \frac{1.3 \cdot 10^{-7}\, Z_u^5}{1 + 4.33 \cdot 10^{-7}\, Z_u^5} \tag{2.23}$$

where Z_u is a dimensionless parameter defined by

$$Z_u = \frac{u_{*b}}{v_{ss}} f\left(Re_p\right); \text{ with } f\left(Re_p\right) = \begin{cases} Re_p^{0.6}, & Re_p \geqslant 3.5 \\ 0.586\, Re_p^{1.23}, & Re_p < 3.5 \end{cases} \tag{2.24}$$

where $Re_p = \frac{\sqrt{RgD_s}D_s}{\nu}$ is the particle Reynolds number based on the characteristic sediment size D_s and ν the kinematic viscosity of water. This relation, as shown on Fig. 2.2, is rather steep and arrives at a maximum constant value where the entrainment coefficient is about $E_s \cong 0.3$. The four-equation model by Parker et al. (1986) explicitly links the sediment erosion to the level of turbulence, rather than to the shear velocity. This linkage is defined by the relationship

$$u_{*b}^2 = \alpha_K K \tag{2.25}$$

where α_K is a dimensionless constant, such that the effective shear velocity is determined by turbulence and is uncoupled from the actual mean flow speed. This means that the sediment entrainment coefficient E_s is also determined by the turbulence level. Turbulence is generated at the boundary, is dissipated viscously within the flow, is diluted by entrainment of ambient water, dissipated by sediment entrainment, sediment suspension, and elevation of the sediment within the flow as the flow thickens. This provides a limit on growth of the flow, because the work of entraining increasing amounts of sediment into suspension eventually removes more energy from turbulence than can be provided through boundary shear.

An independent expression for the viscous dissipation rate ϵ_0 is proposed by Parker et al. (1986) as following

$$\epsilon_0 = \beta \frac{K^{3/2}}{h} \text{ with } \beta = \frac{\frac{1}{2}E_w\left(1 - Ri - 2\frac{C_{D*}}{a}\right) + C_{D*}}{\left(\frac{C_{D*}}{a}\right)^{3/2}} \tag{2.26}$$

where C_{D*} is a bed friction coefficient. The reference concentration, c_{sb} being evaluated close to the bed, $b \cong 0.05h_t$, is given by

$$c_{sb} = r_0\, C_s; \text{ with } r_0 = 1 + 31.5\left(\frac{v_{ss}}{u_{*b}}\right)^{1.46} \tag{2.27}$$

Garcia and Parker (1993) found that r_0 is independent of the dimensionless shear velocity u_{*b}/v_{ss} having a constant value $r_0 = 2.0$.

The settling velocity, v_{ss}, can be calculated with different methods described in the literature. For very fine particles the Stokes equation (Graf, 1971) can be used to calculate the settling velocity

$$v_{ss} = g\frac{\rho_s - \rho_w}{\rho_w}\frac{1}{18\nu}d^2 \tag{2.28}$$

where d is the sediment particle diameter.

It is of interest to note that for the case of a simple conservative density current, for which $v_{ss} = 0$, Eqs. (2.10), (2.12) and (2.20) reduce to the relations of Ellison and Turner (1959).

Bühler and Siegenthaler (1986) conducted experiments to support the concept of approximate self-preservation of turbidity currents and proposed

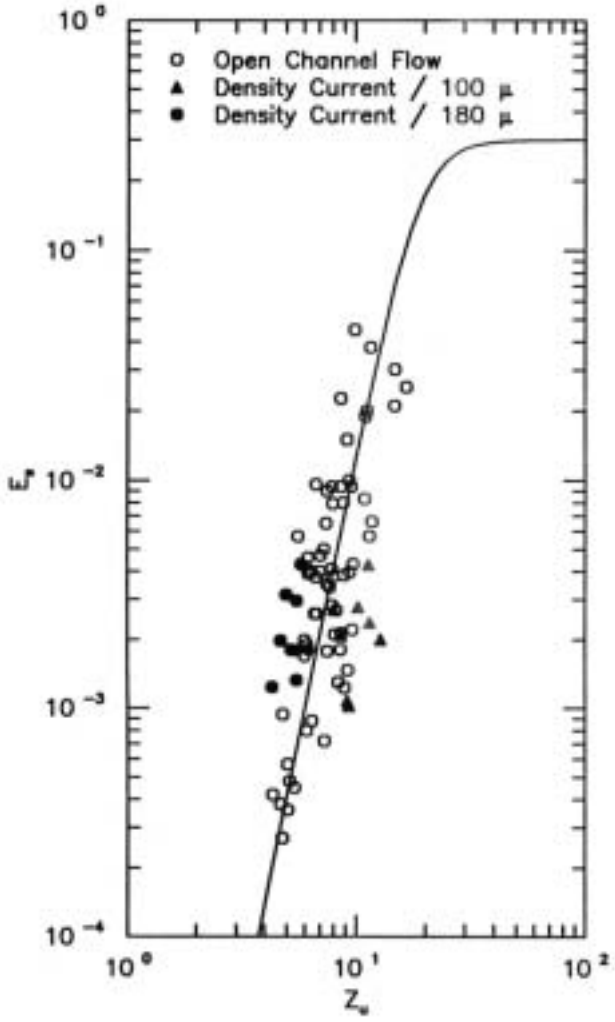

Figure 2.2: Sediment entrainment coefficient, E_s, as a function of the dimensionless parameter Z_u (after Garcia (1993)).

new scales of the dense layer based on the concentration distribution. They modified an approach by Bagnold (1963) to relate erosion or deposition rates to the flow dynamics. Hauenstein (1982) and Hauenstein and Dracos (1984) studied three-dimensional density currents over a sloping bottom. They obtained the similarity solutions for the longitudinal and lateral spreading distances in the buoyancy-dominated region and compared them with the experimental observations. Schläpfer (1990) analyzed the effects of the return flow in the ambient and the bottom roughness on plane steady density currents on inclines. He proposed a mathematical model which consisted of an integral two-layer model, a new entrainment model and a turbulence model describing the impact of stratification. The theoretical calculations were verified by a series of experiments. Other mathematical descriptions of unsteady density currents have been developed by Kranenburg (1993a) and Kranenburg (1993b) using a two-layer model.

The sedimentation patterns of turbidity currents are of great interest in oceanography and earth sciences. Bonnecaze et al. (1996) presented a theoretical model for lock-release flows based on equations similar to Eqs. (2.10), (2.11) and (2.20) and compared the theoretical predictions against data obtained from laboratory experiments. They proposed a simple algebraic method to compute the mass deposited per unit area, and the distribution of particle sizes within deposits arising from two-dimensional currents. The influence of the upper ambient layer has been integrated in Bonnecaze's model by Moodie et al. (2000). Furthermore, the settling velocity was modified to take into account the turbulent energy decay. The computations showed a peak deposition for each particle size depending on the settling velocity. The sediment deposits of an axisymmetric turbidity current were investigated by Dade and Huppert (1995).

2.2 Flow Over an Obstacle

The investigation of the effects of obstacle on the behavior of a gravity current have a wide range of practical applications; for example on the control of accidental escapes of dense gases or in the understanding of small-scale atmospheric flow over mountains and hills. When a density current meets an obstacle some of the denser fluid may flow over the obstacle while a hydraulic jump or bore travels upstream. To examine the effects of obstacles on density current flows the shallow-water analysis has widely been used (Long, 1954; Long, 1970; Turner, 1973; Greenspan and Young, 1978; Rottman et al., 1985; Lane-Serff et al., 1995). In the following developments and descriptions the densimetric Froude number, Fr_d, is used instead of the Richardson number, Ri, in order to establish the comparison with open-channel flows.

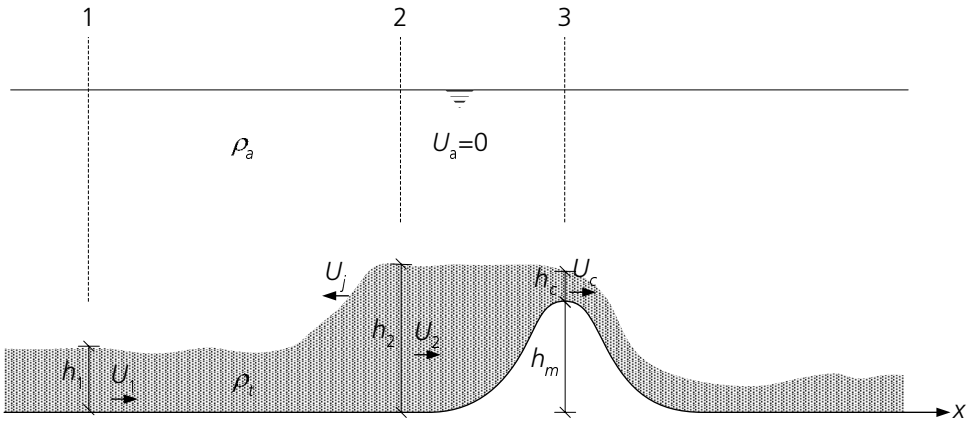

Figure 2.3: Flow over an obstacle.

Consider the partially blocked flow over an obstacle of maximum height h_m of a two-layer fluid, as illustrated in Fig. 2.3. The figure shows for the lower layer a constant upstream depth h_1 and speed U_1, a moving hydraulic jump propagating upstream with speed U_j and a downstream depth h_2 with smaller speed U_2, and finally the critical flow over the obstacle of height h_m. The lower layer has density ρ_t whereas the upper layer has infinite depth and density ρ_a. If the motion of the upper fluid can be ignored ($U_a \cong 0$), the flow has many features in common with the free-surface hydraulics and the shallow-water approximation is valid (Rottman et al., 1985). If the water entrainment and friction can be neglected ($E_w \equiv 0; u_{*b} \equiv 0$), as well as no erosion and deposition occurs ($v_{ss} \equiv 0$), Eqs. (2.10), (2.12) and (2.20) can be combined and simplified to

$$\frac{\mathrm{d}h}{\mathrm{d}t} + \frac{\mathrm{d}}{\mathrm{d}x}(Uh) = 0 \tag{2.29}$$

and

$$\frac{\mathrm{d}U}{\mathrm{d}t} + U\frac{\mathrm{d}U}{\mathrm{d}x} + g'\frac{\mathrm{d}}{\mathrm{d}x}(h_m + h) = 0 \tag{2.30}$$

where h_m is the bottom elevation along the obstacle. The symbol U in these equations represents the horizontal fluid speed vertically averaged over the lower layer. These equations, called the Saint-Venant equations, are derived by Graf and Altinakar (1998) among many others. The flow over an obstacle is characterized by two independent variables, namely the densimetric Froude number of the approaching flow, $Fr_{d1}^2 = U_1^2/(g'h_1)$, and the dimensionless ratio $H_m = h_m/h_1$ of the obstacle height to the height of the oncoming flow.

Steady solutions to these equations are sought by setting the partial derivatives with respect to time equal to zero. The equations then reduce to

$$Uh = U_1 h_1 \tag{2.31}$$

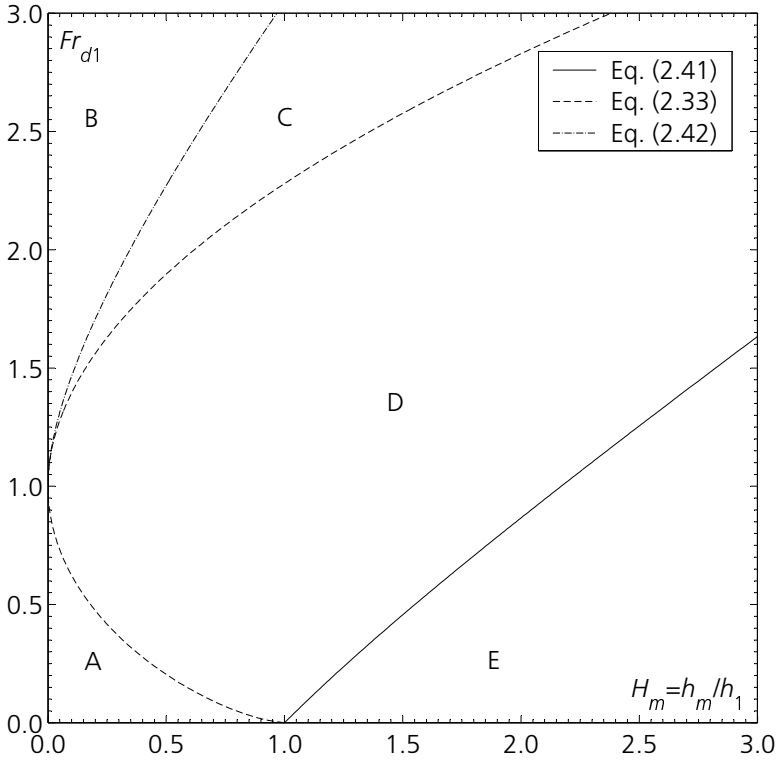

Figure 2.4: Flow regimes for shallow-layer flow over an obstacle with $Fr_{d1} = U_1/\sqrt{g'h_1}$ and $H_m = h_m/h_1$.

and

$$\frac{U^2}{2g'} + h_m + h = \frac{U_1^2}{2g'} + h_1 \tag{2.32}$$

where U_1 and h_1 are upstream values of U and h. It can be shown that for each value of Fr_{d1} a limit $H_m = H_{mc}$ exists, at which the flow on the crest becomes critical. No physically meaningful, steady solution is found for $H_m > H_{mc}$. The equation for H_{mc} can be found by writing the Bernoulli's equation between section 1 and 3 on Fig. 2.3. Its solution is plotted in Fig. 2.4 as a long-dashed line and given by (Long, 1954) as following

$$H_{mc} = 1 + \frac{Fr_{d1}^2}{2} - \frac{3}{2}Fr_{d1}^{2/3} \tag{2.33}$$

Steady flow is possible only to the left of this curve. Supercritical flow occurs in the regions B and C, whereas in region A the flow is subcritical. (A detailed discussion of the regions B and C will follow.) For a flow approaching an obstacle of any height, no steady state solution exists. The main goal of an obstacle, however, is to block the turbidity current either completely or partially. The flow will be partially blocked when H_m is increased above H_{mc} (region D). An internal bore, i.e. a moving hydraulic jump, is then formed

which propagates upstream with velocity U_j (see Fig. 2.3). This internal bore dissipates energy in order to match this steady solution to the upstream flow condition.

The conditions that must be satisfied at the jump are the equation for conservation of mass and momentum (Graf and Altinakar, 1998) written in a reference frame moving with the jump at velocity, U_j. It is assumed that the internal bore moves upstream at a steady speed.

$$(U_1 - U_j)\, h_1 = (U_2 - U_j)\, h_2 \tag{2.34}$$

$$(U_1 - U_j)^2 = \frac{1}{2}\,(g' h_1)\,\frac{h_2}{h_1}\left(1 + \frac{h_2}{h_1}\right) \tag{2.35}$$

The requirement $h_2 > h_1$ ensures that energy is dissipated. Combining Eqs. (2.34) and (2.35) yields the following relation

$$H_j = \frac{h_2}{h_1} = \frac{1}{2}\left(\sqrt{1 + 8Fr_{d1}^2} - 1\right) \tag{2.36}$$

which is analogous to Belanger's equation for single-phase open-channel flow hydraulic jumps. Garcia (1993) conducted laboratory experiments to observe the behavior of turbidity and saline currents in the vicinity of a slope transition inducing a hydraulic jump. The experimental data agreed well with Eq. (2.36) and both, turbidity and saline currents, showed the same characteristics. Furthermore, a significant reduction in bed shear stress downstream of the jump was observed.

In the flow over an obstacle, it is further assumed that the flow over the crest is critical and steady.

$$U_c = \sqrt{g' h_c} = \sqrt{g'(h_2 - h_m)} \tag{2.37}$$

where U_c is the critical velocity of the fluid flowing over the crest and h_c is the critical height. In Eq. (2.37) the variation of the internal surface between section 2 and 3 is neglected.

Using mass conservation between sections 2 and 3 in Fig. 2.3, Eq. (2.37) can be expressed in terms of U_2 as

$$U_2^2 = \begin{cases} (g' h_2)(1 - h_m/h_2)^3, & \text{if } h_m/h_2 < 1 \\ 0, & \text{if } h_m/h_2 \geqslant 1 \end{cases} \tag{2.38}$$

If $h_m/h_2 < 1$, the Eqs. (2.34), (2.35), and (2.38) can be combined to yield two equations for $H_j = h_2/h_1$ and U_j in terms of the given quantities Fr_{d1} and the non-dimensionalized obstacle height, $H_m = h_m/h_1$:

$$U_1 - (1 - H_j)U_j = U_2 H_j = (g' h_1)^{1/2}\,[H_j(1 - H_m/H_j)]^{3/2} \tag{2.39}$$

$$(U_1 - U_j)^2 = \frac{1}{2}(g'h_1)H_j(1 + H_j) \tag{2.40}$$

If $h_m/h_2 \geqslant 1$, then $H_j = H_m$ is constant and the equation for the curve delineating partially from completely blocked flow is given by Baines (1995) and plotted in Fig. 2.4 as solid line

$$Fr_{d1}^2 = (H_m - 1)^2 \left(\frac{H_m + 1}{2H_m}\right) \tag{2.41}$$

In region E, the obstacle is high enough to block the approaching flow completely.

By setting $U_j = 0$ in the above equation, another steady solution without partial blocking was found by Long (1970). H_m as function of Fr_{d1} is the given by

$$H_m = \frac{(8Fr_{d1}^2 + 1)^{3/2} + 1}{16Fr_{d1}^2} - \frac{1}{4} - \frac{3}{2}F_{d1}^{2/3} \tag{2.42}$$

and shown as a dotted line in Fig. 2.4. In region C, a hysteresis exists and the flow will be either supercritical or partially blocked.

Solutions of Eqs. (2.39) and (2.40) in the relevant parameter range are plotted in Fig. 2.5. The values of Fr_{d1} shown in the plot are those appropriate for most gravity currents. A general conclusion that may be drawn from this plot is that $1.5 < h_2/h_1 < 2.5$ for most cases of interest, and a good rule of thumb is that $h_2/h_1 \approx 2$ (Rottman et al., 1985; Lane-Serff et al., 1995; Prinos, 1999). The flow is blocked in the region to the right of the long-dashed line ($H_j = H_m$) and partially blocked in the region of the left.

The proportion of the incoming current that continues over the obstacle, η, can then be calculated by Eq. (2.43) and is shown in Fig. 2.6.

$$\eta = \frac{q_c}{q_1} = \frac{\sqrt{g'h_c^3}}{U_1 h_1} = \frac{\sqrt{g'(h_2 - h_m)^3}}{U_1 h_1} \tag{2.43}$$

where q_c is the critical discharge per unit width over the crest.

The above ideas have been generalized to apply to several layers having arbitrary depths and velocities, notably by many authors (Long, 1954; Long, 1970; Wood and Simpson, 1984; Lane-Serff et al., 1995). Long (1954) concentrated on the case of comparable depths and equal velocities, simulating this experimentally by moving an obstacle through a tank containing immiscible layers, initially at rest. He demonstrated the various regimes of flow over the obstacle and the jump phenomena. Long (1970) considered the case of different velocities in the two layers. Lane-Serff et al. (1995) examined two-dimensional currents over obstacles by lock-exchange laboratory experiments with a triangular obstacle, where the investigation concentrated on the case of no net flow, so that there was a return flow in the (finite depth) upper layer.

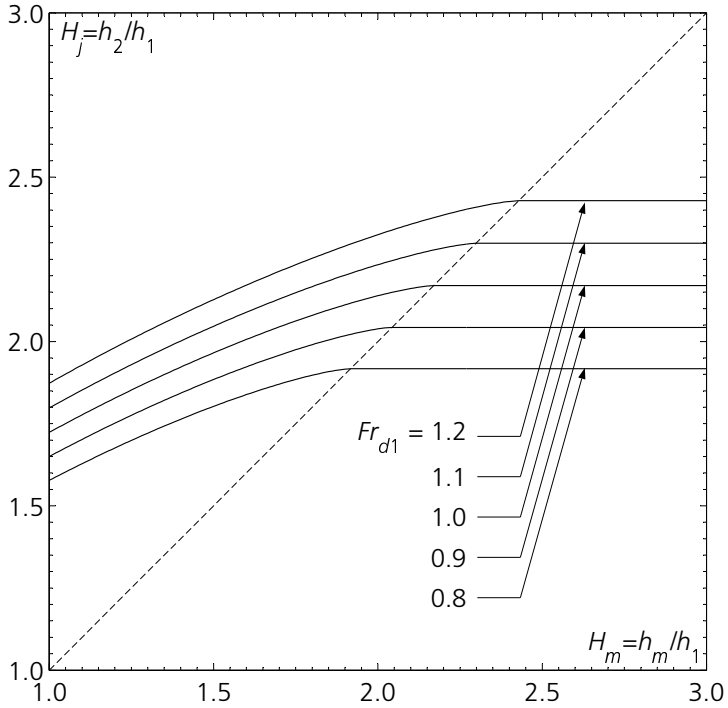

Figure 2.5: Solutions of the steady shallow-water equation for the non-dimensional jump height $H_j = h_2/h_1$, as a function of the non-dimensional obstacle height $H_m = h_m/h_1$, as illustrated in Fig. 2.3.

Lane-Serff et al. (1995) considered three types of conditions for the top of the upper layer: a passive, a rigid lid and a free surface condition. The predictions for the proportion of the flow that continues over the obstacle, the speed of the reflected jump and the depth of the reflected flow were compared with the laboratory experiments and gave reasonable agreement.

Prinos (1999) studied the effects of semicircular and triangular obstacle geometries with the same heights on the motion of two-dimensional, horizontal, density currents. He found that there is no significant effect of the obstacle geometry on the front velocity and the proportion which continues over the obstacle. He also found that for the experiments with $0.7 \leqslant Fr_{d1} \leqslant 0.8$, the flow is completely blocked if $h_m/h_1 \geqslant 2$, which is in agreement with Fig. 2.5. The experimentally found proportion of the incoming flux that continues over the obstacle was compared with predictions, based on theoretical considerations of Lane-Serff et al. (1995). The agreement between observed and theoretical values was satisfactory for all experiments.

For obstacles and for simple ridges or slopes at some angle to the oncoming flow, the reflected jump will be complicated and three-dimensional even if the oncoming flow was two-dimensional. The relation between the angles of the barrier to the oncoming current and to the reflected jump are of some interest as they have implications for estuarine mixing and sediment

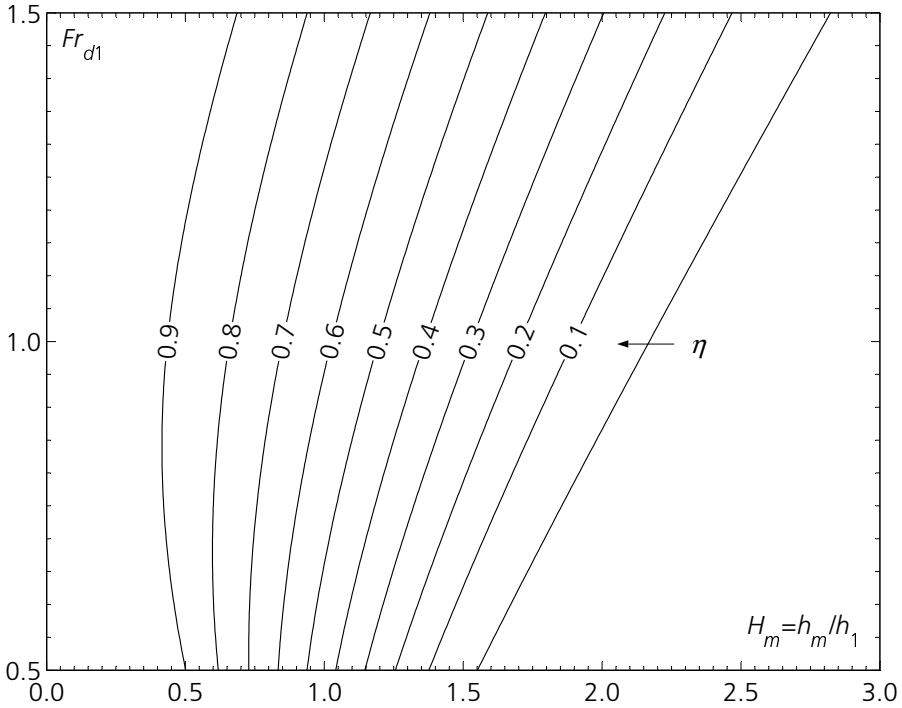

Figure 2.6: Contours showing the proportion of the incoming flow that is predicted to continue over the obstacle, as a function of non-dimensional obstacle height and upstream Froude number.

reworking in the oceanographic context (Kneller et al., 1991; Edwards, 1993). Alexander and Morris (1994) investigated the influence of three-dimensional topography on the deposits and spreading of high-density (10% to 15% by volume), coarse-grained turbidity currents in experiments that concentrated on simple, wedge-shaped obstacles, representing tilted fault blocks, with heights of the same order as the thickness of the flow on a flat tank floor. Particle size, initial particle concentration, and tank floor configuration were varied independently, and the flow paths, sediment distribution, and surface features were recorded. These small topographic features significantly altered sediment distribution.

Bursik and Woods (2000) conducted also a number of turbidity current experiments on geometrically scaled topographic features in order to gain some insight into the general principles of sedimentation patterns produced by a flow passing over a complex topography. They examined the effect of a low, cylindrical ridge. The height of the obstacle compared to the current was small and therefore no upstream flow effects occurred and no significant effect on the deposition patterns could be observed. They also examined the effect of a localized reduction in channel width creating a partial blocking of the current, where in some configurations bores propagated upstream. Experiments, in which such a bore was generated, produced sedimentation patterns strikingly different from those observed in the absence of the bore.

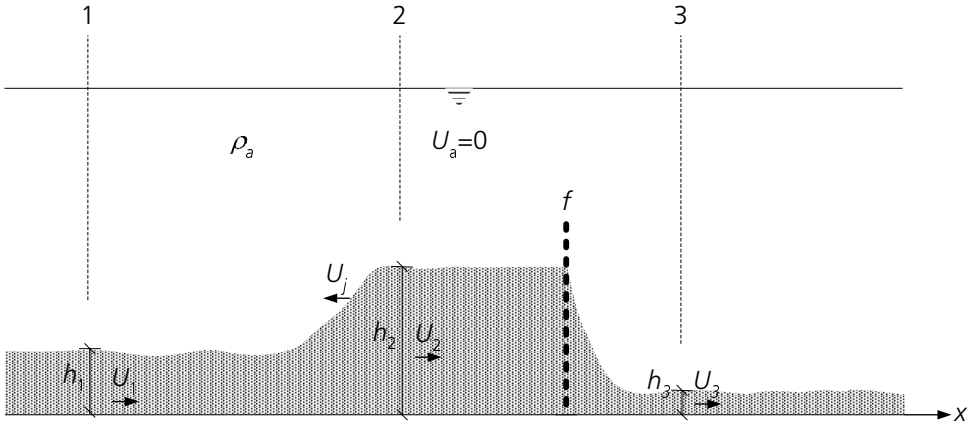

Figure 2.7: Flow through a screen.

The results indicated that local variations in the channel shape lead to significant alongslope variations in the deposit thickness. Bursik and Woods (2000) concluded that the additional sedimentation upstream of the ridge occurred because of the reflected part of the current, the sediment load of which is deposited upstream of the blocking feature.

Pantin and Leeder (1987) conducted experiments, in straight, narrow tanks, with saline flows meeting an opposing slope and generating reflected solitary waves. Upon reflection, a 'bulge' of fluid was generated that moved in the reverse direction and broke down into a series of smooth, symmetrical waveforms interpreted as train of internal solitary waves. Edwards (1993) and Kneller and McCaffrey (1999) also investigated bore–like solitary waves reflected upon low angled ramps (5° to 20°). The reflected flows were bores (moving hydraulic jumps that transport mass) with flow characteristics similar to those of a group of solitary waves ($1 < h_2/h_1 < 2$) of the original density current.

2.3 Flow Through a Screen

The interaction of a gravity current with a screen, after the transient effects have disappeared, can be solved by a method similar to that used in the case for the obstacle. In analogy to the obstacle, it can be expected, that the gravity current front initially increases in height and forms a moving hydraulic jump, which propagates back along the gravity current body as the flow adjusts to a steady state. Since the screen is permeable, the current front does not climb as high as in the case of an obstacle. The strength of the interaction will depend on the porosity of the wall. This has qualitatively been shown by Rottman et al. (1985) who conducted experiments with a porous region consisting of equally-spaced wooden bars with a porosity of about 0.3.

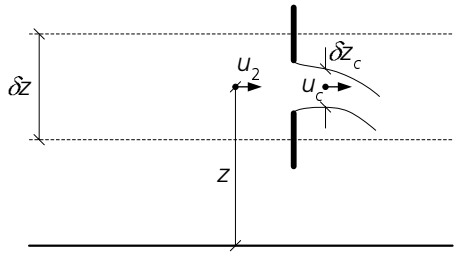

Figure 2.8: Streamlines passing through a screen opening.

The flow of interest in the present study is schematically shown in Fig. 2.7. The figure shows a constant upstream depth h_1 and speed U_1, a hydraulic jump propagating upstream with speed U_j and a downstream depth h_2 and speed U_2. The conditions that must be satisfied at the jump are given by Eqs. (2.34) and (2.35) of Section 2.2.

Since it is assumed that the approach flow in front of the screen is steady, the continuity equation between adjacent streamlines, as shown in Fig. 2.8, is

$$\delta q = u_2 \delta z = u_c \delta z_c = u_c C_c p_g \delta z \tag{2.44}$$

where δq is the incremental discharge per unit width over the incremental height δz, u_2 is the local velocity upstream of the screen, u_c is the velocity at the vena contracta with an incremental height δz_c, C_c is the flow-contraction coefficient (the ratio of the area at the vena contracta to that of the screen opening) including Reynolds number effects, and p_g is the ratio of the screen opening to the total area of the screen (i.e., the geometric porosity of the screen).

Using Eq. (2.44) and the Bernoulli equation along a streamline between the approaching flow and the vena contracta, the pressure difference, Δp across the screen is found to be

$$\Delta p = \frac{1}{2} \rho \, u_2^2 \left(\frac{1}{f^2} - 1 \right) \tag{2.45}$$

where $f = C_c p_g$ is the effective porosity (i.e. the ratio of the flow area at the vena contracta to the total area of the screen).

Assuming that the pressure distribution is hydrostatic on both sides of the screen, the pressure difference across the screen becomes as following

$$\Delta p = \begin{cases} \rho g'(h_2 - h_3), & \text{if } 0 < z \leqslant h_3 \\ \rho g'(h_2 - z), & \text{if } h_3 < z \leqslant h_2 \end{cases} \tag{2.46}$$

where h_3 is the height downstream of the screen in section 3. The flow discharge per unit width, δq is then given by

$$\delta q = \sqrt{2 \frac{f^2}{1 - f^2} \frac{\Delta p}{\rho}} \, \delta z \tag{2.47}$$

Integrating Eq. (2.47) with the conditions of Eq. (2.46) over the depth h_2 leads to

$$\begin{aligned} q = \sqrt{2g'\frac{f^2}{1-f^2}}\left(\int_0^{h_3}(h_2-h_3)^{1/2}\mathrm{d}z + \int_{h_3}^{h_2}(h_2-z)^{1/2}\mathrm{d}z\right) = \\ \sqrt{2g'\frac{f^2}{1-f^2}}\left[h_3(h_2-h_3)^{1/2} + \frac{2}{3}(h_2-h_3)^{3/2}\right] = \\ \sqrt{2g'\frac{f^2}{1-f^2}}\left[\frac{1}{3}(h_2-h_3)^{1/2}(h_3+2h_2)\right] \end{aligned} \tag{2.48}$$

In order to determine the incremental force exerted on the screen, we apply the momentum equation along the horizontal x axis for steady flow of the form

$$\begin{aligned} \delta F = \Delta p\delta z + \rho u_2^2\delta z - \rho u_c^2 f\delta z = \Delta p\delta z + \rho u_2^2\delta z - \rho\left(\frac{u_2}{f}\right)^2 f\delta z = \\ \Delta p\delta z - \left(\frac{1-f}{f}\right)\rho u_2^2\delta z \end{aligned} \tag{2.49}$$

Integrating Eq. (2.49) over the depth h_2, gives the total force on the screen as

$$\begin{aligned} F = \int_0^{h_2}\Delta p\mathrm{d}z - \frac{1-f}{f}\int_0^{h_2}2\Delta p\frac{f^2}{1-f^2}\mathrm{d}z = \\ \left(1-\frac{2f}{1+f}\right)\int_0^{h_2}\Delta p\mathrm{d}z = \left(\frac{1}{2}-\frac{f}{1+f}\right)\rho g'\left(h_2^2-h_3^2\right) \end{aligned} \tag{2.50}$$

The global momentum equation to the fluid domain between sections 2 and 3 as shown in Fig. 2.7 can be applied. Both sections are far enough from the screen so that the flows at both sections are considered to be uniform and the pressure fields are hydrostatic. Neglecting the friction loss along the channel bottom, the total force can be written as

$$\begin{aligned} F = \frac{1}{2}\rho g'(h_2^2-h_3^2) + \rho U_2^2 h_2 - \rho U_3^2 h_3 = \\ \frac{1}{2}\rho g'(h_2^2-h_3^2) - \rho q^2\frac{h_2-h_3}{h_2h_3} \end{aligned} \tag{2.51}$$

where $q = U_2h_2 = U_3h_3$ is the discharge per unit width through the screen.

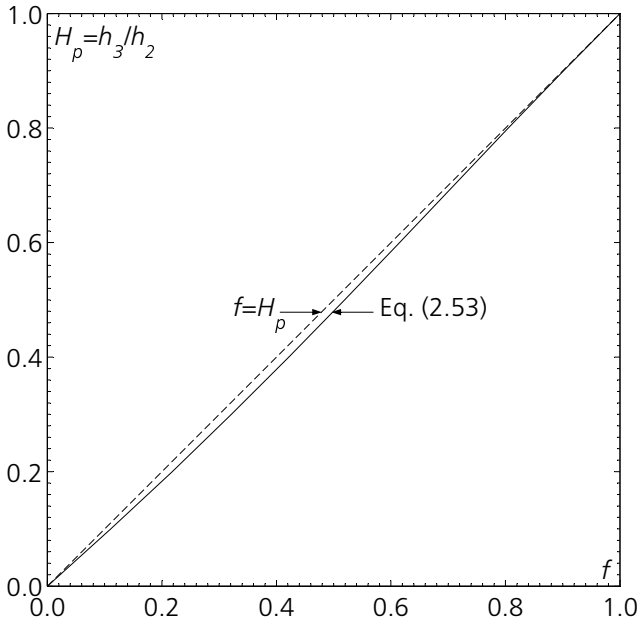

Figure 2.9: Solutions of Eq. (2.53) for the ratio of heights down- and upstream of the screen, $H_p = h_3/h_2$, as a function of the effective porosity, f.

Combining Eqs. (2.50) and (2.51) yields another equation for the discharge through the screen.

$$q = \sqrt{\frac{f}{1+f} g' h_2 h_3 (h_2 + h_3)} \tag{2.52}$$

From Eqs. (2.48) and (2.52), q can be eliminated and the equations can be solved for f to yield

$$f = \frac{9H_p + 9H_p^2}{-2H_p^3 + 3H_p^2 + 9H_p + 8} \tag{2.53}$$

where $H_p = h_3/h_2$ is the ratio of the heights down- and upstream of the screen.

As shown on Fig. 2.9, Eq. (2.53) is almost linear, and the approximation of $H_p = f$ can be made with an error of less than 5%. With this approximation Eq. (2.48) can be solved to yield an expression for U_2 similar to Eq. (2.38) as follows

$$U_2^2 = \frac{q^2}{h_2^2} = (g' h_2) \left(\frac{2}{9} \frac{f^2 (f+2)^2}{1+f} \right) \tag{2.54}$$

Introducing Eq. (2.54) into the jump condition of Eq. (2.34) gives

$$U_1 - (1 - H_j) U_j = (g' h_1)^{1/2} H_j^{3/2} \left(\frac{2}{9} \frac{f^2 (f+2)^2}{1+f} \right)^{1/2} \tag{2.55}$$

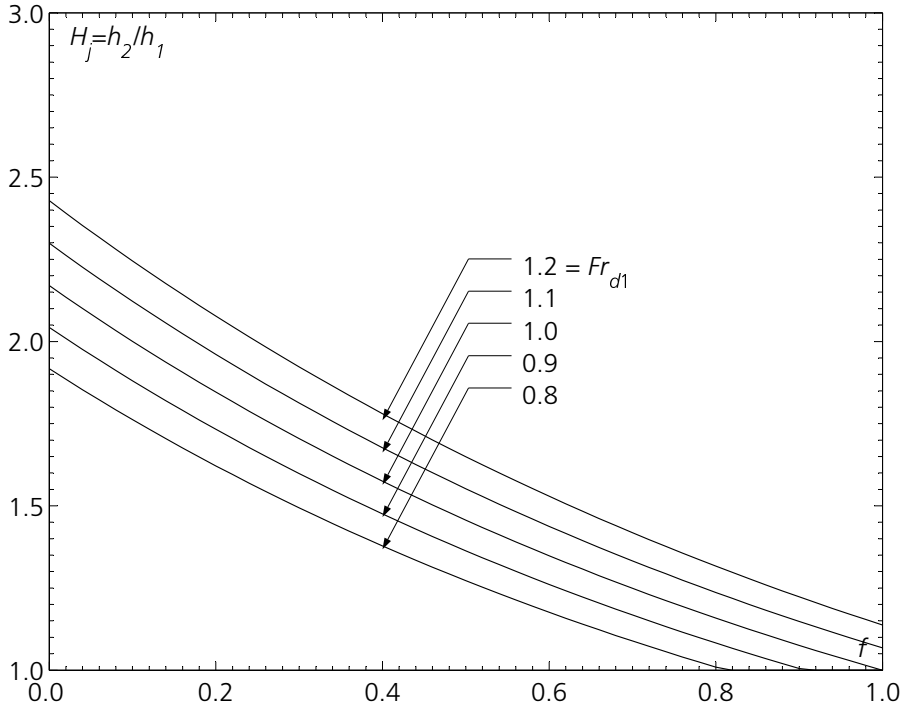

Figure 2.10: Solutions of the steady shallow-water equation for the non-dimensional jump height, $H_j = h_2/h_1$, as a function of the effective porosity, f, as illustrated in Fig. 2.7.

where $H_j = h_2/h_1$. Solutions of Eqs. (2.40) and (2.55) in the relevant parameter range are plotted in Fig. 2.10. The values of Fr_{d1} shown in the plot are those appropriate for most types of gravity currents. For $f = 0$ the flow is completely blocked.

The proportion, η, of the flow which continues over the obstacle, can be calculated by

$$\eta = \frac{U_2 h_2}{U_1 h_1} \tag{2.56}$$

The results are presented in Fig. 2.11 and show that for blocking half of the flow through the screen an effective porosity f of approximately 0.2 is necessary. For these small values of f the proportion of the flow passing through the screen is almost independent of the incoming Froude number.

The force exerted on the screen can easily be calculated from Eq. (2.50) by

$$F = \left(\frac{1}{2} - \frac{f}{1+f}\right)\left(1 - f^2\right)\rho g' h_2^2 \tag{2.57}$$

Yeh and Shrestha (1989) performed experiments to develop a prediction model for the head loss through a screen that is placed in an open channel. Pictures of flow patterns through the screen showed that the water surface decreased immediately behind the screen due to the fluid acceleration by flow

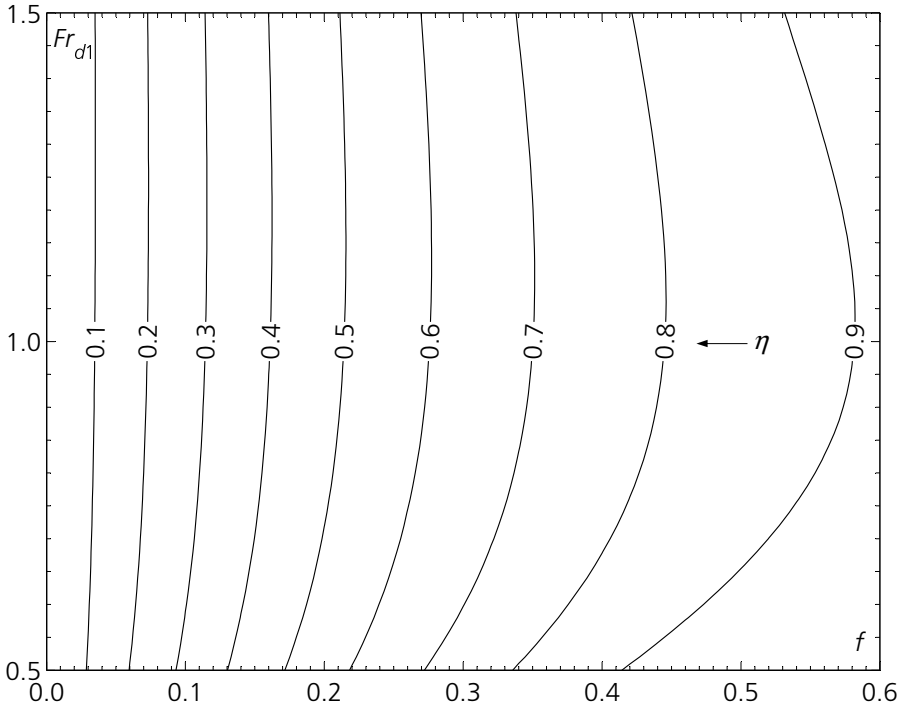

Figure 2.11: Contours showing the proportion of the incoming flow that is predicted to continue through the screen as a function of the effective porosity, f, and the upstream Froude number, Fr_{d1}.

contraction. Hence, even though the flow approaches the screen perpendicularly, the streamlines deflect downward near the free surface.

In the above derivation the deposition was not considered. Barrett et al. (1998) conducted experiments to evaluate the performance of geotextiles for sediment control. They found that essentially no sediment removal was attributable to filtration of the porous textile. Instead, the removal efficiency of 68% to 90% was correlated with the average detention time of the impounded sediment-water mixture behind the screen. Hence, they concluded that screens should be used to maximize the ponded volume behind the screen.

2.4 Flow Across Multiple Jets

In general, the various flow patterns occurring when a turbulent jet is injected into a ambient water body with a certain velocity and density stratification will depend on the hydrodynamical quantities of the jets and ambient flow, and their relative importance. The important characteristics of the jet are its momentum flux, $m_{j0} = U_{j0} q_{j0}$, its buoyancy flux, $b_{j0} = g'_{j0} q_{j0}$, and to a lesser extent, its discharge, $q_{j0} = U_{j0} a_j$ per unit width, in which U_{j0} is the discharge velocity, $g'_{j0} = g(\rho_a - \rho_{j0})/\rho_a$ is the reduced gravitational acceleration of the

jet, ρ_{j0} is the density fluid in the jet and a_j the slot opening of the jet. The ambient water body is characterized with a density and velocity distribution, $\rho_a(z)$ and $U_a(z)$, respectively. Jirka and Doneker (1991) and Jirka and Akar (1991) presented a dimensional analysis and developed a classification scheme of submerged single- and multiport diffuser discharges, based on length-scale representations of all dynamic features.

The trajectory for jets issuing at a certain angle into an ambient moving fluid, commonly referred to as jets in crossflow, is of considerable interest and was the subject of many investigations. A detailed review of the different analytical models for computing the axis of a jet in crossflow is given by Rajaratnam (1976). Dimensional analysis was also widely used to analyze the trajectory problem (Pratte and Baines, 1967; Wright, 1984; Huq and Stewart, 1996; Smith and Mungal, 1998; Hodgson et al., 1999; Han et al., 2000; Hasselbrink and Mungal, 2001). For the case of a jet injected obliquely into a crossflow, Han et al. (2000) showed that a skewed coordinate system agrees well with the experimental results for angles ranging from -45° to +45°.

Moawad and Rajaratnam (1998) considered the case of several jets in a crossflow, where the effect of spacing and the number of ports were investigated. The results indicated that with multiple jets, dilution in the mixing region is generally reduced due to the presence of the neighboring jets. A spacing of 16 times the jet diameter was found to be most effective.

Wright (1984) investigated the effect of ambient stratification on round, turbulent buoyant jets issuing vertically upwards into a uniform crossflow. Although the buoyancy and the initial momentum of the buoyant jet cause the jet to rise vertically, the ambient crossflow will deflect the flow field of the jet. In a stably stratified environment, the jet first behaves like a buoyant jet and mixes with the heavy bottom ambient fluid producing a neutrally buoyant cloud. The density deficit of the buoyant jet will decrease continuously and becomes zero at a certain height. The buoyancy force will be negative from here on, and the flow will be decelerated and turned down after reaching a maximum height. When compared with a similar flow in unstratified fluid, the major effects of density stratification are to limit the vertical rise and to restrict the mixing of the jet flow with the surrounding fluid. By using dimensional analysis, Wright (1984) gave relationships for the prediction of maximum and equilibrium heights-of-rise. Huq (1997) also conducted experiments with a circular jet in a linearly, stratified crossflow. The maximum and equilibrium heights-of-rise were found to be in accord with the results of Wright (1984).

France (1981) presented an investigation of stabilizing the location of hydraulic jumps using jets of water issuing at a certain angle from the bottom to produce a momentum against the oncoming supercritical flow.

In the following, the hydraulics of a jet injected at a certain angle into a stratified, two-layer flow are analyzed by means of shallow-water analysis. The flow of interest is sketched in Fig. 2.12. The figure shows a constant upstream

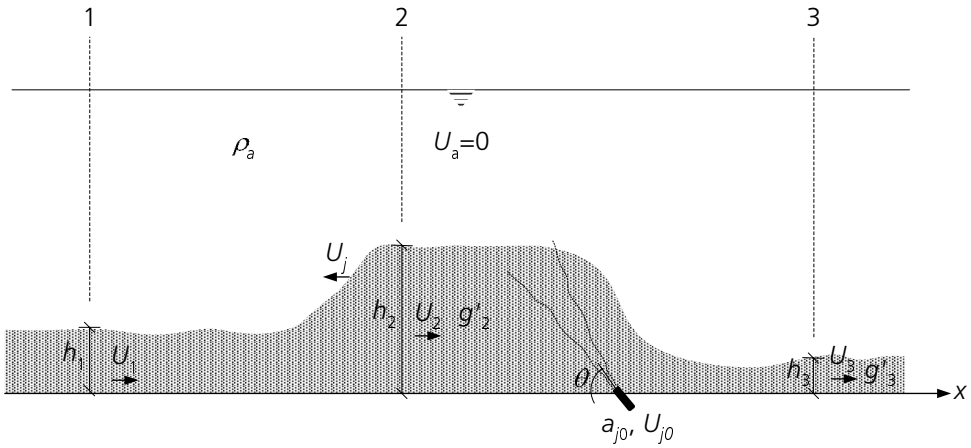

Figure 2.12: Flow across an inclined jet.

depth h_1 and speed U_1, a moving hydraulic jump propagating upstream with speed U_j and a downstream depth h_2 and speed U_2, the jet with slot width a_j, initial velocity U_{j0}, density ρ_{j0} and an angle θ to the horizontal x axis, and finally the downstream depth h_3 and velocity U_3.

Between section 2 and 3 we can write the continuity equation as

$$h_2 U_2 + \Delta q = h_3 U_3 \tag{2.58}$$

where $\Delta q = a_j U_{j0}$ is the injected flow discharge per unit width. As clear water is injected into the bottom layer, the reduced gravitational acceleration g' is changed between section 2 and 3 and we have to consider the conservation equation of the buoyancy flux as

$$g'_2 h_2 U_2 = g'_3 h_3 U_3 = B \tag{2.59}$$

and the momentum equation in x direction reads

$$g'_2 \frac{h_2^2}{2} + U_2^2 h_2 - m_{j0} \cos\theta = g'_3 \frac{h_3^2}{2} + U_3^2 h_3 \tag{2.60}$$

where $m_{j0} = \Delta q U_{j0}$ is the momentum injected per unit width. Eq. (2.60) can also be written in terms of the densimetric Froude number at section 2 and 3 as

$$U_2^2 h_2 \left(1 + \frac{1}{2Fr_{d2}^2}\right) - m_{j0} \cos\theta = U_3^2 h_3 \left(1 + \frac{1}{2Fr_{d3}^2}\right) \tag{2.61}$$

Dividing Eq. (2.61) by $h_2 U_2 B^{1/3}$ the following expression is found

$$Fr_{d2}^{2/3} \left(1 + \frac{1}{2Fr_{d2}^2}\right) - \frac{m_{j0} \cos\theta}{q_2 B^{1/3}} = \left(\frac{q_3}{q_2}\right) Fr_{d3}^{2/3} \left(1 + \frac{1}{2Fr_{d3}^2}\right) \tag{2.62}$$

For the case of a vertical injection ($\theta = \pi/2$), Eq. (2.62) simplifies to

$$Fr_{d2}^{2/3} \left(1 + \frac{1}{2Fr_{d2}^2}\right) = \left(\frac{q_3}{q_2}\right) Fr_{d3}^{2/3} \left(1 + \frac{1}{2Fr_{d3}^2}\right) \tag{2.63}$$

If the upstream densimetric Froude number, Fr_{d1} and the propagation speed of the moving jump, U_j are known, then Eqs. (2.62) and (2.63) in combination with the conditions that must be satisfied at the moving jump, given by Eqs. (2.34) and (2.35) of Section 2.2 may be solved for the downstream densimetric Froude number, Fr_{d3} in section 3.

2.5 Flow Through a Bubble Curtain

A steady release of air under water generates a rising stream of bubbles which entrains the surrounding water and produces a vertical flow of water towards the surface. This phenomenon is referred to as bubble plume. The bubble plume, when considered in terms of time-averaged quantities, is axisymmetric in the case of a point source, whereas line sources result in line plumes or so-called bubble curtains.

Bubble curtains originating from line sources have been proposed for many applications, such as for pneumatic oil barriers (Kobus, 1972; Wilkinson, 1979), for the reduction of the extent of salt-water intrusion in estuaries (Simmons, 1967) and navigation locks (Abraham and Burgh, 1964), to avoid freezing of water near gates or to protect offshore structures from large drifting objects, such as icebergs or ships out of control (Fanneløp et al., 1991). The axisymmetric case is of practical interest for mixing stratified layers to improve water quality in reservoirs and lakes (Baines and Leitch, 1992; Schladow, 1993; Wüest et al., 1992; Lemckert and Imberger, 1993; Hugi, 1993).

The steady-state bubble plume in homogeneous water was in focus of many experimental, theoretical and numerical investigations (Wilkinson, 1979; Kobus, 1972; Milgram, 1983). These papers describe various aspects of the mean flow characteristics of the induced plumes including the velocity distribution, entrainment coefficient and the bubble slip velocity. The analysis is based on so-called integral models, which are capable of predicting the variables of prime interest (mean flow velocity and void fraction) with good accuracy. Hugi (1993) and Kubasch (2001) have summarized the various papers about bubble plume integral models and give also an overview of different model extensions. Hugi (1993) also conducted experiments with a crossflow and further modified the integral model to take the convection by an ambient crossflow into account. The flow at the free surface, when the rising water is deflected sideways, was studied extensively (Fanneløp et al., 1991; Friedl, 1998; Riess and Fanneløp, 1998). In a confined basin, this deflected water can lead to a strong recirculation cell. Riess and Fanneløp (1998) found experimentally that the recirculation cell size induced by the surface spreading in a flume depends on the depth-to-width ratio of the flume.

As in the case of the homogeneous water, the initiation of bubbles in a linear stratification causes the surrounding water to be entrained and carried up with the bubble stream. McDougall (1978) generalized the integral model to include a stratified ambient fluid. For a strongly stratified fluid McDougall (1978) showed, both from the integral model results and from the experimental evidence, that the bubble plume forms a core of rising fluid which is surrounded by an annular downdraught due to buoyant forces exerted by the surrounding light fluid; horizontal intrusions into the ambient fluid formed at regular intervals, drawing mixed fluid from the downdraught. Baines and Leitch (1992) conducted experiments with weak bubble plumes and strong stratifications. Therefore, the lower layer penetrated only a short distance into the upper layer. Asaeda and Imberger (1993) also studied the behavior of bubble plumes in a stratified ambient fluid under a wide range of flow conditions and proposed a double annular plume model.

In Asaeda and Imberger's (1993) experiments for large air flow rates, the rising dense water spread outwards at the surface, decreasing in velocity at distance. At a certain radius blocking by the ambient stratification arrested the horizontal momentum of the radial surface flow and the negative buoyancy caused it to plunge. At that point the heavier water initiated a negatively buoyant plume which again entrained ambient surface water as it moved downwards. The falling plume propagated downwards to a level of neutral buoyancy where it formed a further intrusion; the general appearance was similar to a mushroom. Lemckert and Imberger (1993) extended the theory of Asaeda and Imberger's (1993) to an arbitrary stratification by using an equivalent stratification based on potential energy conservation and the velocity scales of the flow. They predicted the radial extent of the surface jet generated by the bubble plume in the arbitrary stratification.

Schladow (1993) presented a new methodology for the design of bubble plume destratification systems. It is based on the interaction that occurs between a buoyant bubble plume and the density stratified water column through which it rises. The airflow rate that an individual buoyancy source requires to mix the water column efficiently was calculated.

Very little literature is found on the influence of bubble curtains on stratified crossflows or more specifically density currents. Abraham and Burgh (1964) initially used an air curtain to prevent the progress of a density current induced by a lock-exchange flow. They presented a theory to determine the required quantity of air to reduce the intrusion of salt water. Their relationships was depending on the water depth, H and the ratio of the cubic root of the buoyancy flux of the bubble curtain, $b_b^{1/3}$ to the density current front velocity, U_f.

Simmons (1967) presented qualitative laboratory experiments to evaluated the potential benefits of pneumatic barriers in estuaries. The experiments demonstrated that pneumatic barriers can significantly reduce the extent of salt-water intrusions. He also mentions a case, in which the pneumatic barrier

	$b_b^{1/3}/U_a$	$b_b^{1/3}/U$	U/U_a
Type I	< 10	< 2	
Type II	> 10	> 2	< 5
Type III	> 10	> 2	> 5

Table 2.1: Conditions for the appearance of Type I, II, and III saline wedge intrusion through a bubble curtain (after Nakai and Arita (2002)).

is used to maintain the navigation clearance by increasing the turbulence as a means for inhibiting the deposition of sediments in critical areas.

Recently, Nakai and Arita (2002) experimentally investigated the flow mechanism of a saline wedge intrusion in the presence of a bubble curtain. They discussed the hydraulic conditions in which a bubble curtain works most effectively to prevent intrusion of a saline wedge. They discussed the behavior by means of the three external forces written in dimensions of velocities, namely the buoyancy flux of the bubble curtain, $b_b^{1/3}$, the intrusion force of the saline wedge characterized by the velocity $U = \sqrt{g'h}$, with h its height at the bubble curtain, and the inertial force of the approaching ambient water flow above the saline intrusion characterized by its velocity U_a.

They classified the influence of the bubble curtain on the saline wedge into three types:

Type I occurs if the ratio between the buoyancy flux of the bubble curtain and the velocity of the density current is small. In this case some of the denser fluid intrudes through the bubble curtain along the flume.

Type II occurs if the buoyancy force of the bubble curtain is large compared to the velocity of the density current. Here, all the denser fluid can be lifted up to the water surface. When the denser water attains the water surface, the behavior depends on the ratio between the buoyancy flux of the bubble curtain and the ambient water flow. Type II occurs if the crossflow is strong, and all the denser fluid is convected with the crossflow.

Type III occurs if the crossflow is weak, and the bubble-driven upward jet spreads to both sides of the bubble curtain near the water surface. Convection cells are produced, on both sides due to the interaction between the upward flow and the water surface and the circulating flow is intensified by the density current flow at the bottom.

Nakai and Arita's (2002) experiments allowed to delimit the different appearance conditions which may be expressed by the ratios $b_b^{1/3}/U_a$, $b_b^{1/3}/U$ and U/U_a. They presented a graph indicating the different appearance conditions, which was simplified to the approximate values given in Table 2.1.

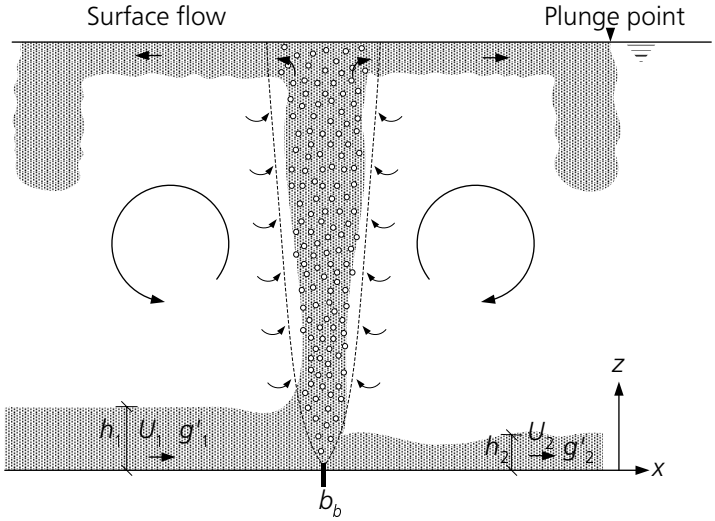

Figure 2.13: Flow through a bubble curtain.

In Fig. 2.13, the case of no crossflow is sketched, where some of the denser fluid is entrained to the surface by the bubble curtain producing convection cells on both sides and some of the denser fluid passes through the bubble plume.

Nakai and Arita (2002) performed additional experiments to investigate the effect of the air bubble size on the phenomenon. No significant change of the phenomenon by a variation of the bubble size in the range of 0.2 mm to 5 mm was observed.

2.6 Conclusions

The flow of gravity currents was studied by many investigators by means of experimental investigations of the head and the body. The flow of turbidity currents is more complicated due to lack of buoyancy conservation. In fact the settling of the suspended particles and the process of deposition and erosion increases the number of parameters necessary to characterize the turbidity current flow. The settling phenomena was investigated by several authors and is usually taken into account by the product of a settling velocity and a representative sediment concentration of the flow. In contrast, less work was done on erosion characteristics and bed forms of turbidity currents. This lack of knowledge is mainly due to the difficulty of an accurate, instantaneous measurement of the deposition-erosion interaction at the bottom.

The flow of a conservative density current over an obstacle was extensively studied by means of shallow-water analysis, where the entrainment between the layers was neglected. The work done on the effect of obstacles on turbidity currents was concentrated mainly on the investigation of the deposition patterns in the field of sedimentology. Less work was done on the study of the

flow structure. No research was yet reported on the flow of turbidity currents through a permeable screen.

The structure and trajectory of jets in a crossflow and in a stratified environment were considered by many researchers and different models for their description were proposed. No research about the effect of jets on gravity or turbidity currents has yet been done.

The review of the studies on the effect of bubble curtains on gravity currents showed that the research mainly focused on the interaction of these positively buoyant plumes with saline intrusions in rivers and navigation locks. No literature about the effect of a bubble curtain on a turbidity current was found.

Based on the existing knowledge of the flow over obstacles, through screens, across jets as well as bubble curtains, the effect of these measures to control reservoir sedimentation due to turbidity currents needs, therefore, further investigation.

3 Experimental Installation and Test Procedure

3.1 Description of the Experimental Installation

3.1.1 Flume Description

The experiments were carried out in a modified multi-purpose tilting flume with at total length of 8.55 m. A second flume was inserted into the multi-purpose flume, and the sides of the inner flume consisted of 8 mm thick transparent PVC plate to allow the observation of the underflow. The inner experimental flume had a section of 27.2 cm wide and 90.0 cm in depth. It is shown together with the multi-purpose flume on Fig. 3.1. The flume can be tilted in a slope range between $0\% \leq S \leq +5\%(2.86°)$.

In Fig. 3.2 a schematic view of the experimental setup and the hydraulic circuit is given. The entire flume was divided into two sections of unequal length by a sliding gate. Adjacent to the experimental flume, a mixing tank with a maximum capacity of 1500 liters was used to prepare and store the dense fluid mixture. The mixing tank was equipped with a propeller-type mixer to create a homogeneous sediment mixture. After filling the experimental flume with tap water, the dense fluid (water-sediment mixture) was pumped up into the stilling box through a 60 mm diameter flexible plastic pipe, passing a calibrated electromagnetic flowmeter. The water-sediment mixture entered the stilling box trough the bottom turning horizontally behind the entrance gate into a slotted pipe. During preparation the sluice gate was closed and the flow returned through a 30 mm orifice and a PVP pipe back into the mixture tank. This circulation ensured a uniform mixture in the stilling tank and an accurate regulation of the pump. A photograph of the mixing tank and the supply is shown on Figs. 3.3(a) and 3.3(b).

The shorter upstream section served as a stilling box and head tank for the mixture to be released by opening the sliding gate to create the turbidity current. The movement of the sliding gate was controlled by a lever mounted on the flume wall. Downstream of this gate a box containing rectangular

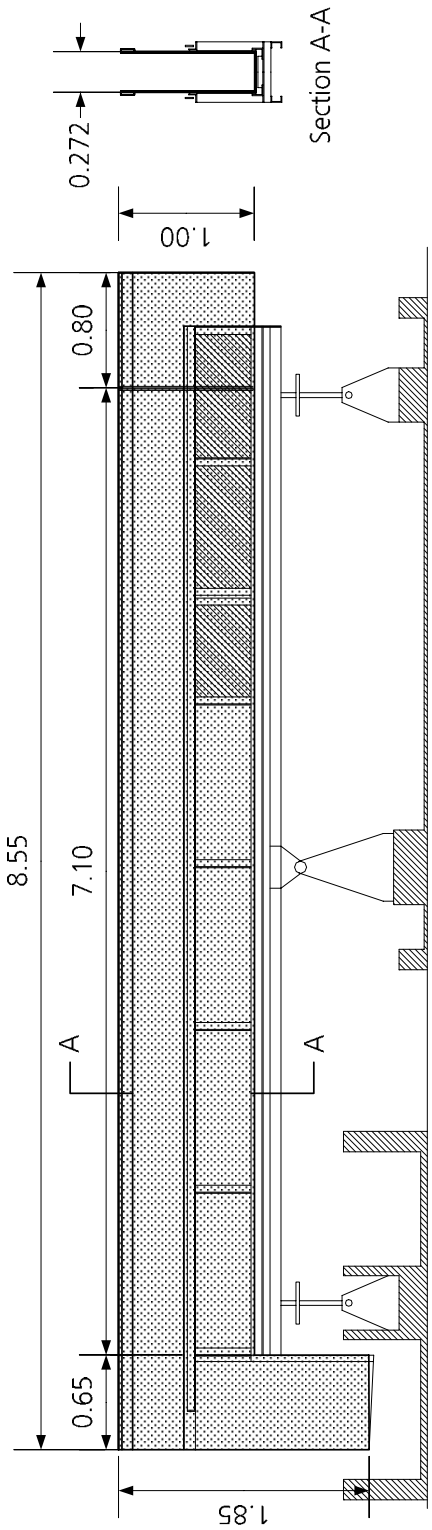

Figure 3.1: General view and transversal cross-section of the flume with modifications for the turbidity current experiments (thick lines).

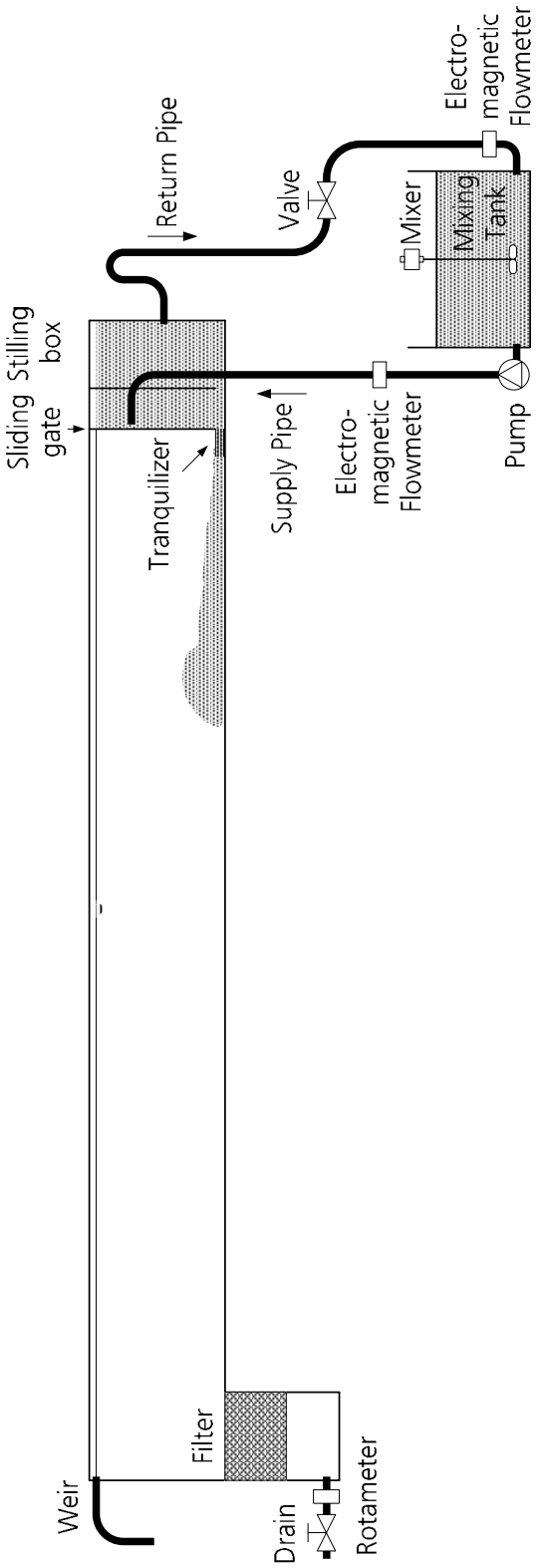

Figure 3.2: Schematic view of the experimental installation.

ρ_s [kg/m^3]	1135
d_{50} [μm]	90
d_{84} [μm]	130
d_{16} [μm]	50
$\sigma_g = \sqrt{d_{84}/d_{16}}$ [–]	1.6

Table 3.1: List of parameters describing the physical properties and grain size distribution curve for the sediment material.

tubes of 1.5 cm diameter, reduced the scale of the initial turbulence (see Fig. 3.3(c)).

The long downstream section simulates a reservoir in which a turbidity current is flowing. A compartment at the end of the flume bottom trapped the turbidity current for withdrawal. The rate of the outflow is controlled by a drainage valve where a rotameter allowed the regulation of the water level. The downstream end of the flume with the drainage valve is shown in Fig. 3.3(d). To prevent a contamination of the hydraulic system of the laboratory with fine sediment, a filter was installed to retain the sediment particles.

A general view of the installation is shown in Fig. 3.4 with the inlet tank at the upper end and the outlet section with the drainage valve at the lower end of the photograph. A platform was built along the flume for easy access.

3.1.2 Properties of the Sediment Materials

Various materials can be used to create turbidity currents in the laboratory. They include different types of clay, bentonite, quartz or marble powder obtained by grinding. For the present study a cohesionless, light weight homogeneous material was chosen, which had a well known and relatively narrow particle size distribution, as well as a small settling velocity. Specifically, the material was ground polymer with a density of 1135 kg/m^3. The grain size distribution of the sediment material was determined with a Mavern Mastersizer (Laser refraction method) and is shown in Fig. 3.5. The material had a fairly narrow grain size range, but the frequency histogram was skewed towards large grain sizes, which is typical for ground particles. The particles have a median diameter, d_{50}, of 90 μm. With a standard deviation, σ_g, of 1.6 the grain size distribution cannot be considered uniform, therefore, some grain sorting effects may occur. In Table 3.1 some of the most commonly used parameters for describing the properties and grain size distribution for the sediment are summarized.

As shown on the microscopic photograph in Fig. 3.6 the particles are not perfect spheres, but have slightly angular shapes, like natural sediments.

The selection of a characteristic grain size of the sediment is important for the calculation of the representative settling velocity of the sediment, which

(a) Mixing tank with supply and measurement table.

(b) Inlet tank.

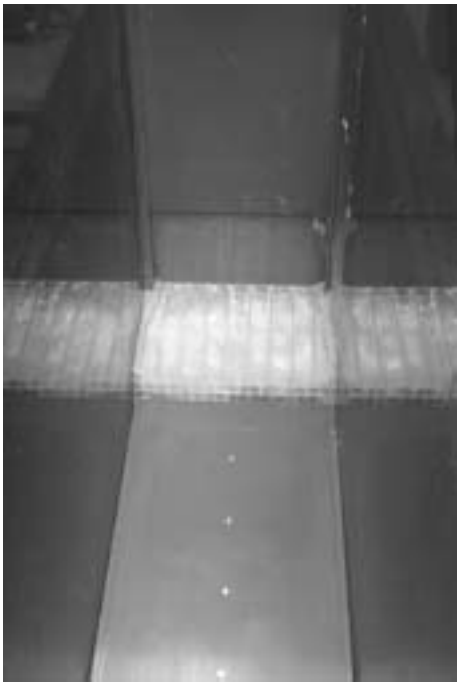

(c) Flume inlet with tranquilizer.

(d) Outlet valve of flume.

Figure 3.3: Photographs of inlet and outlet sections of the flume.

Figure 3.4: Photograph of the flume.

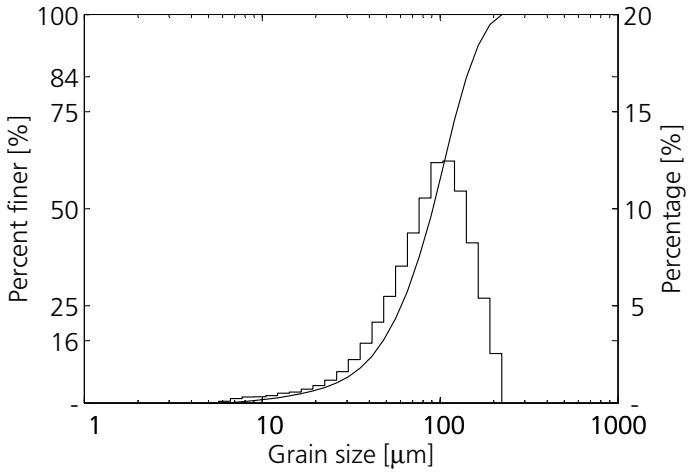

Figure 3.5: Grain size distribution of selected sediment.

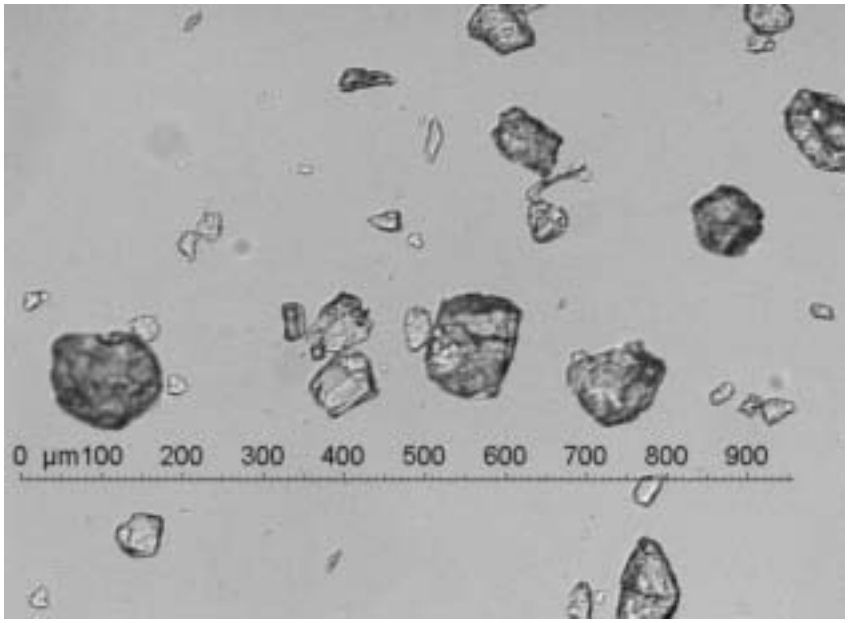

Figure 3.6: Microscopic photograph of the sediment particles used in the experiments (scales are in [μm])

greatly affects the sediment transport. In Table 3.2 representative diameters are shown, which represent different criteria. Altinakar (1988) proposed that the grain size which has a settling velocity equal to the average settling velocity of the sediment material given by Eq. (3.1) to be the representative particle size for the sediment material.

$$v_{ss} = \frac{\sum_i (v_{ss})_i \cdot \Delta_i}{\sum_i \Delta_i} \tag{3.1}$$

where Δ_i represents the percentage of the sediment material falling in the ith size fraction of the frequency histogram and $(v_{ss})_i$ is the settling velocity for that size fraction.

The settling velocity, v_{ss}, can be calculated by means of different methods described in the literature. Here, Stokes' law has been used, considering the small, almost spherical particles and the low Reynolds number, $Re = \frac{d\, v_{ss}}{\nu} < 0.2$. It is expressed as

$$v_{ss} = g\, \frac{\rho_s - \rho_w}{\rho_w}\, \frac{1}{18\nu} d^2 \tag{3.2}$$

To prepare the water-sediment mixtures the particles first had to be wetted in a small pot with a mixer before they were added to the mixing tank. Due to the low sediment concentrations of up to 5% by volume, no corrections for the concentration are made on the settling fall velocity and the viscosity of the water. The mixture is considered to be a Newtonian fluid.

	d [μm]	v_{ss} [mm/s]
Median diameter, d_{50}:	90	0.449
Arithmetic mean diameter, d_a: $d_a = (\sum_i d_i \cdot \Delta_i)/(\sum_i \Delta_i)$	87	0.420
Geometric mean diameter, d_g: $\log d_g = (\sum_i \log d_i \cdot \Delta_i)/(\sum_i \Delta_i)$	75	0.312
Particle-volume weighted mean diameter, d_v: $d_v = \sqrt[3]{(d_i^3 \cdot \Delta_i)/(\sum \Delta_i)}$	105	0.611
Settling-velocity weighted mean diameter, d_s: $v_{ss} = (\sum_i (v_{ss})_i \cdot \Delta_i)/(\sum_i \Delta_i)$	97	0.522

Table 3.2: Comparison of different characteristic particle sizes and the corresponding settling velocities.

3.2 Measuring Instrumentation

3.2.1 Flow Velocity Measurements

An ultrasonic velocity profiler (UVP) was used to measure flow velocities. With this device an instantaneous velocity profile in a liquid flow can be measured along the ultrasonic beam axis. Fig. 3.7 shows the measurement principle. It relies on the detection of the Doppler shift of the echo from an ultrasound burst which is emitted along a measuring line from a transducer and is reflected by small particles suspended within the flow. The UVP used in the current study is described elsewhere (Takeda, 1995; Met-Flow SA, 2000) but a brief summary is given below.

The Doppler shift frequency, f_D, is directly related to the flow velocity of a particle, U, in the measurement volume by the following expression

$$U = \frac{c\, f_D}{2\, f_0} \tag{3.3}$$

where c is the velocity of sound in the fluid being investigated, f_D is the Doppler frequency shift and f_0 is the emitted ultrasound frequency. In this manner, the velocity of a particle can be calculated at one point. However, UVP uses a burst of ultrasound that is emitted from a transducer to obtain simultaneous velocity measurements along a profile as shown in Fig. 3.7. In order to achieve this profiling, the return signal detecting the shift in frequency is gated at predetermined return times, and thereby allows measurement of velocity at up to 128 points along the axis of the beam. The distance to the location of the sample location, x_s, is given by

$$x_s = \frac{c\, t}{2} \tag{3.4}$$

where t is the time laps between the emission and reception of ultrasound pulses.

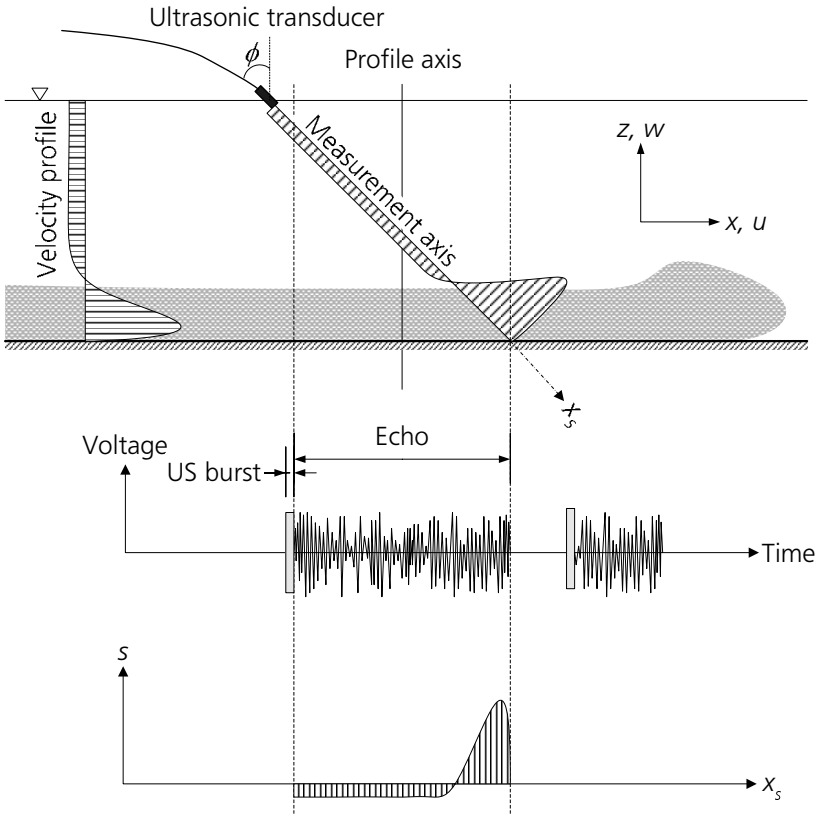

Figure 3.7: Scheme of UVP velocity profile measurement in a turbidity current flow.

The maximum distance to which the UVP may detect, $D_{\max}$, is a function of the frequency of repetition of the ultrasound pulses, f_{prf}, and is given by

$$D_{\max} = \frac{c}{2\, f_{\mathrm{prf}}} \tag{3.5}$$

Additionally, the maximum detectable velocity, $U_{\max}$, is determined by the Nyquist sampling theorem ($f_{D(\max)} < f_{\mathrm{prf}}/2$), and hence

$$U_{\max} < \frac{c\, f_{\mathrm{prf}}}{4\, f_0} \tag{3.6}$$

which together with Eq. (3.5) leads to

$$U_{\max} = \frac{c^2}{8\, f_0\, D_{\max}} \tag{3.7}$$

For an 8-bit resolution of the echo frequency, the velocity resolution, U_{res}, is given by $U_{\max}/127$ for a configuration that is sensitive for the direction. Table 3.3 lists the physical parameters used for the UVP in the current experiments.

Ultrasound frequency, f_0	2 MHz
Transducer diameter	10 mm
Measurement window	100–664 mm / 49–895 mm
Maximum velocity, $U_{\max}$	±91.3 mm/s
Measurement bin length	4.44 mm / 6.66 mm
Velocity resolution, U_{res}	0.7 mm/s
Diameter of measurement 'bin'	
nearest from transducer	7.7 / 3.8 mm
furthest from transducer	51.0 / 68.7 mm
Sound velocity, c	1480 m/s
Sampling time for each profile	66 ms (20 ms)
(and delay time between transducers)	
Pulse repetition frequency, f_{prf}	493 Hz
Output voltage	150 V
Repetitions for one profile	32 with 6 cycles per burst

Table 3.3: Parameters of the ultrasonic Doppler velocity profiler.

The length of the measuring volume along the axis of detection was chosen to be 4.44 mm or 6.66 mm depending on the experiments. The window size for a profile is then defined as 128 times the measuring volume length. The cross-beam width of each bin at different distances away from the probe is determined by the angle of spread of the beam, which for the present transducer was 2.2°. This value can be used to calculate the cross-beam width of the measurement bins nearest and furthest away from the probes as given in Table 3.3.

Two assumptions are inherent in the use of UVP in sediment-laden flows. First, it is implied that the sediment and fluid travel at the same velocity, i.e. that there is no slip velocity between the two phases. This assumption is likely to be valid for our fine, predominantly suspended sediment. Secondly, the spatial change in density within the current, and therefore change in ultrasound velocity, must be less than the error limits of the technique. Best et al. (2001) also conducted UVP measurements in turbidity currents and investigated the effect of change in density on the ultrasound velocity. They progressively added greater amounts of silica flour to yield densities of 1.000 to 1.065 g/cm^3, and the velocity of sound was adjusted to give the same depth value as in clear water. In this manner, the velocity of ultrasound in different concentrations of suspended sediment could be assessed. Results from their simple tests showed that the maximum difference in sound velocity between clear water and the sediment-water mixture was 13 m/s. The maximum density in the present experiments was only of 1.006 g/cm^3. Therefore, the error due to sound velocity change can be neglected and a value of 1480 m/s was used.

In the present experiments an array of up to seven 2 MHz ultrasonic transducers was used which were multiplexed with the UVP processor. The time taken for each profile measurement is a function of both the maximum measurement distance and the finite time that is required for data processing and switching between transducers. In the current configuration, the sampling time for each profile was 66 ms, the delay time between transducers was 20 ms.

The echo of the flowing turbidity current was strong enough to allow fast measurements, only 3 successive profiles were taken per transducer before switching to the next transducer. The temporal resolution between two consecutive transducers was therefore less than 200 ms. The time required to scan all transducers (corresponding to one measuring cycle) was around 1.5 s. The cycles were repeated continuously during the experiments giving a quasi-instantaneous velocity information at the profile locations over a total duration of 600 s (450 cycles).

The transducers were mounted with plastic clamps fixed on a brass rod, which could be mounted, turned and moved along the flume as shown in Fig. 3.8.

The beam directions and the penetration length were chosen in order to cover the interior of the advancing turbidity current as well as the return flow of the ambient water. The profiles were taken in the center plane of the flume with a predetermined angle of 20°or 25°. The locations of the transducers were adapted to each experiment series and are presented in detail in Section 3.4.

As shown in Fig. 3.7, only the velocity component, s, in the beam axis is measured with the UVP. In a two-dimensional flow field (u,w) this velocity component, s, is calculated as following

$$s = u \sin\phi - w \cos\phi \tag{3.8}$$

where ϕ is the angle of the transducer with the vertical. To get the u velocity component parallel to the flume bottom as sketched in Fig. 2.1, it is assumed that the w velocity component perpendicular to the flume bottom is small compared to the u velocity ($|\frac{u}{w}| > 100$). This assumption is only justified in the body of the turbidity current behind the head in an undisturbed flow (without obstacles, fences or jets). For a typical angle of the transducer of 25°, Eq. (3.8) becomes then

$$u = \frac{s}{\sin\phi} \pm \frac{1}{50}u = \frac{s}{\sin\phi} \pm 2\% \tag{3.9}$$

The maximum error is, therefore, of the same order as the velocity resolution, (U_{res}=0.7 mm/s).

To obtain a vertical profile of the streamwise velocity u, it is further assumed that no significant change of the velocity distribution occurs in the x

Figure 3.8: Photograph of the UVP transducer as well as the bottom and reference electrodes.

direction, and that the vertical velocity profile can be obtained from a velocity profile along the beam axis as shown in Fig. 3.7. The vertical coordinate, z writes than as

$$z = x_s \cos \phi \tag{3.10}$$

Since a source of experimental error may arise from slight misalignment of the UVP transducers, great care was taken in positioning the probes before each experiment. The error in inclination of the transducers is estimated as less than 0.5°, resulting in a velocity error of approximately ±3%.

3.2.2 Front Velocity and Time Measurements

The front velocity of the head of the turbidity current is determined from video recordings by reading the time at which the head passes predetermined positions. In turbidity current experiments, the interface between the current front and the ambient fluid could be easily observed. Since the camera was only 4 m away from the flume, a parallax correction was made; the actual positions of the head were measured from scales drawn on both the front and back walls of the flume. Unfortunately, no measurements could be taken on the first 2 meters because of the opaque wall of the multi-purpose flume. A digital chronometer was used to link the internal clock of the digital camera with the start of the experiment. The frame rate of the camera is 25 frames per second and the screen resolution is 720x576.

The digital video records were analyzed to determine the position of the turbidity current head as a function of time. Generally, 35 to 40 measuring points were taken. In all the experiments the front velocity was nearly constant over the whole length, and was determined from a least-square fit. The relative change of the front velocity measurements was less than 1%.

At the end of each experiment the watch was stopped with the closing of the gate and the duration of the experiment was read from the chronometer.

3.2.3 Density and Temperature Measurements

In all experiments clear tap water was used as the ambient fluid. During the experimental work it was observed that the temperature of the water shows diurnal variations. The density of the sediment mixture and the clear water was measured before and after the experiment by means of a hydrometer, which allowed determination of the density to a precision of $\pm 0.1\,\mathrm{g/l}$.

Care was taken to obtain a turbidity current mixture of approximately the same temperature as the clear water in the flume. Such that the density difference between turbidity current mixture and the ambient fluid was only due to the presence of sediment. Prior to the experiment the temperatures of the mixture prepared in the mixing tank and the temperature of the clear water in the flume were measured using a mercury thermometer with a resolution of $\pm 0.1\,^{\circ}\mathrm{C}$.

3.2.4 Auxiliary Measurements

The flowmeter of the inflowing pump is monitored during the experiments, which allowed to check the stability of the inflow.

During each experiment the depths of the free surface at the upstream end of the flume, and in the stilling tank were measured by means of ultrasonic level probes. This allowed a verification that the boundary conditions were constant during the experiments.

3.2.5 Deposition Measurements

It is greatly desirable to measure the deposition thickness during physical experiments of turbidity currents. Most of the experimental techniques described in the literature are designed to measure the deposition after the experiment, but give no information on the variation in time (Bonnecaze et al., 1993; Garcia, 1994; Altinakar, 1988). They often used a suction method, by which they siphoned up the particles deposited on a known area at several locations in the tank, dried them and weighted the samples. The advantage of this method is that by means of a sieve analysis the sample can be analyzed and the segregation of the particles can be investigated, see Altinakar (1988) for example.

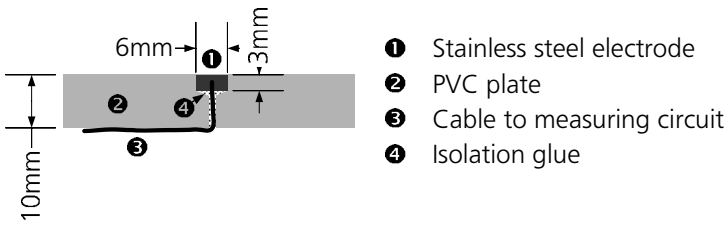

Figure 3.9: Schematic picture of deposition measuring electrode.

In the present work, a new device to measure the local sediment layer thickness was developed based on work done by De Rooij et al. (1999). The technique is based on the fact that the electrical resistance of a layer of particles depends on its thickness. In the present experiments a polymer powder as described in Subsection 3.1.2 was used. The electrical resistance of this material is much higher than that of clear water, which implies that the current passes through liquid phase, when one applies a voltage. When a large volume fraction is occupied by particles, the resistance increases and the current is reduced. These high concentrations are present in the sediment layer that accumulates on the bottom. The thickness of the layer can thus be determined by measuring its resistance. It is important to note here that the particle size, and shape, affect the packing density, and therefore the resistance of the layer. The apparatus thus has always to be calibrated for the specific particles used.

The resistance of the sediment layer was measured by placing a reference electrode rod in the clear water above the layer and several electrodes on the tank bottom below the layer. In the experimental apparatus a stainless steel rod, 6.5 m long and 6 mm diameter, mounted horizontally at one third of the flume width, and at 50 cm above the bottom, was used as a reference electrode. The size of the bottom electrodes determines the range of layer thicknesses that can be measured. De Rooij et al. (1999) tested different diameters of 1, 2, 4 and 6 mm and found the 6 mm electrode to be the most adequate for small deposition thicknesses.

The bottom electrodes were glued into holes in a plate along the centerline of the flume with a longitudinal spacing of 10 cm. Special attention was paid to the insulation of the leads, so that all current passed through the electrodes installed flush with the bottom of the flume as shown in Fig. 3.9.

To measure the small changes in the resistance accurately, the electrodes were connected to a Wheatstone bridge circuit depicted schematically in Fig. 3.10. The bridge was reasonably well balanced so that the resistor R_1 was always lower than the measured resistances. Measuring the voltage applied across the Wheatstone bridge ($U_{63} + U_{64} = U_W$) and the measured output voltage ($U_{1..62} = U_{mi}$), the variable resistance R_{mi} of electrode i can be found

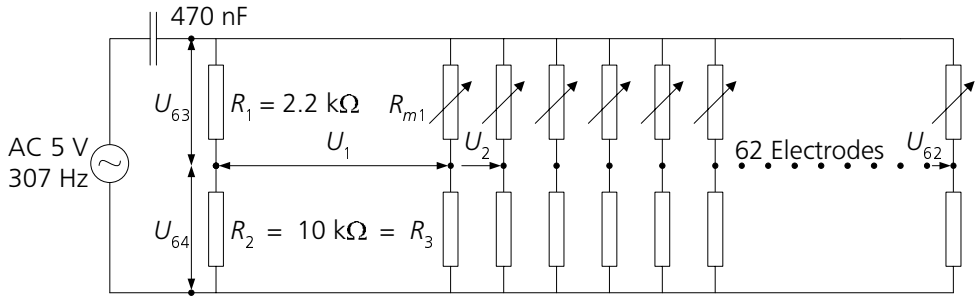

Figure 3.10: Scheme of the electronic measuring circuit.

from the following equation

$$\frac{U_{mi}}{U_W} = \frac{R_{mi}}{R_{mi} + R_3} - \frac{R_1}{R_1 + R_2} \tag{3.11}$$

To avoid electrolysis of the water, an AC electrical source with a frequency of 304 Hz and a 5 V output signal was used. It was found that always a small DC offset of the signal prevailed, which caused electrolysis. This is the reason, why a capacitor was added to eliminate this part of the signal. Several tests were made to ensure that the signal from the electrodes is not influenced by external sources such as electromagnetic fields.

Due to the presence of the capacitor, the voltage applied across the Wheatstone bridge, U_W, varies with a change in the variable resistances, R_{mi}. As a consequence, the voltage applied across the Wheatstone bridge, U_W was measured together with the output voltages, U_{mi}.

The output of the electrodes was connected to an analog-to-digital converter (ADC) with a 64-channels data acquisition board (PCI-DAS6402/16) in a PC. The sampling rate of this ADC was 3004 Hz per channel, which allowed to obtain 10 data points per signal cycle with an accuracy of 16 bits. A software module was written in LabVIEW$^{\text{TM}}$6 to allow easy logging of the data (National Instruments, 2000). The data was filtered with a 15th-order Butterworth Bandpass filter to eliminate any undesirable frequencies; such as the 50 Hz noise. The measured signal was further conditioned by computing the root-mean-square (RMS) of the sinusoidal signal in a moving time frame of 0.2 s (600 data points).

Several tests were performed to confirm that the ADC reading remained unchanged after suspending up to 4 g/l particles in the clear water, and that the ambient suspension concentration did not affect the resistance between electrodes. As the resistivity of the water changes with temperature an analysis of the changing of resistance due to temperature change was performed. It was found that temperature change had to be considered during the calibration process.

The measured resistance R_m is the sum of the resistance of the clear water R_{water} depending on the water temperature and the resistance of the

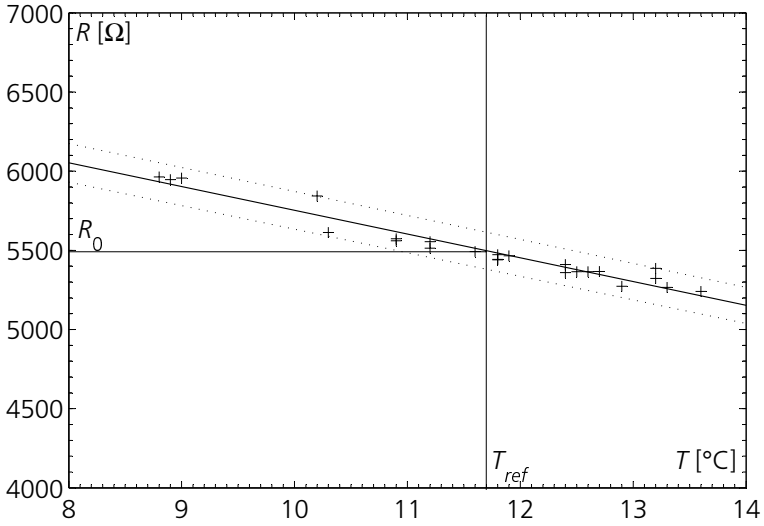

Figure 3.11: Variation of resistance of water with temperature.

sediment layer R_{layer} as following

$$R_m = R_{\text{water}} + R_{\text{layer}} \tag{3.12}$$

The resistance of the water, R_{water}, decreases with increasing temperature because the mobility of the ions in solution increases with temperature. This property of solutions is the opposite of the behavior of metallic (electronic) conductors where the resistivity increases with temperature. If the temperature range is not too large, it can be assumed that the resistance is a linear function of the temperature, T, and can be expressed as

$$R_{\text{water}} = R_0 \left[1 + \alpha_T (T - T_{\text{ref}})\right] \tag{3.13}$$

where T_{ref} is the reference temperature taken as 11.7 °C, T the temperature of interest, R_0 the resistance at reference temperature, R_{water}, the resistance at temperature of interest and α_T the temperature coefficient of resistance. If the resistance is measured at several different water temperatures without sediment deposits, a graph of the data will be linear with a slope of $\alpha_T R_0$ and a vertical intercept at T_{ref} of R_0 as shown in Fig. 3.11.

To obtain an equation which represents the resistance of the sediment layer, R_{layer}, De Rooij et al. (1999) suggest simplifying the electrical field in the proximity of the bottom electrode by assuming that the field lines are straight, and lie on conical surfaces as depicted in Fig. 3.12. Further they assumed that all field lines originate at a virtual origin at a distance a_v below the middle of the electrode of radius r which determines the smallest angle γ between field lines and the horizontal plane.

To calculate the resistance of the layer, which has a constant resistivity ρ_{el}, one integrates the resistance of the cone from $z = a_v$ to $z = a_v + d_b$ as

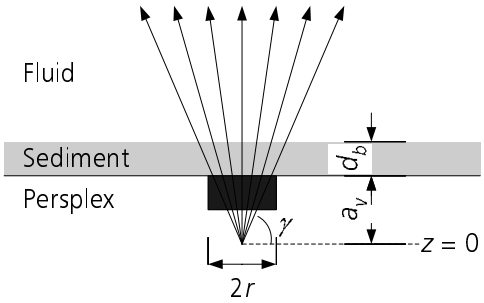

Figure 3.12: Electrical field lines through the sediment layer above a bottom electrode.

$$R_{\text{layer}} = \int_{a_v}^{a_v+d} \frac{\rho_{el}}{A(z)} \mathrm{d}z \tag{3.14}$$

where $A(z)$ denotes the cross-sectional area of the cone, $A(z) = (z/a_v)^2\pi^2$. Substituting this into Eq. (3.14) and integrating yields

$$R_{\text{layer}} = \frac{\rho_{el} d_b}{r^2\pi} \left(1 + \frac{d_b}{r \tan\gamma}\right)^{-1} \tag{3.15}$$

It is further assumed that the sediment layer thickness, d_b is proportional to the sediment mass per unit area, m_b. Finally, solving Eq. (3.15) for the sediment layer thickness, respectively the sediment mass per unit area leads to

$$m_b = \frac{C_2\, R_{\text{layer}}}{C_1 - C_2 C_3\, R_{\text{layer}}} \tag{3.16}$$

where C_1, C_2 and C_3 are constants determined experimentally by calibration and proportional to ρ_{el}, $r^2\pi$ and $(r\tan\gamma)^{-1}$, respectively. The resistance of the layer, R_{layer}, can then be calculated from the measured resistance and the resistance of the water with Eqs. (3.12) and (3.13).

To determine the constants C_1, C_2 and C_3 in Eq. (3.16), the flume was divided in 0.5 m compartments as shown in Fig. 3.13. Carefully weighed amounts of particles were added to the fluid in the tank and the fluid was thoroughly stirred vertically with a grid to obtain a homogeneous suspension. The stirring was stopped and the particles were allowed to settle completely. It was assumed that this sediment layer was of homogeneous thickness.

The bridge output and water temperature was measured for each calibration sample. To determine the constants of Eq. (3.16) a least-square fit optimization was performed. The resulting calibration curve of the mass per unit area, m_b, versus the resistance of the layer, R_{layer} for an electrode is shown in Fig. 3.14, together with the measured values and the error bars.

Figure 3.13: Photograph of the flume divided for the calibration

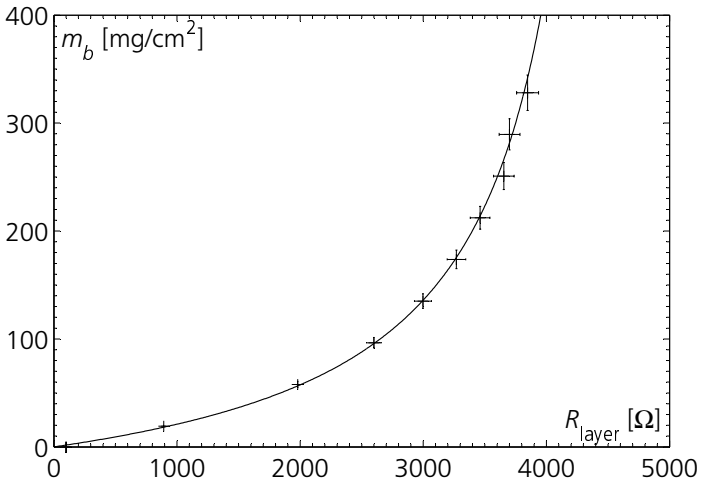

Figure 3.14: Calibration curve with Eq. (3.16).

In all the experiments the evolution of the deposition was measured for a duration of 600 s. The data was further averaged over 1 s with a spline least-square fit and converted into mass per unit area using Eq. (3.16). The measured values were then plotted in intervals of 10 s to represent the time-dependent evolution.

3.3 Experimental Procedure

Basically the experimental procedure followed the same lines for all experiments. For this reason only the experimental procedure for carrying out a standard continuously-fed turbidity current experiment will be described. The specific set-ups for each set of experiments, and the experimental conditions for each run are outlined in detail in Section 3.4.

3.3.1 Mixture and Flume Preparation

Prior to each experiment, the mixing tank and the flume were cleaned and then filled with tap water. The mixing tank was filled from the flume through the pipe system which allowed flushing and cleaning of the system from sediment depositions. After this, sediment was added to the mixing tank until the desired fluid density was achieved. The mixer guaranteed a homogenous mixture in the tank. Difficulties were encountered wetting the relatively light sediment. A kitchen blender was used to prepare a highly concentrated mixture, which then was added to the mixing tank. Once the dense fluid was ready, it was recirculated with a pump through the stilling box. The electromagnetic flowmeter and a valve were then used to adjust the desired inflow rate for a given experiment.

Standard mercury thermometers were used to measure fluid temperatures in the mixing tank and in the flume. This was done to ensure that the only source of density difference was the sediment. A temperature difference of 1 °C corresponds to a density difference on the order of $0.0001\,\mathrm{g/cm^3}$, which is only 2% of the density difference generated during the experiments. This estimate indicated that the difference in water temperatures would have to be considerable to have any significant influence on the dynamics of the underflow. The temperature differences between clear water and the injected mixture was at most ∼2.9 °C and the difference in the density due to this difference in temperature was less than $\sim 0.0005\,\mathrm{g/cm^3}$.

The density of the mixture was measured by means of a hydrometer when the installation was ready for the experiment. At the end of the experiment a second density measurement was taken to verify that no change in density had occurred during the experiment. Generally, the density of the mixture slightly decreased, by at most 5%, during the experiment due to the sedimentation in the inflow tank. The average density was then retained. As the preparation

of the mixture and flume was always carried out immediately before the experiment, the change in temperature due to the mechanical energy supplied by the mixer was negligible and only one temperature measurement was necessary.

3.3.2 Preparation of Measuring Instruments

UVP probes were placed at selected measuring stations at defined inclination angles. For the deposition measurement the reference electrode was put in place and an initial measurement of the resistivity of the clear water was carried out.

All the runs were filmed with a digital video camera to view the experiment, and determine the propagation of the front and reflected bores.

3.3.3 Experimental Run

Generally, each run involved the participation of two people, one in charge of the opening of the inflow sluice and the other one in charge of the drainage valve. In the case of water or air injection a third person was needed to manipulate the valve for dye injection.

A typical run was started when the water levels in both sections of the flume were equal to each other. The sliding gate was slowly opened to a predetermined height of 4.5 cm to let the mixture enter into the flume. Simultaneously, the valve for the return flow was closed and a sediment-laden bottom current was delivered at a specified discharge. The level of the water in the flume was kept at a constant level by means of the drainage valve, which also released the turbid water. The drainage discharge was kept close to the inflow discharge to minimize the variation of the water surface in the flume. The variations stayed within 1–2 cm for a water depth of 70 cm during an experiment of 10 minutes duration. Hence, no adverse influence of these manipulations of the flow on the general behavior of the current was observed.

Automatic data acquisition started before the gate was opened. The digital video camera recording was started after a measured time delay at the moment when the turbidity current became visible in the test section. The head of the turbidity current was then followed to later determine its velocity. A chronometer time measurement allowed the time calibration between the different measurements.

When the underflow reached the end of the flume, a reflected wave started to propagate upstream. For the continuously-fed turbidity current experiments (Series A), the inflow sliding gate was closed at the moment when the head reached the downstream end of the flume. For the other series the experiment was stopped when the reflected wave reached the test section. The maximum

acquisition time of the UVP and deposition measurement device was 600 s. Typically, the experiments lasted about 5 to 10 minutes.

3.4 Description of Experiments

During the thesis work altogether six different series (A to F) of experiments were carried out. The independent variables for these experiments are the initial discharge, Q_0 or initial discharge per unit width, q_0; the density and temperature of the inflow, ρ_0 and T_0; the density and temperature of the ambient fluid, ρ_a and T_a; and the bed slope, S. All the experiments were carried out with an initially fixed bed (flume bed) and the inflow opening height, h_0, was always 4.5 cm. Two different bed slopes, S, were used: a rather steep slope of S=4.64% and a horizontal bottom (S=0.00%). The water depth at the sliding gate, h_w varied only slightly between different experiments and was approximately 57 cm±2% for the experiments with S=4.64% and 89 cm±1% for the experiments with a horizontal bottom, respectively.

Experimental conditions and other useful information for these six series of runs are summarized in Tables 3.7 to 3.12. In the following paragraphs, each series is briefly discussed and the modifications of the experimental installation are described.

3.4.1 Continuously-Fed Turbidity Current – Series A

These experiments were the first ones carried out with this experimental installation. In this series nine turbidity current runs with a slope of 4.64% and one run with a horizontal bottom were carried out. The detailed experimental parameters of Series A can be found in Table 3.7.

All the experiments were filmed with the digital camera and the front velocities were obtained from the films. Six velocity profiles were measured by means of UVP measurements at distances shown in Fig. 3.15. The evolution of the sediment deposition was also recorded during all experiments except for the run A09.

3.4.2 Flow over an Obstacle – Series B

In this series five turbidity current runs over an obstacle were made. The obstacle used in this study was a ridge 24 cm high, running across the full width of the flume. It had a Gaussian shape defined by

$$z = h_m \cdot e^{-50(x-x_m)^2} \tag{3.17}$$

where h_m is the maximum height of the obstacle, and x_m the position of the maximum height in meters. This particular form is used because it is quite

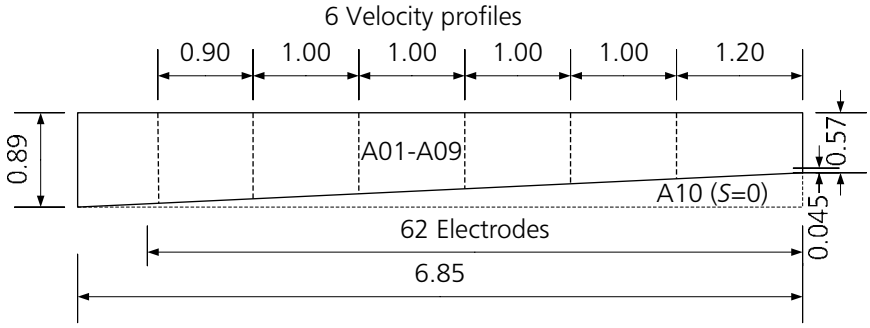

Figure 3.15: Experimental set-up for continuously-fed turbidity current flows (Series A) with locations of velocity profiles.

similar to an embankment dam, but does not have any edges creating flow singularities.

The obstacle was shaped with PVC sheets and fixed on the bottom with weights at a distance of x_m=5 m from the inlet. Fig. 3.16 shows the obstacle installed in the flume. The first three runs were carried out with a horizontal bottom (B01–B03), whereas experiments B04 and B05 were made with a slope of S=4.64%. The detailed experimental parameters of Series B can be found in Table 3.8.

All the experiments were filmed with the digital camera and the front velocities of the turbidity current approaching the obstacle were obtained from the films. Furthermore, the front velocity of the turbidity current head continuing downstream of the obstacle was also measured. For four experiments the propagation velocity of the bore reflected from the obstacle and travelling back upstream was estimated from the video records. Four velocity profiles are measured by means of UVP measurements at the locations shown in Fig. 3.17. The evolution of the sediment deposition is also recorded

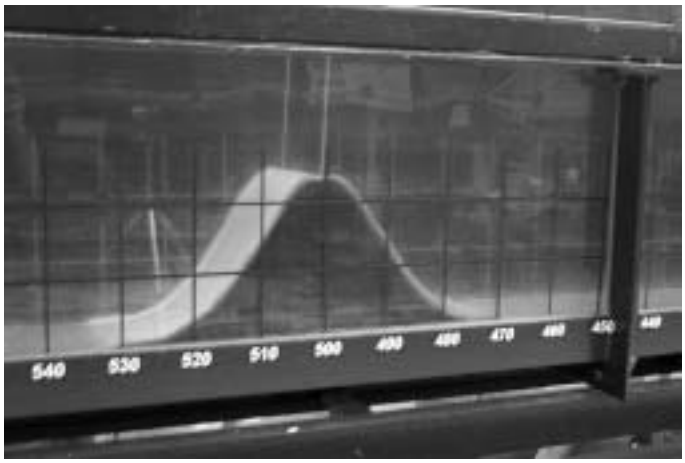

Figure 3.16: Photograph of the obstacle in the flume.

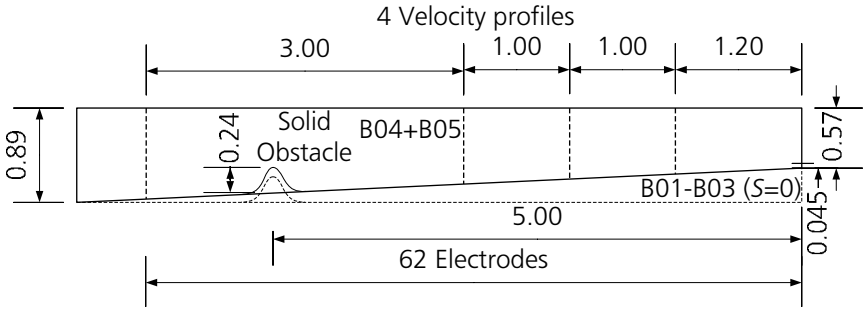

Figure 3.17: Experimental set-up for flow over an obstacle (Series B) with locations of velocity profiles.

during all experiments. No deposition measurements could be made over the obstacle as the electrodes were fixed in the bottom of the flume.

3.4.3 Flow Through a Screen – Series C

In this series five turbidity current runs through a screen of 0.5 m height located at 5.05 m from the inlet were carried out. Two different types of geotextiles were used for the screen as shown on the photographs in Fig. 3.18. Table 3.4 summarizes the characteristics of the geotextiles. In Fig. 3.19 a photograph of the screen installed in the flume is shown. The geotextile was fixed on a rigid frame made of 8 mm brass rods, which reduced the width of the flume by 6%.

The first three runs were carried out with a slope of S=4.64%, whereas experiments C04 and C05 were made with a horizontal bottom. Experiments C01, C02 and C05 were made with the geotextile Tricopor ® 120, whereas in experiments C03 and C04 the geotextile Tricopor® 118 was used. The experimental parameters of Series C can be found in Table 3.9.

All the experiments were filmed with the digital camera and the front velocity of the turbidity current approaching the screen were obtained from the films. Furthermore, the front velocity of the turbidity current head continuing downstream of the screen was also measured. For all experiments the propagation velocity of the bore reflected from the screen and travelling back upstream was estimated from the video records. Five velocity profiles are measured by means of UVP measurements at the locations shown in

Geotextile		Tricopor® 118	Tricopor® 120
Porosity	[−]	36%	41%
Material		PET coated Multifil	PEHD Monofil
Thickness	[mm]	0.30	0.45
Hydraulic diameter	[mm]	1.2	0.5

Table 3.4: Characteristics of geotextiles used in Series C.

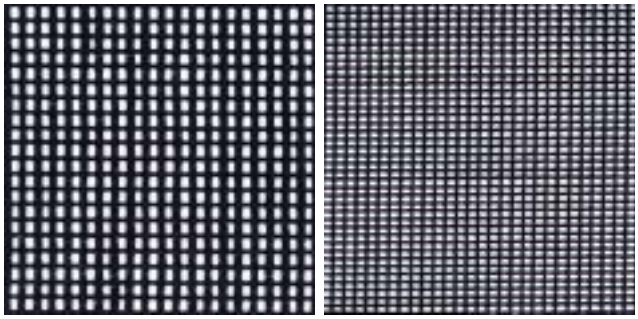

(a) Tricopor® 118. *(b)* Tricopor® 120.

Figure 3.18: Photographs of geotextiles at scale 1:1.

Figure 3.19: Photograph of the screen in the flume.

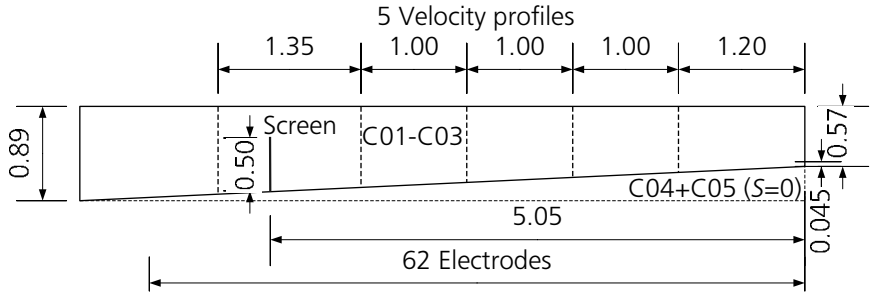

Figure 3.20: Experimental set-up for flow through a screen (Series C) with locations of velocity profiles.

Fig. 3.20. The evolution of the sediment deposition is also recorded during all experiments at all electrodes.

3.4.4 Flow Across a Multiport Diffuser – Series D and E

The turbidity current flow across a vertical (Series D) and an inclined multiport-diffuser (Series E) was investigated. The jets emerged from a rectangular box 60 cm long, 27.2 cm wide, and 7 mm thick consisting of PVC which was placed on the channel bottom. The box was supplied from above through two rectangular ducts 6 mm thick and 60 mm wide. The whole jet injection installation was placed inside the flume as shown in Fig. 3.21. The sections in the streamwise direction of the flume were held very thin to prevent any influence on the flow due to the geometry of the installation.

The box provided a uniform pressure field, so that the jet exiting from the nozzles had the same velocity over the whole width of the flume. In Series D the jets are vertical and emerged from two rows of 27 holes each with a diameter of 2 mm and a spacing of 1 cm as shown in Fig. 3.22. In Series E the diffuser was inclined to 45°and consisted of one row with 27 nozzles of 2.2 mm in diameter and 8 mm in length.

Tap water was used for the jets, and the discharge was measured with a rotameter with an error of 3 cm^3/s. For visualization purposes, a tank filled with dyed fluid was connected to the supply circuit. A pump generated the necessary head to inject very small quantities of dyed fluid into the discharge box.

Runs D01 to D03 as well as E03 and E04 were carried out with a horizontal bottom, whereas the other experiments were made with a slope of 4.64%. The total area of the jet nozzles A_j was 1.697 cm^2 for Series D and 1.026 cm^2 for Series E. In Table 3.5 the discharge, Q_{j0}, velocity, U_{j0} and momentum, $M_{j0} = Q_{j0}U_{j0}$ of the jets for series D and E are presented. Furthermore, the discharge per unit width, q_{j0} and the momentum per unit width, m_{j0}, are calculated. The detailed experimental parameters of the

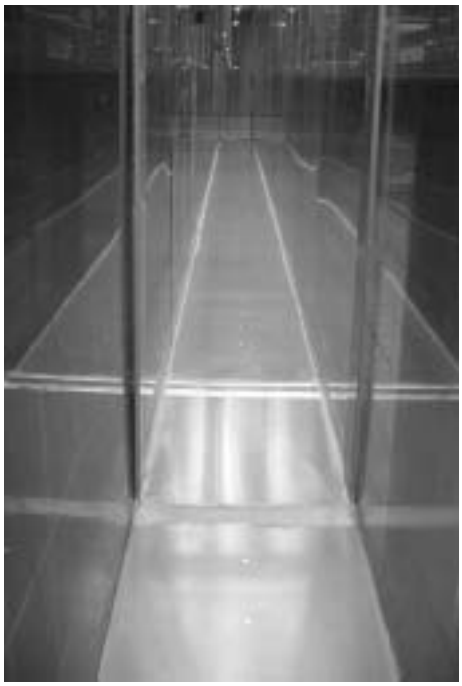

Figure 3.21: Photograph of the water jet injection apparatus.

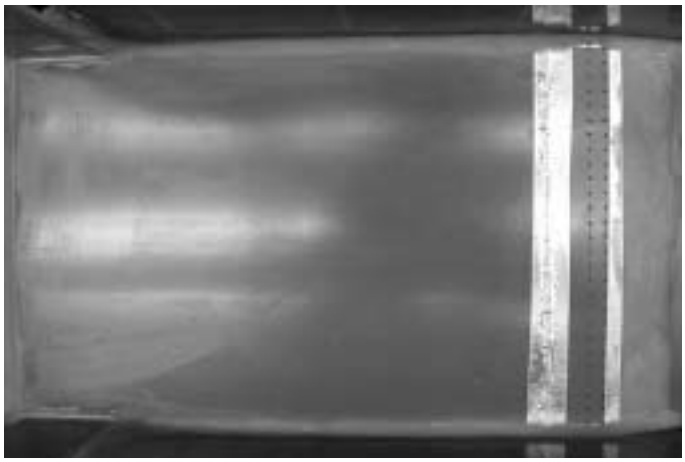

Figure 3.22: Photograph of nozzles of the water jet injection apparatus.

Exp	Q_{j0}	A_j	U_{j0}	M_{j0}	q_{j0}	m_{j0}
[–]	[cm^3/s]	[cm^2]	[cm/s]	[cm^4/s^2]	[cm^2/s]	[cm^3/s^2]
D01	104	1.697	61.3	6374	3.824	234.3
D02	57	1.697	33.6	1915	2.096	70.4
D03	78	1.697	46.0	3585	2.868	131.8
D04	84	1.697	49.5	4158	3.088	152.9
E01	107	1.026	104.3	11159	3.934	410.3
E02	163	1.026	158.9	25896	5.993	952.0
E03	105	1.026	102.3	10746	3.860	395.1
E04	98	1.026	95.5	9361	3.603	344.1

Table 3.5: Experimental parameters of the vertical jet diffuser (Series D) and the inclined jet diffuser (Series E).

turbidity currents for Series D and E can be found in Tables 3.10 and 3.11.

All experiments were filmed with the digital camera and the front velocity of the turbidity current approaching the jet diffuser were obtained from the films. Furthermore, the front velocity of the turbidity current head continuing downstream of the jet diffuser was also measured for all experiments except runs D01 and E02. For experiment E01 the propagation velocity of the bore reflected from the jet diffuser and travelling back upstream was estimated from the video records. Five velocity profiles were measured by means of UVP measurements at the locations shown in Fig. 3.23. The evolution of the sediment deposition was recorded during all experiments except D03 and E04. No deposition measurements could be made in a region of 60 cm downstream of the jet because the jet injection installation covered the electrodes on the bottom of the flume.

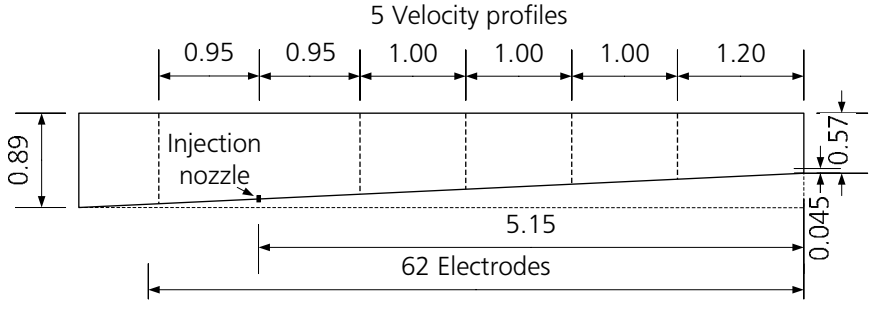

Figure 3.23: Experimental set-up for flow through multiple jets (Series D and E) with locations of velocity profiles.

Exp [–]	Q_b [cm^3/s]	B_b [cm^4/s^3]	q_b [cm^2/s]	b_b [cm^3/s^3]
F01	416.7	408783	15.32	15029
F02	30	29430	1.10	1082

Table 3.6: Experimental parameters of the bubble curtain used in Series F.

3.4.5 Flow Through a Bubble Curtain – Series F

In Series F the turbidity current flow through a bubble curtain was investigated. The discharge box described in Subsection 3.4.4 was used. Two experiments were carried out. In run F01, 14 holes of 2 mm in diameter were used, whereas in run F02, 27 holes of approximately 0.5 mm in diameter were tested. Compressed air was conveyed to the bubble curtain installation through a small tube via a flowmeter. The maximum bubble size was generally less than 4 mm; the tank was of insufficient depth to allow bubbles to coalesce or expand, and the bubble size remained essentially constant over the depth of the tank. Hence, the bubble size and the gas flow rate were a function only of the pressure in the air feeder tube.

Both runs were carried out with a horizontal bottom. In Table 3.6 the discharge, Q_b, and buoyancy flux, $B_b = gQ_b$ of the bubble curtain are listed. Furthermore, the discharge per unit width, q_b and the buoyancy flux per unit width, b_b, are calculated. The detailed experimental parameters of the turbidity current for Series F can be found in Table 3.12.

Both experiments were filmed with the digital camera and the front velocity of the turbidity current approaching the jet diffuser were obtained from the films. The front velocity of the turbidity current head continuing downstream of the jet diffuser was also measured for run F02. Five velocity profiles are obtained by means of UVP measurements at the same locations as in Series D and E. The evolution of the sediment deposition was recorded for run F02. No deposition measurements could also be made in a region of 60 cm downstream of the bubble curtain because the bubble curtain injection installation covered the electrodes on the bottom of the flume.

Exp	S	h_0	h_w	T_a	ρ_a	T_0	ρ_0	$\Delta\rho$	C_s	$\Delta\rho/\rho_a$	g'_0	Q_0	q_0	B_0
[–]	[%]	[cm]	[cm]	[°C]	[g/cm^3]	[°C]	[g/cm^3]	[g/cm^3]	[%]	[%]	[m/s^2]	[m^3/s]	[m^2/s]	[m^3/s^3]
A01	4.64	4.5	56.6	13.0	0.9993	10.8	1.0040	4.72	3.477	0.472	0.0463	0.00096	0.003529	0.0001635
A02	4.64	4.5	56.9	10.2	0.9998	11.3	1.0031	3.22	2.382	0.322	0.0316	0.00075	0.002757	0.0000871
A03	4.64	4.5	56.5	8.9	0.9999	10.4	1.0046	4.71	3.486	0.471	0.0462	0.00072	0.002647	0.0001223
A04	4.64	4.5	56.5	8.8	0.9999	11.3	1.0027	2.79	2.066	0.279	0.0274	0.00085	0.003125	0.0000855
A05	4.64	4.5	58.0	13.2	0.9994	10.3	1.0056	6.28	4.630	0.628	0.0616	0.00137	0.005037	0.0003105
A06	4.64	4.5	57.3	9.0	0.9998	10.8	1.0033	3.53	2.610	0.353	0.0353	0.00086	0.003162	0.0001095
A07	4.64	4.5	56.9	12.1	0.9995	11.0	1.0041	4.67	3.448	0.468	0.0459	0.00050	0.001838	0.0000843
A08	4.64	4.5	57.2	10.3	0.9997	11.8	1.0039	4.20	3.105	0.420	0.0412	0.00063	0.002316	0.0000955
A09	4.64	4.5	57.5	10.5	0.9995	11.0	1.0057	6.17	4.554	0.617	0.0606	0.00071	0.002610	0.0001581
A10	-	4.5	57.0	12.9	0.9995	12.2	1.0040	4.57	3.371	0.457	0.0449	0.00073	0.002684	0.0001204

Table 3.7: Experimental parameters of Series A with a continuously-fed turbidity current.

Exp	S	h_0	h_w	T_a	ρ_a	T_0	ρ_0	$\Delta\rho$	C_s	$\Delta\rho/\rho_a$	g'_0	Q_0	q_0	B_0
[–]	[%]	[cm]	[cm]	[°C]	[g/cm^3]	[°C]	[g/cm^3]	[g/cm^3]	[%]	[%]	[m/s^2]	[m^3/s]	[m^2/s]	[m^3/s^3]
B01	-	4.5	87.5	13.2	0.9996	11.7	1.0031	3.48	2.570	0.348	0.0342	0.00073	0.002684	0.0000917
B02	-	4.5	87.6	12.4	0.9996	11.4	1.0022	2.59	1.913	0.259	0.0254	0.00080	0.002941	0.0000748
B03	-	4.5	87.2	11.9	0.9997	13.3	1.0030	3.29	2.432	0.329	0.0323	0.00071	0.002610	0.0000843
B04	4.64	4.5	55.9	11.8	0.9996	12.0	1.0031	3.54	2.614	0.354	0.0347	0.00056	0.002059	0.0000715
B05	4.64	4.5	54.8	11.6	0.9996	13.6	1.0032	3.57	2.637	0.357	0.0350	0.00083	0.003051	0.0001069

Table 3.8: Experimental parameters Series B with a flow over an obstacle.

Exp	S	h_0	h_w	T_a	ρ_a	T_0	ρ_0	$\Delta\rho$	C_s	$\Delta\rho/\rho_a$	g'_0	Q_0	q_0	B_0
[–]	[%]	[cm]	[cm]	[°C]	[g/cm^3]	[°C]	[g/cm^3]	[g/cm^3]	[%]	[%]	[m/s^2]	[m^3/s]	[m^2/s]	[m^3/s^3]
C01	4.64	4.5	56.4	12.5	0.9994	11.8	1.0041	4.66	3.437	0.466	0.0457	0.00079	0.002904	0.0001329
C02	4.64	4.5	n.d.	11.2	0.9995	11.1	1.0049	5.36	3.956	0.536	0.0526	0.00070	0.002574	0.0001094
C03	4.64	4.5	54.4	11.2	0.9995	10.5	1.0040	4.46	3.292	0.446	0.0438	0.00068	0.002500	0.0001094
C04	-	4.5	87.6	10.9	0.9997	11.0	1.0029	3.24	2.395	0.324	0.0318	0.00063	0.002316	0.0000736
C05	-	4.5	87.6	11.8	0.9997	11.0	1.0030	3.32	2.454	0.332	0.0326	0.00068	0.002500	0.0000814

Table 3.9: Experimental parameters of Series C with a flow through a screen.

Exp	S	h_0	h_w	T_a	ρ_a	T_0	ρ_0	$\Delta\rho$	C_s	$\Delta\rho/\rho_a$	g'_0	Q_0	q_0	B_0
[–]	[%]	[cm]	[cm]	[°C]	[g/cm^3]	[°C]	[g/cm^3]	[g/cm^3]	[%]	[%]	[m/s^2]	[m^3/s]	[m^2/s]	[m^3/s^3]
D01	-	4.5	86.8	12.7	0.9996	12.0	1.0033	3.75	2.769	0.375	0.0368	0.00066	0.002426	0.0000893
D02	-	4.5	87.6	12.6	0.9994	11.2	1.0032	3.75	2.765	0.375	0.0368	0.00073	0.002684	0.0000988
D03	-	4.5	87.7	12.1	0.9995	11.2	1.0024	2.91	2.147	0.291	0.0286	0.00074	0.002721	0.0000777
D04	4.64	4.5	58.2	12.4	0.9995	11.9	1.0033	3.82	2.818	0.382	0.0375	0.00081	0.002978	0.0001117

Table 3.10: Experimental parameters of Series D with a flow across a vertical multiport-diffuser.

Exp	S	h_0	h_w	T_a	ρ_a	T_0	ρ_0	$\Delta\rho$	C_s	$\Delta\rho/\rho_a$	g'_0	Q_0	q_0	B_0
[–]	[%]	[cm]	[cm]	[°C]	[g/cm^3]	[°C]	[g/cm^3]	[g/cm^3]	[%]	[%]	[m/s^2]	[m^3/s]	[m^2/s]	[m^3/s^3]
E01	4.64	4.5	57.9	13.6	0.9992	12.2	1.0033	4.06	2.990	0.406	0.0399	0.00078	0.002868	0.0001143
E02	4.64	4.5	56.3	13.2	0.9993	11.6	1.0030	3.78	2.785	0.378	0.0371	0.00066	0.002426	0.0000900
E03	-	4.5	86.0	13.3	0.9994	12.6	1.0033	3.92	2.890	0.392	0.0385	0.00072	0.002647	0.0001019
E04	-	4.5	87.5	10.9	0.9995	11.1	1.0033	3.78	2.790	0.378	0.0371	0.00076	0.002794	0.0001037

Table 3.11: Experimental parameters of Series E with a flow through an inclined multiport-diffuser.

Exp	S	h_0	h_w	T_a	ρ_a	T_0	ρ_0	$\Delta\rho$	C_s	$\Delta\rho/\rho_a$	g'_0	Q_0	q_0	B_0
[–]	[%]	[cm]	[cm]	[°C]	[g/cm^3]	[°C]	[g/cm^3]	[g/cm^3]	[%]	[%]	[m/s^2]	[m^3/s]	[m^2/s]	[m^3/s^3]
F01	-	4.5	87.6	9.8	0.9995	10.8	1.0034	3.85	2.841	0.385	0.0378	0.00070	0.002574	0.0000972
F02	-	4.5	86.9	11.8	0.9996	12.1	1.0034	3.78	2.792	0.378	0.0371	0.00080	0.002941	0.0001091

Table 3.12: Experimental parameters of Series F with a flow through a bubble curtain.

4 Experimental Results

4.1 Continuously-Fed Turbidity Current

In each experiment, as the turbid flow spread down the slope, the leading edge of the current formed a front similar to the one shown in Fig. 4.1. The velocity flow field in the turbidity current head has a complicated three-dimensional pattern. As the UVP flow measurements were made along one measurement axis, only the measured values after the passing of the head were retained for analysis. This steady-state region was determined by visualizing the complete time series of the velocity measurement for a given transducer and selecting start and end time of the steady-state region. These time series lasted typically one minute and consisted of more than 100 single velocity profiles.

The velocity profiles were then averaged and the integral turbidity current height, h, and the layer-averaged velocity, U determined at each measuring station with the aid of Eqs. (2.6) and (2.7) as follows

$$U = \frac{\int_0^{h_t} u^2 \, \mathrm{d}z}{\int_0^{h_t} u \, \mathrm{d}z} \tag{4.1}$$

$$h = \frac{\left(\int_0^{h_t} u \, \mathrm{d}z\right)^2}{\int_0^{h_t} u^2 \, \mathrm{d}z} \tag{4.2}$$

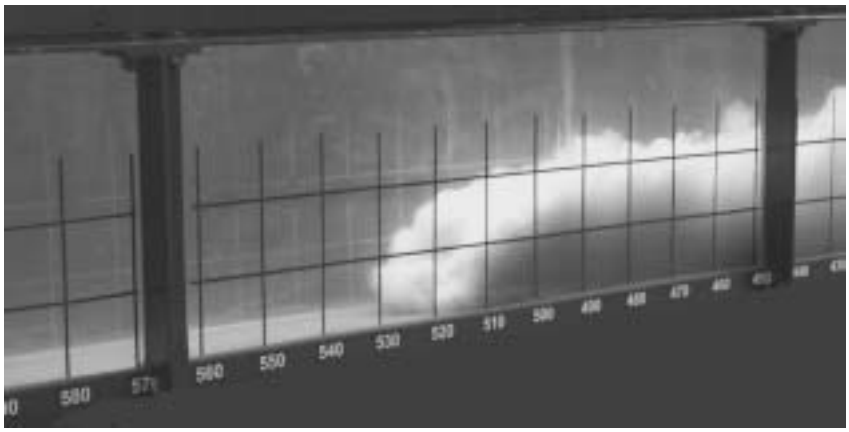

Figure 4.1: Turbidity current front in experiment A03.

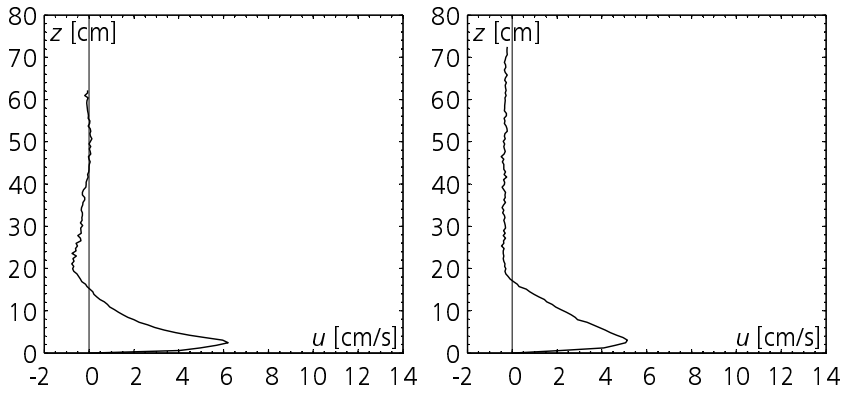

(a) x=320 cm. *(b)* x=520 cm.

Figure 4.2: Measured vertical velocity profiles of experiment A07.

where h_t is the height of the current at which the velocity equals zero. The maximum velocity, U_{max} and the height of maximum velocity, h_{max} were also determined from the measured profiles. Two measured velocity profiles for experiment A07 are shown in Fig. 4.2. Values of the layer-averaged velocity ,U and turbidity current height, h at all measuring stations for this experiment are summarized in Table 4.1. Measured velocity profiles and computed integral scale values for all Series A experiments can be found in Appendix A.1 on page 193.

The turbidity currents generated at the inlet developed within the first one or two meters from the gate. In some experiments the flow at the first profile at 120 cm was still partially affected by the initial momentum. From the profile at a distance of x=220 cm downstream, the turbidity currents then grow due to the water entrainment in the mixing region between the turbidity current and the ambient water as shown in Table 4.1.

In Fig. 4.3, velocity profiles at different locations for runs A06 and A07 are plotted on the same graph in normalized form with the corresponding layer-averaged velocity, U, and the current height, h. It can be seen that the

x [cm]	h [cm]	U [cm/s]	h_{max} [cm]	U_{max} [cm/s]	U_{max}/U [–]	h_{max}/h [–]
120	6.71	4.68	1.81	6.44	1.38	0.27
220	6.87	4.72	1.81	6.82	1.44	0.26
320	9.43	4.06	2.41	6.20	1.53	0.26
420	10.78	3.62	1.81	5.45	1.51	0.17
520	12.48	3.58	3.02	5.14	1.44	0.24
610	16.38	2.95	2.41	4.67	1.58	0.15

Table 4.1: Integral scale and maximum values at all measuring locations of experiment A07.

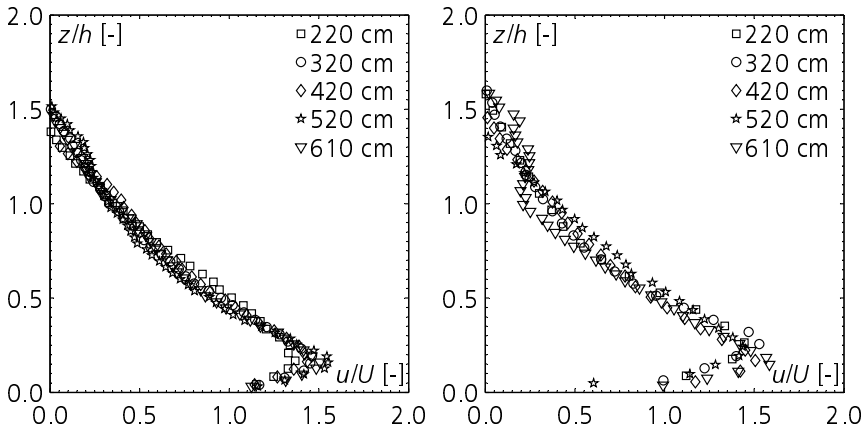

(a) Experiment A06. *(b)* Experiment A07.

Figure 4.3: Similarity collapse of velocity profiles at different locations.

similarity collapse is quite good for the different locations. The vertical spacing between the measuring points in Fig. 4.3(a) is 4.4 mm which allows a high resolution in the boundary layer extending up to the maximum velocity. The average ratio between the maximum velocity, U_{max} and the average velocity, U in the experiments of Series A was found to be 1.41 with a standard deviation of 0.09, which is similar to the value found by Garcia (1989) and slightly higher than the value of 1.3 given by Altinakar et al. (1996). The ratio of the height of maximum velocity, h_{max}, to the average height, h is 0.25 with a standard deviation of 0.07, which is lower than the value of 0.3 reported by Altinakar et al. (1996) and higher then the value of 0.15 found by Garcia (1989). This difference might be due to the different measuring methods used. The UVP measurement has a much higher resolution and is non-intrusive compared to the micro-propeller current-meter used by Altinakar et al. (1996). Therefore, there are many measuring points close to the bottom and the maximum velocity can be better captured with the UVP measurement.

A way to visualize the advancement of the turbidity current head is to plot the position of the front against time. Such curves for all experiments of Series A are presented in Fig. 4.4. The measured head velocity, $U_{f1\text{meas}}$, for a given experiment is represented by the slope, $\mathrm{d}x/\mathrm{d}t$, and calculated by a least square linear fit to the data as listed in Table 4.2. All individual distance versus time plots share the same ordinate axis. In order not to have intersecting lines, the t=0 points are shifted 60 s (or multiples) to the right.

As the walls were not transparent in the upper part of the flume, no measurements could be made over the first 220 cm. Nevertheless, the time delay from the opening of the gate to the first measuring point was measured, and a dotted line, representing the invisible section, was also plotted on the figure. Inspecting the data in Fig. 4.4, it can be seen that the front velocity in each experiment was approximately constant over the measuring section. This

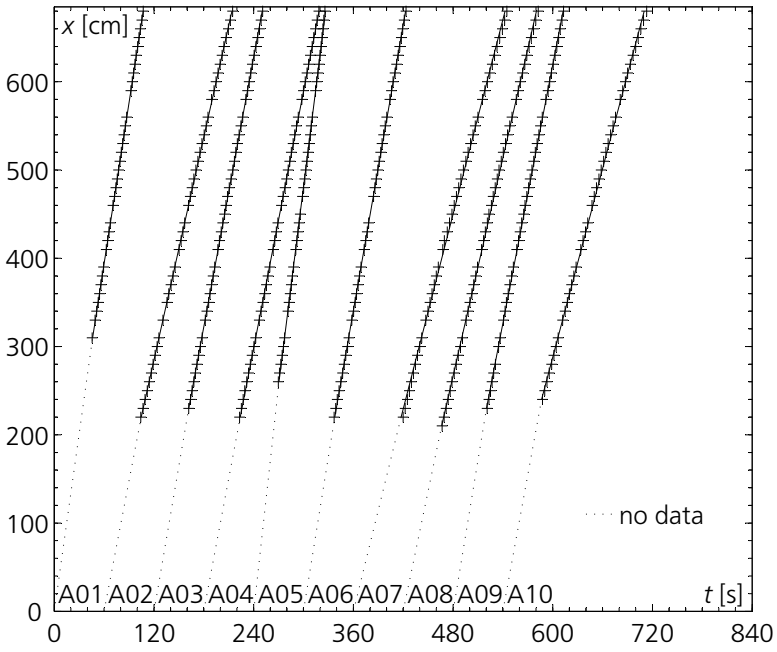

Figure 4.4: Measured front velocities of Series A.

linearity was also observed by Altinakar et al. (1996) for the experiments on slopes exceeding 1%. One can also see a slight change of slope in the dashed lines upstream of 220 cm, which is probably due to the flow development at the early stages.

During the experiments, sediments deposited on the bottom and the buoyancy flux, B of the current decreased. Following Britter and Linden (1980) and other investigators, the front velocity is proportional to the 1/3 power of the buoyancy flux (see Section 2.1). Therefore, one would expect the front velocity to decrease due to the loss of sediments. The lack of a noticeable slowdown could be due to the fact that this dependence on the buoyancy flux is weak. Another explanation for the constant front velocity may be the influence of the varying relative submergence ratio h/H. Altinakar (1988) further investigated the reason for an almost constant front velocity and demonstrated that it can be attributed to the influence of the grain size distribution of the sediment. After the current has deposited the coarser part of its sediment load, it continues to advance with size fractions having a smaller representative distribution of the sediment.

From the front velocity, $U_{f1\mathrm{meas}}$, and the initial buoyancy flux, B_0, the

Exp	[–]	A01	A02	A03	A04	A05	A06	A07	A08	A09	A10
$U_{f1\mathrm{meas}}$	[cm/s]	6.07	4.22	5.09	4.85	7.50	5.38	3.67	4.11	4.87	3.56
$\frac{U_{f1\mathrm{meas}}}{B_0^{1/3}}$	[–]	1.11	0.95	1.03	1.10	1.11	1.12	0.84	0.90	0.90	0.72

Table 4.2: Measured front velocities, $U_{f1\mathrm{meas}}$, of Series A.

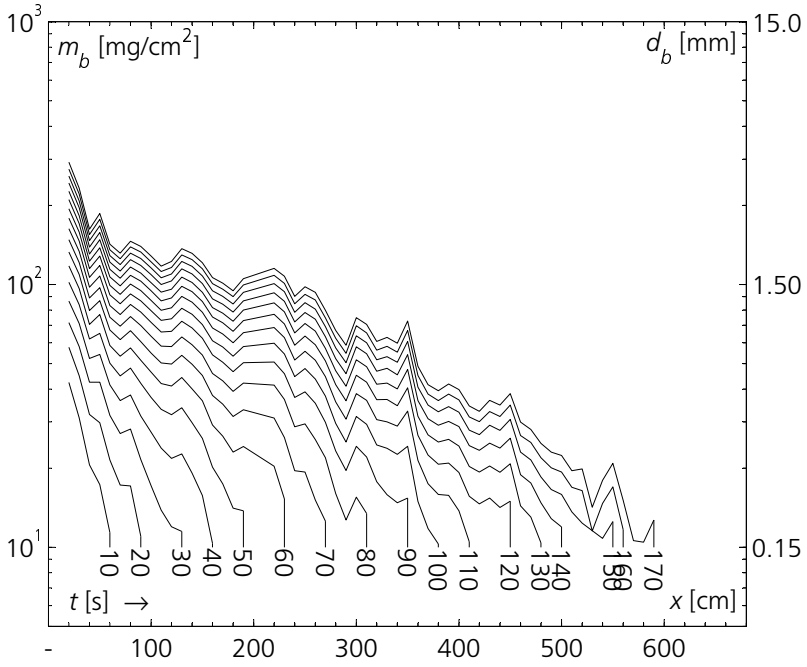

Figure 4.5: Measured deposition evolution of experiment A07 in time steps of 10 s.

non-dimensional ratio of $U_{f1\mathrm{meas}}/B_0^{1/3}$ can be calculated and is also shown in Table 4.2. The values lay in the range of 0.84–1.12 for the experiments with a bottom slope and a value of 0.72 was found in the experiment A10 with a horizontal bottom. These values are in good agreement with Eq. (2.3) and the values found by Altinakar et al. (1996).

During all experiments the evolution of the deposited sediment mass per unit area was measured with the device described in Subsection 3.2.5. The evolution of deposition of experiment A07 with a time interval of 10 s is presented in Fig. 4.5, where the deposited sediment mass per unit area is plotted on a log-linear axis so that an ideal exponentially decreasing sedimentation should plot along a straight line. On the right axis the corresponding deposition thickness in millimeters is shown for a porosity of 0.57. Time is shown at the lower end of each curve.

Fig. 4.5 shows also how the turbidity current propagates, and how the deposition thickness grows with time. Near the inflow, vigorous mixing and high speed of the current tended to make the sedimentation pattern irregular. Nevertheless, after the initial momentum had decayed due to entrainment at approximately x=50 cm, the deposits exponentially decreased to a very good approximation. This was also observed by Garcia (1989). Furthermore, one can see the high precision of the measuring device, which lays approximately at 10 mg/cm^2 or 0.15 mm. The results of the deposition measurements for all experiments of Series A are presented in Appendix A.1 on page 193.

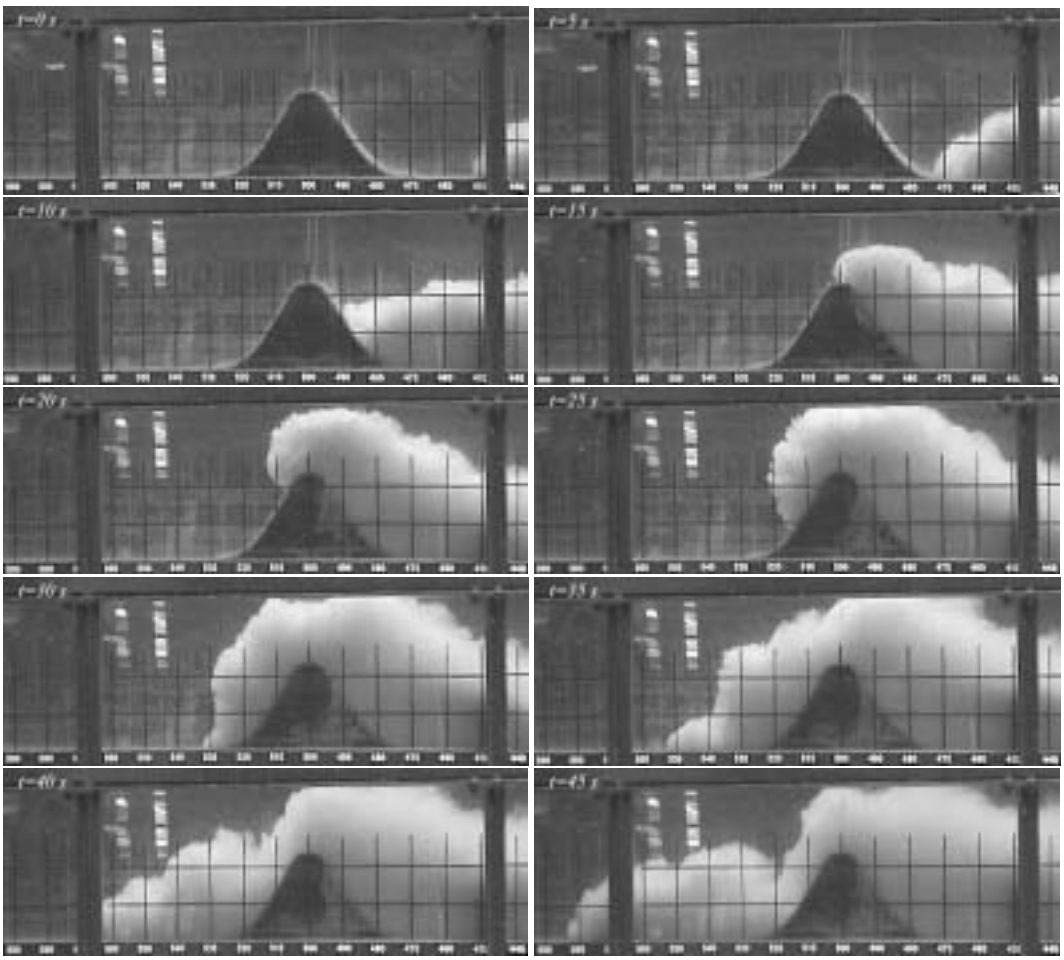

Figure 4.6: Photographic sequence of turbidity current flow over an obstacle at time intervals of 5 s of experiment B01 (S=0.00%).

4.2 Effect of an Obstacle

The experimental parameters and the characteristics of the obstacle were presented in Subsection 3.4.2. Five turbidity current runs over an obstacle of 24 cm high located at a distance of 5.0 m from the inlet were carried out with the parameters given in Table 3.8.

The turbidity current upstream of the obstacle had a standard form as found in the experiments without an obstacle, i.e. a head region somewhat higher than the following body. When the turbidity current reached the obstacle, it climbed up, decelerating only slightly as shown in the photographic sequence of experiment B01 in Fig. 4.6. The photos show that the turbidity current head passes over the obstacle, whereas a cut occurs behind the head. A slender current follows the head region and keeps flowing over the top of the obstacle down the flume. The standard shape of the current was reestablished as its front advanced downstream of the obstacle.

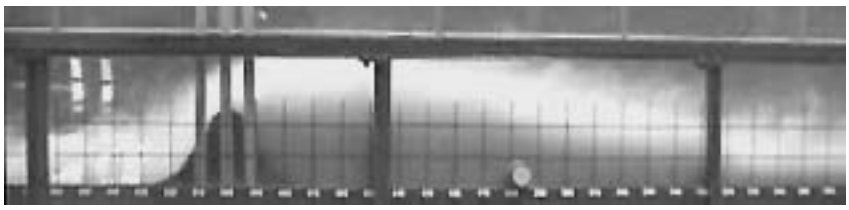

(a) Undular bore in experiment B03 with horizontal bottom.

(b) Strong bore in experiment B05 with inclined bottom.

Figure 4.7: Photographs of reflected bores in experiments of turbidity currents flowing over an obstacle (Series B).

Due to the presence of the obstacle and the change in flow rate, the turbidity current was partially reflected and an internal bore travelling upstream was observed. This phenomenon is similar to a moving hydraulic jump in open-channel flows in which there is a sudden increase of the water depth associated with a change in the flow rate, for example. In the experiments with horizontal bottom the reflected bore was observed to be an undular bore: a smooth change in depth with a train of internal waves as shown in Fig. 4.7(a). Wood and Simpson (1984) found that undular bores occur where the change in depth is by a factor of approximately 2.5 or less. For larger steps the bore advances very similar to a turbidity current front. In a bore the mechanical energy is not conserved. In the undular case, the loss of energy occurs in the bore, and is effected by waves each of which carries energy as it moves away. The more intense bores cannot radiate enough energy by this method and the energy excess is dissipated by turbulence in the leading edge (Simpson, 1997). Such strong bores were observed in the experiments with an inclined bottom, where the bore propagated upstream forming a well recognizable front as shown in Fig. 4.7(b).

Once the reflected jump or bore has moved away from the obstacle, a steady flow is observed upstream of the obstacle as shown in Fig. 4.8. The lower layer flows over the crest and down the downstream side of the obstacle in a fast shallow layer similar to single layer flow over a weir. For the experiments with an inclined bottom slope, no hydraulic jump could be seen downstream of the obstacle which indicates that the turbidity current stayed supercritical over the 2 meters downstream of the obstacle. The turbidity current flow downstream of the obstacle was similar to (but slower than) the original oncoming current.

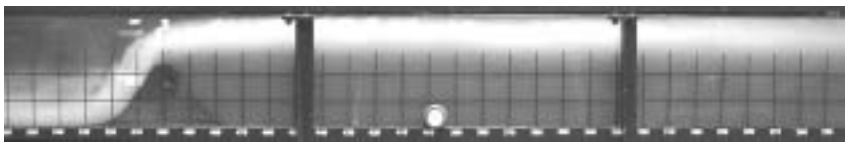

Figure 4.8: Steady state in experiment B01.

From the video recordings the front velocity of the oncoming turbidity current, $U_{f1\mathrm{meas}}$, was determined up to the foot of the obstacle. Furthermore, the front velocity of the outgoing (continuing) turbidity current which formed downstream of the obstacle, $U_{f2\mathrm{meas}}$, was measured. Finally, the velocity of the upstream propagating bore, $U_{fb\mathrm{meas}}$, was estimated from the video sequence. In the experiments with horizontal bottom, the gradual variation of the lower-layer depth made a determination of the precise position of the jump difficult. The jump position was taken as the point where the lower-layer depth started to increase. Fig. 4.9 shows the distance versus time plots for the front of the oncoming and outgoing turbidity current as well as the reflected bore in the Series B experiments. As can be seen in Fig. 4.9, the least-square linear fit shows good agreement with the measuring points in the regions upstream and downstream of the obstacle. This indicates that again constant front velocities, except in a region directly influenced by the obstacle, exists. In the region approximately two times the obstacle height up- and downstream of the crest no linear relationship exists. This explains the fact that the fitted lines in Fig. 4.9 do not coincide at the obstacle crest. The values of the front velocities and the propagation speeds of the jump are given in Table 4.3.

The values in Table 4.3 show that the front velocity decreases considerably after the obstacle due to the decrease of the buoyancy flux at the obstacle. The velocity of the bore propagating upstream is 2–3 times smaller than the front velocity of the outgoing turbidity current.

As described above a slender turbidity current is formed downstream of the obstacle. The velocity profile measurements were made at three locations upstream of the obstacle and one profile was taken 1.2 m downstream of the obstacle crest. Within the reflected jump the velocity component perpendicular to the bottom is not negligible anymore and no quantitative measurement with a single UVP transducer is possible. Therefore, only the measurements of

Exp	[–]	B01	B02	B03	B04	B05
$U_{f1\mathrm{meas}}$	[cm/s]	3.91	3.62	3.40	4.30	5.06
$U_{f2\mathrm{meas}}$	[cm/s]	3.22	2.62	2.37	2.70	3.28
$U_{fb\mathrm{meas}}$	[cm/s]	n.d.	-1.40	-1.07	-0.75	-1.12

Table 4.3: Measured front velocities upstream, $U_{f1\mathrm{meas}}$, and downstream, $U_{f2\mathrm{meas}}$, of the obstacle as well as propagation speed of the reflected bore, $U_{fb\mathrm{meas}}$, in Series B.

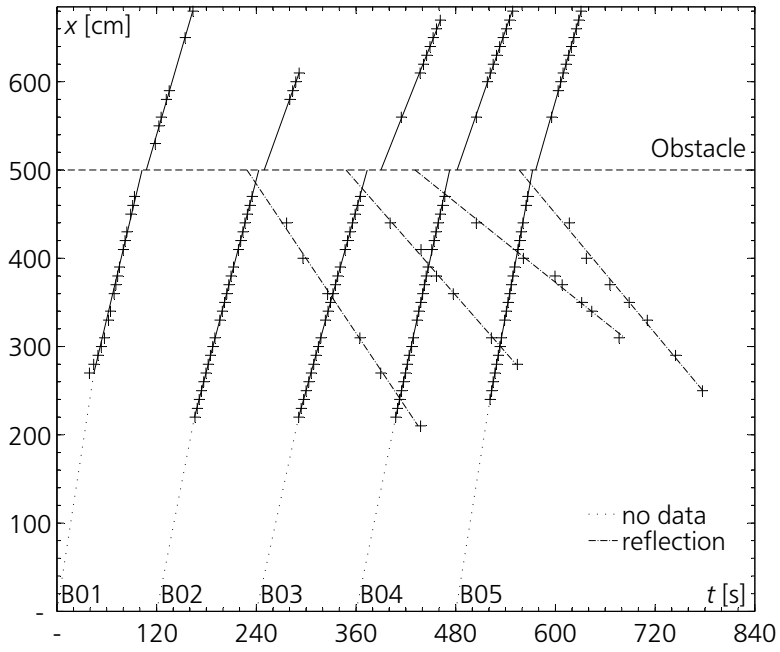

Figure 4.9: Measured front velocities of experiments with a turbidity current flowing over an obstacle (Series B).

the oncoming turbidity current upstream of the bore were used. Similarly, only velocity profiles in the body of the outgoing current were processed. Fig. 4.10 shows the measured velocity profiles upstream (4.10(a) and 4.10(c)) as well as downstream of the obstacle (4.10(b) and 4.10(d)) for an experiment with a horizontal slope (experiment B02) and an inclined slope (experiment B05).

The ratio of the obstacle height, h_m to the height of the current, h, upstream of the obstacle as introduced in Section 2.2 is approximately 2.0 for experiment B03 and 2.5 for experiment B05. Even if the ratio is similar for both experiments, it can clearly be stated from the comparison of the velocity profiles that the effect of the obstacle is much stronger in experiment B03 with a horizontal bottom. In experiment B03, the height of the turbidity current doubles and the velocity decreases considerably after the obstacle, whereas in experiment B05 the increase in height and decrease in velocity after the obstacle is much smaller.

The evolution of the deposits in experiment B03 with a horizontal bottom and B05 with an inclined bottom are shown in Fig. 4.11. For experiment B03, the deposition rate increases upstream of the obstacle due to the reduced flow velocity between the reflected bore and the obstacle (see Fig. 4.11(a)). A logarithmic least-square fit to the last deposition measurement was performed to indicate an exponential decrease of the sediment thickness upstream and downstream of the obstacle. The deposition rate downstream of the obstacle is reduced significantly and the slope of the exponential decrease of the deposition thickness is larger. In experiment B05, the deposition increases

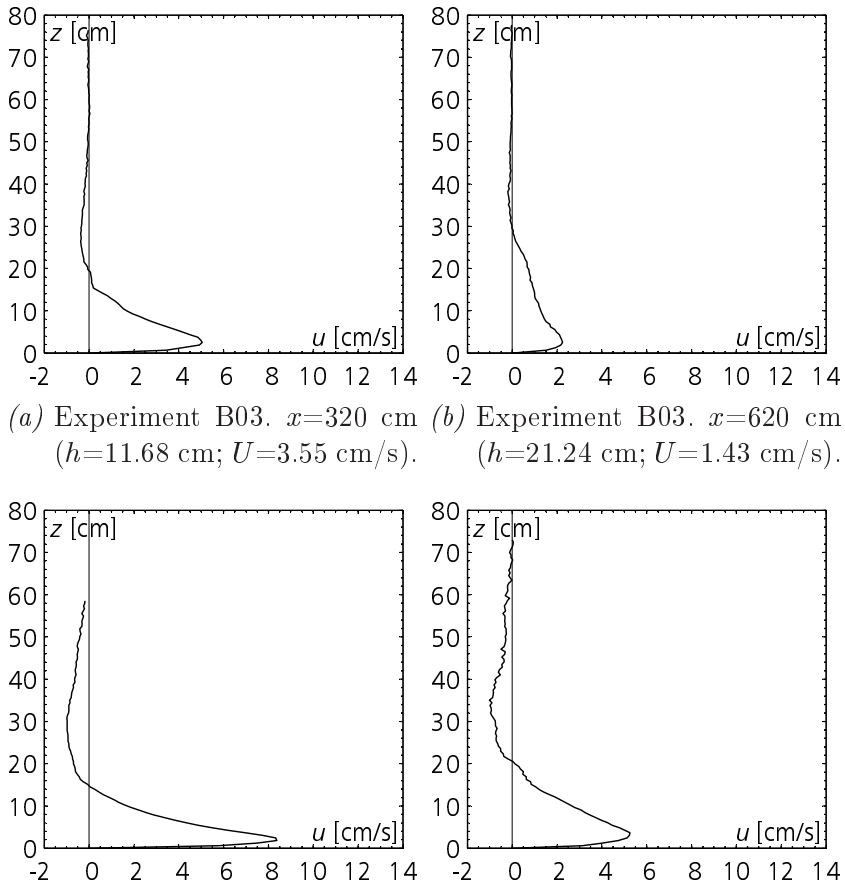

(a) Experiment B03. x=320 cm (h=11.68 cm; U=3.55 cm/s).

(b) Experiment B03. x=620 cm (h=21.24 cm; U=1.43 cm/s).

(c) Experiment B05. x=320 cm (h=9.47 cm; U=5.69 cm/s).

(d) Experiment B05. x=620 cm (h=14.00 cm; U=3.69 cm/s).

Figure 4.10: Velocity profiles of Series B of the oncoming turbidity current (4.10(a) and 4.10(c)) and the turbidity current continuing downstream of the obstacle (4.10(b) and 4.10(d)).

also upstream of the obstacle, but the effect of the obstacle on the deposition evolution is less pronounced (see Fig. 4.11(b)). The difference in deposition thickness upstream and downstream of the obstacle is smaller and the slope of the exponential decrease of the deposition thickness stays almost identical to the upstream slope.

The experimental results for all experiments with an obstacle are presented in Appendix A.2 on page 211.

4.3 Effect of a Screen

The experimental parameters and the characteristics of the screen were presented in Subsection 3.4.3. Five turbidity current runs through a screen of

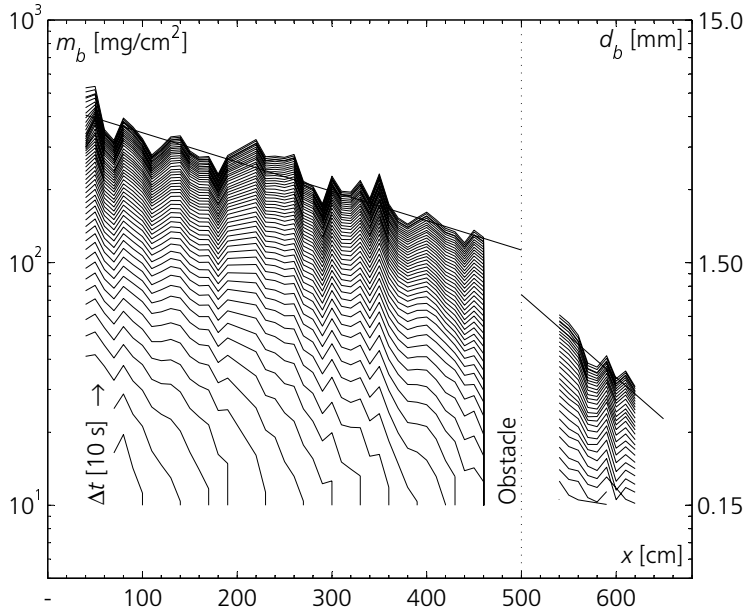

(a) Experiment B03 (S=0.00%).

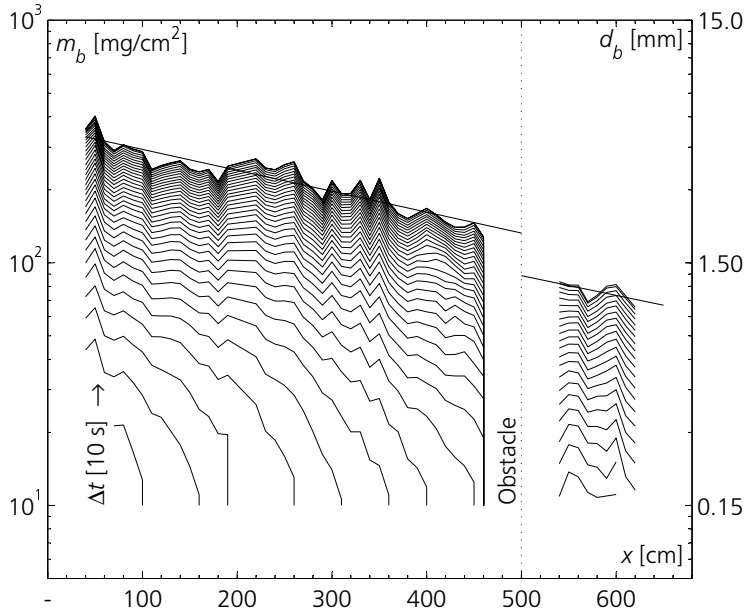

(b) Experiment B05 (S=4.64%).

Figure 4.11: Measured deposition evolution along the flume axis, x, with time intervals of 10 s for the flow over an obstacle (Series B).

Figure 4.12: Turbidity current flowing through a screen at time intervals of 5 s of experiment C01 (S=4.64%).

50 cm high located at 5.05 m from the inlet with two different types of screens (geotextiles) were carried out with the parameters given in Table 3.9.

No influence of the screen on the approaching turbidity current was observed and the flow was similar to the experiments without a screen. When the turbidity current reached the vertical screen, it was almost blocked due to the increased flow resistance as shown on the photographic sequence of experiment C01 in Fig. 4.12. The turbidity current then shoots up on the screen to a height of 2 to 3 times the height of the oncoming turbidity current, and decelerates as it rises. The photos show that the turbidity current then seeps through at the bottom of the screen driven by the pressure gradient. As the level upstream of the screen raises, more fluid passes through the screen forming a slender outgoing turbidity current. Due to the flow resistance of the screen, some part of the flow is reflected similar to the experiments with an obstacle.

In the experiments with horizontal bottom the reflected bore was again an undular one whereas in the experiments with an inclined bottom slope the

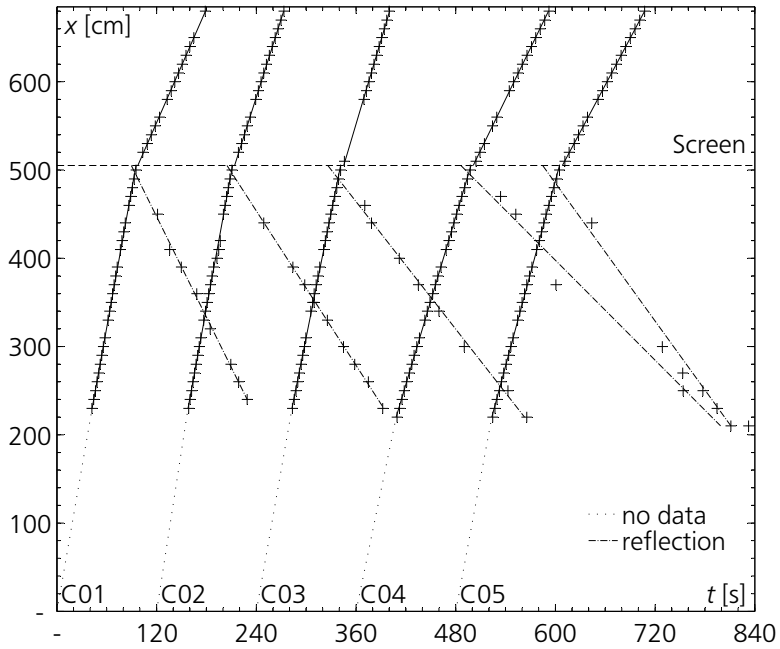

Figure 4.13: Measured front velocities of experiments with a turbidity current flowing through a screen (Series C).

bore formed a well recognizable front. Once the reflected jump or bore has moved away from the screen, a steady flow is again observed in the region of the screen. The turbidity current flow downstream of the obstacle was similar to (but slower than) the original oncoming current.

The front velocities of the oncoming and outgoing turbidity current, $U_{f1\mathrm{meas}}$ and $U_{f2\mathrm{meas}}$, as well as the velocity of the upstream propagating bore, $U_{fb\mathrm{meas}}$, were determined from the video sequence and are presented in Fig. 4.13. As can be seen in Fig. 4.13, the linear least-square fit shows good agreement with the measuring points in the regions upstream and downstream of the screen. This indicates that again constant front and bore velocities exist except in a region directly influenced by the screen. The values of the front velocities and the propagation speed of the bore are given in Table 4.4.

The values in Table 4.4 show that the front velocity again decreases considerably after the screen due to the decrease of the buoyancy flux and the

Exp	[–]	C01	C02	C03	C04	C05
$U_{f1\mathrm{meas}}$	[cm/s]	5.18	5.13	4.71	3.16	3.50
$U_{f2\mathrm{meas}}$	[cm/s]	2.15	2.96	3.17	1.93	1.77
$U_{fb\mathrm{meas}}$	[cm/s]	-1.90	-1.46	-1.20	-0.93	-1.25

Table 4.4: Measured front velocities upstream, $U_{f1\mathrm{meas}}$, and downstream, $U_{f2\mathrm{meas}}$, of the screen as well as propagation speed of reflected wave, $U_{fb\mathrm{meas}}$, in Series C.

loss of energy occurring at the screen. The velocity of the bore propagating upstream is approximately half the front velocity of the outgoing turbidity current. Even if the tested geotextiles had similar geometric porosities, a difference in the behavior was observed. The geotextile Tricopor® 120 used in experiment C01, C02 and C05, had a higher flow resistance resulting in smaller outgoing front velocities and higher propagation speed of the bore, whereas in the other experiments (C03 and C04) with the geotextile Tricopor® 118 the outgoing front velocity was higher and consequently, the velocity of the upstream propagating bore was smaller. These results are interesting, because they clearly show the influence of the mesh size of hydraulic diameter of the openings. In fact, the geotextile Tricopor® 118 has slightly smaller porosity than the Tricopor® 120, but the mesh opening is much bigger (cf. Table 3.4).

The velocity measurements were made in the steady state at four locations upstream of the screen and one profile was taken 0.5 m downstream of the screen. Fig. 4.14 shows the measured velocity profiles upstream (4.14(a) and 4.14(c)) as well as downstream of the screen (4.14(b) and 4.14(d)) for an experiment with a horizontal slope (experiment C04) and an inclined slope (experiment C03).

It is interesting to note that the difference between the horizontal (C04) and inclined bottom experiments (C03) is smaller than in the experiments with an obstacle (see Fig. 4.10). The increase in height downstream of the screen is also less important than for the experiments with an obstacle, where the height of the turbidity current for some experiments nearly doubles.

The deposition evolution of experiments C04, with horizontal bottom, and C03, with an inclined bottom, are shown in Fig. 4.15. For experiment C03 in Fig. 4.15(b), no significant difference in the deposition thickness upstream and downstream of the screen was found. This result is somewhat surprising because the front velocity and average velocity of the outgoing turbidity current is reduced considerably, but might be explained by the fact that the driving force through the screen is the density difference and hence more denser fluid than lighter fluid passes. With a horizontal bottom a certain amount of sediments is retained behind the screen, but still less than with the obstacle. For the screen with the other geotextile more sediments were retained as shown in Fig. 4.16.

The experimental results for all experiments with a screen are presented in Appendix A.3 on page 223.

4.4 Effect of Multiple Jets

The experimental parameters and the characteristics of the multiport diffuser were presented in Subsection 3.4.4. Four turbidity current runs across a vertical multiport diffuser (Series D) and four turbidity current runs across

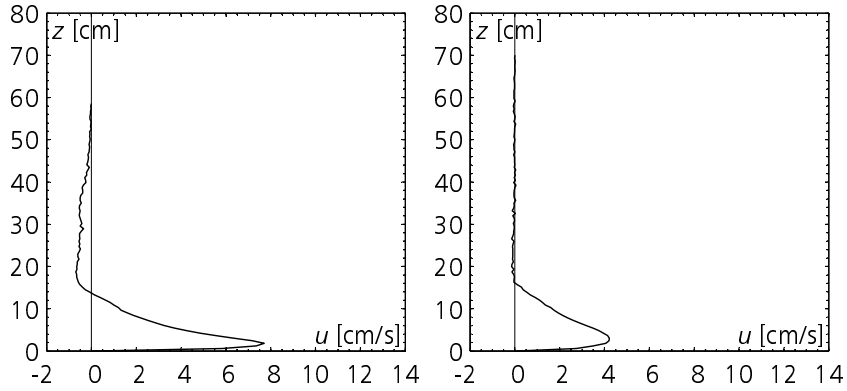

(a) Experiment C03. x=320 cm (h=8.76 cm; U=5.05 cm/s).

(b) Experiment C03. x=555 cm (h=11.67 cm; U=3.07 cm/s).

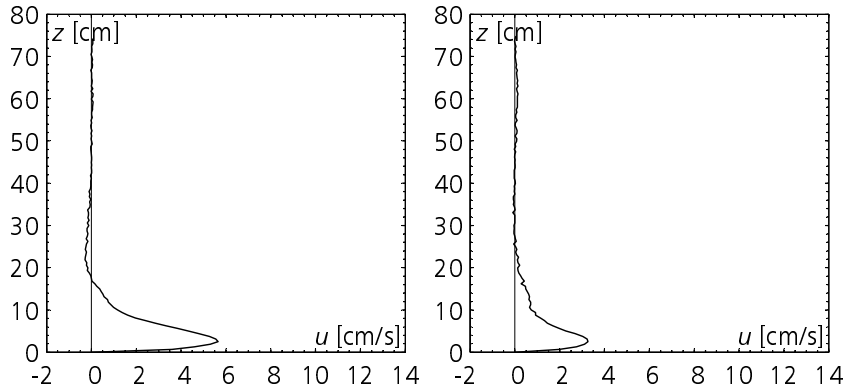

(c) Experiment C04. x=320 cm (h=10.18 cm; U=3.91 cm/s).

(d) Experiment C04. x=555 cm (h=12.63 cm; U=2.01 cm/s).

Figure 4.14: Velocity profiles of Series C of the oncoming turbidity current (4.14(a) and 4.14(c)) and the turbidity current continuing downstream of the screen (4.14(b) and 4.14(d)).

an inclined multiport diffuser (Series E) located at 5.15 m from the inlet were made with the parameters given in Tables 3.10 and 3.11.

The oncoming turbidity current upstream of the diffuser had the standard form as was found in the experiments without the diffuser. When the turbidity current reached the zone of the jets, colored dye was added to visualize the trajectory and diffusion of the jets. Fig. 4.17 shows a photographic sequence of the transient interaction of the turbidity current front with the vertical jets. It can be seen that the jets at the beginning passed through the turbidity current and entrained some fluid in the ambient layer above the turbidity current, but then they got diverted by the turbidity current and the dye was convected downstream by the turbidity current flow. After a short time a steady state occurred, where the injected dyed water stayed within the turbidity current layer and diluted the flow as was assumed in the developments of Section 2.4 in Chapter 2. The turbidity current then flows

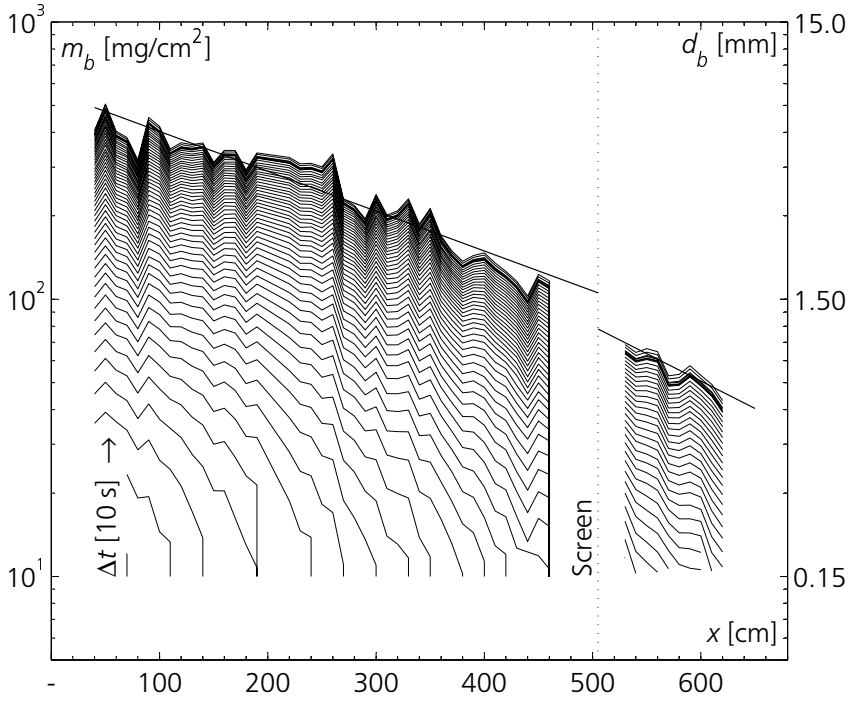

(a) Experiment C04 (S=0.00%).

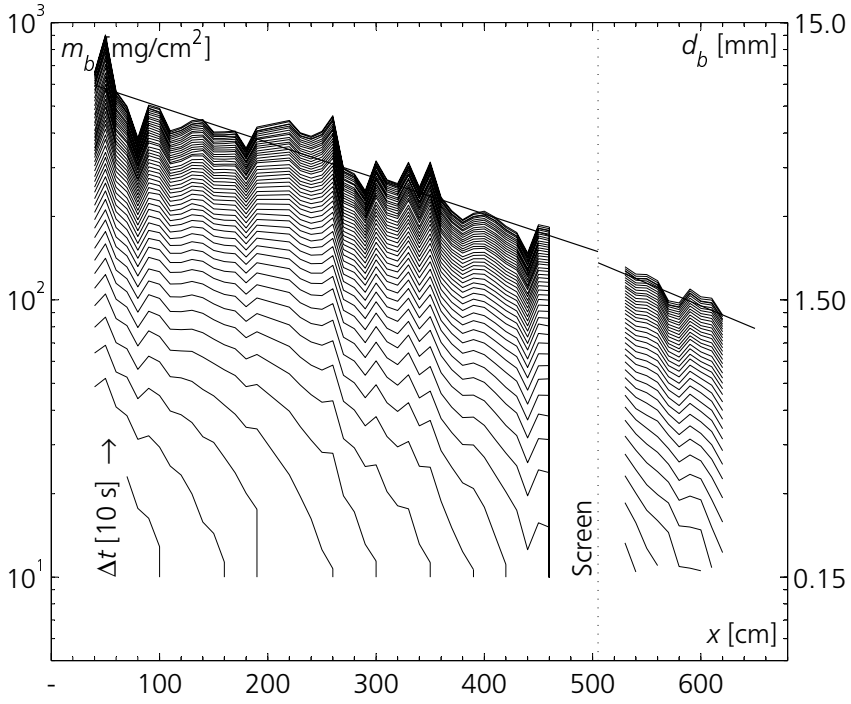

(b) Experiment C03 (S=4.64%).

Figure 4.15: Measured deposition evolution along the flume axis, x, with time intervals of 10 s (Triopor® 118).

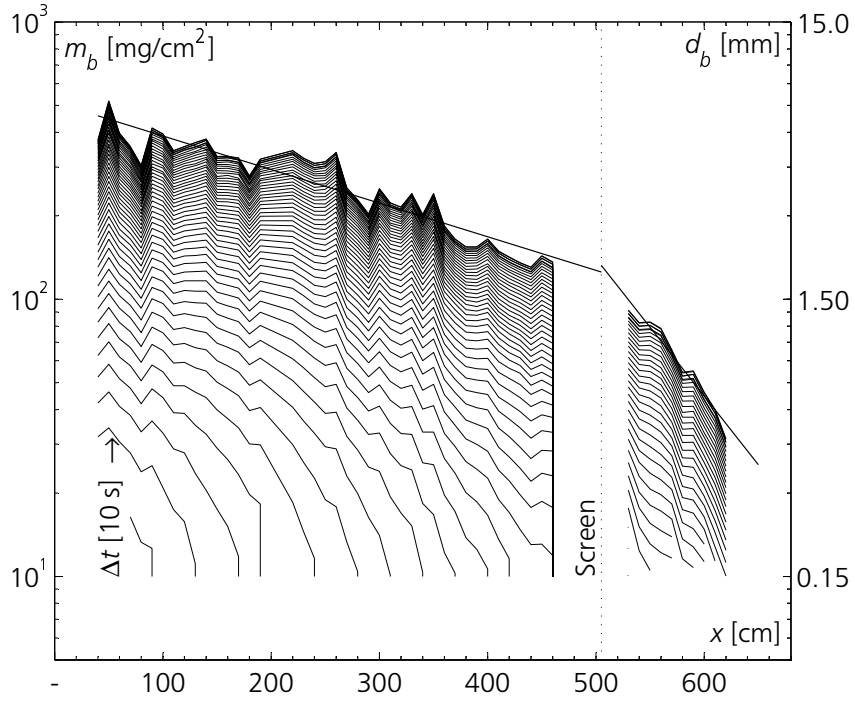

(a) Experiment C05 (S=0.00%).

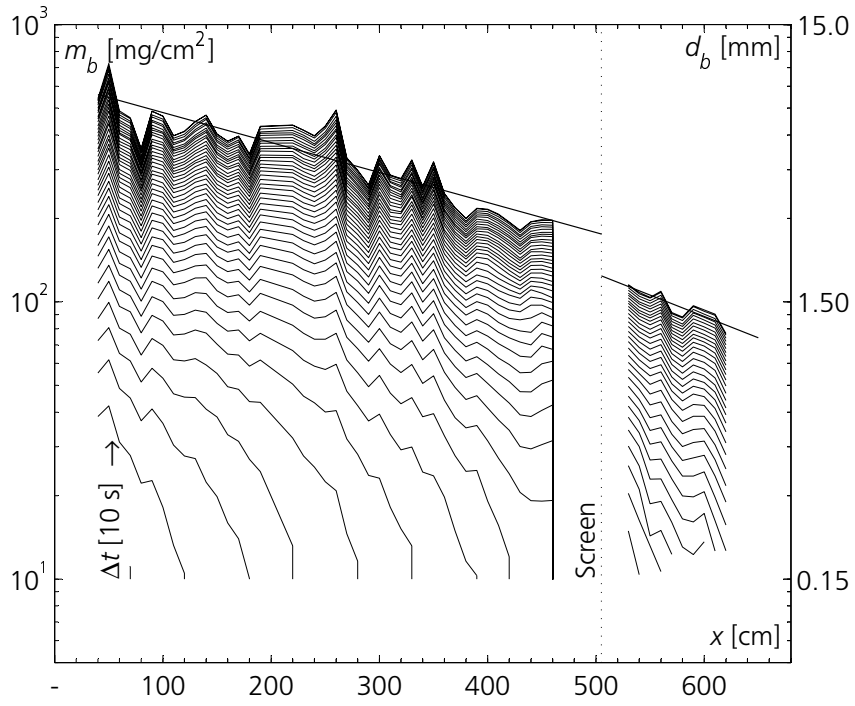

(b) Experiment C02 (S=4.64%).

Figure 4.16: Measured deposition evolution along the flume axis, x, with time intervals of 10 s (Triopor® 120).

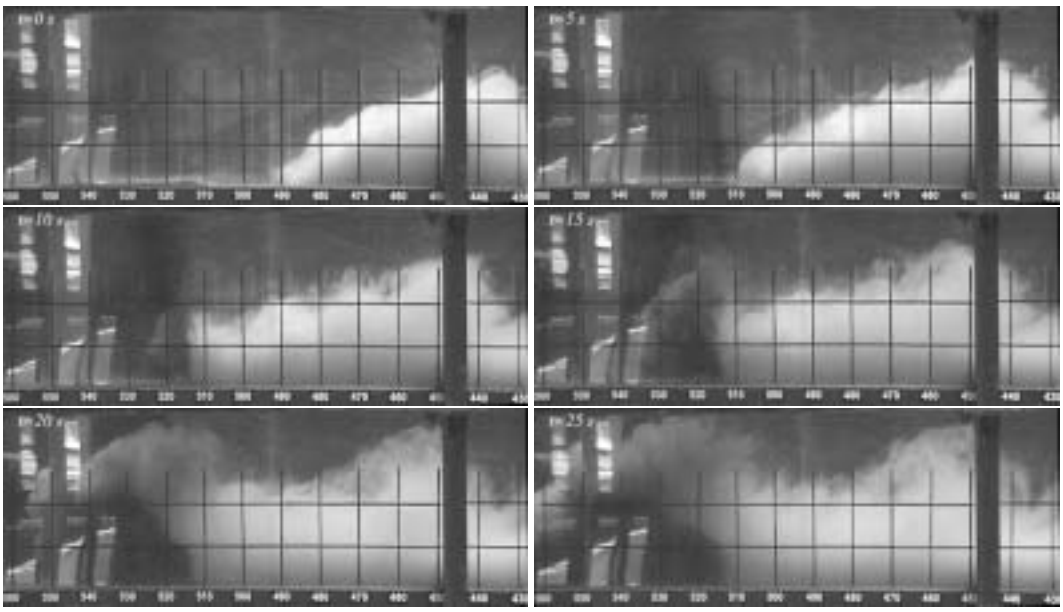

Figure 4.17: Turbidity current flowing through vertical jets at time intervals of 5 s of experiment D02.

downwards as thicker turbidity current due to the dilution. An influence of the jet on the turbidity current upstream of the injection point was observed only for experiment D01, where the jet entrained the turbidity current up to the surface. In the other experiments no effect of the vertical jets on the approaching flow was seen. Fig. 4.18 shows a zoom of the injection of the colored dye into the turbidity current for the experiments D02. It can be seen that the jet is completely convected downstream.

The front velocity of the oncoming and outgoing turbidity current were determined and are plotted in Fig. 4.19. The values of the front velocities are given in Table 4.5. As can be seen, the front velocity decreases slightly downstream of the jet injection point.

The velocity measurements were carried out in the steady state at four locations upstream of the diffuser and one profile was taken 0.95 m downstream of the diffuser. Fig. 4.20 shows the measured velocity profiles upstream (4.20(a) and 4.20(c)) and downstream of the vertical jet diffuser (4.20(b) and 4.14(d)) for an experiment with a horizontal slope (experiment D02) and an inclined slope (experiment D04).

Exp	[–]	D01	D02	D03	D04
$U_{f1\mathrm{mes}}$	[cm/s]	3.32	3.79	3.54	4.69
$U_{f2\mathrm{mes}}$	[cm/s]	n.d.	2.72	2.45	3.44

Table 4.5: Measured front velocities upstream, $U_{f1\mathrm{mes}}$, and downstream, $U_{f2\mathrm{mes}}$, of the vertical jets of Series D (n.d.=no data).

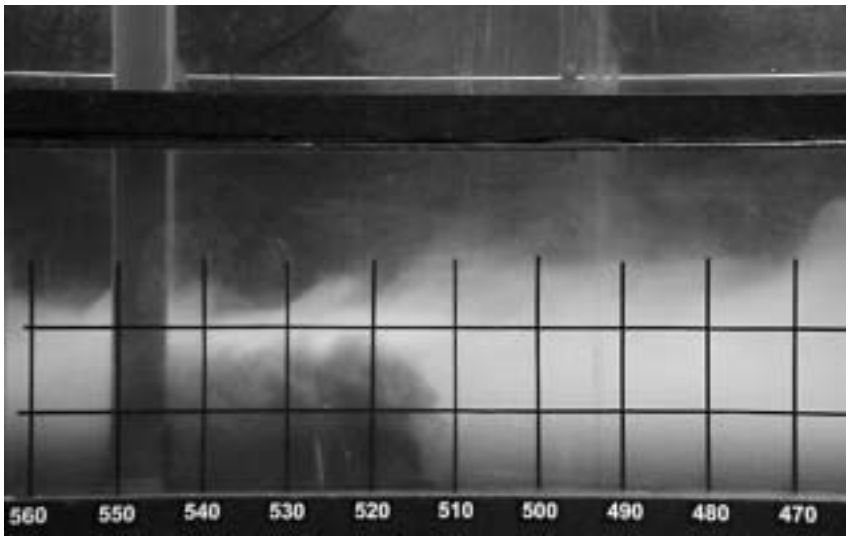

Figure 4.18: Zoom on vertical jet in experiment D02 (q_{j0}=2.10 cm^2/s; m_{j0}=70.4 cm^3/s^2).

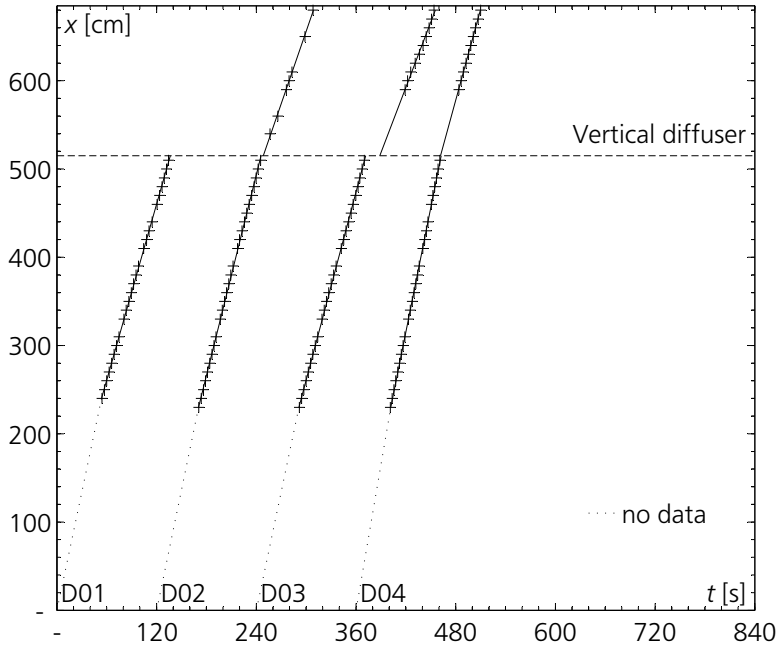

Figure 4.19: Measured front velocities for experiments with a flow through vertical jets (Series D).

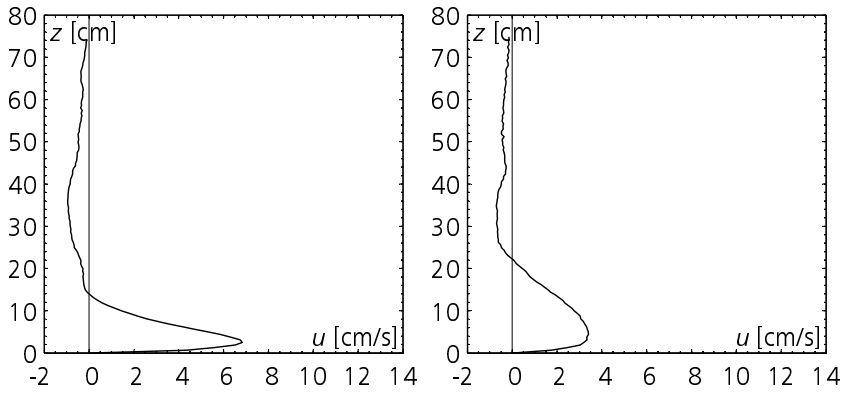

(a) Experiment D02. x=420 cm (h=9.42 cm; U=4.94 cm/s).

(b) Experiment D02. x=610 cm (h=17.33 cm; U=2.66 cm/s).

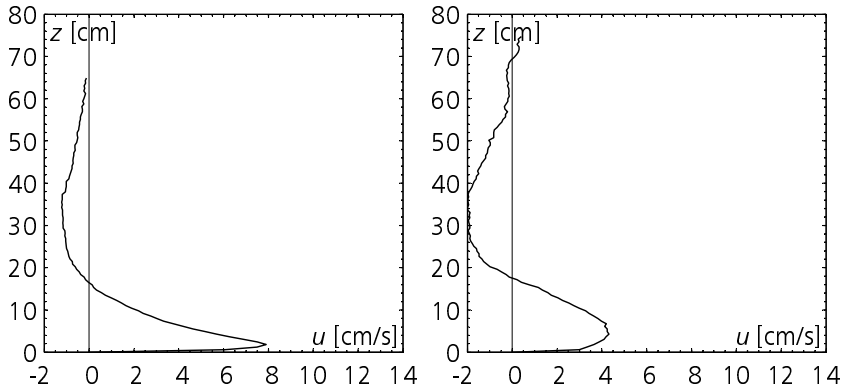

(c) Experiment D04. x=420 cm (h=10.49 cm; U=5.21 cm/s).

(d) Experiment D04. x=610 cm (h=14.51 cm; U=3.44 cm/s).

Figure 4.20: Velocity profiles of D series of the oncoming turbidity current (4.20(a) and 4.20(c)) and the turbidity current continuing after the vertical jet diffuser (4.20(b) and 4.20(d)).

It is interesting to note that the vertical injection of ambient water and momentum had such an influence on the velocity distribution. The velocity decreased in both configurations and the height was almost doubled for experiment D02 with a horizontal bottom slope.

From the velocity profile closest to the jet diffuser (x=420 cm) the average height and velocity of the turbidity current were determined and compared to the characteristics of the vertical jet diffuser. Table 4.6 shows the discharge, q_{j0}, and the momentum in z direction per unit width, m_{j0z}, of the jet in comparison with the height, h, the discharge, $q = Uh$, and the momentum m per unit width of the turbidity current in the profile 95 cm upstream of the diffuser (neglecting the density difference between the two fluids). It can be seen that the discharge ratios of the jet and the turbidity current are between 1/20 and 1/10. If we assume that the buoyancy flux stays constant, this results in a reduction of the concentration in the turbidity current by 5 to

	Jet		Turbidity current				
Exp	q_{j0}	m_{j0z}	h	q	m	q_{j0}/q	l_M
[–]	[cm^2/s]	[cm^3/s^2]	[cm]	[cm^2/s]	[cm^3/s]	[–]	[cm]
D01	3.82	234	9.24	39.73	171	0.10	12.67
D02	2.10	70	9.42	46.53	230	0.05	2.88
D03	2.87	132	12.42	53.41	230	0.05	7.13
D04	3.09	153	10.49	54.65	285	0.06	5.63

Table 4.6: Characteristics of vertical jet and turbidity current flow.

10%. The last column in Table 4.6 indicates the length scale characterizing the interaction of the jet with the crossflow, $l_M = m_{j0z}/U^2$, as proposed by Jirka and Akar (1991). It can be seen that the jet in experiment D02 is the weakest and strongly influenced by the crossflowing turbidity current. In experiment D01 the jet was very strong and passed through the turbidity current up to the surface.

The deposition evolution of experiments D02 with horizontal bottom and D04 with an inclined bottom are shown in Fig. 4.21. For both experiments, a significant difference in the deposition thickness upstream and downstream of the jet diffuser was found. It is assumed that due to the dilution and the injection of vertical momentum the density distribution within the turbidity current is modified so that the concentration close to the bed is reduced. This induces a reduced deposition rate in the region just downstream of the jet.

In the Series E experiments the jets were inclined by 45°in upstream direction. When the turbidity current reached the zone of the jet diffuser, colored dye was again added to the jet to visualize the trajectory and diffusion of the jet. Fig. 4.22 shows a photographic sequence of the transient interaction of the turbidity current front with the inclined jets. It can be seen that the jets at the beginning stop the turbidity current and entrain its fluid in the ambient layer above the turbidity current. But as the heavier fluid is raised it is slowly convected downstream by the ambient velocity in the flume. The heavier fluid with a form of a mushroom finally passes over the zone of influence of the jet and sinks down behind it forming a new turbidity current. Due to the injected momentum opposing the turbidity current a change in the flow rate occurs which induces a bore propagating upstream as shown in Figs. 4.23(a) and 4.23(b). It is interesting to note that some injected dye is also transported upstream within the bore, indicating that due to the density difference between the approaching flow and the reflected bore a return flow above the main body of the turbidity current exists.

The front velocities of the oncoming and outgoing turbidity current, $U_{f1\mathrm{meas}}$ and $U_{f2\mathrm{meas}}$, as well as the velocity of the upstream propagating bore, $U_{fb\mathrm{meas}}$, were determined from the video sequence and are presented in Fig. 4.24. As can be seen in Fig. 4.24, the linear least-square fit shows good

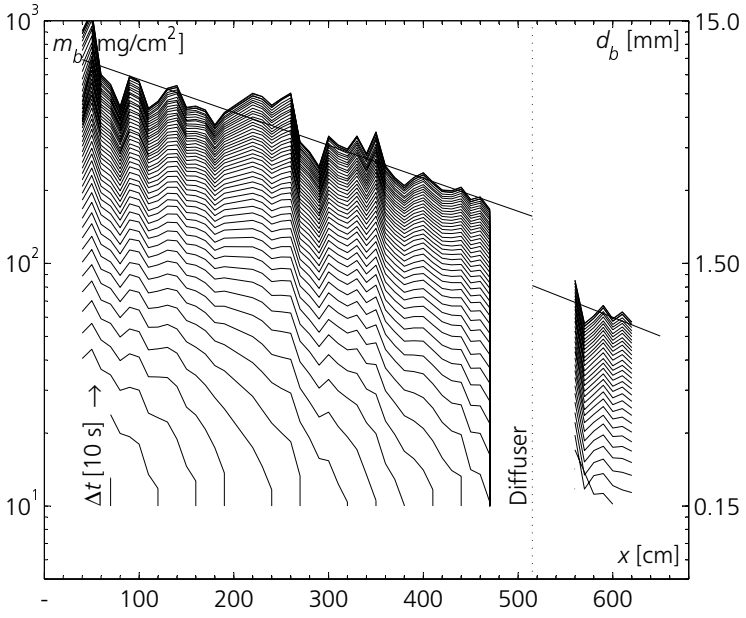

(a) Experiment D02 (S=0.00%).

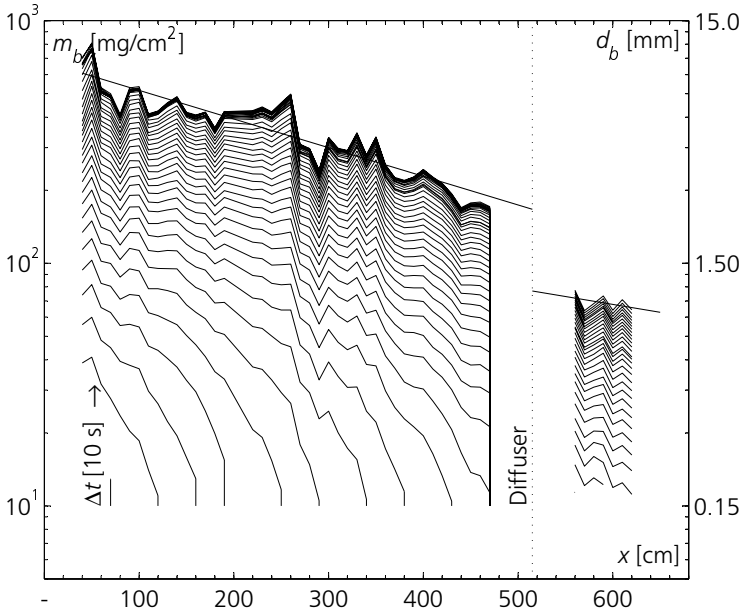

(b) Experiment D04 (S=4.64%).

Figure 4.21: Measured deposition evolution along the flume axis, x, with time intervals of 10 s.

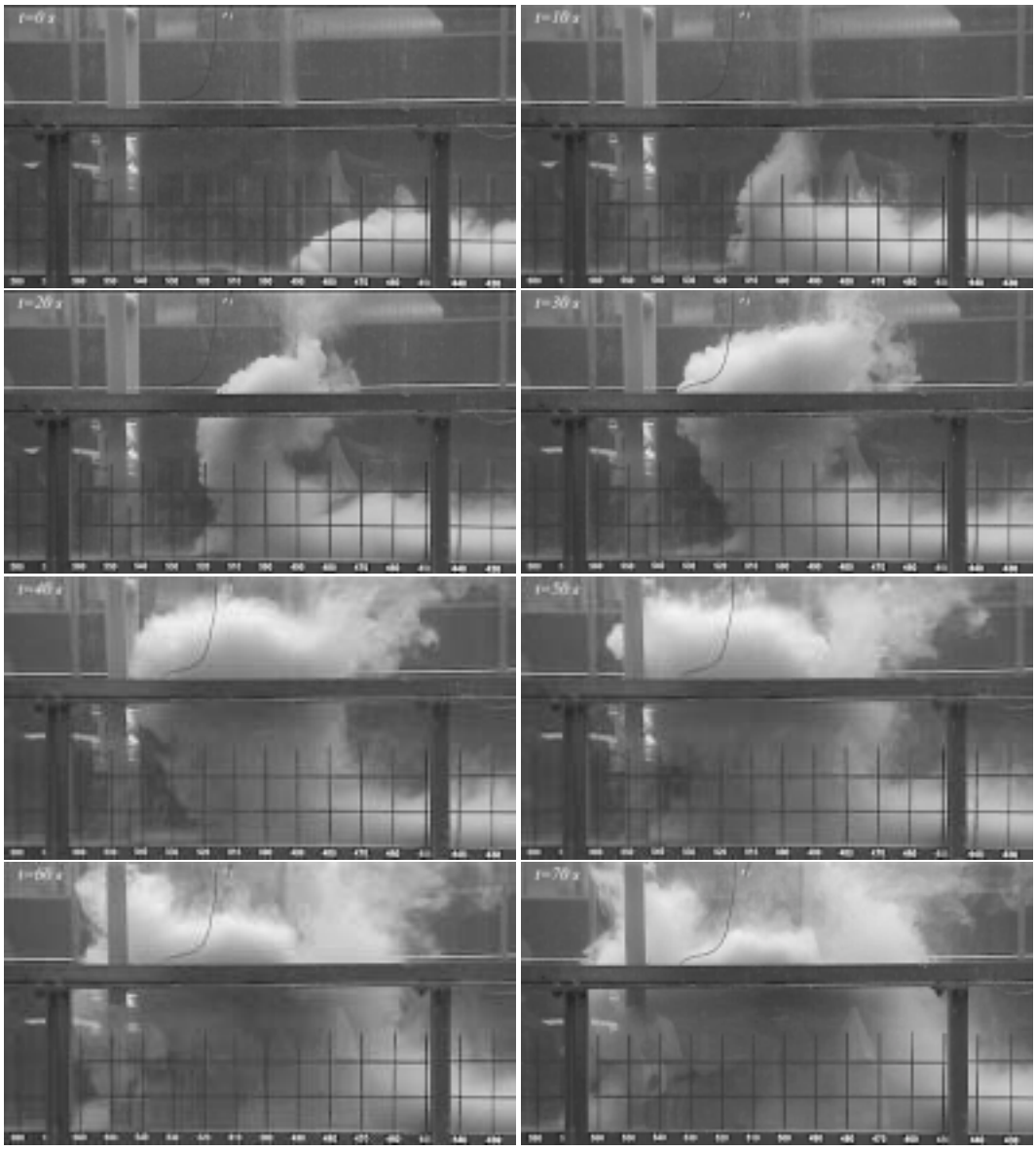

Figure 4.22: Turbidity current flowing through inclined jets at time intervals of 10 s of experiment E04.

(a) Experiment E01 (S=4.64%).

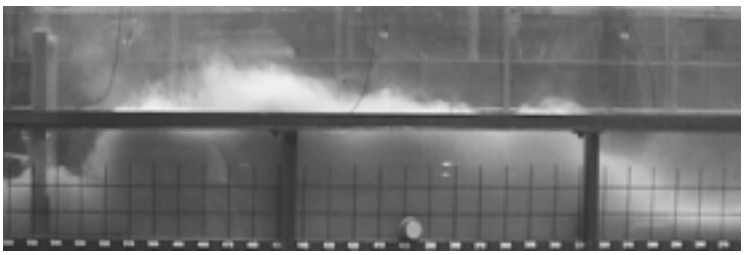

(b) Experiment E04 (S=0.00%).

Figure 4.23: Photographs of bores propagating upstream in Series E experiments.

agreement with the measuring points in the regions upstream and downstream of the diffuser. This indicates that again constant front velocities exist except in a region directly influenced by the inclined jet. It can also be seen in the figure that the turbidity current is slowed down in the zone of influence of the inclined jets, especially in experiment E02 with the strongest jet. The values of the front velocities and the propagation speed of the bore are given in Table 4.7.

The velocity measurements were again made in the steady state at four locations upstream of the diffuser and one profile was taken 0.95 m downstream of the diffuser. Fig. 4.25 shows the measured velocity profiles upstream (4.25(a) and 4.25(c)) as well as downstream of the inclined jet diffuser (4.25(b) and 4.25(d)) for an experiment with a horizontal slope (experiment E03) and an inclined slope (experiment E01).

The injection of ambient water and momentum has a strong influence on the velocity distribution of the turbidity current. The velocity downstream

Exp	[–]	E01	E02	E03	E04
$U_{f1\mathrm{meas}}$	[cm/s]	4.93	4.56	3.64	4.19
$U_{f2\mathrm{meas}}$	[cm/s]	3.41	n.d.	2.20	2.35
$U_{fb\mathrm{meas}}$	[cm/s]	-1.46	n.d.	n.d.	n.d.

Table 4.7: Measured front velocities upstream, $U_{f1\mathrm{meas}}$, and downstream, $U_{f2\mathrm{meas}}$, of the inclined diffuser as well as propagation speed of reflected bore, $U_{fb\mathrm{meas}}$, in Series E (n.d.=no data).

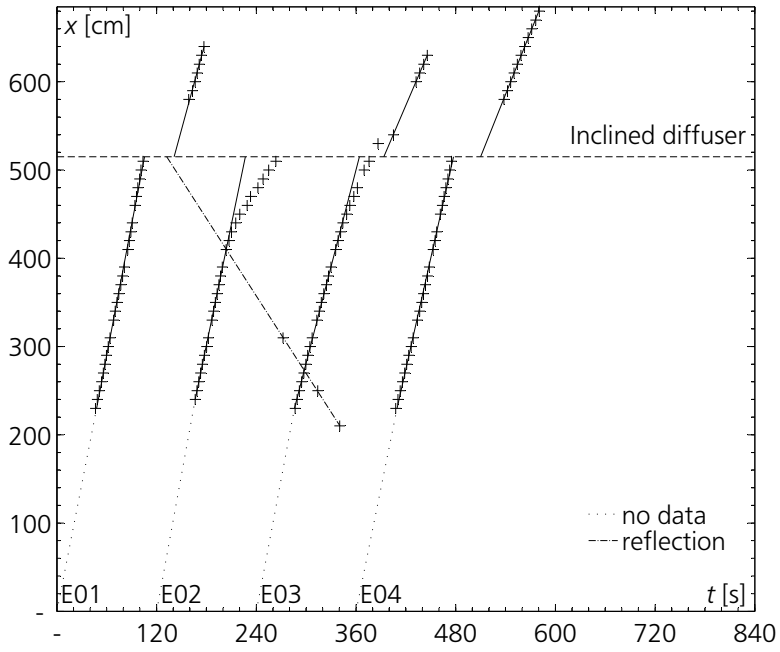

Figure 4.24: Measured front velocities of Series E.

of the diffuser decreased and the height was more than doubled for both experiments, indicating that the turbidity current was considerably slowed down. From the velocity profile closest to the jet diffuser (x=320 cm) the average height and velocity of the turbidity current were determined and compared to the characteristics of the inclined jet as shown in Table 4.8.

It can be seen that the discharge ratios of the jet and the turbidity current were between 1/14 and 1/7. Assuming that the buoyancy flux stays constant, this results in a reduction of the concentration in the turbidity current by 7 to 12%. The last column in Table 4.8 indicates again the length scale characterizing the interaction of the jet with the crossflow. It can be seen that the jet in experiment E01 is the weakest whereas in experiment E02 the jet was very strong and entrained the turbidity current up to the water surface. The ratio of the opposing momentum of the jet to the momentum of the turbidity current is approximately equal to unity for experiments E01 and

	Jet		Turbidity current					
Exp	q_{j0}	$m_{j0x,z}$	h	q	m	q_{j0}/q	m_{j0x}/m	l_M
[–]	[cm^2/s]	[cm^3/s^2]	[cm]	[cm^2/s]	[cm^3/s]	[–]	[–]	[cm]
E01	3.93	290	9.53	50.41	267	0.08	1.09	10.37
E02	5.99	673	9.32	43.34	202	0.14	3.34	31.13
E03	3.86	279	9.17	40.99	183	0.09	1.52	13.98
E04	3.60	243	10.59	48.71	224	0.07	1.09	11.50

Table 4.8: Characteristics of inclined jet and turbidity current flow.

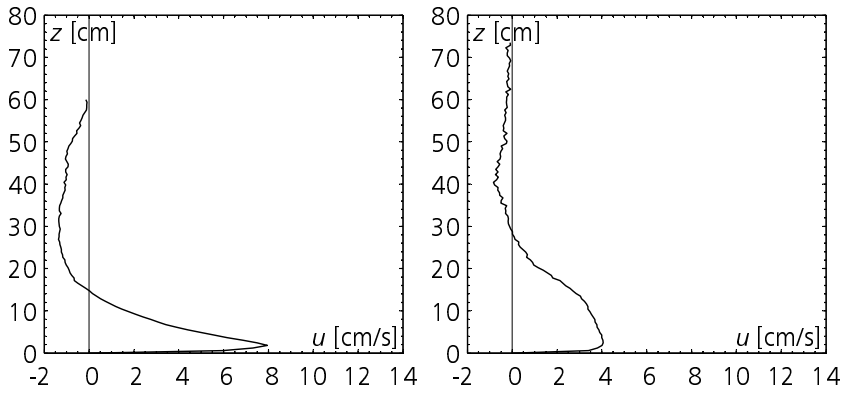

(a) Experiment E01. x=320 cm (h=9.53 cm; U=5.29 cm/s).

(b) Experiment E01. x=610 cm (h=21.00 cm; U=3.19 cm/s).

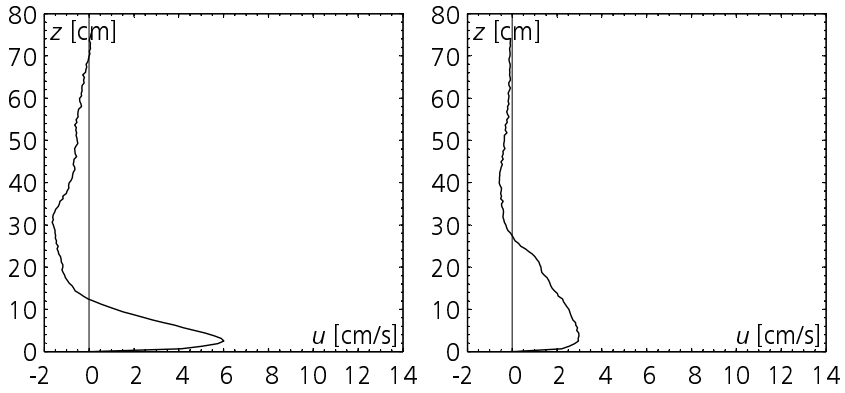

(c) Experiment E03. x=320 cm (h=9.17 cm; U=4.47 cm/s).

(d) Experiment E03. x=610 cm (h=21.18 cm; U=2.28 cm/s).

Figure 4.25: Velocity profiles of Series E of the oncoming turbidity current (4.25(a) and 4.25(c)) and the turbidity current continuing downstream of the inclined jet diffuser (4.25(b) and 4.25(d)).

E04, and equals 1.5 for experiment E03. The jet in experiment E02 was too strong and is not further discussed.

The deposition evolution of experiments E03 with horizontal bottom and E02 with an inclined bottom are shown in Fig. 4.26. For both experiments, a significant difference between the deposition thickness upstream and downstream of the diffuser was found. This might be explained by a combined effect of blocking due to the opposing momentum and the dilution of the turbidity current as observed in Series D. The deposition downstream of the obstacle is reduced significantly and the slope of the exponential decrease of the deposition thickness is slightly higher for experiment E01.

The experimental results for all experiments with a vertical and inclined multiport diffuser are presented in Appendix A.4 on page 235.

4.5 Effect of a Bubble Curtain

The last series of experiments investigated the effect of a bubble curtain on the turbidity current flow. The experimental parameters and the characteristics of the bubble curtain were presented in Subsection 3.4.5. Two turbidity current runs were carried out with the parameters given in Table 3.12.

The steady release of air generated a rising stream of bubbles which entrained the surrounding water and produced a vertical flow of water towards the surface. The flow was deflected sideways at the free surface leading to two recirculation cells as was described by Riess and Fanneløp (1998). These cells extended on the surface to a certain distance where the flow plunged and returned along the bottom back to the bubble curtain source. In experiment F01 the upstream recirculation cell had a size of approximately 3–4 times the water depth. In experiment F02 the buoyancy flux was 15 times smaller and the extent of the upstream recirculation cell was about one water depth. Upstream of this recirculation cell, the oncoming turbidity current again had the standard shape as found in the experiments without a bubble curtain. When the turbidity current reached the upstream recirculation zone, the turbidity current was accelerated due to the recirculating flow. In experiment F01, this flow was so strong, that the turbidity current was torn to pieces.

When the turbidity current reached the bubble curtain, the sediment-laden fluid was convected vertically to the surface as shown in Fig. 4.27. In experiment F01 the buoyancy flux was so strong that the turbidity current was completely lifted up to the surface and no sediments were able to cross the bubble curtain (see Fig. 4.27(a)). When the buoyancy flux was smaller, the turbidity current was divided into a part continuing after the bubble curtain and a part which was lifted to the surface as shown in Fig. 4.27(b). At the surface the sediment-laden fluid was deflected sideways up to the limit of the recirculation cells. There it plunged down and reentered the oncoming turbidity current flowing at the bottom. After a duration of five minutes the

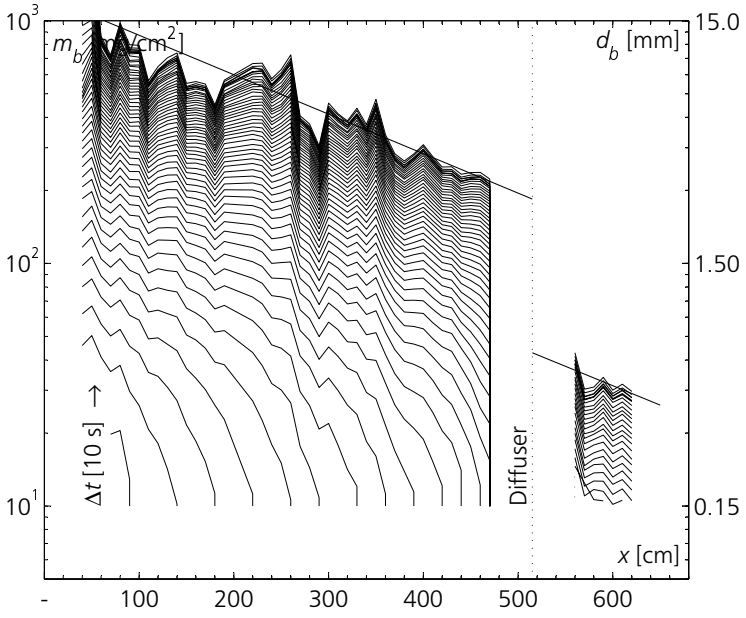

(a) Experiment E03 (S=0.00%).

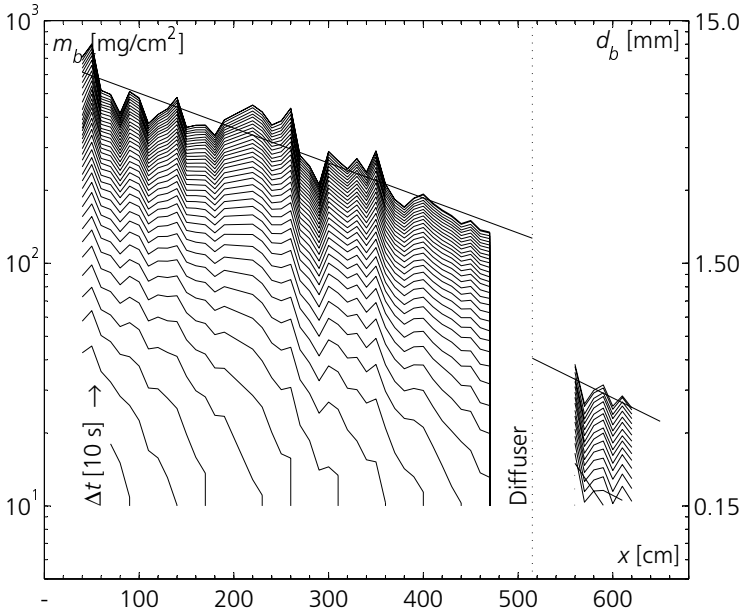

(b) Experiment E01 (S=4.64%).

Figure 4.26: Measured deposition evolution along the flume axis, x, with time intervals of 10 s.

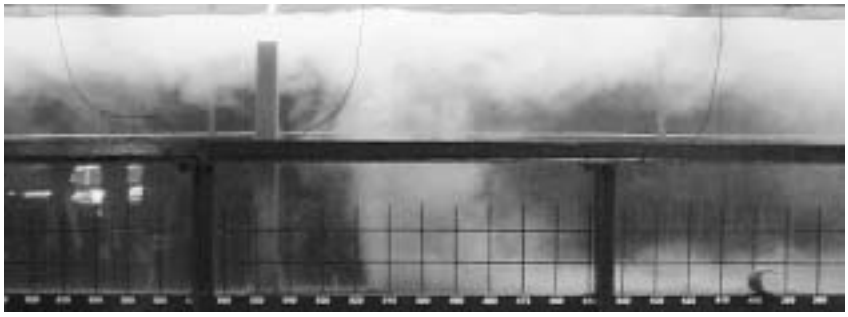

(a) Turbidity current flowing through a bubble curtain in experiment F01.

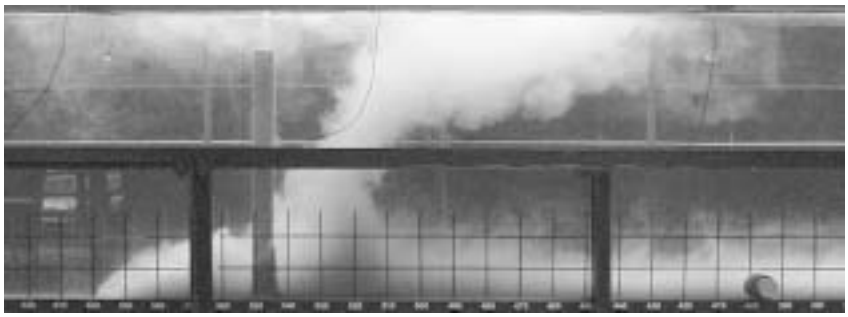

(b) Turbidity current flowing through a bubble curtain in experiment F02.

Figure 4.27: Photographs of Series F experiments.

water in the recirculation area was completely opaque due to the diluted sediments, but up- and downstream of the cells no mixing occurred and the water stayed clear. The recirculation cells were not located symmetrically on the bubble curtain, due to the weak return flow in the upper layer of the flume as can be seen in Fig. 4.27(b).

The front velocities of the oncoming and outgoing turbidity current were determined and are plotted in Fig. 4.28. The values of the front velocities are given in Table 4.9. The least-square fit shows good agreement with the measuring points for experiment F02. Furthermore, it can be seen that for experiment F02 the turbidity current was accelerated in the zone of influence of the recirculation cell. In experiment F01 the recirculation cell extended almost over the whole measuring area and therefore the front velocity was strongly influenced by the recirculating flow.

For experiment F02, velocity measurements were made at three locations upstream of the bubble curtain and at 0.95 m downstream of the bubble curtain. Figs. 4.29(a) and 4.29(b) show the measured velocity profiles upstream and downstream of the bubble curtain.

The injection of vertical positive buoyancy flux entrains some of the sediments, which reduces the buoyancy flux of the turbidity current and reduces its velocity. From the velocity profile closest to the bubble curtain

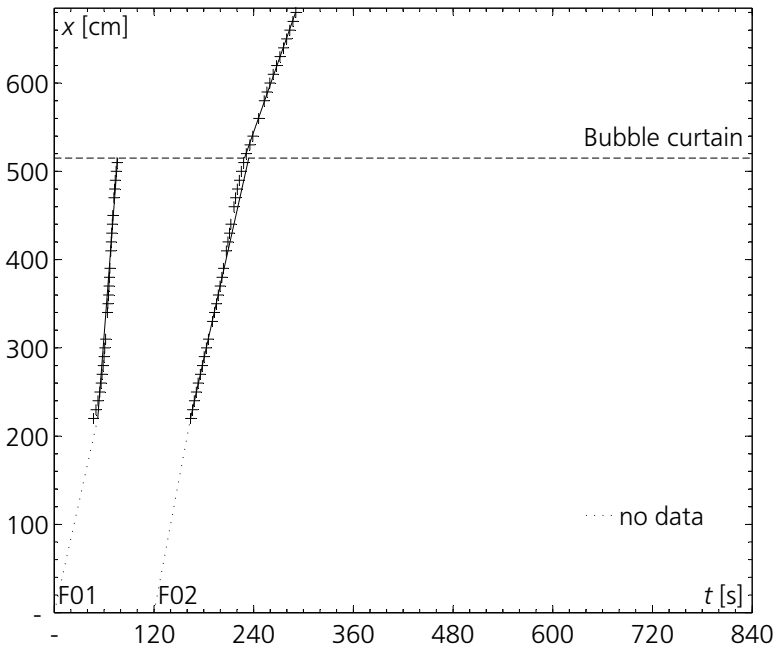

Figure 4.28: Measured front velocities of Series F.

Exp	[–]	F01	F02
$U_{f1\text{meas}}$	[cm/s]	15.26	4.20
$U_{f2\text{meas}}$	[cm/s]	n.d.	2.69

Table 4.9: Measured front velocities upstream, $U_{f1\text{meas}}$, and downstream, $U_{f2\text{meas}}$, of the bubble curtain in Series F (n.d.=no data).

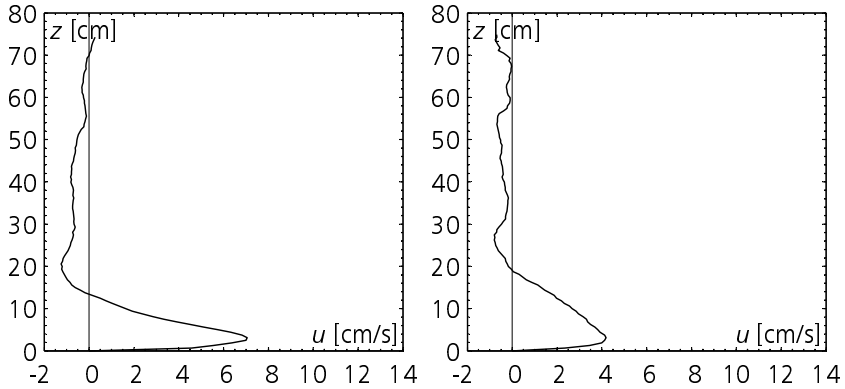

(a) Experiment F02. x=320 cm (h=9.61 cm; U=5.15 cm/s).

(b) Experiment F02. x=610 cm (h=15.01 cm; U=3.10 cm/s).

Figure 4.29: Velocity profiles of Series F of the oncoming turbidity current (4.29(a)) and the turbidity current continuing downstream of the bubble curtain (4.29(b)).

Exp	Bubble curtain		Turbidity current				
	q_b	b_b	q	b	q_b/q	b_b/b	$b_b^{1/3}/U$
[–]	[cm^2/s]	[cm^3/s^3]	[cm^2/s]	[cm^3/s^3]	[–]	[–]	[–]
F01	15.32	15029	n. d.	n.d.			
F02	1.10	1082	41.1	49.1	0.026	22	2.0

Table 4.10: Characteristics of bubble curtain and turbidity current.

(x=320 cm) the average height, velocity and buoyancy flux of the turbidity current were determined and compared to the characteristics of the bubble curtain. Table 4.10 shows the discharge, q_b, and the buoyancy flux, b_b, per unit width of the bubble curtain in comparison with the discharge, q, and the buoyancy flux b of the turbidity current.

It can be seen that for experiment F02 the discharge ratio of the bubble curtain and the turbidity current is approximately 1/40. The buoyancy flux of the bubble curtain was approximately 22 times larger than the buoyancy flux of the turbidity current. The last column in Table 4.10 indicates the ratio of the cubic root of the buoyancy flux of the bubble curtain to the average velocity of the turbidity current similar to the ratio proposed by Nakai and Arita (2002) for the saline wedge intrusions in rivers.

The deposition evolution of experiment F02 with horizontal bottom is shown in Fig. 4.30. No significant difference between the deposition thickness upstream and downstream of the bubble curtain was found. Hence, the bubble curtain lifted only a small amount of sediments up into suspension. In experiment F01 where the discharge and buoyancy flux were almost 14 times larger no sediment deposits occurred during the experiment as the sediments were kept in suspension.

The complete experimental results for experiment F02 with a bubble curtain are presented in Appendix A.5 on page 253.

4.6 Conclusions

The experiments of a continuously fed turbidity current allowed comparison of the measured velocity profiles and front velocities with other reported experiments. The similarity collapse of the velocity profiles at different locations confirmed the self-similarity of the turbidity current runs. The ratio between the maximum and average velocity, U_{max}/U was found to be 1.4, which is similar to the value found by Garcia (1989) and slightly higher than the value of 1.3 given by Altinakar (1988). The ratio of the height of maximum velocity to the average height, h_{max}/h was 0.25, which is lower than the value of 0.3 reported by Altinakar (1988) and higher then the value of 0.15 found by Garcia (1989). This differences might be due to a dependence of the ratios on the bed slope. In fact, the values given by Garcia (1989) were measured

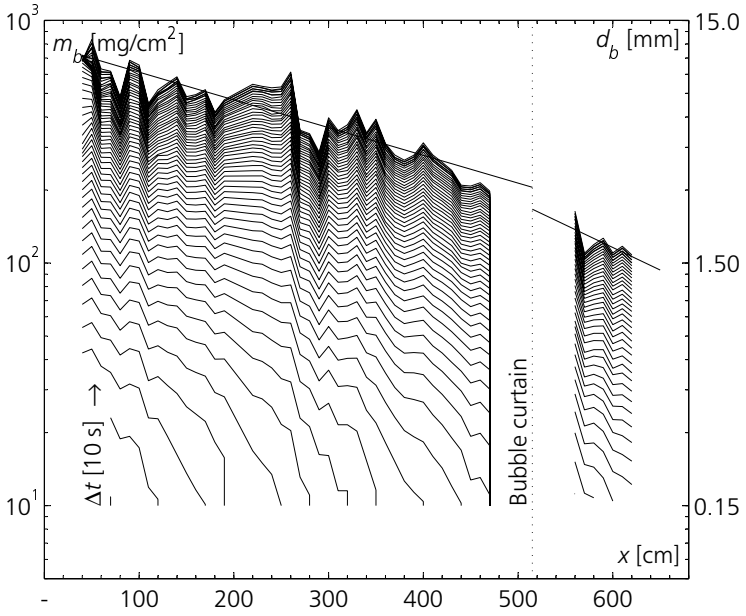

Figure 4.30: Measured deposition evolution along the flume axis, x, with time intervals of 10 s.

for a relatively steep slope of 8%, whereas the values of Altinakar (1988) were found for slopes ranging from 0.0 to 3.6%. Another explanation might also be the different measurement method, by the high-resolution, non-intrusive UVP measurement, which allowed to capture the maximum velocity and its height more accurately.

Constant front velocities were found in all continuously-fed turbidity current experiments. The dimensionless ratio of the front velocity to the cubic root of the initial buoyancy flux, $U_f/B_0^{1/3}$, varied between 0.84 and 1.12 with an average value of 1.02 for the experiments having an inclined bottom (S=4.64%), and between 0.72 and 0.96 with an average value of 0.81 for the experiments with a horizontal bottom. These values confirm the influence of the slope on the front velocity, and are in good agreement with the values found by other investigators.

The deposition measuring device, which was developed, allowed an accurate measurement of the evolution of deposits both in space and time. The precision of the device is estimated to approximately 10 mg/cm^2, which corresponds to a layer thickness equal to the maximum grain size (d_{90} ≅150 μm). An exponential decrease of deposits with distance was observed.

Due to the presence of an obstacle, the flow rate is changed and an internal bore, travelling upstream, occurs. A significant difference in the behavior depending on the approaching flow conditions was observed. For a horizontal bottom, i.e. a subcritical turbidity current, the reflected bores showed a smooth change in depth with a train of internal waves. In the case of the inclined bottom, i.e. a supercritical approach flow, a strong bore was observed

with a front or leading edge moving upstream. Constant front velocities were measured for the oncoming and outgoing turbidity current as well as for the bore.

In the case of the horizontal bottom, the height of the obstacle was approximately twice the average height of the approaching turbidity current. For the inclined bottom the ratio of the obstacle height to the average height of the turbidity current was 2.5. A significant effect of the obstacle on the deposition pattern was observed. In the upstream section, between the bore and the obstacle, the flow velocities were reduced, which increased the deposition rate. In the section downstream of the obstacle, the deposition measurements showed that for the subcritical experiments the exponential decrease of the deposits was considerably higher than in the upstream region indicating that the concentration within the outgoing turbidity current was significantly reduced. For the supercritical experiments with an inclined bottom this decrease could not be observed, which leads to the conclusion that for a supercritical turbidity current a major part of its main body continues over the obstacle.

The experiments with a turbidity current flowing through a screen showed a similar behavior as the flow over an obstacle. Due to the flow resistance of the screen, a part of the flow was retained and a bore was propagating upstream. The other part seeped through the screen and formed a similar but smaller turbidity current downstream. An important difference in the deposition pattern downstream of the two tested geotextiles was measured. For one type of geotextile (Tricopor® 118), no major effect of the screen on the deposits downstream was found. The experiments with the other geotextile (Tricopor® 120), showed an important reduction and significantly higher exponential decrease of the deposits downstream. It is interesting to note that in comparison to the obstacle, a higher exponential decrease was also observed for the supercritical turbidity current. This observation confirms the results of the shallow-water analysis, shown in Fig. 2.11 on page 31, which states that for low porosities the proportion of the flow passing through the screen is almost independent of the approaching flow conditions.

In the experiments of a turbidity current flowing across a vertical diffuser, an effect of the jets on the upstream flow could only be observed for the experiment D02 with a ratio between the height of the current and the crossflow length scale of the jet, h/l_M, being smaller than unity. In the other experiments this ratio varied from 1.7 to 3.3 and no effects upstream were seen in both subcritical and supercritical runs. Nevertheless, the deposition measurements revealed that in all experiments the vertical jets significantly reduced the deposits downstream. This might be explained by the fact that the injected momentum modifies the concentration distribution within the body of the turbidity current. This reduces the near-bed concentration and the deposition rate directly downstream of the diffuser, but has no effect on the sediment flux passing across the diffuser.

The resistance due to the opposing momentum of the jets, inclined by 45°against the turbidity current, induced a change in flow rate. A bore, therefore, propagated upstream similar to the experiments with an obstacle. The front velocities of the oncoming and outgoing turbidity current as well as of a bore were found to be constant except in the proximity of the jets. The discharge ratios between the jet and the turbidity current ranged from 1/14 to 1/7 and the ratios of the momentum in the streamwise direction between the jet and the turbidity current varied from 1 to 1.5.

It was clearly observed on the deposition pattern, that due to the effect of the inclined jets, the deposits increased upstream of the diffuser due to the reduced flow velocities. It may be assumed that due to the injected vertical momentum also an effect on the downstream region, similar to the one described above for the vertical jets, exists. In general, the interaction of the jet with the turbidity current was transient and oscillatory.

The last experiments with a turbidity current flowing through a bubble curtain showed that depending on the intensity of the buoyancy flux of the bubble curtain the turbidity current is completely or partially entrained up to the surface. In experiment F01, the buoyancy flux was much too large and the raising bubble curtain induced a recirculation cell extending almost over the whole measuring area. In this run the turbidity current was completely entrained to the surface, and the turbid water was convected in the recirculation cell. This caused a distribution of the suspended sediments over the whole flume.

In the second experiment the buoyancy flux was 15 times smaller and the turbidity current was only partially entrained by the bubble curtain. A smaller recirculation cell existed which extended laterally over one water depth on both sides. In this experiment, the ratios of discharge and buoyancy flux between bubble curtain and turbidity current were 1/40 and 22, respectively. The ratio of the cubic root of the buoyancy flux of the bubble curtain to the average velocity of the turbidity current, $b_b^{1/3}/U$ was approximately 2. The deposition measurements indicated that no significant effect of the bubble curtain on the deposits occurred.

5 Description of the Numerical Model

5.1 Generalities

Unsteady numerical simulations of turbidity currents were performed mainly by solving one- or two-dimensional depth-averaged formulations of the conservation equations of the turbidity current as presented in Eqs. (2.10), (2.12), and (2.20) in Section 2.1. Bonnecaze et al. (1993) presented a one-dimensional numerical model of a settling turbidity current flow over a horizontal surface from a lock-exchange experiment. They included a two-layer approach in which the conservation equations for the upper layer of the ambient water were also solved. Choi and Garcia (1995) developed a finite element computational algorithm for the solution of one-dimensional, unsteady, single-layer, depth-averaged turbidity currents, which was further expanded to two dimensions (Choi, 1999). Extensive comparison with experimental data available in the literature was done with satisfactory agreement. Bradford and Katopodes (1999b) developed a mathematical model for unsteady, two-dimensional, turbid underflows driven by nonuniform, noncohesive sediment. The numerical solution was obtained by a high-resolution, finite-volume numerical model. The model was also capable of tracking the evolution and development of an erodible bed, due to sediment entrainment and deposition. This was accomplished by solving a bed-sediment conservation equation at each time step, independent of the hydrodynamic equations. A sensitivity analysis was also performed to illustrate deposition and erosion in an existing submarine channel (Bradford and Katopodes, 1999a).

A challenging problem in the depth-averaged formulations is the simulation of the front of the turbidity current. Bonnecaze et al. (1993) used a relationship suggested by Middleton (1966) and given by Eq. (2.1) in Section 2.1, whereas Choi and Garcia (1995) and Bradford and Katopodes (1999b) used some kind of front tracking method to simulate the turbidity current front. Integral models allow a good prediction of average quantities for turbidity current flows in deep water where the influence of the upper layer may be neglected and no stratification in the ambient water is present.

Karpik and Raithby (1990) presented a two-dimensional transient model for the prediction of thermally stratified reservoir flows, where the three-

dimensional laminar equations of motion were laterally averaged to produce a set of two-dimensional equations in a vertical plane that is oriented along the principal axis of the reservoir. They obtained the velocity distribution within this plane, and presented some computed vertical velocity profiles.

As computing resources expand, fully three-dimensional models for turbidity-current hydrodynamics become more feasible. Only recently, some authors have considered the problem by solving the whole set of the three-dimensional Navier-Stokes equations using some kind of turbulence model to close the system. Olsen and Tesaker (1995) compared numerical simulations of a turbidity current flowing down a slope with physical measurements. A modified turbulent viscosity depending on the local Richardson number was combined with the standard k-ε turbulence model and no deposition or erosion was considered. Hermann et al. (1994) investigated powder snow avalanches as turbidity currents both numerically and by physical modelling. They used a two-phase formulation of the Navier-Stokes equations and added a constant settling velocity to the concentration equation. Simulations over a complex three-dimensional topography were compared with physical experiments and showed good agreement. Naaim (1995) also simulated powder avalanches-turbidity currents and further included an erosion-deposition model to account for the interaction of the flow with the sediments at the bottom.

A completely different method of numerical simulations of a density current was described by Monaghan et al. (1999), who used a Lagrangian particle method. They compared experiments and numerical simulations of a gravity current flowing down a ramp in a tank stratified in two layers with good agreement.

Recently, De Cesare et al. (2001) presented three-dimensional numerical simulations of a turbidity current in the Luzzone Reservoir in Switzerland. The model is based on the commercial flow solver CFX-4, where user routines were added to take into account the settling character of the suspended sediments and the erosion-deposition at the bottom. The sediment exchange between flow and bed followed the ideas of Parker et al. (1987). Choi and Garcia (2002) simulated numerically saline density currents developing two dimensionally on a slope with the k-ε turbulence model. The computed profiles of velocity and concentration were compared with measured data. Furthermore, the impact of a parameter representing the stratification level in the k-ε model was investigated and appropriate values of this parameter were given. Bombardelli and Garcia (2001) performed three-dimensional computations of density currents within the Chicago River using the commercial solver FLOW-3D.

In the following sections the numerical model based on the commercial flow solver CFX-4.4 from AEA Technologies is described (AEA Technology, 2001). This solver was used because it allows implementation of user Fortran routines to adapt the standard solver to specific problems.

5.2 Model Equations

For calculating the flow field, the assumption is made that the flow development is only influenced by the presence of sediments through the change of density as a function of sediment concentration. This assumption is justified since the concentration of suspended sediment is small and the bed-load layer is thin. However the sediments may have an indirect effect on the flow in that they present a roughness which changes the boundary conditions at the bed. This will be accounted for through the bed boundary conditions. It is further assumed that the flow is isothermal and incompressible with variable density. The sediment concentration is small, so that the fluid is Newtonian and Stokes' law of friction may be used. With the above assumptions, the flow field is determined by the following Reynolds-averaged continuity and Navier-Stokes equations written in Cartesian form,

$$\frac{\partial \rho}{\partial t} + \frac{\partial \left(\rho U_i\right)}{\partial x_i} = 0 \tag{5.1}$$

$$\frac{\partial \left(\rho U_i\right)}{\partial t} + \frac{\partial \left(\rho U_i U_j\right)}{\partial x_j} = -\frac{\partial p'}{\partial x_i} + \frac{\partial \tau_{ij}}{\partial x_j} + B_i \tag{5.2}$$

where ρ is the fluid density, $U_i \equiv (u, v, w)$ are the velocity components along the Cartesian coordinates $x_i \equiv (x, y, z)$, t is time, B_i is a body force (e.g., Coriolis or buoyancy force), and p' is a modified pressure, where the hydrostatic pressure is removed, defined by

$$p' = p - \rho_w g z + \frac{2}{3}\rho k \tag{5.3}$$

where p is the total pressure, ρ_w a reference density such as the density of the ambient water, z is the vertical coordinate, and k is the turbulent kinetic energy. The turbulent stresses τ_{ij} are calculated with the k-ε turbulence model (Rodi, 1980), which employs the eddy-viscosity hypothesis

$$\tau_{ij} = \mu_{\text{eff}} \left(\frac{\partial U_i}{\partial x_j} + \frac{\partial U_j}{\partial x_i} \right) \tag{5.4}$$

where μ_{eff} is the effective viscosity which, with the adoption of an eddy-viscosity model, is the sum of the molecular viscosity, μ, and the turbulent viscosity, μ_T defined in the standard k-ε turbulence model as

$$\mu_T = C_\mu \rho \frac{k^2}{\varepsilon} \tag{5.5}$$

where k is turbulent kinetic energy, ε its dissipation rate, and C_μ is a constant given in Table 5.1. Analogous to the eddy-viscosity hypothesis, there is the

C_μ	$C_{1\varepsilon}$	$C_{2\varepsilon}$	σ_k	σ_ε	$C_{3\varepsilon}$
0.09	1.44	1.92	1.0	1.3	1.0 (G>0); 0–0.2 (G<0)

Table 5.1: Values of constants in the k-ε model (Rodi, 1985).

eddy-diffusivity hypothesis, where Γ_T is the eddy diffusivity, usually defined by

$$\Gamma_T = \frac{\mu_T}{\sigma_\Phi} \tag{5.6}$$

where σ_Φ is the turbulent Prandtl number of the scalar Φ. Eddy diffusivities are then defined by specifying the turbulent Prandtl number.

The transport equations for the turbulent kinetic energy k and the turbulence dissipation rate ε are given by Rodi (1985) as follows

$$\frac{\partial(\rho k)}{\partial t} + \frac{\partial(\rho U_i k)}{\partial x_i} - \frac{\partial}{\partial x_i}\left[\left(\mu + \frac{\mu_T}{\sigma_k}\right)\frac{\partial k}{\partial x_i}\right] = P + G - \rho\varepsilon \tag{5.7}$$

$$\begin{aligned}\frac{\partial(\rho\varepsilon)}{\partial t} + \frac{\partial(\rho U_i \varepsilon)}{\partial x_i} - \frac{\partial}{\partial x_i}\left[\left(\mu + \frac{\mu_T}{\sigma_\varepsilon}\right)\frac{\partial \varepsilon}{\partial x_i}\right] = \\ C_{1\varepsilon}\frac{\varepsilon}{k}(P + C_{3\varepsilon}G) - C_{2\varepsilon}\rho\frac{\varepsilon^2}{k}\end{aligned} \tag{5.8}$$

where σ_k and σ_ε denote the turbulent Prandtl numbers related to the diffusive transport of k and its dissipation rate ε, respectively. P is the shear production defined by

$$P = \mu_{\text{eff}}\frac{\partial U_i}{\partial x_j}\left(\frac{\partial U_i}{\partial x_j} + \frac{\partial U_j}{\partial x_i}\right) \tag{5.9}$$

and G is the production due to the buoyancy defined by

$$G = -g_i\frac{\mu_{\text{eff}}}{\rho_w\,\sigma_c}\frac{\partial \rho}{\partial x_i} \tag{5.10}$$

where $g_i = (0, 0, g)$ is the gravity vector with $g = -9.81$ m/s^2 the acceleration due to gravity, and σ_c the turbulent Prandtl number for the suspended sediment concentration.

Values of the constants in Eqs. (5.7) and (5.8) are given in Table 5.1. Controversy in the choice of constant $C_{3\varepsilon}$ exists and as indicated in Table 5.1, different values need to be taken for flows with negative buoyancy production (e.g., stable stratification, G<0) and cases with positive buoyancy production (unstable stratification, G>0).

The body force in the momentum equation, Eq. (5.2), is given by

$$B_i = B_{i\,\text{buoy}} + B_{i\,\text{rot}} \tag{5.11}$$

where $B_{i\,\text{buoy}}$ is the buoyancy force term and $B_{i\,\text{rot}}$ the rotational force term (i.e., Coriolis force). The hydrostatic pressure is removed in the buoyancy force

term, which then becomes

$$B_{i\,\text{buoy}} = (0, 0, (\rho - \rho_w)g) \tag{5.12}$$

and the Coriolis force term is defined by

$$B_{i\,\text{rot}} = (\rho\, 2\Omega \sin\xi\, v, -\rho\, 2\Omega \sin\xi\, u, 0) \tag{5.13}$$

where Ω =0.0000075 rad/s is the angular velocity of the earth rotation, and $\xi = 46.5°$is the latitude of the region considered.

The general convection-diffusion equation for additional scalars Φ is given by

$$\frac{\partial(\rho\Phi)}{\partial t} + \frac{\partial(\rho U_i \Phi)}{\partial x_i} - \frac{\partial}{\partial x_i}\left(\Gamma_{\text{eff}} \frac{\partial \Phi}{\partial x_i}\right) = S_\Phi \tag{5.14}$$

where Γ_{eff} is the diffusion coefficient, and S_Φ is a source or sink term representing creation or destruction of Φ.

5.2.1 Buoyancy-Extensions to k-ε Model Equations

Turbidity currents are strongly stratified flows with high density gradients. The flow may be characterized by an active bottom layer in which turbulence is produced or maintained by ground shear, a sharp density interface, and a relatively uniform non-active layer representing the still water body. The stratification is mostly stable as density decreases in the vertical direction. This fact influences the structure of turbulence, since vertical motions and mixing are directly affected by buoyancy forces. Therefore, the accuracy of computational predictions in strongly stratified flows is expected to depend mainly on the treatment of turbulence in the vicinity of the interface and on the modelling of diffusive transport. To properly account for these additional effects of stratification, the buoyancy extensions of the standard k-ε model as proposed by Burchard and Petersen (1999) was included.

The buoyancy extension proposed by Burchard and Petersen (1999) introduces two stability functions, f_1 and f_2, acting on the eddy viscosity, μ_T and diffusivity, Γ_T defined by

$$\mu_T = f_1 \left(c_\mu^0\right)^3 \rho \frac{k^2}{\varepsilon}; \quad \Gamma_T = f_2 \left(c_\mu^0\right)^3 \rho \frac{k^2}{\varepsilon}. \tag{5.15}$$

The values of the parameters in the transport equations of k and ε, Eqs. (5.7) and (5.8), are given in Table 5.2. The values stay the same except c_μ^0, σ_ε, and $C_{3\varepsilon}$, which becomes negative in stable flows.

The role of the stability functions f_1 and f_2 is to correct the eddy viscosity and diffusivity for further effects of stratification (stratification effects are already included in the buoyancy production term G on the right-hand sides of the k and ε equations). Stability functions generally damp turbulent

c_μ^0	$C_{1\varepsilon}$	$C_{2\varepsilon}$	σ_k	σ_ε	$C_{3\varepsilon}$
0.5562	1.44	1.92	1.0	1.08	1.0 (G>0); -0.4 (G<0)

Table 5.2: Values of constants in the buoyancy-extension to the k-ε model as proposed by Burchard and Petersen (1999).

exchange for stable stratification and enhance turbulent mixing for unstable stratification. The stability functions depend only on two non-dimensional parameters for stratification and shear, represented by α_N

$$\alpha_N = \frac{g_i}{\rho_w} \left(c_\mu^0\right)^6 \frac{k^2}{\varepsilon^2} \frac{\partial \rho}{\partial x_i} \tag{5.16}$$

where c_μ^0 is given in Table 5.2.

For strong convection, Galperin et al. (1988) recommended a lower limit for $\alpha_N > -0.0466$. In practice, much smaller values of α_N may occur. In order to guarantee a smooth transition into this convective regime, Burchard and Petersen (1999) proposed a modified $\tilde{\alpha}_N$ as following

$$\tilde{\alpha}_N = \max\left(\alpha_N, \alpha_N - \left(\alpha_N - \alpha_c\right)^2 / \left(\alpha_N + \alpha_{\min} - 2\alpha_c\right)\right) \tag{5.17}$$

where α_c equals to -0.04, and $\alpha_{\min}$ is -0.0466. An upper limit for $\tilde{\alpha}_N$ is given by $\tilde{\alpha}_N < 0.56$. The following stability functions f_1 and f_2 are suggested

$$f_1 = \frac{c_\mu^0 + 2.182\,\tilde{\alpha}_N}{1 + 20.40\,\tilde{\alpha}_N + 53.12\,\tilde{\alpha}_N^2} \quad \text{and} \quad f_2 = \frac{0.6985}{1 + 17.34\,\tilde{\alpha}_N} \tag{5.18}$$

The standard k-ε equations may be obtained by using f_1 and f_2 with $\alpha_N = 0$, and thus neglecting the influence of stratification in the stability functions (Burchard et al., 1998). The stability functions f_1 and f_2 are shown in Fig. 5.1 for different values of α_N.

5.3 Suspended Sediment Transport Models

There are two main transport processes for suspended sediment transport: convection and diffusion. The vertical transport due to the settling velocity of the sediments is also a type of convective transport. The other process is turbulent diffusion of sediments. This is due to turbulent mixing in regions of concentration gradients. The turbulent mixing process is usually modelled with an effective diffusivity coefficient, Γ_{eff}.

To calculate the transport of the suspended sediment particles, one needs to take into account their settling. In the present model, the particle diameters are assumed to be sufficiently small, so that the flow is drag dominated and the terminal particle velocities are reached after short spatial length scales.

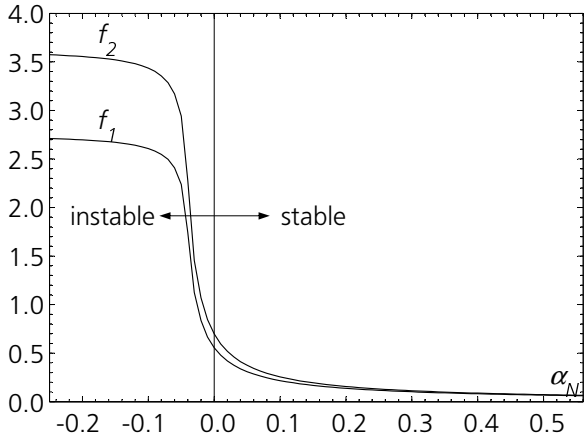

Figure 5.1: Stability functions f_1 and f_2 according to Burchard and Petersen (1999).

Therefore, the slip velocity between particles and fluid, approximated with Stokes' settling velocity, v_{ss}, is introduced in the convection term of the Reynolds-averaged scalar transport equation, Eq. (5.14), replacing the scalar Φ by the suspended sediment concentration, c_s, which leads to

$$\frac{\partial\left(\rho c_s\right)}{\partial t}+\frac{\partial\left(\rho\left[U_i+\delta_{i3}v_{ss}\right]c_s\right)}{\partial x_i}-\frac{\partial}{\partial x_i}\left(\Gamma_{\text{eff}}\frac{\partial c_s}{\partial x_i}\right)=S_c \tag{5.19}$$

where c_s is the local volumetric sediment concentration, δ_{i3} the Kronecker delta with $i=3$ indicating the vertical direction, and S_c represents the source or sink terms at the bed due to erosion or deposition of sediments. The eddy diffusivity Γ_T is calculated by means of Eq. (5.6).

For turbidity currents with a non-uniform grain size distribution of the suspended load several transport equations (one for each size fraction) can be solved simultaneously to obtain the fractional transport. In the present model three transport equations were solved for grain diameters d_{16}, d_{50} and d_{84}. To model saline gravity currents, v_{ss} and S_c can be set equal to zero.

In open-channel flow calculations with suspended sediment transport, the density variation due to the sediment concentration can generally be ignored. Instead, turbidity currents are driven by the difference in density. Therefore, it is crucial to calculate the density, ρ, at every iteration as follows

$$\rho=\rho_w+\sum_{i=1}^{N}c_{si}\left(\rho_s-\rho_w\right) \tag{5.20}$$

where ρ_w is the reference density which equals the density of the ambient water, c_{si} is the concentration of size fraction i and ρ_s is the sediment density.

The boundary condition for the sediment concentration at the bed is a challenging problem, because the sediments should be able to both settle

and erode, depending on the shear stress at the bed, the sediment particle size distribution, the in and outflow of sediments from a section and the availability of sediments for erosion. The boundary condition is implemented by introducing a source or sink term in the cell closest to the bed with $S_c = S_E - S_D|_{z_1}$ being the net flux of erosion and deposition. To model the erosion term S_E and the deposition term S_D at the bed two principal approaches can be found in the literature

- Assume an equilibrium concentration in the cell closest to the bed.
- Use relationships for the pick-up rate and the settling rate of sediments.

The next paragraphs describe these two concepts, which were both implemented.

Equilibrium Concentration Approach. The theory of equilibrium concentration at the bed was first described by Einstein (1968), in his formula for suspended sediment transport. The method has since then been expanded and a widely used contribution is from Van Rijn (1984b). The deposition rate, S_D at the interface is defined essentially as in Eq. (2.19). Models for the entrainment or erosion rate, S_E were proposed by Van Rijn (1984b) as well as Celik and Rodi (1988), who assumed that the entrainment rate is equal to the one under equilibrium conditions (i.e., $S_E = S_D$), so that

$$S_E = |v_{ss}| c_{sb\star} \tag{5.21}$$

where $c_{sb\star}$ is the equilibrium concentration close to the bed at distance $z = a$. The sediment flux at the lower boundary of the suspended load is then

$$S_c = S_E - S_D = |v_{ss}| \left(c_{sb\star} - c_{sb}\right). \tag{5.22}$$

where c_{sb} is the effective concentration close to the bed. Hence, erosion occurs when the concentration close to the bed is lower than the equilibrium concentration and if the effective concentration is higher than the equilibrium concentration sediments are deposited.

An empirical relation of Van Rijn (1984b) was used for determining the equilibrium concentration $c_{sb\star}$ at a given reference level a as follows

$$c_{sb\star} = 0.015 \frac{d_{50}\, T_\star^{1.5}}{a\, D_\star^{0.3}} \tag{5.23}$$

where $T_\star = \frac{u_\star - u_{\star \mathrm{cr}}}{u_\star}$ is the non-dimensional excess bed-shear stress with $u_\star$, the bed-shear velocity computed from the wall boundary condition described in Subsection 5.4.3, $u_{\star \mathrm{cr}}$ is the critical shear velocity at incipient motion given by Shield's diagram and $D_\star$ is the particle size parameter given by

$$D_\star = d_{50} \left[\frac{(\rho_s - \rho_w)\, g}{\rho_w\, \nu^2}\right]^{1/3} \tag{5.24}$$

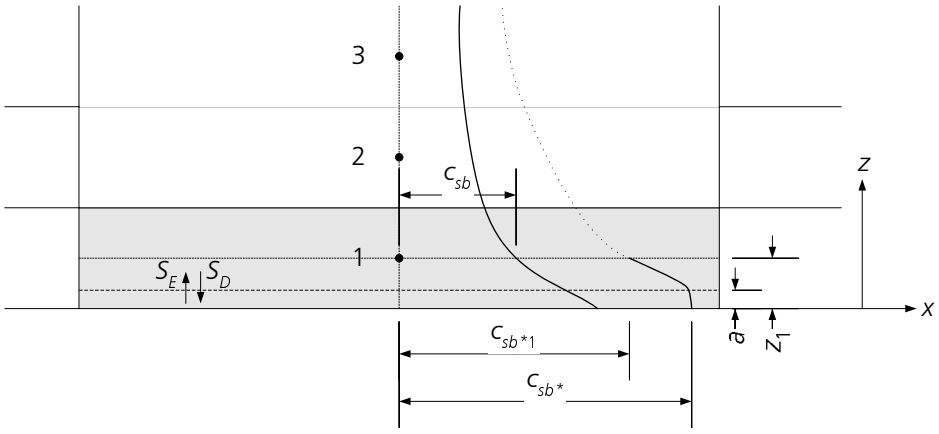

Figure 5.2: Near-bed control volume with sediment deposition, S_D, and erosion, S_E, as well as near-bed concentration, c_{sb} and equilibrium concentration, $c_{sb\star}$.

The net flux, S_c is introduced at the center of the cell closest to the bed in the finite-volume approach. For the calculation of the local volumetric sediment concentration close to the bed, c_{sb}, the concentration in the near-bed cell was used, as shown in Fig. 5.2.

To obtain the equilibrium concentration $c_{sb\star}$, it is assumed that no bed forms exist. The reference level is chosen to be at $a = 3\,d_{90}$ which is commonly used for flat beds. For determining the equilibrium concentration at z_1, it is assumed, following the ideas of Wu et al. (2000), that the concentration distribution between a and the first grid point z_1 (point 1 in Figure 5.2) is the same as under equilibrium conditions which gives

$$c_{sb\star 1} = c_{sb\star}\, e^{[(v_{ss}/\Gamma_{\text{eff}})(z_1 - a)]} \tag{5.25}$$

For small exponents of e and hence small distances $z_1 - a$ this relation is close to a linear distribution.

Pick-up and Settling Rate Approach. To describe the sediment exchanges between the flow and the bed using a pick-up and settling rates, the ideas of Parker et al. (1987) and Garcia and Parker (1993) as described in detail in Section 2.1 were implemented. The sediment flux at another reference level, b, close to the wall is then given by Eqs. (2.18) and (2.19) as found in the conservation equation for the suspended sediments, Eq. (2.20). In terms of net flux evaluated at the reference level, b, it follows that

$$S_c = S_E - S_D = |v_{ss}|\,(E_s - c_{sb}) \tag{5.26}$$

where E_s is the sediment entrainment coefficient given by Eqs. (2.23) and (2.24), and c_{sb} is the sediment concentration at level b. The settling velocity, v_{ss} is calculated with Stokes'law as given in Eq. (2.28) of Section 2.1

and the bed-shear velocity, $u_\star$ is computed from the wall boundary condition described in Subsection 5.4.3.

The erosion, S_E and deposition, S_D terms need to be calculated at the center of the cell closest to the bed at distance z_1. Parker et al. (1986) and Garcia and Parker (1993) calculated this net flux at a reference level of $b = 0.05\,h$, where h is the integral turbidity current height as found in Eq. (2.20). As the height is difficult to determine within the head of the turbidity current or in a complex three-dimensional flow, the reference level was fixed to a value approximately equal to 5% of the mean turbidity current height. Furthermore, care was taken that the cell height closest to the bed was constant within the computational domain and equal to approximately twice the reference level.

To determine the local volumetric sediment concentration, c_{sb}, at the reference level, a similar procedure as described in the first approach is used. From the concentration in the near-bed cell, c_{s1}, the local volumetric sediment concentration, c_{sb} then becomes

$$c_{sb} = c_{s1}\, e^{[(v_{ss}/\Gamma_{\text{eff}})(b-z_1)]} \tag{5.27}$$

For small exponents of e and hence small distances $b - z_1$ this relation is again close to linear.

5.4 Boundary Conditions

Boundary conditions must be set for each variable at every boundary on the domain. The following boundary conditions are used.

5.4.1 Inlet

At the inlet boundary, constant values for all variables except pressure are specified (Dirichlet boundary condition). Pressure is extrapolated from the outlet boundary. Inlet values for k and ε must also be specified. The inlet values of k and ε are assigned average values calculated from a mixing-length model by specifying a turbulence intensity i_T and a dissipation length scale D (AEA Technology, 2001). The value for k and ε are then calculated as follows

$$k_{\text{in}} = 1.5\,(i_T\, U_{\text{in}})^2 \tag{5.28}$$

and

$$\varepsilon_{\text{in}} = \frac{{k_{\text{in}}}^{3/2}}{0.3\,D} \tag{5.29}$$

where U_{in} is the normal inlet velocity. The turbulence intensity i_T was given a standard value of 0.037 and the dissipation length was chosen equal to the opening height of the gate, D =0.045 m.

5.4.2 Free Surface

For the free surface the rigid-lid assumption is made, so that the surface remains at the initial specified height and the free surface is modelled as a plane of symmetry. A free-slip condition for the velocity components tangential to the surface is made and the velocity component normal to the boundary is set to zero. For all variables, including pressure, zero normal gradient boundary conditions are specified (Neumann boundary condition) except for the turbulent kinetic energy, k, which is set to zero at the water surface (Dirichlet boundary condition).

5.4.3 Smooth and Rough Wall

At the solid boundary, a no-slip condition applies so that both mean and fluctuating velocities are zero (i.e., $u = v = w = 0$); in contrast, the dissipation rate ε is finite. When the boundary conditions are specified right at the wall, the equations must be integrated through the viscous sublayer, which is undesirable for two reasons. Firstly, very steep gradients prevail in the viscous sublayer so that, for proper resolution, many grid points have to be placed in this layer and the computation becomes expensive; secondly, viscous effects are important in this layer so that the high-Reynolds-number turbulence models introduced above are not applicable. However, integration through the sublayer is normally not necessary because empirical laws (i.e., logarithmic law of the wall) are available that relate the wall shear stress vector τ_w to the dependent variables, such as the velocity tangential to the wall, U_T, and turbulent kinetic energy, k_1, at the first grid point just outside the viscous sublayer. The following relationships given by Wu et al. (2000) and AEA Technology (2001) are used:

$$\tau_w = -\lambda_w U_T \tag{5.30}$$

with λ_w given by

$$\lambda_w = \begin{cases} \frac{\mu}{z} & z_1^+ < z_0^+ \\ \frac{\rho C_\mu^{1/4} k_1^{1/2} \kappa}{\ln(E\, z_1^+)} & z_1^+ \geqslant z_0^+ \end{cases} \tag{5.31}$$

where subscript 1 refers to the point at the first control volume center at the wall, z_1 is the normal distance from the wall, $z_1^+ = u_\star z_1/\nu$ a dimensionless distance with $\nu = \mu/\rho$ as kinematic viscosity, $u_\star = \sqrt{\tau_w/\rho}$ the bed-shear velocity, κ the von Karman constant ($\cong 0.41$) and E the roughness parameter. The continuity of the velocity profile at the cross-over point between the viscous sublayer and the logarithmic region, z_0^+, requires that E and z_0^+ satisfy

$$z_0^+ = \frac{1}{\kappa} \ln(E\, z_0^+) \tag{5.32}$$

In the wall-function approach, it is further assumed that close to the wall the production term balances the dissipation term in the equation for the turbulent kinetic energy, k. The values of the shear stress τ_w are then related to the turbulent kinetic energy k by

$$\tau_w = \rho\, C_\mu^{1/2}\, k_1 \tag{5.33}$$

The turbulence dissipation equation is not applied in the control volume next to the wall; instead, ε is set equal to

$$\varepsilon_1 = \frac{C_\mu^{3/4}\, k_1^{3/2}}{\kappa\, z_1} \tag{5.34}$$

The standard wall boundary condition in CFX-4.4 is hydraulically smooth. To further adapt the boundary condition to rough walls as well as the transition zone, the roughness parameter, E in Eq. (5.31) was related to the roughness Reynolds number $k_s^+ = u_\star\, k_s/\nu$ with k_s as the equivalent roughness height of the bed by

$$E = e^{\kappa(\psi - \Delta\psi)} \tag{5.35}$$

where ψ an additive constant ($\cong 5.3$) and $\Delta\psi$ the roughness function of k_s^+ determined by Cebeci and Bradshaw (1977) as

$$\Delta\psi = \begin{cases} 0 & k_s^+ < 2.25 \\ \left[\psi - 8.5 + \frac{1}{\kappa}\ln k_s^+\right] \sin\left[0.4258\,(\ln k_s^+ - 0.811)\right] & 2.25 \le k_s^+ < 90 \\ \psi - 8.5 + \frac{1}{\kappa}\ln k_s^+ & k_s^+ \ge 90 \end{cases} \tag{5.36}$$

For smooth beds, $\Delta\psi = 0$. For stationary flat beds as considered in the present work, the equivalent roughness height, k_s is set to $3\,d_{90}$ as proposed by Van Rijn (1984b).

The diffusive flux of k through the wall is taken to be zero, yielding the boundary condition that the normal derivative of k is zero. For the concentration a zero gradient boundary condition is used at the bottom.

5.4.4 Outlet

A pressure boundary condition is used for the outlet boundary. This choice was made over other possible boundary conditions, such as a specified mass flow boundary, because the pressure boundary condition is more suitable for outlets in which the flow is not fully developed. A constant pressure of zero (an arbitrary reference value) is specified for the outlet boundary at the top of the outlet (Dirichlet boundary condition). Zero normal gradients are applied to all other variables (Neumann boundary condition). The boundary conditions, and variables which have to be defined are summarized in Table 5.3.

Boundary	U_i	p	k	ε	c_s
Symmetry	Free-slip	Neumann	Neumann	Neumann	Neumann
Wall	No-slip	Neumann	Neumann	Dirichlet	Neumann
Inlet	Dirichlet	Neumann	Dirichlet	Dirichlet	Dirichlet
Outlet	Neumann	Dirichlet	Neumann	Neumann	Neumann

Table 5.3: Summary of boundary conditions used in the numerical model.

5.5 Commercial Flow-Solver CFX-4.4

This chapter gives details of the numerical schemes, grid generation and solution methods used in the commercial flow-solver CFX-4.4. The details are fully described in AEA Technology (2001).

5.5.1 Numerical Schemes

The basis of the code is a conservative finite-volume method with all variables defined at the center of control volumes (non-staggered grid) which fill the physical domain being considered. Each equation is integrated over each control volume to obtain a discrete equation which connects the variable at the center of the control volume with its neighbors. All the terms in the equations are discretized in space using second-order centered differencing apart from the convection terms, described below, and the convection coefficients obtained using an improved Rhie-Chow interpolation formula. The SIMPLER method is used to obtain the pressure field.

The treatment of the convection terms determines the accuracy of the solutions of the model equations in CFX-4.4. The following schemes to discretize the convective terms were used:

Momentum equation (5.2) A third-order accurate quadratic upwind scheme (QUICK) was used for the three velocity components.

Concentration equation (5.19) A modified quadratic upwind scheme (CCCT) which is bounded to positive values was used for the concentration of sediments of different sizes.

Turbulence equations (5.7) and (5.8) In the simple geometry of the flume the modified quadratic upwind scheme (CCCT) was used. For the computations in the complex geometry, a hybrid differencing scheme was used which switches from second-order central to first-order upwind differencing when the Peclet number is greater than 2.

In the time stepping procedures a quadratic fully-implicit, backward-difference, time-stepping procedure is used, which is second-order accurate. These are then solved using the standard steady state techniques. A constant

time step was chosen depending on the grid size and the flow velocities to have typical Courant numbers below 1.

5.5.2 Grid Generation

CFX-4.4 uses a non-orthogonal, structured multi-block grid. The coordinate system and the computational grid are entirely distinctive entities. The coordinates in the physical space are often referred to as a body-fitted coordinate system. After a Jacobian matrix coordinate transformation applied to the physical space, the converted space is exactly rectangular with a uniformly distributed finite-difference grid. It is also referred to as the computational space, as it is in this space in which the equations are solved.

The boundary conditions and the information on the erosion-sedimentation interaction model are stored in dummy cells glued around the computational domain. The finite volume mesh is invariable in time, since the amplitude of the newly formed local sediment depositions and erosion is negligible compared to flow depth.

5.5.3 Solution Methods

Iterations are used at two levels: an inner iteration that solves for the spatial coupling for each variable, and an outer iteration that solves for the spatial coupling between variables. The inner iteration was run with under-relaxation factors between 0.3 and 0.7 for each equation, where unity would be no under-relaxation (successive substitution). The inner iterations are run for each equation in the following order: p, u momentum, v momentum, w momentum, k, ε and concentration equations. The Full Field Stone's Method linear solver (Stone) is used to solve the momentum and concentration equations. The Preconditioned Conjugate Gradients solver (ICCG) is used to solve the pressure equation. The k and ε equations are solved using the Line Relaxation solver (Line Solver).

For turbulent flows, a common problem is the rapid divergence, where the residuals suddenly increase to extremely large numbers and the solver crashes. This problem is usually due to the cross-diffusion terms in the k and ε equations. For the computations in a complex geometry, it was found necessary turning off these terms which resulted in faster convergence with no decrease in the accuracy of the solution. This procedure is commonly used as "deferred correction".

5.6 Modelling of Experiments

The following subsections describe the adaptation and modification of the model for the simulation of the physical experiments which were presented

	N_x	N_{z1}	N_{z2}
No. of cells	137	6	40
Distribution	uniform	uniform	g.p.
Distribution factor	1.0	1.0	1.025

Table 5.4: Characteristics of the discretisation for Series A (g.p.=geometric progression).

in Chapter 4. For all the simulations of the experiments, no modification to the k-ε model was found necessary in contrast to the conclusions of Oehy and Schleiss (2001a). The pick-up and settling rate approach proposed by Garcia and Parker (1993) was used for the modelling of the erosion and deposition fluxes with three characteristic grain sizes (d_{16}, d_{50} and d_{84}). The reference level, b, was set equal to 0.5 cm, which corresponded to approximately 5% of the turbidity current height.

A sensitivity analysis was preformed on different meshes to get a grid independent solution. The time step was chosen so that the Courant number using the front velocity and the cell length was below 1. In general, a time step of 0.5 s was sufficient.

5.6.1 Continuously-Fed Turbidity Current

The flume was discretized only in the longitudinal and vertical directions, because the comparison of three-dimensional computations (i.e., with transversal discretisation) showed no significant difference with the two-dimensional computations. In the vertical direction 6 cells with a uniform distribution were used over the inlet height of 0.045 m for the whole length of the flume (N_{z1}). Attention was paid that the first grid point laid outside of the viscous sublayer, so that the logarithmic wall law was applicable. The upper area was discretized with the aid of 40 cells having a geometric progression (N_{z2}). The longitudinal discretisation was uniform with 137 cells of 0.05 m length (N_x). The characteristics of the discretisation are given in Table 5.4. The numerical grid together with the boundary conditions for the Series A experiments is presented in Fig. 5.3.

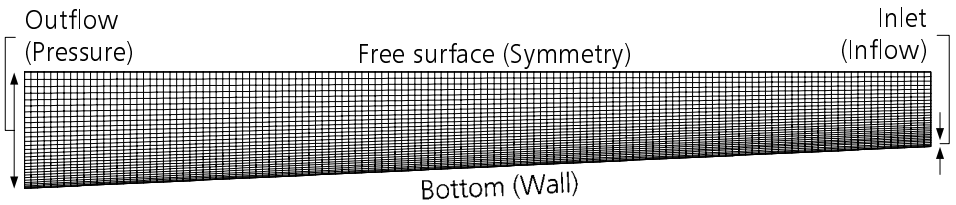

Figure 5.3: Body-fitted grid with boundary conditions for Series A experiments (N=6302 cells).

	N_{x1}	N_{x2}	N_{x3}
No. of cells	90	30	27
Distribution	uniform	sym.g.p.	uniform
Distribution factor	1.0	0.9	1.0

Table 5.5: Characteristics of the discretisation for Series B (sym.g.p.=symmetric geometric progression).

5.6.2 Flow over an Obstacle

For the Series B experiments no modification of the numerical model were necessary and the same model and boundary conditions as for the experiments without an obstacle could be used.

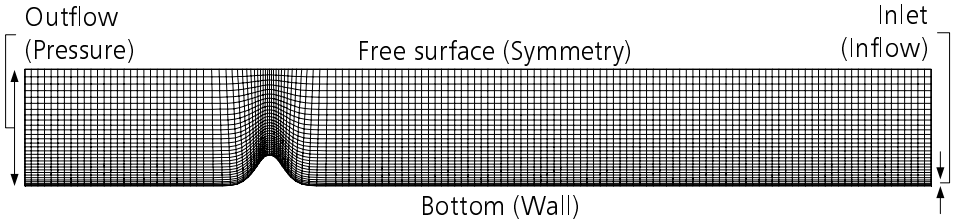

(a) Horizontal bottom, (S=0.00%).

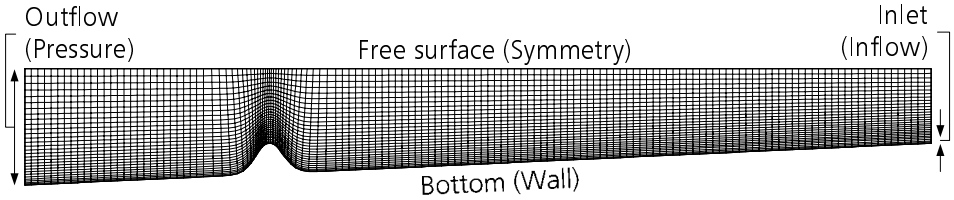

(b) Inclined bottom (S=4.64%).

Figure 5.4: Body-fitted grid with boundary conditions for Series B experiments (N=6762 cells).

The discretisation in the vertical direction was similar to the simulations of a continuously-fed turbidity current. The longitudinal discretisation was uniform up to a distance of 0.5 m up- and downstream from the obstacle crest, where the numerical grid was adapted to the obstacle geometry described in Subsection 3.4.2. Over the obstacle a grid refinement was made and 30 cells were used as shown in Fig. 5.5. The characteristics of the discretisation in the horizontal direction with the grid refinement are given in Table 5.5. The numerical grid together with the boundary conditions for the Series B experiments over a horizontal and an inclined bottom are presented in Figs. 5.4(a) and 5.4(b). A time step of 0.5 s was used in all computations.

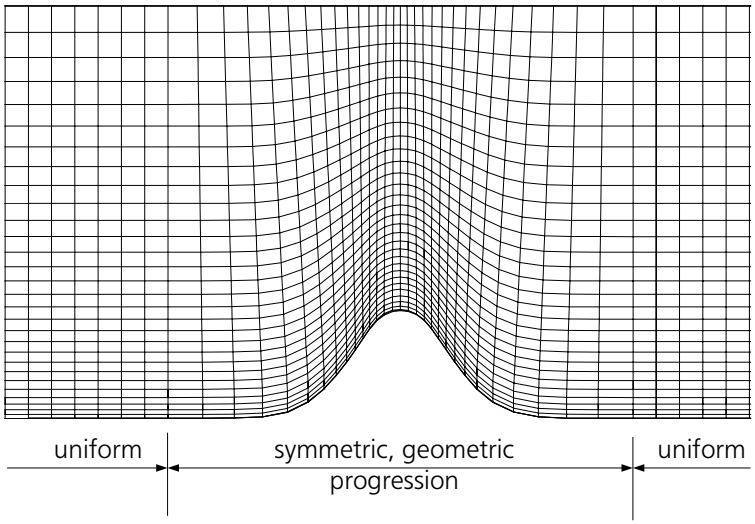

Figure 5.5: Zoom of body-fitted grid over the obstacle for Series B experiments.

5.6.3 Flow Through a Screen

The permeable screen was modelled as a porous region with a given volume porosity, β and a body force resistance term due to friction loss. In CFX-4.4 the porous regions are modelled using a generalization of the Navier-Stokes equations and of Darcy's law. In deriving the equations, it is assumed that control volumes and surfaces are large relative to the interstitial spacing of the porous medium. The equations of conservation of mass and momentum in the porous region are then written as

$$\frac{\partial(\beta\rho)}{\partial t} + \frac{\partial(\beta\rho U_i)}{\partial x_i} = 0 \tag{5.37}$$

$$\frac{\partial(\beta\rho U_i)}{\partial t} + \frac{\partial(\beta\rho U_i U_j)}{\partial x_j} - \frac{\partial}{\partial x_j}\left(\mu_{\text{eff}}\left[\frac{\partial(\beta U_i)}{\partial x_j} + \frac{\partial(\beta U_j)}{\partial x_i}\right]\right) = -\beta\frac{\partial p'}{\partial x_i} + \beta B_i - \beta F_i \tag{5.38}$$

where F_i is a resistance force to the flow due to friction.

The success of the numerical approach for simulating the turbidity current–screen interaction depends largely on the accuracy of the empirical formulas and coefficients used to describe the frictional or resistance forces exerted by the screen. Many investigators proposed relationships for the frictional forces in porous regions, which generally may be written as a combination of linear and non-linear head losses as follows (Trussel and Chang, 1999)

$$F_i = \frac{\partial p}{\partial x_i} = \alpha_p U_i + \beta_p |U_i| U_i \tag{5.39}$$

Geotextile	α_p [kg s^{-}1 m^{-}3]	β_p [kg m^{-}4]
Tricopor® 118	4750	395000
Tricopor® 120	35250	350000

Table 5.6: Resistance force coefficients for the two types of geotextiles.

where α_p is a linear coefficient, and β_p a non-linear coefficient. There is no exact data available for the drag of the two geotextiles, therefore, the values of α_p and β_p were determined by using the relationship for the local head loss of a flow through thick grids as proposed by Idel'cik (1969). It is assumed that the local head loss, ΔH, may be written as pressure difference Δp acting over the length or thickness of the porous region, Δx, as following

$$\frac{\Delta p}{\Delta x} = \frac{\rho g \Delta H}{\Delta x} \text{ with } \Delta H = \xi_{Re} \frac{U^2}{2g} \tag{5.40}$$

where ξ_{Re} is a loss coefficient determined with the relationship proposed by Idel'cik (1969). The Reynolds numbers through the screen are small $Re \leq 25$, therefore, the flow resistance is depending on the Reynolds number and contains linear and non-linear terms. The values for α_p and β_p can then be determined using the physical characteristics of the screen as described in Section 3.4.3 and combining Eq. 5.39 with Eq. 5.40. Table 5.6 summarizes the coefficients for the two geotextiles with a thickness of the porous region equal to Δx=2 mm.

The turbulence model in the porous region is the same as the turbulence model specified for the rest of the flow. The volume porosities are smoothed internally by the program to ensure a monotonic change in velocity across the discontinuity. This smoothing occurs across four control cells, therefore, a grid refinement was made in a region of 0.3 m up- and downstream from the screen as shown in Figs. 5.6 and 5.7. The screen in the numerical model was 3 mm thick and consisted of three cells (N_{x3}). The discretisation in the vertical direction was similar to the experiments without a screen. The characteristics of the discretisation in the horizontal direction with the grid refinement are given in Table 5.7. The numerical grid together with the boundary conditions for the Series C experiments over a horizontal bottom and a slope of S=4.64% are presented in Figs. 5.6(a) and 5.6(b). A time step of 0.5 s was used in all computations.

5.6.4 Flow Across a Multiport Diffuser

The standard k-ε model was used extensively to simulate the turbulent jets in a crossflow. Chochua et al. (2000) investigated the flow field induced by a single circular jet issuing perpendicularly from a flat plate into a crossflow. Keimasi and Taeibi-Rahni (2001) calculated the three-dimensional flow of

	N_{x1}	$N_{x2} = N_{x4}$	N_{x3}	N_{x5}
No. of cells	91	30	3	26
Distribution	uniform	g.p.	uniform	uniform
Distribution factor	1.0	1.1	1.0	1.0

Table 5.7: Characteristics of the discretisation for Series C (g.p.=geometric progression).

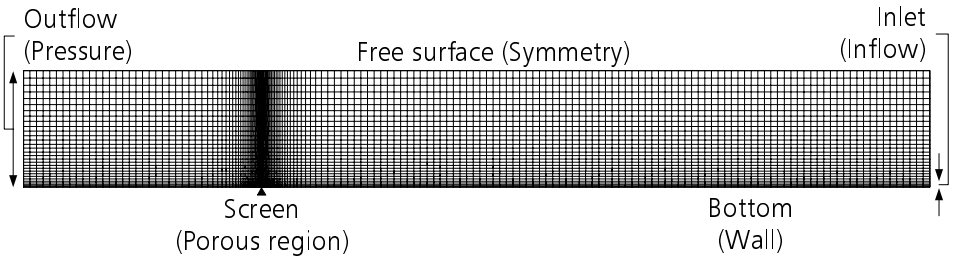

(a) Horizontal bottom, S=0.00%.

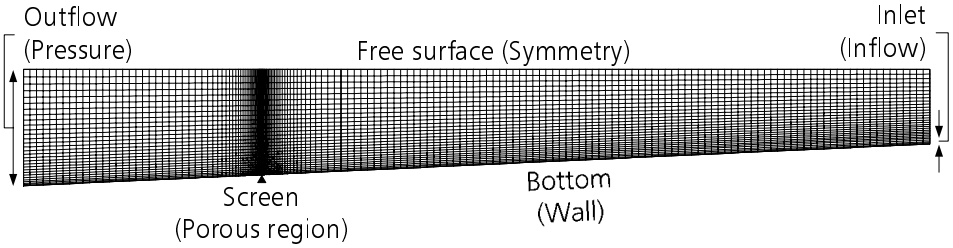

(b) Inclined bottom S=4.64%.

Figure 5.6: Body-fitted grid with boundary conditions for Series C experiments (N=8280 cells).

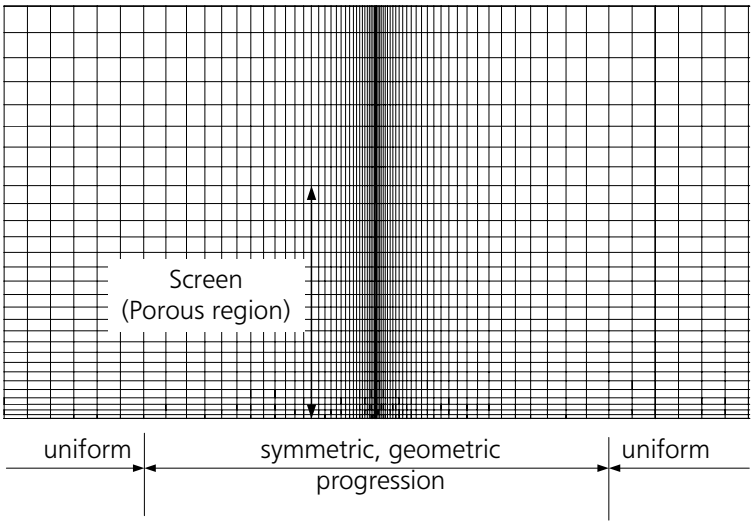

Figure 5.7: Zoom of body-fitted grid around the screen for Series C experiments.

a row of square jets injected perpendicularly into a crossflow. They also give a good literature review on recent numerical investigations of jets in crossflows. Kalita et al. (2002) predicted the turbulent plane jet in a weak or moderate crossflow and found satisfactory agreement by comparison with experimental data. Hwang and Chiang (1995) and Hwang et al. (1995) investigated a vertical forced plume in a uniform crossflow of stably linear stratified environment, using a three-dimensional numerical model. They evaluated the performance by comparison of the numerical results with available experimental measurements.

As was described in the previous paragraphs, the k-ε model was widely used for simulating jets in crossflows with or without stratification, therefore, the k-ε model without any modification was also used for the present simulations. From the characteristics of the multiport diffuser used in the experiments, the equivalent slot width for a two-dimensional jet having the same momentum and discharge can be determined. This leads to a slot width of approximately 0.4 to 0.6 mm, which would need a very fine numerical grid to be solved satisfactorily. To overcome this problem, it is assumed that the governing parameters of the interaction between the jet and the turbidity current are the injected discharge and momentum and that the internal structure of the jet plays a minor role. Therefore, a larger slot width of 5 mm injecting the exact discharge was used in the numerical simulations. It is evident that due to the larger slot width the injected momentum is underestimated considerably. To compensate for this shortfall a local momentum source was added in the second cell above the diffuser. The inlet of the diffuser nozzle was placed horizontally, so that only the vertical velocity component, U_{j0z} contributed to the discharge injection. The additional momentum in the x and z direction, M^+_{j0x} and M^+_{j0z}, respectively were then computed for the vertical and inclined jet from the physical jet characteristics as shown in Table 5.8. One can note that for the experiment D04 with a vertical jet and an inclined bottom there is also a momentum component in x direction due to the inclination.

For k and ε the jet inlet conditions were chosen following Eqs. (5.28) and (5.29). With the turbulence intensity i_T equal to 0.026 and a dissipation length scale equal to 0.3 mm.

The discretisation in the vertical direction was similar to the experiments with a continuously-fed turbidity current. The numerical grid was refined in a region of 0.3 m up- and downstream from the diffuser as shown in Figs. 5.8 and 5.9. The characteristics of the discretisation in the horizontal direction with the grid refinement are given in Table 5.9. As described above the jet slot in the numerical model was 5 mm wide and consisted of two cells (N_{x3}). For the initialization of the simulation of the turbidity current flow through the diffuser, a steady state solution of the jet was first computed, where the additional momentum was linearly increased for stability reasons to the maximum value. A time step of 0.5 s was used in all computations.

	Physical experiments		Numerical simulations			
Exp	Q_{j0}	M_{j0}	U_{j0z}	M_{j0z}	M^+_{j0x}	M^+_{j0z}
[–]	[cm^3/s]	[cm^4/s^2]	[cm/s]	[cm^4/s^2]	[cm^4/s^2]	[cm^4/s^2]
D01	104	6374	9.56	994	-	5379
D02	57	1915	5.24	299	-	1616
D03	78	3585	7.17	559	-	3026
D04	84	4158	7.72	649	194	3505
E01	107	11159	9.83	1052	-7514	7197
E02	163	25896	14.98	2442	-17438	16702
E03	105	10746	9.65	1013	-7598	6585
E04	98	9361	9.01	883	-6619	5736

Table 5.8: Physical and numerical diffuser characteristics for the simulation of the turbidity current flowing across multiple jets.

	N_{x1}	$N_{x2} = N_{x4}$	N_{x3}	N_{x5}
No. of cells	97	30	2	28
Distribution	uniform	g.p.	uniform	uniform
Distribution factor	1.0	1.1	1.0	1.0

Table 5.9: Characteristics of the discretisation for Series D and E (g.p.=geometric progression).

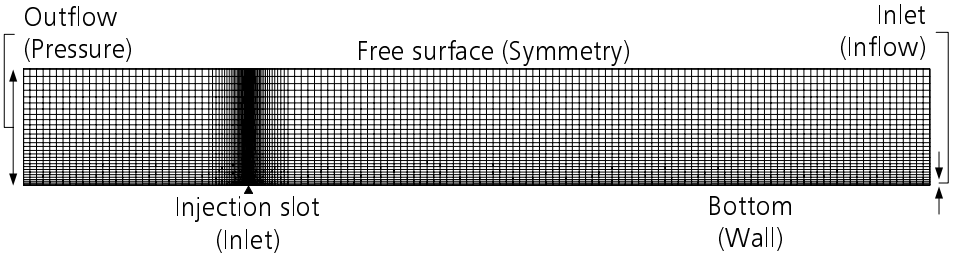

(a) Horizontal bottom, S=0.00%.

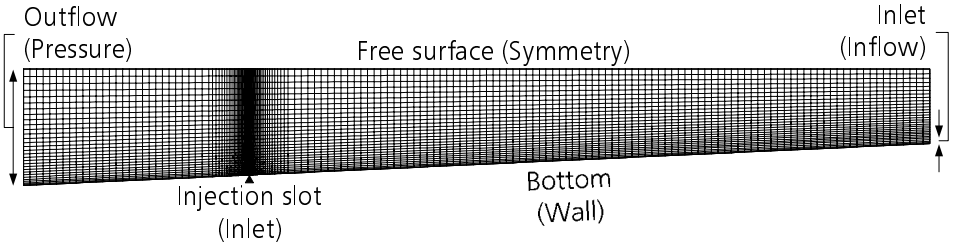

(b) Inclined bottom, S=4.64%.

Figure 5.8: Body-fitted grid with boundary conditions for Series D and E experiments (N=8602 cells).

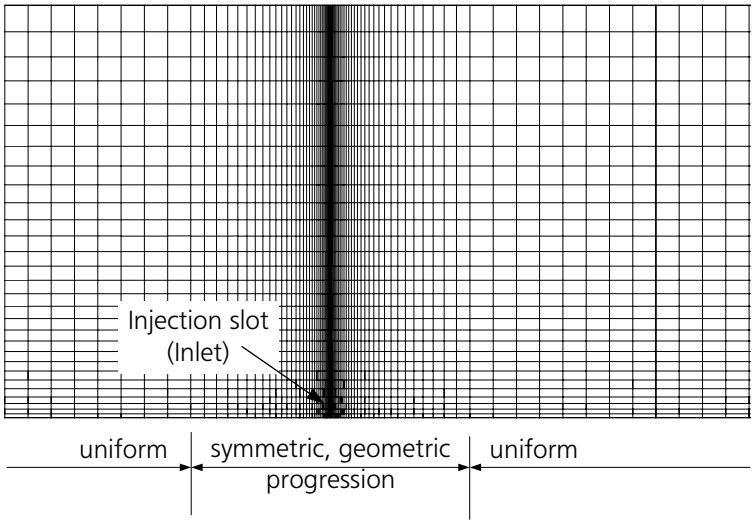

Figure 5.9: Zoom of body-fitted grid around the injection slot for Series D and E experiments.

6 Comparison of Physical Experiments and Numerical Simulations

6.1 Continuously-Fed Turbidity Current

In this section the experimental results presented in Section 4.1 are compared with the predictions of the numerical model described in Chapter 5. Three experiments on continuously fed turbidity current experiments (A07 to A09) were simulated and some of the results are presented here. The complete simulation results can be found in Appendix B.1 on page 257.

To compare the measured velocity profiles with the numerical computations, time histories of u, w, k, ε, c_{s16}, c_{s50} and c_{s84} were generated at the locations at which physical measurements were made. The averaged profiles were then determined in the same manner as the measured profiles, i.e. the start and end point of the time series were chosen after the head had passed, and the values were averaged over the quasi-steady flow of the turbidity current body. The comparison of the computed and measured velocity profiles of experiment A09 at five locations is shown in Fig. 6.1.

It can be seen that the numerical model predicts with good agreement the measured vertical velocity distribution of the component u parallel to the bottom. A systematic difference between the measured and computed values exists in the ambient water return flow where the velocity is small. This can be explained by the fact that the u-velocity resolution of the UVP measurements is approximately 1.7 mm/s which may generate large relative errors for small velocities.

The distribution of the turbulent kinetic energy, k, and the sediment concentration, c_s, were also plotted on the same graphs. It is interesting to note that the height at which the concentration equals zero coincides well with the height of zero velocity. Further, the distribution of the turbulent kinetic energy, k, shows a maximum at the bottom, where turbulence is generated by friction, then it abruptly decreases in the region of maximum velocity and maximum density gradient, and increases again due to the shear between the turbidity current flow and the ambient water layer. After having reached

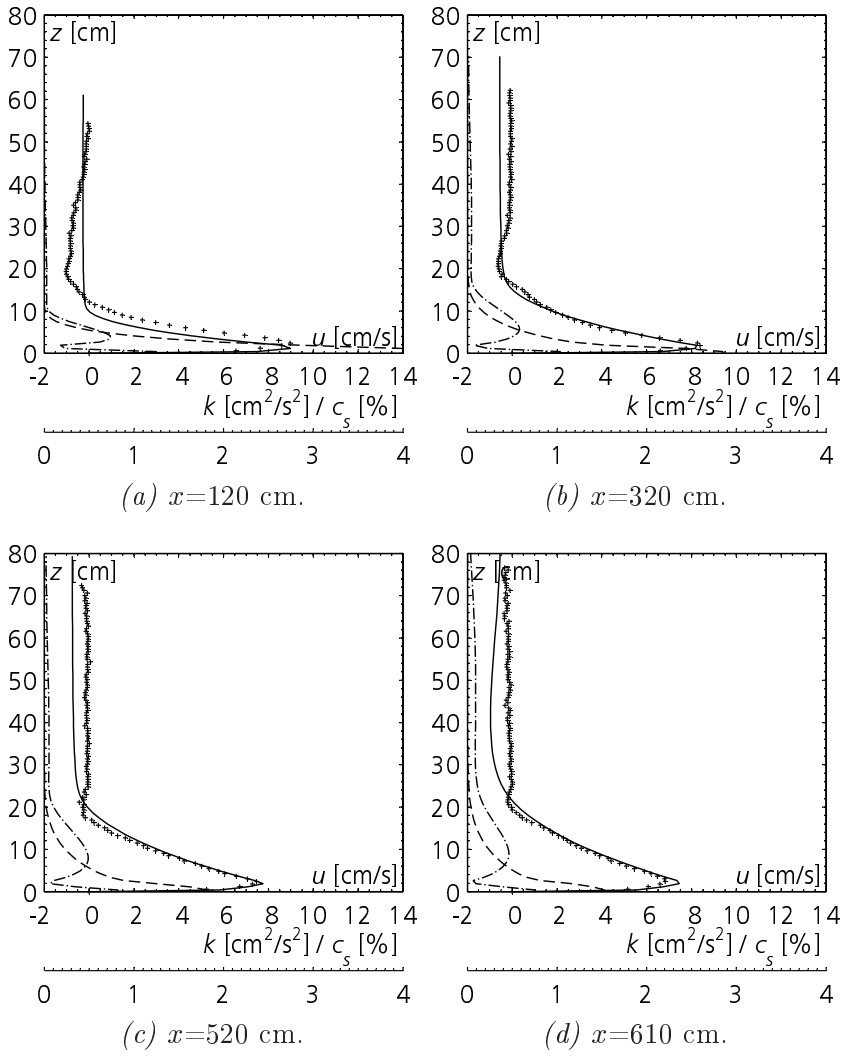

(a) x=120 cm. *(b)* x=320 cm.

(c) x=520 cm. *(d)* x=610 cm.

Figure 6.1: Vertical profiles of computed velocity, u (thick solid line), measured velocity (thin solid line), computed concentration, c_s (thick dashed line) and turbulent kinetic energy, k of experiment A09.

another peak value, the turbulent kinetic energy decreases and almost vanishes finally at height of zero velocity or concentration.

The integral flow scales were also calculated from the computed velocity profiles and were compared with the values determined from the experiments. Generally, the differences between the computed and measured values (see Table B.3 of Appendix B.1) were within ±10%, which is satisfactory considering the highly transient phenomena and short averaging periods. In fact, due to the reflection from the downstream wall, the quasi-steady time frame over which the averaging could be done, lasted only between one and two minutes after the head has passed. Other authors reported experiments where they maintained a steady current over more than 10 minutes.

Exp [–]	$U_{f1\text{meas}}$ [cm/s]	$U_{f1\text{calc}}$ [cm/s]
A07	3.67	3.62 (−1)
A08	4.11	3.97 (−3)
A09	4.87	5.01 (+3)

Table 6.1: Comparison of the measured and computed head velocities of the experiments with a continuously-fed turbidity current with in parenthesis the relative percentage differences.

From the flow scales resulting from the numerical simulations the Richardson number was calculated. It attained an almost constant value after a short distance of less than 100 cm from the inlet. The bottom slope of the experiments was 4.64%, which explains the relatively small Richardson numbers ranging from 0.44 to 0.48. Hence, the flow down the inclined flume was always supercritical.

Plots showing the isolines of the computed volumetric concentration c_s at time steps of 10 s are given in Fig. 6.2. The line delimiting the current represents a density difference of approximately 0.1 g/l or a value of $\Delta\rho/\rho = 0.01\%$. The different isolines are plotted in intervals of $\Delta\rho$ =0.1 g/l. The plots of the concentration field give a good idea of the motion of the turbidity current down the slope. The head of the turbidity current can clearly be distinguished from the body. Also the characteristic form of the head with its 'nose' raised above the bottom is well reproduced. The velocity field around the head of the turbidity current is shown in Fig. 6.3. A strong vortex motion can be seen which carries surrounding ambient above the front into the rear of the head.

The head propagation velocity of the turbidity current was also determined from the numerical simulation, and compared with the experimental results. Table 6.1 shows the measured and computed values for the three simulations with the relative percentage difference. Generally, the head velocities agreed quite well with the measured velocities for these turbidity current experiments without any obstacles, or jets.

The deposition along the flume in the numerical simulation was obtained by integrating in time the fluxes at the bottom. The evolution of the deposition was determined at time steps of 10 s to allow a direct comparison with the measured deposition evolution. Fig. 6.4 shows the measured and computed evolution of deposition in experiment A07. The comparisons for the other simulations of the Series A can be found in Appendix B.1.

The comparison in Fig. 6.4 shows that the evolution is well reproduced both qualitatively and quantitatively. A small difference exists in the region up to 200 cm where the deposition is overestimated by the numerical model. As the computations were performed with three grain sizes characterizing the grain size distribution, the distribution of the deposition corresponding to

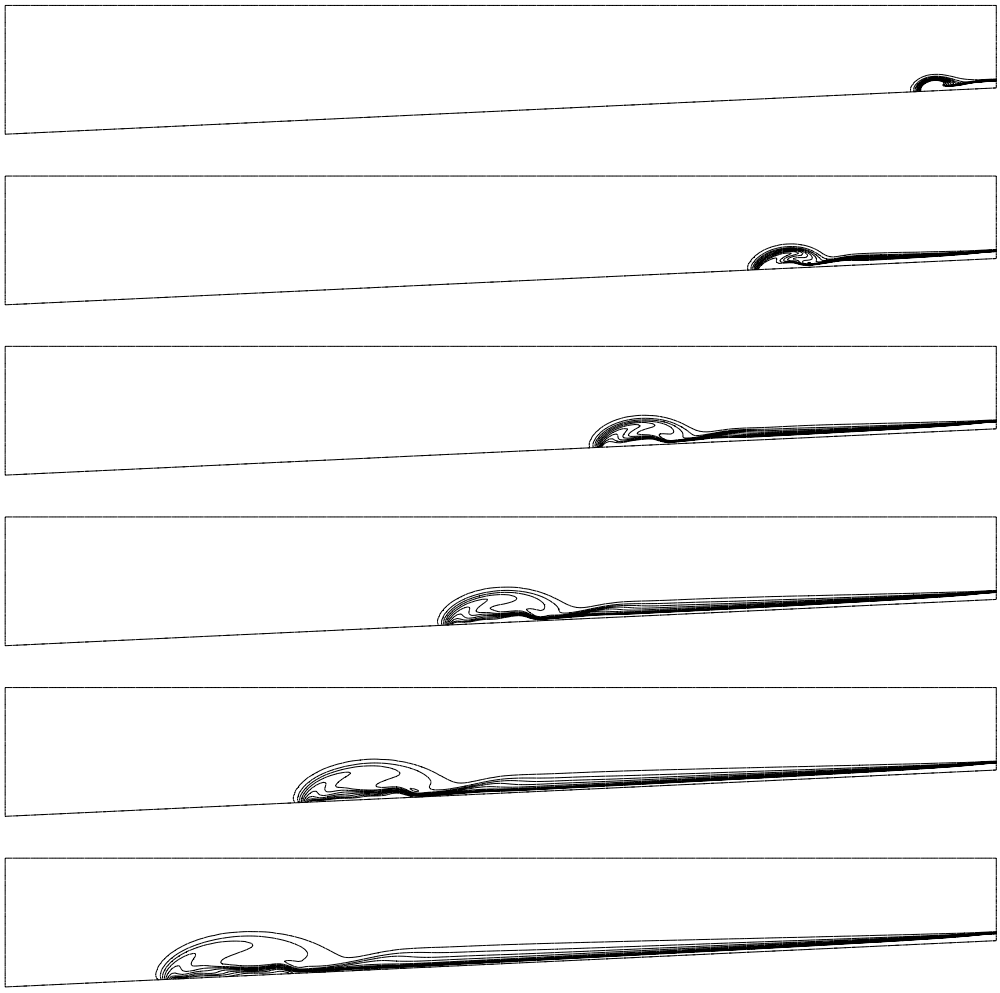

Figure 6.2: Concentration isolines in time intervals of 20 s of the simulation of a continuously-fed turbidity current (experiment A09). The different isolines are plotted in intervals of $\Delta\rho$ =0.1 g/l.

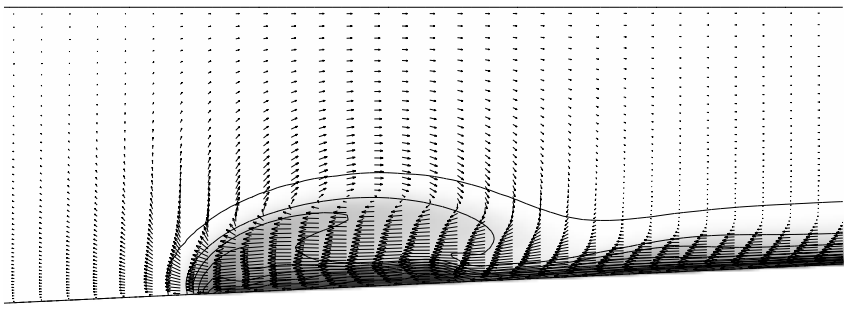

Figure 6.3: Two-dimensional velocity field around the turbidity current head with isolines of concentration.

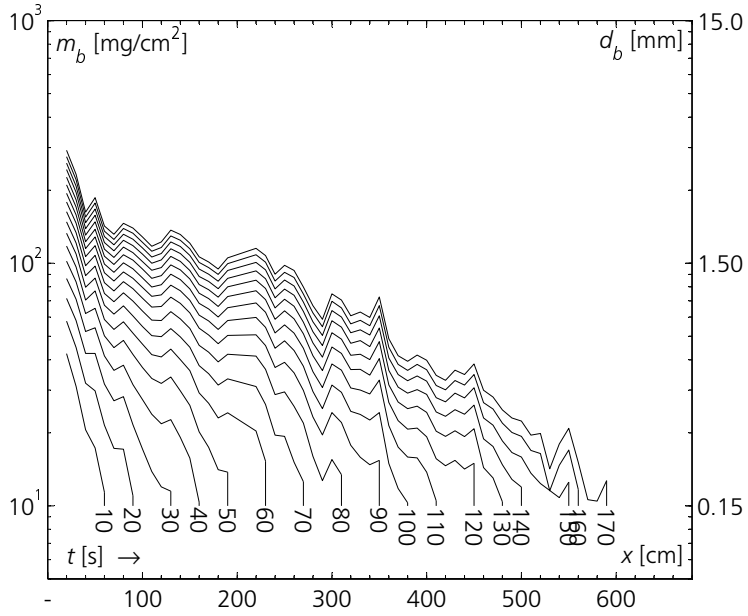

(a) Measured evolution of deposition.

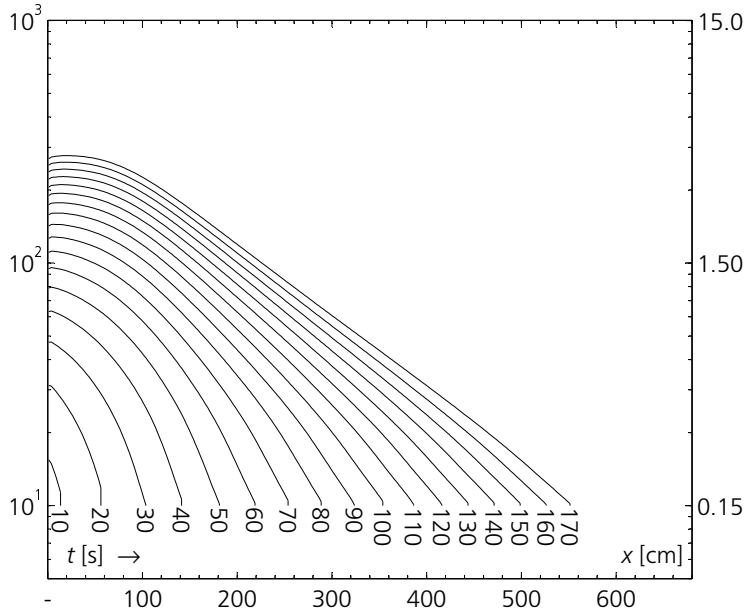

(b) Computed evolution of deposition.

Figure 6.4: Comparison of measured and computed evolution of the sediment deposition in experiment A07.

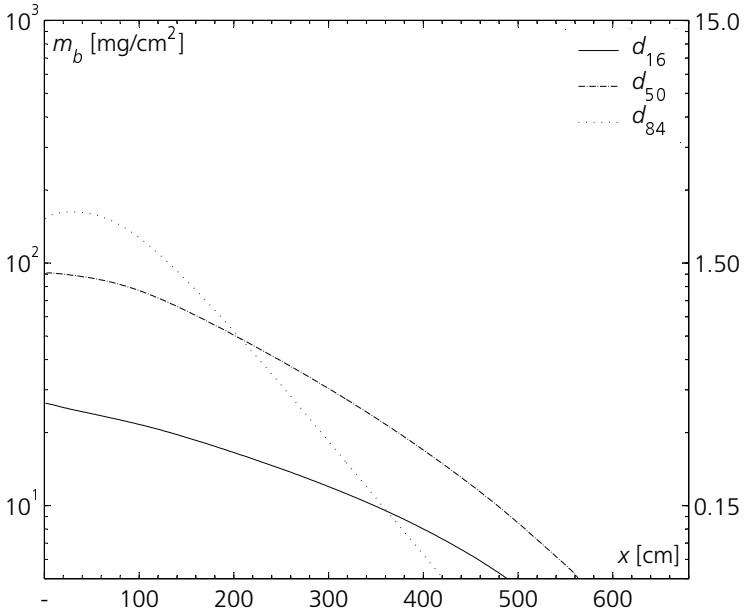

Figure 6.5: Deposition thickness of three grain sizes, d_{16}, d_{50} and d_{84} at the end of experiment A07 (t=170 s).

each grain size is shown in Fig. 6.5 for t=170 s.

It is interesting to see on the figure that the fractional sediment deposition is important, especially for the largest grain size d_{84}, which settles mostly in the upper part of the flume. This also indicates that the concentration of coarser grains within the turbidity current decreases much more in the streamwise direction and therefore the characteristic grain size of the grain size distribution becomes finer.

6.2 Flow Over an Obstacle

In this section the experiments presented in Section 4.2 of a turbidity current flow over an obstacle are compared with the predictions of the numerical model described in Chapter 5. Two experiments (B03 and B05) were simulated, and some of the results are presented here. The complete simulation results can be found in Appendix B.2 on page 269.

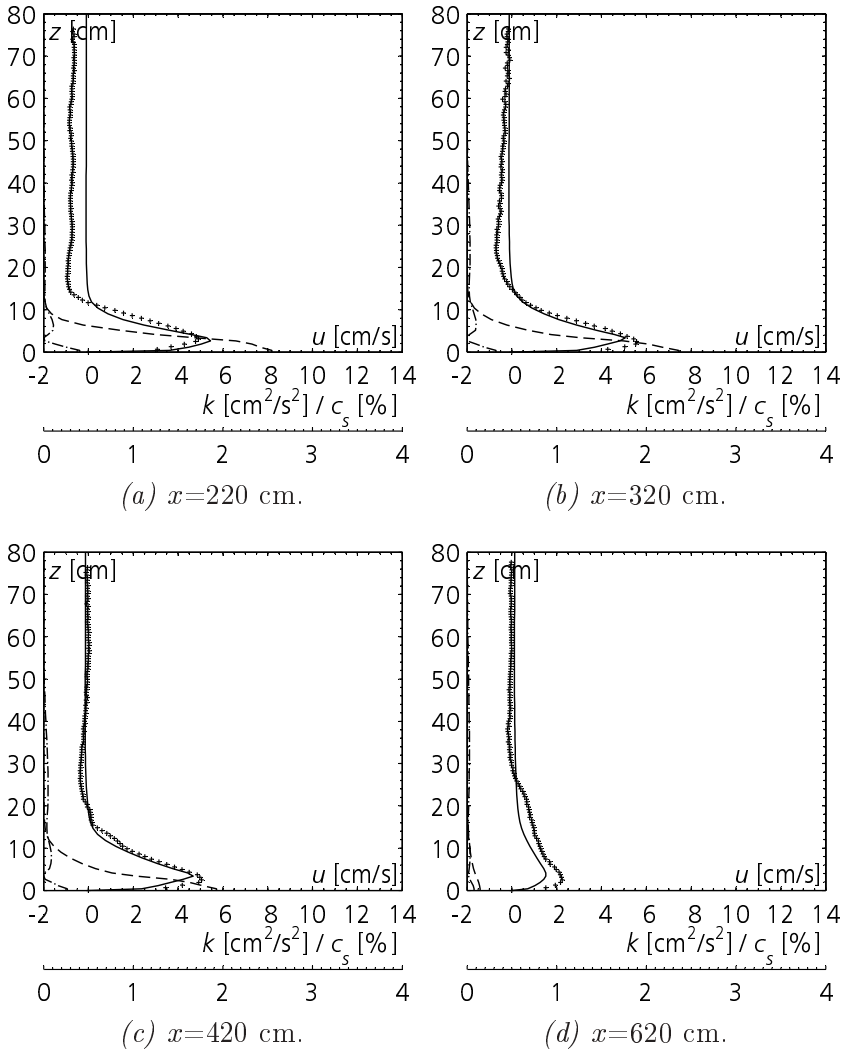

(a) x=220 cm. *(b)* x=320 cm.

(c) x=420 cm. *(d)* x=620 cm.

Figure 6.6: Vertical profiles of computed velocity, u (thick solid line), measured velocity (thin solid line), computed concentration, c_s (thick dashed line) and turbulent kinetic energy, k of experiment B03.

The comparison of the computed and measured velocity profiles at four locations of experiment B03 with a horizontal bottom are shown in Fig. 6.6. It can be seen that again the numerical model predicts with good agreement the measured vertical velocity distribution of the component u parallel to the

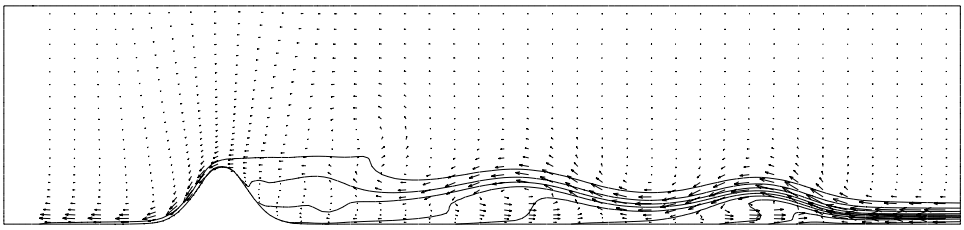

(a) Undular bore travelling upstream as a group of solitary waves in experiment B03.

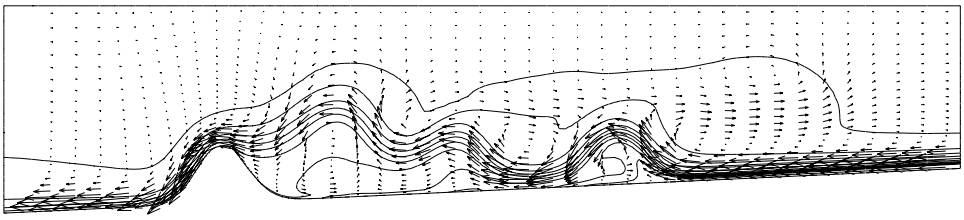

(b) Strong bore travelling upstream as a front in experiment B05.

Figure 6.7: Concentration isolines and velocity vectors within the reflected bores of experiments B03 and B05.

bottom. The effect of the obstacle can clearly be seen between the profile upstream of the obstacle shown in Fig. 6.6(c) and the profile downstream of the obstacle in Fig. 6.6(d). The velocity is strongly reduced, the height increased and the concentration decreased. It is interesting to note that in the experiment with a horizontal bottom the turbulent kinetic energy, k, is much lower compared to the inclined flume experiment.

The integral flow scales were also calculated from the computed velocity profiles and were compared with the values determined from the experiments. Generally, the differences between the computed and measured values were within $\pm 10\%$ in the upstream profiles and slightly higher in the profile downstream of the obstacle (see Table B.6 of Appendix B.2). The computed Richardson numbers of approximately 1.17 upstream of the obstacle indicate that the turbidity current was subcritical in experiment B03 with a horizontal bottom. The experiment with inclined bottom (B05) had a Richardson number of 0.44.

A detailed calculation of the partially blocked flow in experiments B03 and B05 is shown in Figs. 6.8 and 6.9. The sequence with a time interval of 20 s starts just before the turbidity current encounters the obstacle. To visualize the flow the isolines of the volumetric sediment concentration were plotted similar to the simulations of a continuously-fed turbidity current.

As can be clearly seen on the figures, a part of the turbidity current passes over the obstacle but most of it is reflected and propagates backwards. Downstream of the obstacle, a new turbidity current with a weaker front

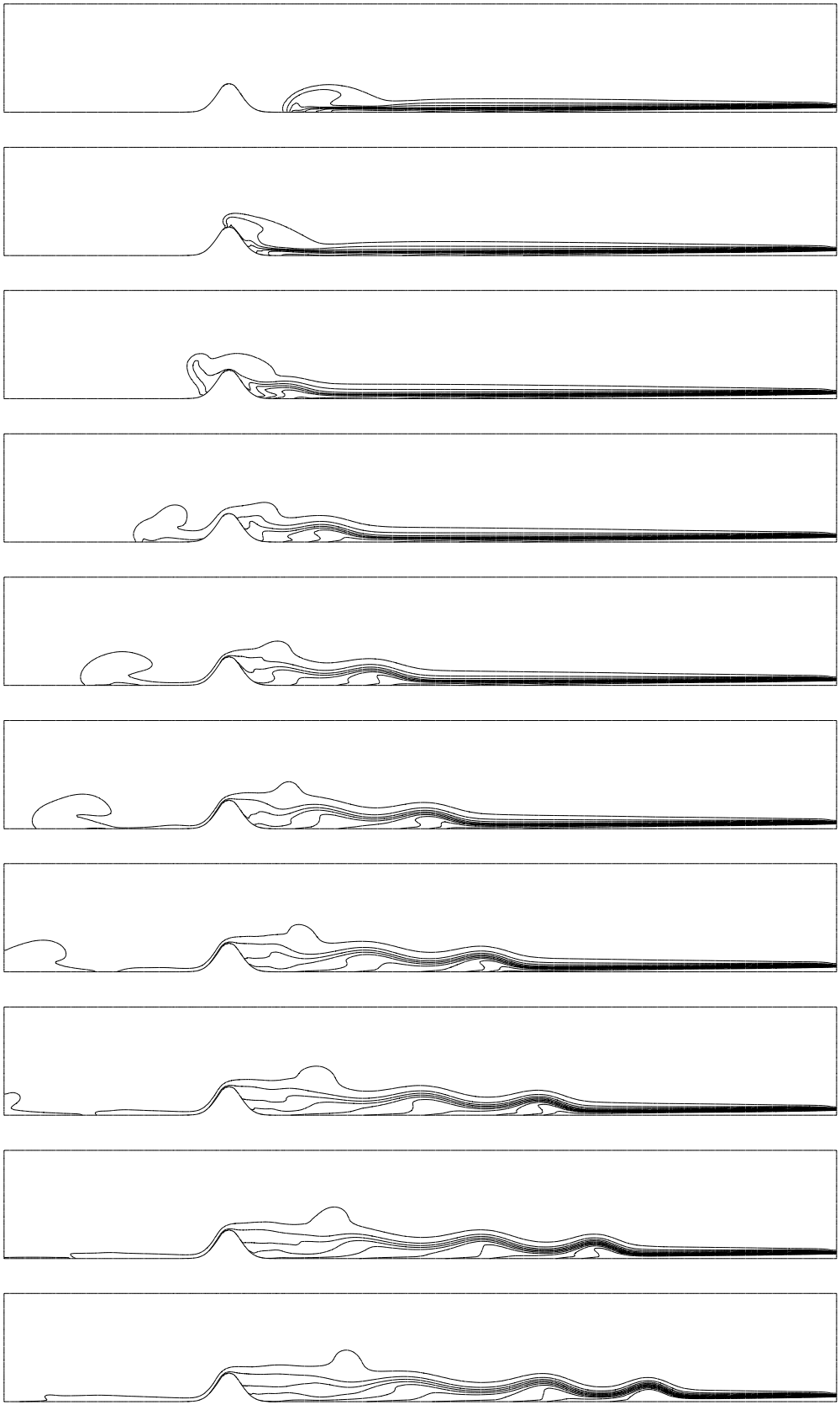

Figure 6.8: Concentration isolines in time intervals of 20 s of the turbidity current flow simulation over an obstacle (experiment B03). The different isolines are plotted in intervals of $\Delta\rho$ =0.1 g/l.

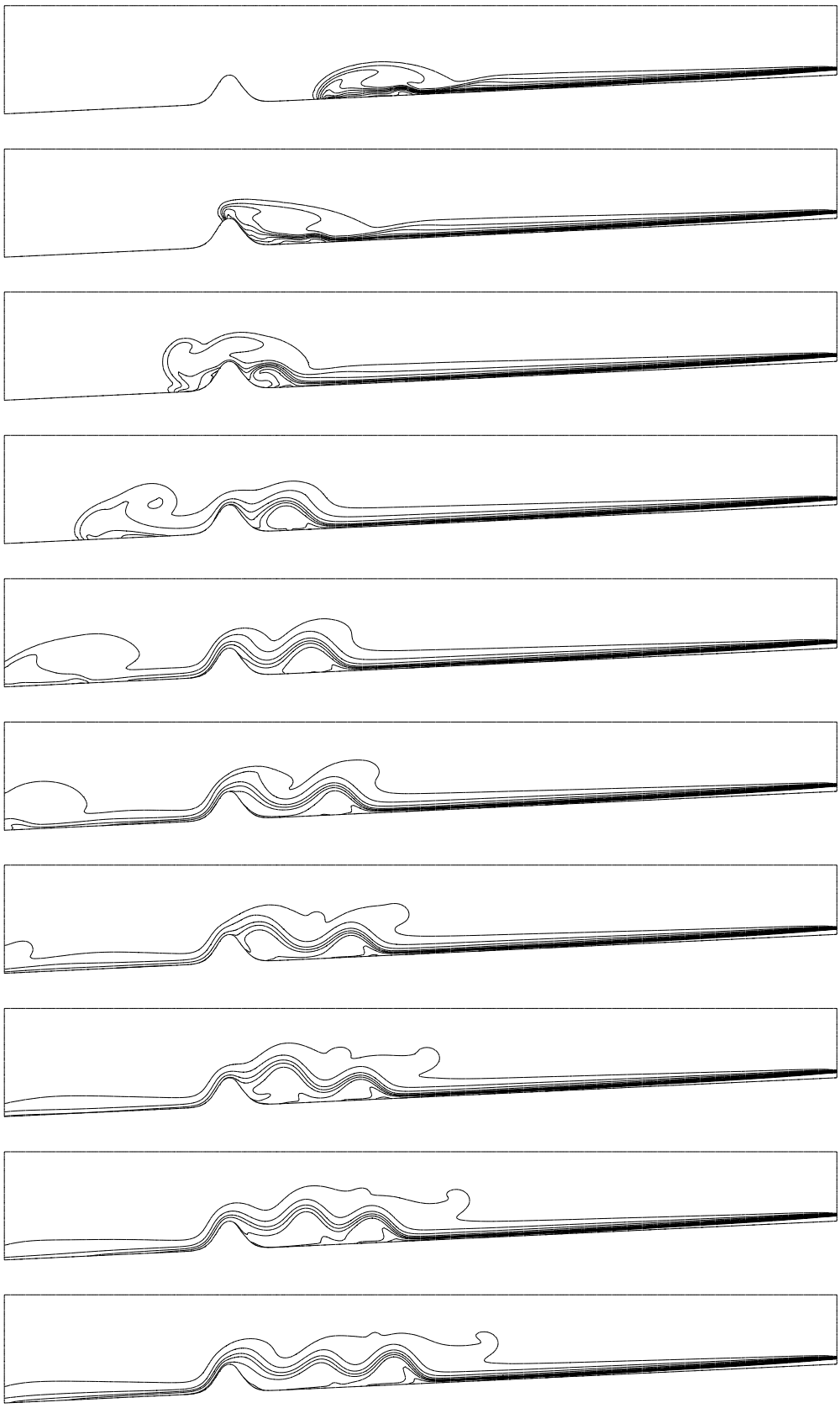

Figure 6.9: Concentration isolines in time intervals of 20 s of the turbidity current flow simulation over an obstacle (experiment B05). The different isolines are plotted in intervals of $\Delta\rho$ =0.1 g/l.

is formed and travels further down the flume. As described in Section 4.2, the reflected flows are bores (moving hydraulic jumps that transport mass). In the case of experiment B03 in Fig. 6.8 the bottom slope was horizontal and the initial turbidity current was subcritical. The reflected bore has flow characteristics in common with a group of solitary waves as proposed by Edwards et al. (1994) which travel upstream. After some time, a second reflection occurs at the upper end wall which causes the waves to return back to the obstacle.

In experiment B05 the turbidity current was supercritical, therefore a strong bore with characteristics in common with the original turbidity current was reflected as shown in Fig. 6.9. The difference between strong bores and weak bores can be seen in the plots of Fig. 6.7, where the velocity field is shown as well. In Fig. 6.7(a) with the weak bore from experiment B03, orbital fluid motions can be found within the internal solitary wave. This phenomenon has also been observed by Kneller et al. (1997), who conducted two-dimensional UVP measurements of the velocity and turbulence structure within internal solitary waves. In the strong bore of experiment B05 shown in Fig. 6.7(b), the front of the reflected current can clearly be seen and flows over the initial, denser turbidity current. In the region between the obstacle and the reflected front an undular, inclined velocity pattern exists, which overflows a dead zone upstream of the obstacle.

The computed propagation velocities of the turbidity current front upstream and downstream of the obstacle, as well as the propagation velocity of the reflected bore for experiments B03 and B05 were determined and compared with the measurements. Table 6.2 shows the measured and computed values for the two experiments with the relative percentage differences. The results show that the front velocity downstream of the obstacle was underestimated for the horizontal bottom and overestimated in the case of an inclined bottom. The velocity of the bore in experiment B05 was well reproduced.

Exp [–]	$U_{f1\mathrm{meas}}$ [cm/s]	$U_{f1\mathrm{calc}}$ [cm/s]	$U_{f2\mathrm{meas}}$ [cm/s]	$U_{f2\mathrm{calc}}$ [cm/s]	$U_{fb\mathrm{meas}}$ [cm/s]	$U_{fb\mathrm{calc}}$ [cm/s]
B03	3.40	3.46 (+2)	2.37	2.14 (−10)	n. d.	-2.07
B05	5.06	4.61 (−9)	3.28	3.54 (+8)	-1.12	-1.14 (+2)

Table 6.2: Comparison of the measured and computed front velocities upstream of the obstacle, U_{f1}, downstream of the obstacle, U_{f2}, and the propagation speed of the reflected bore, U_{fb} with in parenthesis the relative percentage differences.

The deposition along the flume in the numerical simulation was obtained by integrating in time the sediment fluxes at the bottom. The evolution of the deposition was determined at time steps of 10 s to allow a direct comparison with the measured evolution as presented in Section 4.2. Fig. 6.10 shows the measured and computed evolution of the sediment deposition for experiment

B05. The comparison for the experiment B03 can be found in Appendix B.2 on page 269.

The comparison in Fig. 6.10 shows that the evolution of the deposit is reproduced satisfactorily. The numerical model predicts a lower deposition rate than the one measured both upstream and downstream of the obstacle. Nevertheless, the difference between upstream and downstream deposition agrees well with the measurements. In experiment B03, the results of the numerical model underestimate the deposition rate downstream of the obstacle, indicating that in the numerical model more sediment is retained behind the obstacle than in the experiments.

To measure the efficiency of an obstacle in retaining dense gas clouds, Gröbelbauer (1995) introduced an obstacle efficiency η to describe the ability of a specific obstacle configuration to block the arriving cloud. He defined η as the ratio of the retained flow rate to the total flow rate approaching the obstacle. For the present study a similar definition is used, which compares the sediment flux passing over the obstacle crest with the sediment flux at the same location without the obstacle written as following

$$\eta \equiv \frac{q_s}{q_{s0}} \tag{6.1}$$

where q_s is the sediment flux over the obstacle, and q_{s0} is the sediment flux without the obstacle. For simplification, the constant sediment flux after the passage of the head was taken for q_{s0}. The ratio η then varies from 0 (completely blocked) to 1 (unblocked or no effect).

Fig. 6.11 shows the evolution of the ratio, η, as a function of time for the experiments B03 and B05. The first peak clearly indicates the passage of the head in both experiments. For experiment B03 in Fig. 6.11(a) with a horizontal bottom, a nearly constant sediment flux exists after the passage of the head until the first reflected wave from the upstream wall arrives. The following peaks indicate the arrival times of train of waves reflected at the upstream flume wall. The value of $\eta \cong 7\%$ shows that a major amount of sediments is retained in experiment B03 with a non-dimensional obstacle height of $H_m = h_m/h_1 \approx 2.2$ and an upstream densimetric Froude number of $Fr_d = 0.92$. This corresponds quite well with the simple analytical shallow-water considerations of Section 2.2, which lead to a complete blocking (0%).

In the case of a supercritical approach flow as in experiment B05 with inclined bottom, the sediment flux keeps fluctuating. As can be seen on Fig. 6.11(b), η starts at 50% and increases up to 80%. This transient phenomena was also observed in the physical experiments where waves were passing over the obstacle, creating an oscillatory change in sediment flux. In the case of an inclined bottom, the analytical shallow-water consideration based on a horizontal bottom gives considerably lower values of η than the ones computed (η only approximately 30%). This discrepancy might be primarily due to the inclined bottom.

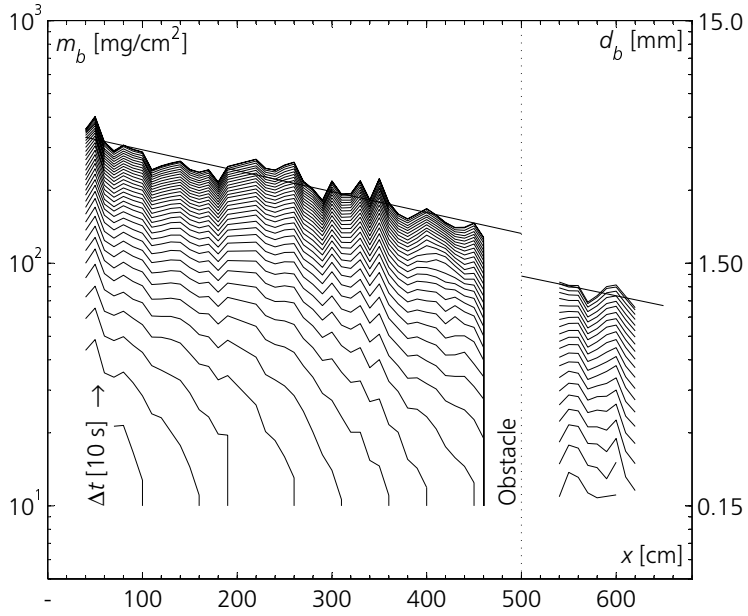

(a) Measured evolution of deposition.

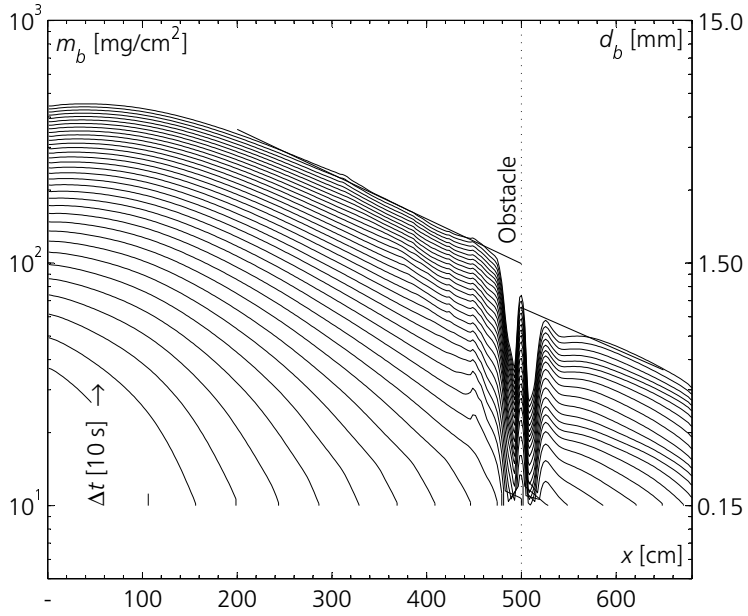

(b) Computed evolution of deposition.

Figure 6.10: Comparison of measured and computed evolution of the sediment deposition in experiment B05 with an obstacle.

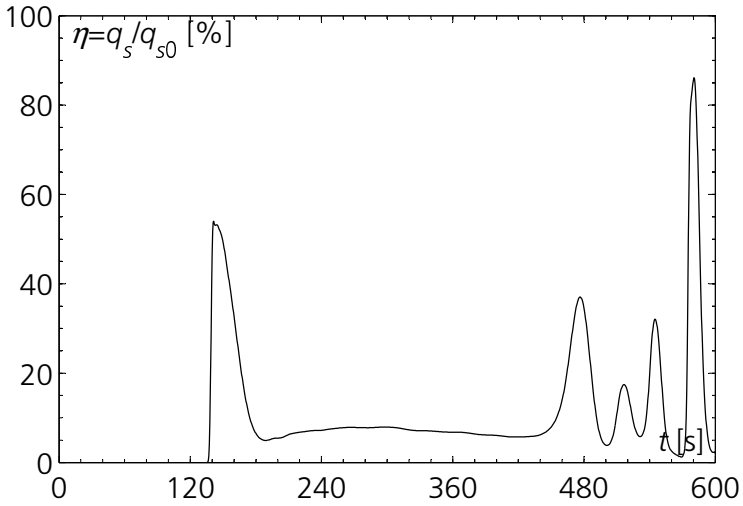

(a) Experiment B03. S=0.00%.

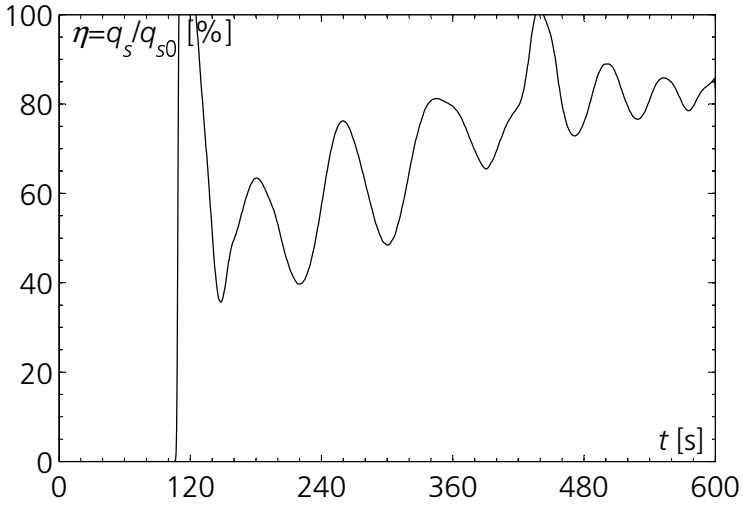

(b) Experiment B05. S=4.64%.

Figure 6.11: Ratio of the sediment flux passing over the obstacle crest, q_s, to the sediment flux passing through the same cross-section without the obstacle, q_{s0}.

6.3 Flow Through a Screen

In this section the experiments of a turbidity current flow through a screen presented in Section 4.3 are compared with the predictions from the adapted numerical model, which was described in Subsection 5.6.3. Two experiments (C03 and C04) were simulated, and some of the results are presented here. The complete simulation results can be found in Appendix B.3 on page 279.

As for the obstacle, the computed velocity profiles were compared with the experimental results as shown in Appendix B.3. Generally, the profiles were in fair agreement with the measured profiles. The integral scale values from the computed velocity profiles were compared with the measured values. In the profiles downstream of the screen, the velocity is strongly reduced, the height increased and the concentration decreased. The numerical model systematically underestimates the height downstream of the screen. This might be due to the fact, that the numerical model does not take into account correctly the generation of turbulence due to the flow through the screen.

For experiment C04 with horizontal bottom, the computed Richardson number was approximately 1.25 upstream of the screen, and it increased to 1.99 downstream of the screen. The experiment with inclined bottom (C03) had a Richardson number of 0.46 upstream and 0.64 downstream of the screen. This shows well that energy of the flow is dissipated due to the resistance of the screen.

A detailed calculation of the flow through a screen for experiments C03 with an inclined bottom is shown in Fig. 6.12 with a time interval is 20 s. To visualize the flow the isolines of the volumetric concentration were plotted similar to the simulations for an obstacle. It can be seen that the reflected bore has a similar form as for the obstacle. The seeping flow through the screen and the downwards flow behind the screen are well reproduced. The other simulation with a horizontal bottom (experiment C04) showed the same undular bore travelling upstream as for the same experiment with an obstacle (experiment B03).

The comparison of the computed front velocities of the turbidity current upstream and downstream of the screen as well as the propagation velocity of the reflected bore with the measurements for the experiments C03 and C04 are shown in Table 6.3. The results show that the front velocities agree well with the measured values and that the propagation velocity of the reflected bore is satisfactorily predicted. In experiment C03 with the inclined bottom the velocity of the bore is overestimated by 32%.

The deposition along the flume in the numerical simulation was obtained as for the obstacle. Fig. 6.13 shows the measured and computed evolution of the deposition for experiment C04. The comparison for the experiment C03 can be found in Appendix B.3 on page 279. The comparison in Fig. 6.13 of experiment C04 shows again that the evolution is reproduced with good agreement. The numerical model predicts a slightly thicker deposition than

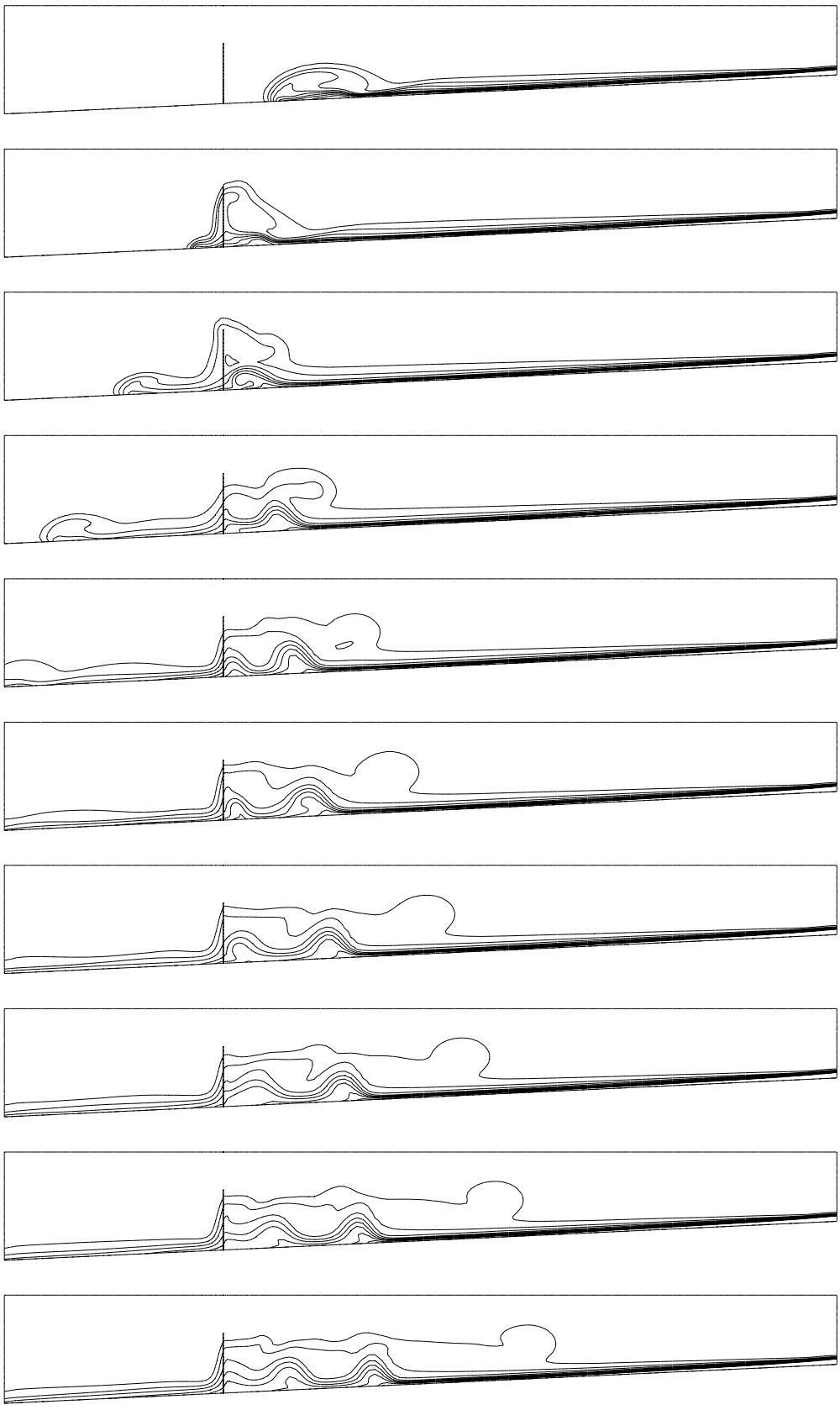

Figure 6.12: Concentration isolines in time intervals of 20 s of the computed turbidity current flow through a screen (experiment C03). The different isolines are plotted in intervals of $\Delta\rho$ =0.1 g/l.

Exp [–]	U_{f1meas} [cm/s]	U_{f1calc} [cm/s]	U_{f2meas} [cm/s]	U_{f2calc} [cm/s]	U_{fbmeas} [cm/s]	U_{fbcalc} [cm/s]
C03	4.71	4.60 (−2)	3.17	3.02 (−5)	-1.20	-1.58 (+32)
C04	3.16	3.31 (+5)	1.93	1.83 (−5)	-0.93	-0.86 (−8)

Table 6.3: Comparison of measured and computed front velocities of experiments with a screen with in parenthesis the relative percentage differences.

was measured in the region just after the inflow, but the difference in deposition upstream and downstream of the screen agrees well with the measurements. In experiment C03, the results with the numerical model underestimate the deposition downstream of the screen indicating that in the numerical computation less sediments pass through the screen than in the experiments.

As a measure of the blocking effect, the ratio of the sediment flux passing through the screen to the sediment flux passing through the cross-section without the screen is again used. Fig. 6.14 shows the evolution of this ratio, η, as a function of time for experiments C04 and C03. The first peak clearly indicates the passage of the head in both experiments. For experiment C04 with horizontal bottom and subcritical approach flow the passing sediment flux starts at 30% and increases almost linearly to 50% before the bore reflected from the upstream wall returns to the screen.

In contrast to the supercritical experiment with an obstacle, there exists a smooth increase of η from 40% to 70% for the supercritical experiment C03. This is interesting as the oscillatory change of sediment flux as found in the flow over an obstacle is smoothed by the presence of the screen. Furthermore, the results of the shallow-water analysis, that for a given porosity, the passing flow through a screen is less sensitive to the Richardson number of the approaching flow compared with the flow over an obstacle, are confirmed.

The reason for the linear increase with time of the sediment flux passing through the screen may be explained by the constrained geometry of the flume. In fact the upstream region slowly fills up until a steady state with a horizontal level upstream of the screen or obstacle exists, as was shown in Fig. 4.8 on page 78. The retention volume behind the obstacle or screen is smaller in the configuration with an inclined bottom and the sediment flux passing through increases faster in these experiments (C02 and B05).

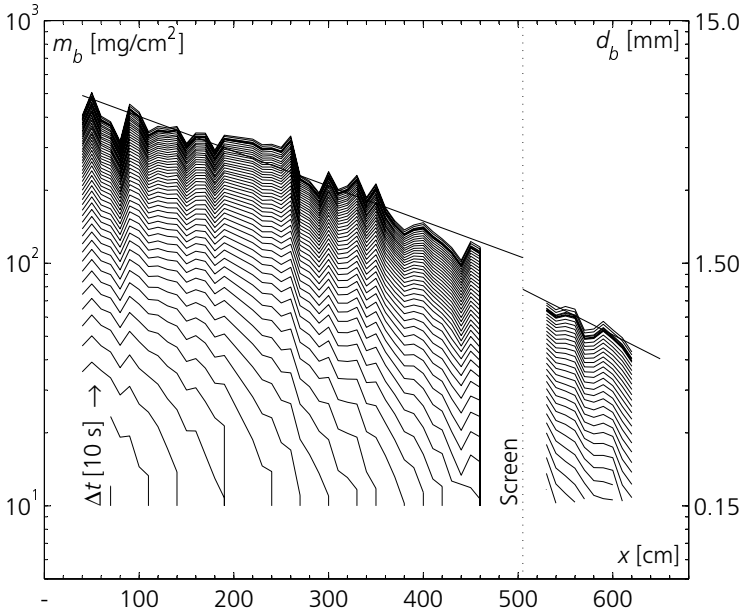

(a) Measured evolution of deposition.

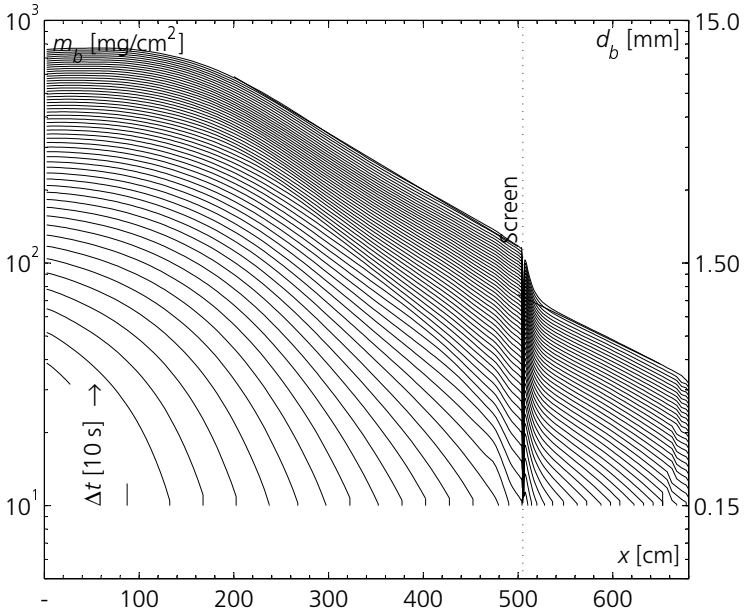

(b) Computed evolution of deposition.

Figure 6.13: Comparison of measured and computed evolution of the sediment deposition in experiment C04 with a screen.

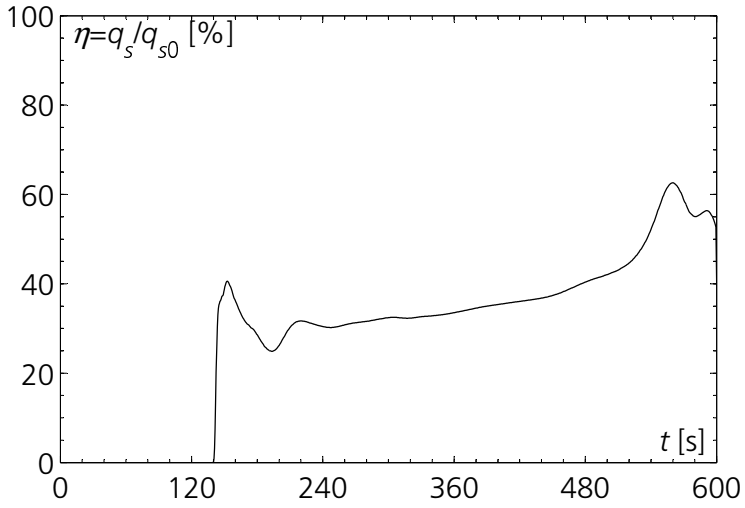

(a) Experiment C04. S=0.00%.

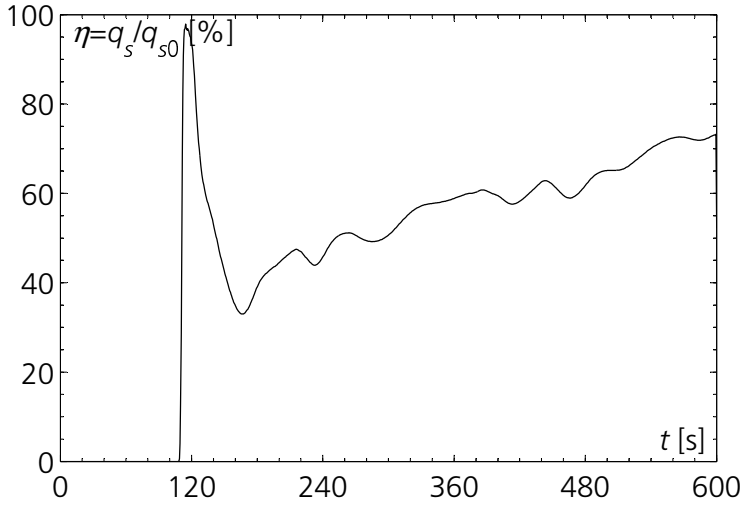

(b) Experiment C03. S=4.64%.

Figure 6.14: Ratio of the sediment flux passing through the screen, q_s, to the sediment flux passing through the same cross-section without the screen, q_{s0}.

6.4 Flow Across a Diffuser

In this section the experiments of a turbidity current flowing across a vertical or inclined multiport diffuser presented in Section 4.4 are compared with the predictions from the numerical model, which was described in Subsection 5.6.4. Two experiments of both a vertical diffuser (D02 and D04) and a 45°-inclined diffuser (E01 and E03) were simulated. The complete simulation results can be found in Appendix B.4 on page 289.

As for the obstacle, the computed velocity profiles were compared with the experimental results as shown in Appendix B.4. For the experiments with an inclined bottom, the profiles upstream of the jet showed good agreement for both configurations (vertical and inclined diffuser). For the experiments with horizontal bottom instead the agreement was less satisfactory, because the velocity was underestimated by more than 20%. In general, the differences between the measured and computed profiles downstream of the jet were higher than for the other simulated configurations. This is not surprising, because the flow measurements clearly showed that there is no "steady" state. Therefore the averaged profiles of the measurements and the computations depend strongly on the averaging time frame. Nevertheless, the integral scale values from the computed velocity profiles were compared to the measured values and it can be stated, that in the profiles downstream of the diffuser, the velocity is reduced, the height increased and the concentration lowered.

For experiments D02 and E03 with a horizontal bottom, the computed Richardson numbers upstream of the diffuser, before any disturbance from the jet occurred, were approximately 1.3 and 1.8, respectively. These values decreased to 0.9 and 1.2, respectively, downstream of the diffuser. Both experiments with inclined bottom (D04 and E01) had a Richardson number of 0.45 upstream of the diffuser, which changed only slightly to 0.49 and 0.40, respectively downstream of the diffuser.

In the following the simulation of the vertical and inclined diffuser is discussed separately, because the flow behavior is quite different. In the experiments with a vertical diffuser no reflected bore could be observed. Therefore, only the computed propagation velocities of the turbidity current front upstream and downstream of the jet diffuser were compared with experimental results. Table 6.4 shows the measured and computed values for the two experiments with the relative percentage differences. The results show that the front velocities upstream and downstream of the screen agree well with the measured values for experiment D02, but for experiment D04 with the inclined bottom the front velocity after the jet diffuser is overestimated by 14%. It is somehow surprising that the front velocity in experiment D02 was correct, as a considerable difference between the computed and measured velocity profiles exists. Maybe the inclination angle of the UVP transducer was not correct, which can cause an important error on the measured velocity profile and its integral velocity. The fact that the error in the integral height,

Exp [–]	U_{f1meas} [cm/s]	U_{f1calc} [cm/s]	U_{f2meas} [cm/s]	U_{f2calc} [cm/s]
D02	3.79	3.68 (−3)	2.72	2.62 (−4)
D04	4.69	4.73 (+1)	3.44	3.92 (+14)

Table 6.4: Comparison of measured and computed front velocities of experiments with a vertical jet with in parenthesis the relative percentage differences.

which is not influenced by the inclination of the transducer, is much smaller further supports this argument.

A detailed calculation of the flow across the vertical diffuser for experiments D02 with a horizontal bottom is shown in Fig. 6.15 with a time interval of 20 s. To visualize the jet in the numerical simulation a passive tracer was introduced, the color intensity of which represents its concentration. In the first plot the fully developed jet can be seen, which is deflected downstream due to the uniform cross-flow. To visualize the turbidity current flow the isolines of the volumetric concentration were plotted again. It can be seen that the jet is completely captured within the turbidity current and convected downstream, like in the physical experiments. It is interesting to note that a small effect on the upstream flow can be observed, because the approaching flow conditions were subcritical. This effect disappeared in the computation with the inclined bottom, where no effect on the flow upstream of the diffuser could be found, which is normal for supercritical flow conditions.

The comparison of the measured and computed evolution of deposits along the flume for experiment D02 is shown in Fig. 6.16. The comparison for the computed experiment D04 can be found in Appendix B.4 on page 289. The comparison shows that the evolution is reproduced with good agreement. This is very interesting because firstly, it shows also that the vertical diffuser has an influence on the downstream deposition and secondly, it confirms that the deposition measuring technique was not influenced by the jets. The examination of the computed concentration profiles shows that the concentration at the bottom is significantly reduced in the profile downstream of the jet, whereas the height of the concentration increased. This confirms the argument that the concentration distribution is influenced by the vertical jet and that deposition is reduced just downstream of the diffuser.

As a measure of efficiency, the ratio of the sediment flux passing the cross-section of the vertical jet to the sediment flux passing through the same cross-section without the jet is again determined. Fig. 6.17 shows the evolution of this ratio, η, as a function of time for the experiment D02 with a horizontal bottom. The first peak clearly indicates the passage of the head, then the passing sediment flux starts at 80% and increases almost linearly to reach 95%. This high value is explained by the small retention volume as can be seen on the last plot of Fig. 6.15. For the experiment D04 with a supercritical

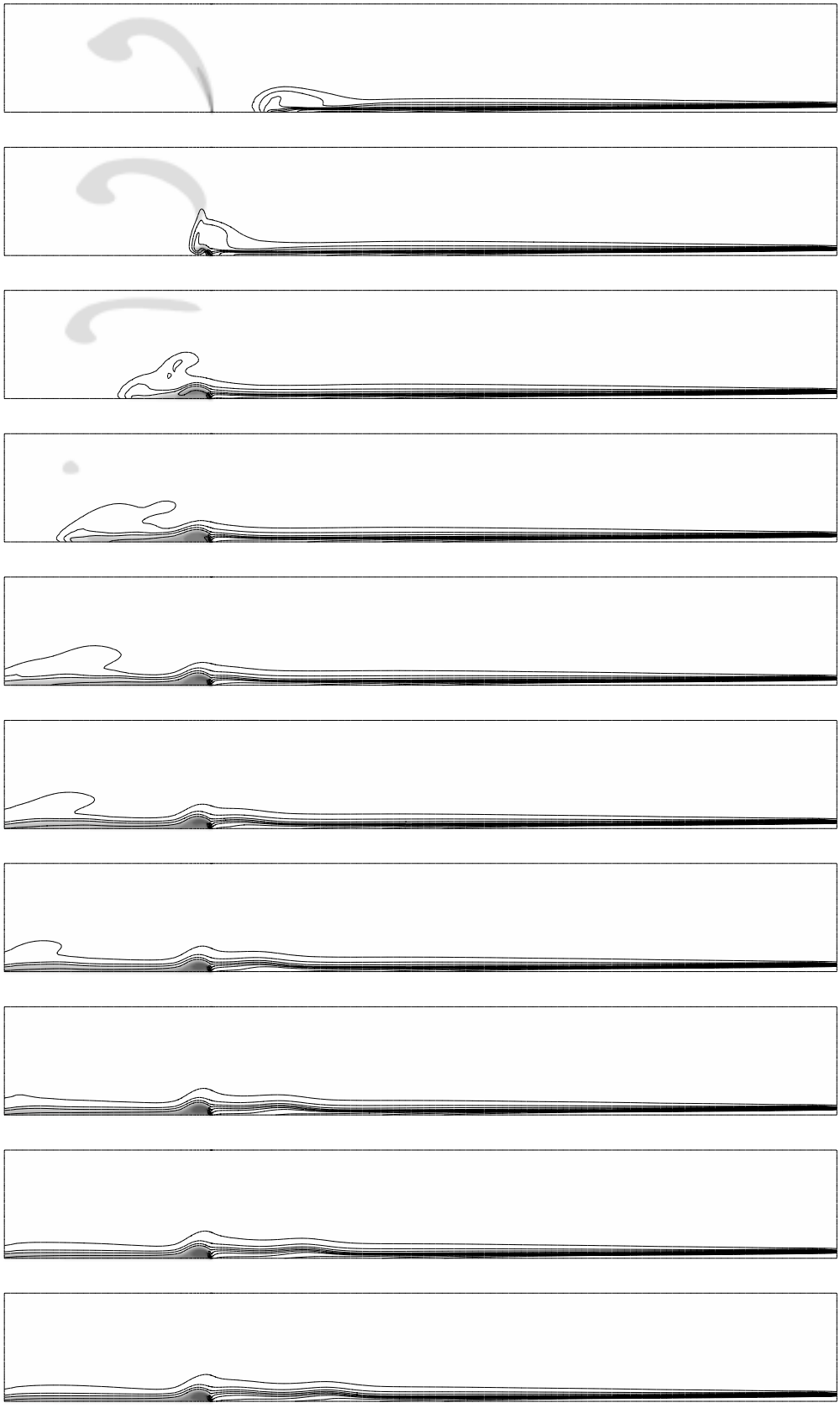

Figure 6.15: Concentration isolines in time intervals of 20 s of the turbidity current flow across a vertical diffuser (experiment D02). The different isolines are plotted in intervals of $\Delta\rho$ =0.1 g/l.

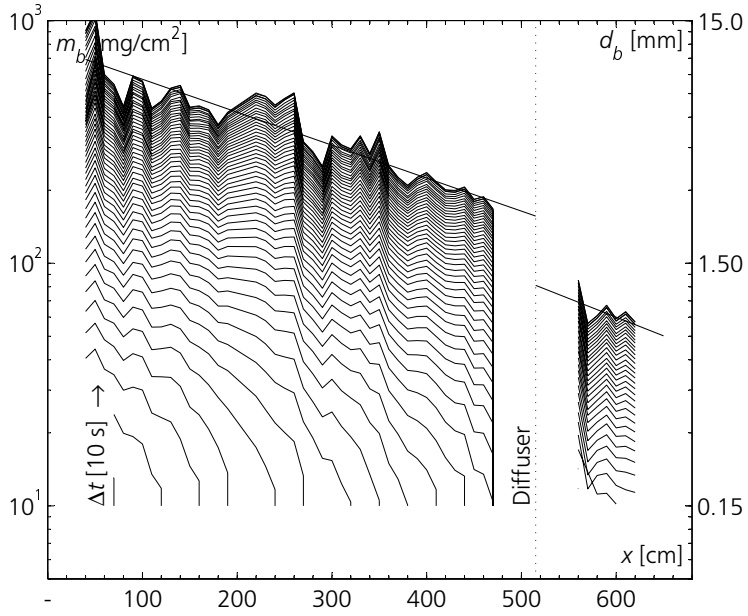

(a) Measured evolution of deposition.

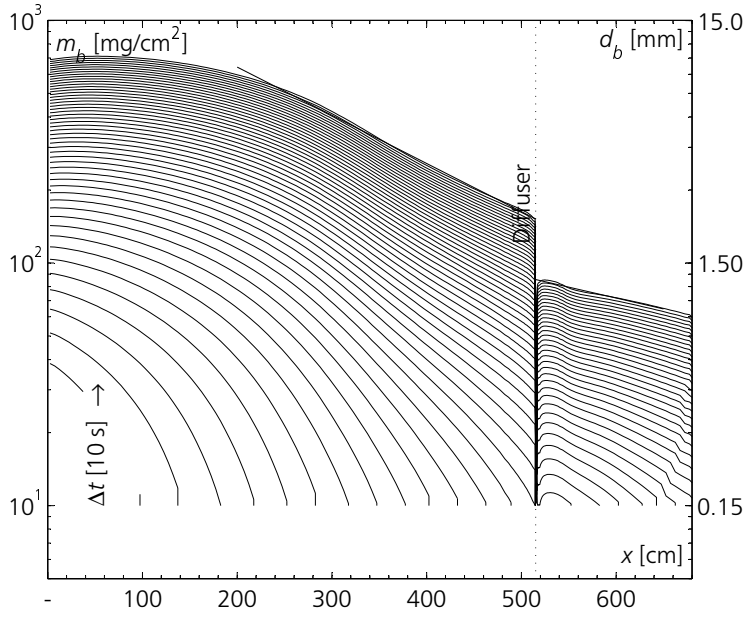

(b) Computed evolution of deposition.

Figure 6.16: Comparison of measured and computed evolution of the sediment deposition in experiment D02 with a vertical jet.

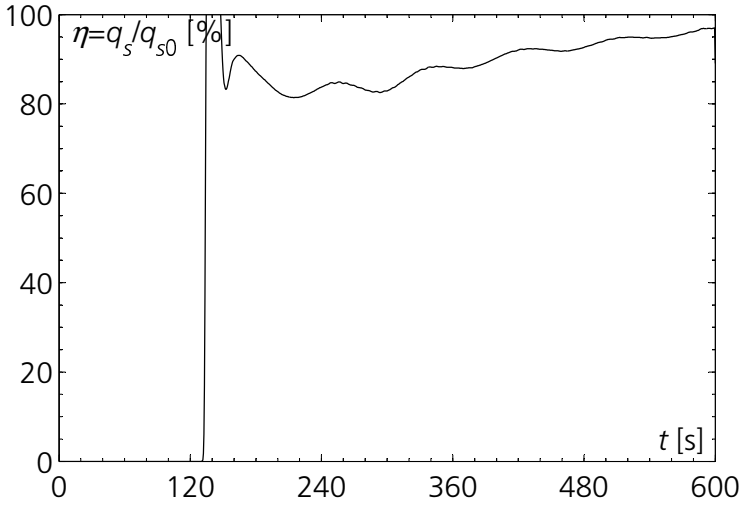

Figure 6.17: Ratio of the sediment flux passing through the cross-section of the vertical jet, q_s, to the sediment flux passing at the same cross-section without the diffuser, q_{s0} for experiment D02 (S=0.00%).

approach flow no effect on the sediment flux existed ($\eta = 100\%$), which further confirms that the difference in deposition thickness upstream and downstream of the jet is due to a change of the sediment concentration distribution within the turbidity current.

In contrast to the vertical jet, a reflected bore was present in the experiments with an inclined jet. This reflected bore can also be seen in the calculation of the flow through the inclined jet for experiment E01 with an inclined bottom as shown in Fig. 6.18 for a time interval of 20 s. In the first plot the fully developed jet can be seen again, which is deflected downstream due to the uniform cross-flow.

It can be seen that the injected momentum of the jet acts as a resistance to the flow and a change in discharge occurs, which generates a bore propagating upstream. The tracer of the jet stays within the turbidity current and is convected downstream. In the simulation with horizontal bottom, the approaching flow was subcritical and some of the tracer travelled upstream within the reflected bore. This phenomena was also observed in the physical experiments. The physical experiments of the turbidity current with the inclined jet showed that their interaction is highly unsteady and oscillatory. This phenomena was also found in the numerical simulations.

The computed front velocities of the turbidity current upstream and downstream of the inclined jet as well as the propagation velocity of the reflected bore for the experiments E01 and E03 were also compared with the experimental results (see Table 6.5). The results show that the front velocities upstream and downstream of the jet diffuser agree well with the measured values for experiment E01, whereas in the experiment E03 with the horizontal

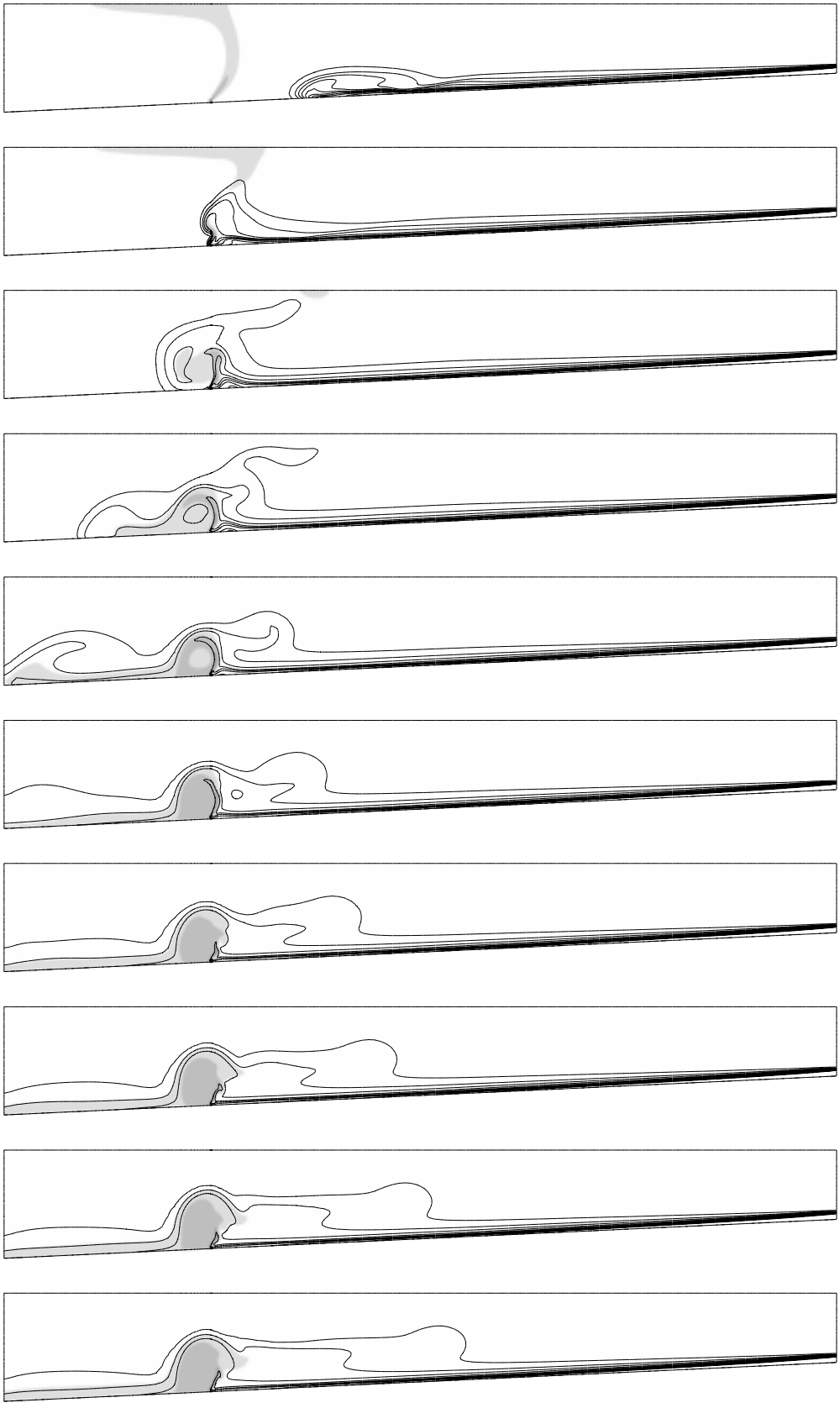

Figure 6.18: Concentration isolines in time intervals of 20 s of the turbidity current flow across an inclined diffuser (experiment E01). The different isolines are plotted in intervals of $\Delta\rho$ =0.1 g/l.

Exp [–]	$U_{f1\text{meas}}$ [cm/s]	$U_{f1\text{calc}}$ [cm/s]	$U_{f2\text{meas}}$ [cm/s]	$U_{f2\text{calc}}$ [cm/s]	$U_{fb\text{meas}}$ [cm/s]	$U_{fb\text{calc}}$ [cm/s]
E01	4.93	4.94 (+0)	3.41	3.30 (−3)	-1.46	-1.40 (−4)
E03	3.64	4.03 (+11)	2.20	1.67 (−24)	n.d.	-1.55

Table 6.5: Comparison of measured and computed front velocities of experiments with an inclined jet with in parenthesis the relative percentage differences.

bottom the front velocity is overestimated upstream and underestimated downstream of the diffuser.

The comparison of the measured and computed evolution of deposition along the flume for experiment E01 is shown in Fig. 6.19. The comparison for the computed experiment E03 can be found in Appendix B.4 on page B.4. The comparison shows that the evolution is reproduced with good agreement. It can be seen that the deposition downstream of the diffuser is significantly reduced and the deposition upstream is increased due to the flow retention. The effect of the change in the concentration distribution downstream of the diffuser as found for the vertical jet might also be present in the experiment with an inclined jet.

The time evolution of the ratio of the sediment flux passing the cross-section of the inclined jet to the sediment flux passing at the same cross-section without the jet is shown in Fig. 6.20. For experiment E03 with a horizontal bottom, the first peak again indicates the passage of the head, then the passing sediment flux has a nearly constant value of only 5% until the reflected waves from the upstream wall return. The passing sediment flux then changes from 5% to 100% and back to 5% at the passage of every wave. This effect is clearly due to the limited length of the flume. It is interesting to note that the sediment flux passing through is reduced drastically before the arrival of the waves.

For the experiment E01 with a supercritical approach flow no such reflection of waves from the upstream wall exists. The passing sediment flux starts at approximately 65% after the passage of the head and increases linearly to 100% due to the limited retention volume as shown Fig. 6.21. The oscillatory motion in the region of the jet can also be recognized in the oscillatory increase of the sediment flux passing through. The period of this motion is approximately 25 s.

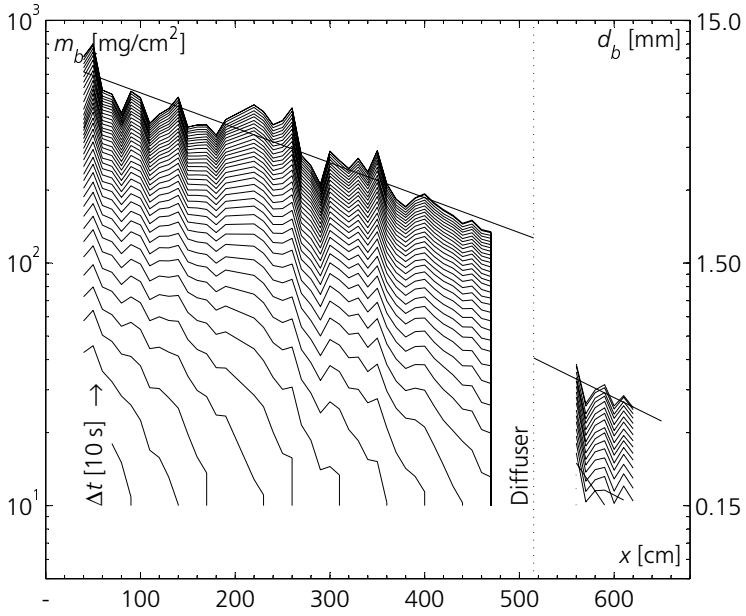

(a) Measured evolution of deposition.

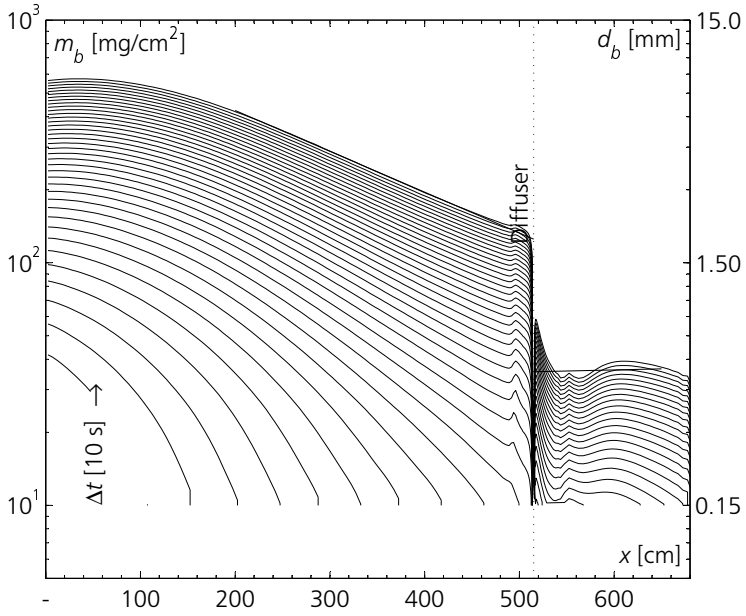

(b) Computed evolution of deposition.

Figure 6.19: Comparison of measured and computed evolution of the sediment deposition in experiment E01 with an inclined jet.

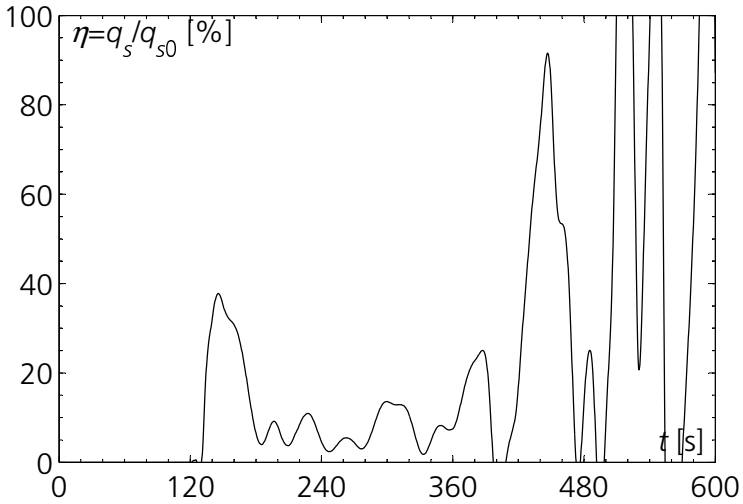

(a) Experiment E03. S=0.00%.

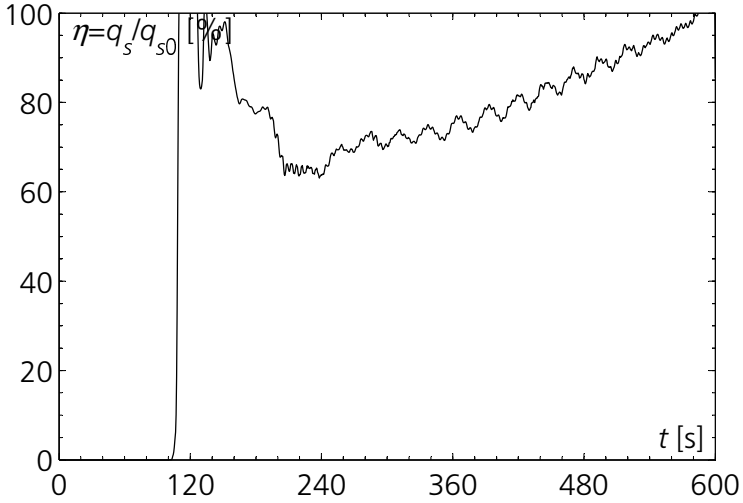

(b) Experiment E01. S=4.64%.

Figure 6.20: Ratio of the sediment flux passing at the cross-section of the inclined diffuser, q_s, to the sediment flux passing at the same cross-section without the diffuser, q_{s0}.

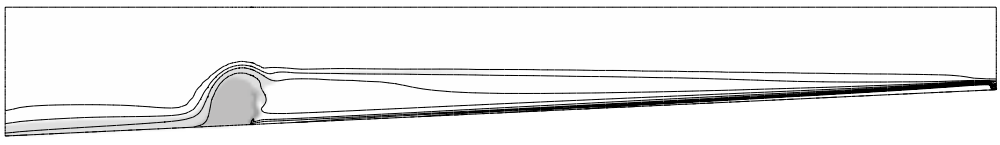

Figure 6.21: Concentration isolines at time t=600 s of the turbidity current flow across an inclined diffuser (experiment E01).

6.5 Conclusions

The comparison of the numerical simulations of the turbidity current with the measured velocity profiles and front velocities shows good agreement. The evolution of the deposits, using three grain sizes and the deposition-erosion approach proposed by Parker et al. (1987) and Garcia and Parker (1993) is also well reproduced.

The flow of a turbidity current over an obstacle is simulated satisfactorily for subcritical as well as supercritical approaching flow conditions. The visualization of the reflected bores by means of isolines of concentration and velocity vectors, shows a different flow behavior of weak and strong bores similar to the observations in the physical experiments. It is observed that in the case of a subcritical turbidity current, the streamwise velocity is reduced quite uniformly over the depth in the region between the obstacle and the undular bore. Furthermore, orbital motions within the bores, as measured and described by Kneller et al. (1997) are also reproduced. For the supercritical flow, the reflected bore forms a front flowing back on top of the body of the approaching turbidity current. Upstream of the obstacle a dead zone develops, which the approaching current is overflowing in an undular motion up to the obstacle crest. These results further confirm the conclusion that in the case of a supercritical turbidity current, a major part of its body continues to flow over the obstacle.

To measure the blocking effect of the obstacle a ratio, η is defined as the proportion of the sediment flux passing the obstacle crest compared to the sediment flux passing at the same cross-section without the obstacle. For the subcritical flow almost complete blocking occurs until the waves propagating upstream return due to the reflection from the upper end of the flume. This result corresponds quite well with the analytical shallow-water considerations. In the case of the supercritical approach flow, the evolution of the passing sediment flux is oscillatory increasing from 50% up to 80%. This transient phenomena was also observed on the video recordings of the experiments. An explanation may be that internal waves originating at the front of the bore are propagating downstream.

The simulations of the turbidity current flowing through a screen are carried out by modelling the screen as a thin porous region with a certain resistance force (drag force). The predictions of the flow agree fairly well with the measurements. In particular, the difference in the evolution of the deposits upstream and downstream of the screen is well reproduced. The simulated geotextile was quite permeable, therefore, values of η increasing with time from 30% to 50% for the subcritical and from 40% to 70% for the supercritical flow are calculated. The linear increase of the passing sediment flux is explained by the constrained geometry of the upstream region of the flume, which is slowly filled up. It is found that the oscillatory change in sediment flux found in the flow over an obstacle is smoothed by the presence of the screen. The

computations also confirm the results of the shallow-water analysis, that for a given porosity, the passing flow through a screen is less sensitive to the approaching flow conditions compared to the flow over an obstacle.

To simulate the experiments with vertical and inclined jets, a special treatment for the jet source is necessary. The injection of the discharge through a wider slot with the additional momentum being introduced in the cells above, give reasonable results for the prediction of the jet flow. The simulations of the turbidity current flowing across a vertical diffuser are satisfactorily compared with the experimental results. These simulations confirm that in the case of a supercritical turbidity current no blocking effect on the passing sediment flux as well as no influence on the upstream flow occurs. On the other hand, the computed evolution of the deposits showed a significant effect on the deposition rate downstream of the jet, similar to the experimental measurements. Therefore, it is concluded, that due to the injection of the vertical momentum, the distribution of the sediment concentration within the turbidity current is modified, and the near-bed concentration as well as the deposition rate are reduced over a certain distance downstream of the jet.

The complicated interaction of the inclined jet with the turbidity current is simulated satisfactorily. The comparison of the computed and measured evolution of deposits shows very good agreement, and confirms the blocking and dilution effect due to the injected water. For the subcritical approaching flow only 5% of the sediment flux passes the jet until the reflected waves from the upstream wall return. For the simulation with a supercritical approach flow, η changes with time in an oscillatory increase from 65% to 100%, as the retention volume is filled up.

The simulations clearly show that the turbidity current flow over an obstacle, through a screen and across a jet can be modelled numerically with good agreement to the experimental data. Furthermore, the numerical simulation proofs a good help to investigate the blocking effect of the various experimental configurations.

7 Case Study of Submerged Dams in Lake Grimsel

7.1 Generalities

In Lake Grimsel, in Switzerland, an ongoing design project consists of heightening the two existing dams by 23 m (Spitallamm Arch Dam 114 m; Seeuferegg Gravity Dam 42 m). The excavation and demolition works necessary for the planned heightening generate approximately 150'000 m^3 of rock material. This large amount of materials has to be stocked somewhere near the construction site. This led to the idea of building some kind of obstacle in the form of a submerged embankment dam to prevent sediment deposition due to the turbidity currents in the area near the intake structures. A case study is, therefore, presented to investigate the occurrence and impact of turbidity currents on the reservoir sedimentation and to check the efficiency of such submerged obstacles to retain the sediments (see also (Oehy and Schleiss, 2001b; Oehy and Schleiss, 2002).

Based on bathymetric measurements of the reservoir and on the initial, topographical map of the valley, the physical domain was discretized using a body-fitted, non-orthogonal, structured grid. The shoreline has no direct effect on the behavior of the turbidity current, flowing only at the bottom of the lake. The reservoir geometry was, therefore, slightly simplified to get a topologically rectangular physical space. The grid consisted of 250 cells in the streamwise direction, 30 in the lateral, and 20 cells in the vertical directions, resulting in a total number of 150'000 cells. The cells had a mean horizontal mesh size of about 25 by 25 m^2 and in the vertical direction the cell height was growing in size in a geometrical progression from 0.3 m at the bottom to 6.0 m at the free surface. The bathymetric map as well as the inflow and outflow locations are shown in Fig. 7.1 and a view of the discretized lake is shown in Fig. 7.4. The reservoir is approximately 5.5 km long and 300 m wide. The depth is regularly increasing from the inflow to the middle of the lake where a hollow upstream of the canyon exists. The intake and bottom outlet structures are located in the deepest area, approximately 90 m deep, downstream of the canyon. To the east of the deepest area, the reservoir bottom increases by more then 50 m to a branch of the lake. The outflow boundary was placed in this branch of the lake where no turbidity current flow could occur.

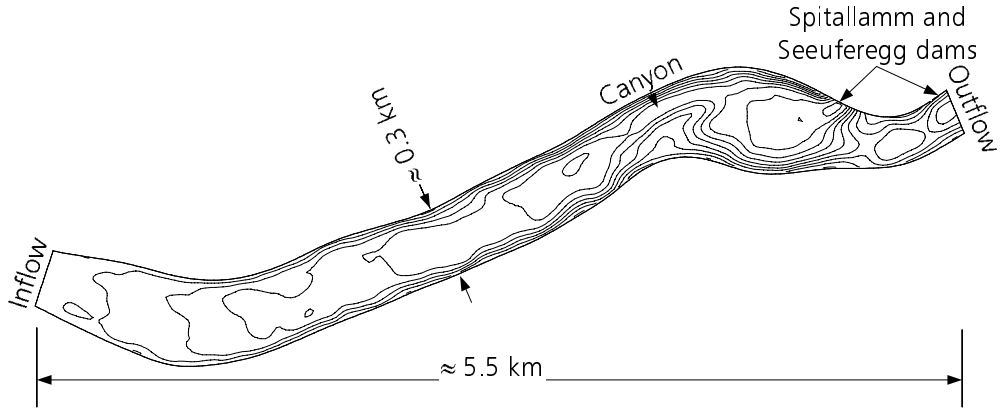

Figure 7.1: Bathymetric map of Lake Grimsel with locations of inflow and outflow boundaries.

At the river mouth a uniform spatial distribution was chosen for the inflowing boundary conditions of velocity and concentration. By the examination of floods in mountainous regions, Hager (1984) suggested a hydrograph in the form of an asymmetrical bell corresponding to the statistical distribution of Maxwell, a simple relationship entirely defined by three parameters as

$$Q(t) = Q_p \left[\frac{t}{t_p} e^{\left(1 - \frac{t}{t_p}\right)} \right]^n \tag{7.1}$$

where Q is the inflow discharge as a function of time, Q_p is the peak discharge, t is time, t_p is the time to peak and n is a form factor ($n \geqslant 2$). The determination of these parameters was based on a back-calculation of the river inflow from measured reservoir water-level fluctuations and turbined water volumes during a flood event in October 2000 as shown in Fig. 7.2. The time to peak and the peak discharge were taken from the back-calculated river inflow, whereas the form factor was determined in order to get the same inflow volume. As can be seen in Fig. 7.2, the flood event lasted over more than three days with a peak discharge of approximately $40\,\mathrm{m}^3/\mathrm{s}$.

It is commonly accepted that during flood events high suspended sediment concentrations can occur in Alpine rivers. De Cesare (1998) analyzed concentration measurements in an Alpine river during a whole summer and recorded several times values of more than $15\,\mathrm{g/l}$. In Lake Grimsel no measurements for the concentration at the inflow were available, therefore it was assumed that the concentration evolution is proportional to the discharge and that the peak concentration had a value of $15\,\mathrm{g/l}$.

Because no stratification due to temperature difference is present in the Alpine lake, the clear water density was assumed constant in the whole reservoir. At the water surface, the rigid-lid assumption was adopted, which implies that the free water surface is fixed to a given level. This assumption was justified as the water level in the deep lake changed only slightly (2–4 m) during the simulation period.

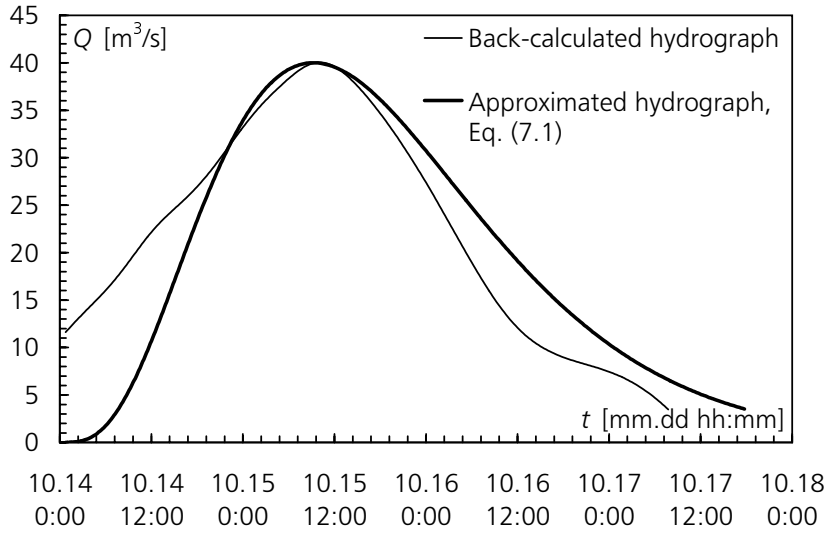

Figure 7.2: Back-calculated and approximated hydrograph of the river inflow in Lake Grimsel during the flood event in October 2000 with a peak discharge of 40 m^3/s.

For the numerical simulation the model presented in Chapter 5 was used. A single transport equation was solved for the median grain-size diameter of d_{50}=40 mm, determined from field samples. The erosion-deposition source and sink terms at the bottom of the reservoir are introduced through the erosion-deposition model proposed by Van Rijn (1984a) which was described in Section 5.3.

Along the bottom and the walls, a log-law velocity distribution was applied changing continuously from smooth to rough wall conditions as proposed by Wu et al. (2000) and described in Subsection 5.4.3. It was assumed that no additional roughness due to bed forms exists at the bottom, because no measurements or data were available.

It is commonly accepted that in large-scale simulations the turbulence model k-ε needs modification to take into account the stratification. Olsen and Tesaker (1995) used a modified turbulent viscosity depending on the local Richardson number combined with the standard k-ε turbulence model to model turbidity currents in a reservoir. Rodi (1987) gives a good review of examples of calculation methods for flow and mixing in stratified flows. Here, the buoyancy extension of the standard k-ε model proposed by Burchard and Petersen (1999) was included to properly account for these additional effects of stratification (see also Subsection 5.2.1).

To get reasonable computation times for the flood event, a time step of 60 s was chosen, which resulted in CPU times of 40–45 hours on a DEC alpha station.

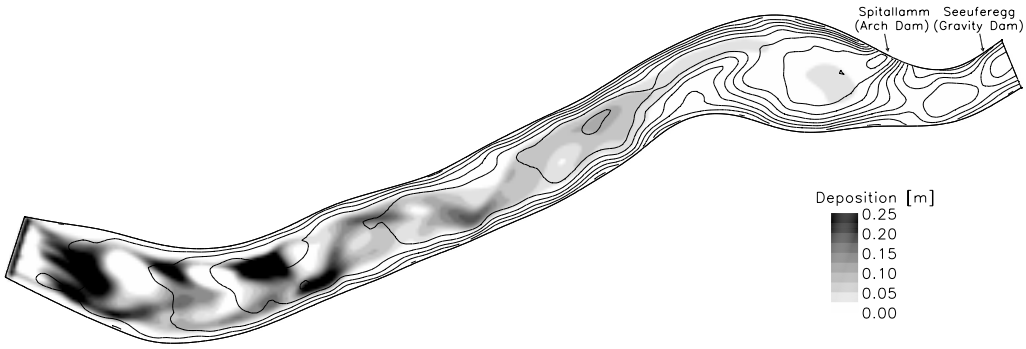

Figure 7.3: Deposition after the flood in October 2000 with deposits in the area of the intake and bottom outlet structures.

7.2 Turbidity Current Simulation of Flood Event in October 2000

The results of the high flood event occurring in October 2000 revealed that a turbidity current develops and propagates to the deepest area of Lake Grimsel close to the dam. During such an event considerable sediment deposits are created in the area of the intake and bottom outlet structures as shown in Fig. 7.3 where the deposition at the end of the flood event are represented. The elevation contour lines are also represented to emphasize the topographical features of the lake such as the canyon to the lower part of the lake.

The complete propagation of the flow in the reservoir is presented in the figures of Appendix C in 4 hours time-steps during the 100 hours run. In these figures the deposition evolution is shown combined with the concentration contour line of 1 g/l suspended sediments. It can be seen that the canyon with the negative slope causes a slowing down of the current and deposition takes place upstream of this place. After passing the ridge the current accelerates again and finally dies out in the deepest area of the lake with maximum deposit heights of approximately 0.10 m. It can also be noted how the turbidity current develops with increasing sediment and water discharge. After the peak the driving force of the current decreases and the turbidity current starts to die out until it finally disappears after 84 hours.

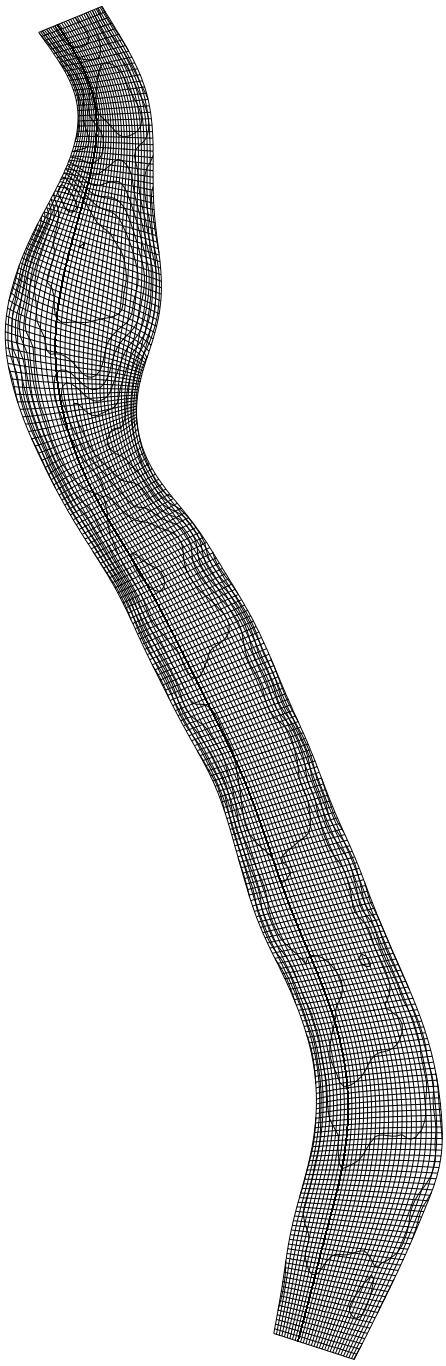

Figure 7.4: Top view of the discretized reservoir with the slice presented in Fig. 7.5 (black thick line in longitudinal direction).

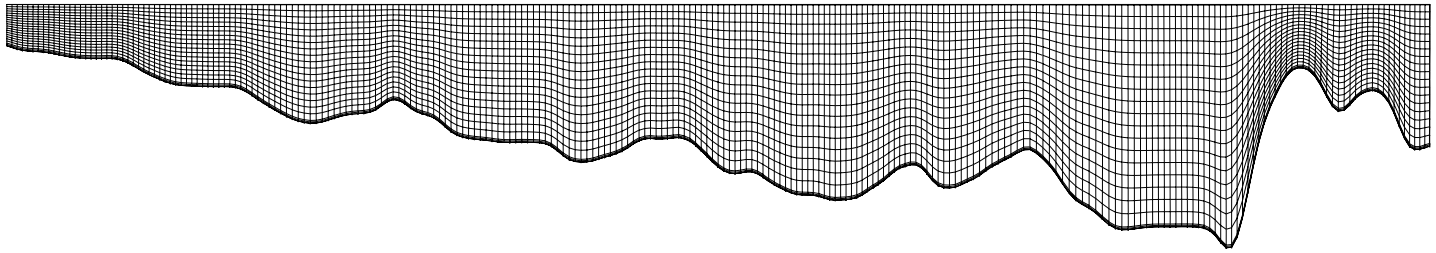

(a) Vertical and longitudinal discretisation.

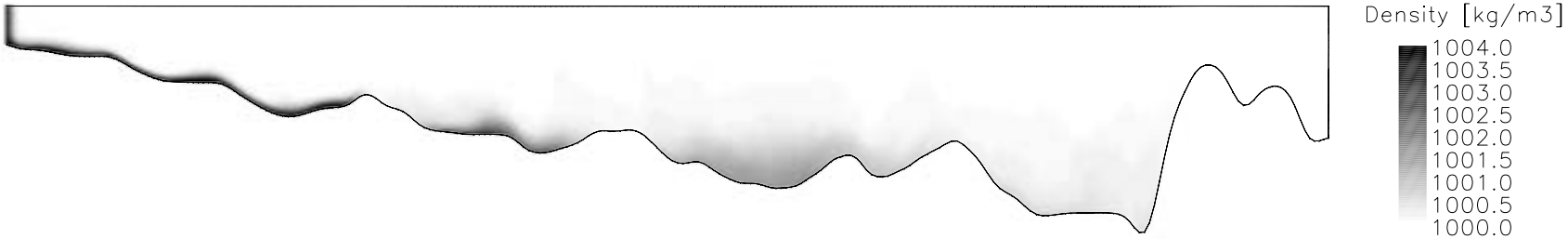

(b) Density field at peak discharge of 40 m^3/s after 36 hours.

Figure 7.5: Slice shown in Fig. 7.4 over the complex topography of Lake Grimsel.

To illustrate the complex topography of the reservoir, a vertical slice approximately in the longitudinal direction of the thalweg is presented in Fig. 7.5(a). In the vertical discretisation, attention was paid to the bottom cell in that the cell height was kept the same for all bottom cells. This should ensure that during the computation of the near-bed concentration c_{sb} all bottom cells are treated similar. In Fig. 7.5(b), the propagating turbidity current in the reservoir at peak discharge is shown. The intensity of the coloring represents the density of the current where the vertical dimension is 10 times distorted to enhance the readability. It can be noted that the concentration decreases continuously from the inflow at the left-hand side to the deepest are at the right-hand side.

7.3 Turbidity Current Passing Over Submerged Dams

To prevent reservoir sedimentation in the deepest area close to the intake and bottom outlet structures, the efficiency of submerged obstacles was numerically investigated. Two possible configurations for these obstacles were evaluated. The first configuration consisted of a dam, 15 m high and 150 m long, situated upstream of the canyon in a counter-slope of the lake as presented in Fig. 7.6. The second configuration is also shown in Fig. 7.6 and consists of two submerged dams placed in the middle of the lake one after each other in a displaced manner, so that the current needs to turn around or overflow them. In this case, the height of the two dams was 10 m with a length of 210 m each. Both configurations do not extend over the whole width of the valley to keep a free passage for the water flow during emptying of the reservoir. To simulate the obstacle, a thin surface has been introduced in the grid. This surface is assumed to be located between control volumes and allows to set wall boundary conditions on this patch.

In the figures of Appendix D the complete propagation of the flow in the reservoir with the configuration of one submerged dam upstream of the canyon is presented in 4 hours time-steps during the 100 hours run. In these figures the deposition evolution as well as the concentration contour line of 1 g/l suspended sediments are presented. It can be stated that the obstacle clearly blocks the flow and reflects the major part of the turbidity current. A considerable amount of sediment deposits occurs, therefore, upstream of the obstacle. Figs. 7.7(a) and 7.7(b) show the deposition for the two tested obstacle configurations after the same flood event of October 2000, that was presented in Fig. 7.3.

As was described in Sections 4.2 and 6.2, some of the fluid of the turbidity current flows over the obstacle while a bore will be reflected. The same observations were made in the numerical simulation of the flow over

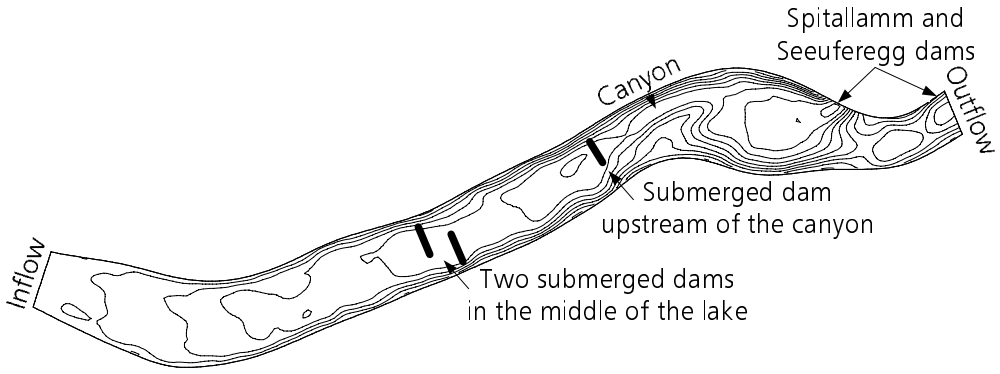

Figure 7.6: Locations of the investigated obstacles: *a)* a submerged dam upstream of the canyon and *b)* two submerged dams in the middle of the lake.

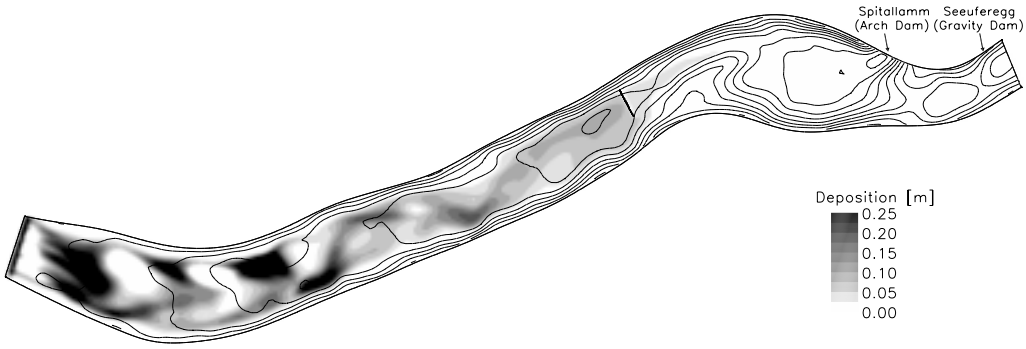

(a) Submerged dam upstream of the canyon (Height: 15 m, Length: 150 m).

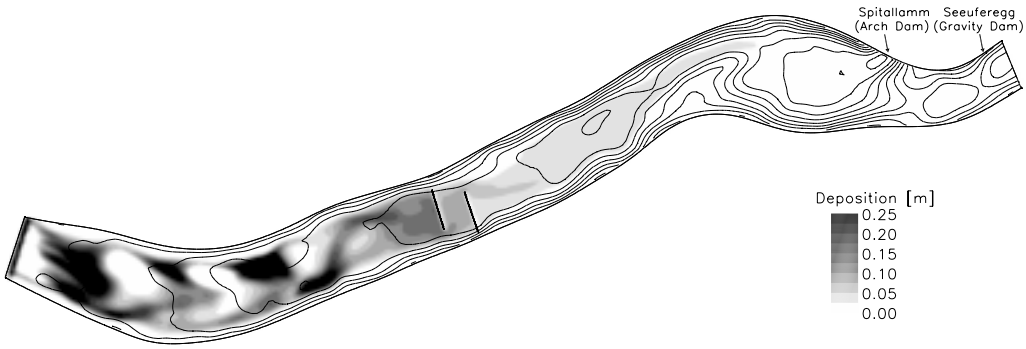

(b) Two submerged dams in the middle of the lake (Heights: 10 m, Lengths: 200 m).

Figure 7.7: Deposition after the flood event in October 2000 with the submerged dams configurations.

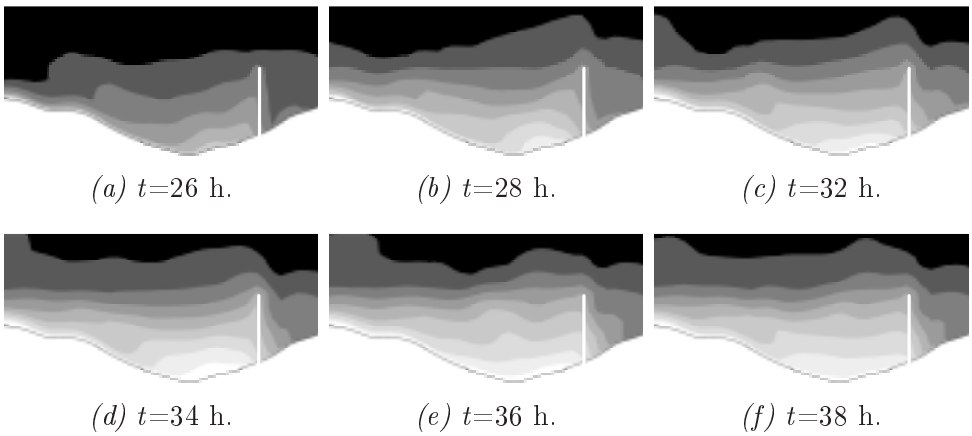

(a) t=26 h. *(b)* t=28 h. *(c)* t=32 h.

(d) t=34 h. *(e)* t=36 h. *(f)* t=38 h.

Figure 7.8: Density plots upstream of the dam (white line) in 2 hours intervals where the vertical dimension is 10 times distorted to enhance readability.

the submerged dams. To illustrate the reflection of the turbidity current upstream of the obstacle a slice located perpendicular to the dam is presented in Figs. 7.8(a) to 7.8(f) for the configuration with one submerged dam (see also Fig. 7.7(a)). It can be seen that bores travel upstream as was observed in the physical experiments and their numerical simulation. The retention volume upstream of the obstacle is slowly filled with the turbid fluid until it starts overtopping. Because the dam does not block the valley completely a small part of the current continues also flowing around the obstacle.

7.4 Conclusions

The turbidity current flow over the complex topography of Lake Grimsel shows that significant amounts of suspended sediments are transported to the deepest area of the reservoir, where they settle down. For a single flood event these deposits attained approximately 10 cm in height.

The effect of an embankment dam, built of demolition and excavation materials from the heightening of the Grimsel dams, was investigated. In agreement with the physical experiments, it is found that the height should at least extend to twice the height of the approaching turbidity current to block the flow efficiently. A height of the dam of 15 m is sufficient and ensures that the elevation of the dam crest is below the minimum operation level of the reservoir. It is estimated that the retention of sediments behind the dam lasts for at least 20 to 50 years.

It can be concluded that the recycling of the demolition and excavation materials to build a submerged embankment dam gives an excellent example to control reservoir sedimentation due to turbidity currents.

8 Recommendations and Concluding Remarks

8.1 Recommendations

In the following paragraphs some recommendations, given as rules of thumb, are presented to illustrate possible applications of the investigated measures to control reservoir sedimentation due to turbidity currents. As an example, the rules are applied to a turbidity current with the characteristics determined from the physical experiments by Froude similarity at the location of the measure. The computed prototype values for a subcritical ($U = 0.21$ m/s) and supercritical ($U = 0.35$ m/s) flow with Richardson numbers of 1.1 and 0.4, respectively, are shown in Table 8.1 with the corresponding scale and model values.

	Model	→	Scale	→	Prototype
U	0.03 m/s / 0.05 m/s	→	$\lambda_U \approx 7$	→	0.21 m/s / 0.35 m/s
h	0.10 m	→	$\lambda_h \approx 100$	→	10 m
$\Delta\rho$	1.0 g/l	→	$\lambda_C \approx 1/2$	→	0.5 g/l
g'	0.01 m/s^2	→	$\lambda_C \approx 1/2$	→	0.005 m/s^2
t	600 s	→	$\lambda_t \approx 14$	→	2 h 20 min

Table 8.1: Up-scaling of subcritical and supercritical turbidity current experiments, where λ_U is the velocity scale, λ_h the length scale, λ_C the concentration scale and λ_t the time scale.

Based on these prototype values the dimensions of the investigated measures are determined in the following paragraphs.

Obstacles. The experiments and simulations showed that obstacles only provide efficient blocking if the approaching flow is subcritical. In this case, a criteria for complete blocking is proposed as follows:

Obstacle height at least equal to twice the turbidity current height

For the prototype application this criteria leads to an obstacle height of 20 m. It is important to note that the retention volume behind the obstacle

needs to be as large as possible to stock a maximum of the turbid water and prevent overtopping. The ideal location to place such an obstacle, is in a zone of a reservoir where the slope is weak or horizontal. As shown in the case study, the obstacle was placed after a hollow in a counter-slope, so that a large retention volume upstream of the obstacle was created.

These obstacles can be built as embankment dams or walls. It is important that they do not extend over the whole width of the valley to keep a free passage for the water flow in case of emptying of the reservoir.

In general, this kind of technical measure might also be useful for the diversion of turbidity currents in areas of a lake, where the deposits do not harm operation of the intake structures. In other cases, where the bottom outlet is remote from the dam and intake structures, the efficiency of flushing through the bottom outlet can be increased by favoring the sediment deposition in their proximity. Or finally, submerged dykes could be used to guide and concentrate the turbidity current in reservoirs, where turbidity current venting is practiced.

Screens. The blocking effect of the permeable screen or geotextile depends mainly on its porosity. The analysis and simulations showed that the efficiency of screens to block turbidity currents is less sensitive to the approaching flow conditions. To obtain a significant blocking effect, a design criteria may be formulated as:

Screen height at least equal to three times the height of the turbidity current with porosities smaller than 30%

At prototype scale this gives a screen or grid of approximately 30 m in height. It is proposed that a mesh size in the order of 10 cm is used to prevent clogging by the sediments. The maximum force on the screen occurs when the turbidity current hits the screen. In the present example, neglecting the porosity at the initial impact, this would lead to a total force on the screen per unit width of approximately 0.7 kN/m for the subcritical flow and 1.5 kN/m for the supercritical current.

Similar to obstacles, such screens might also be used for diversion or to increase the efficiency of flushing through the bottom outlet. It is obvious, that the screens can also be placed on top of obstacles or in series.

Jets. The experiments and simulations showed that a turbidity current can be blocked by means of inclined jets. In the experiments an inclination of 45°was used with a jet discharge 14 times smaller than the turbidity current discharge. For subcritical approaching conditions, the flow can be almost completely blocked if the following criteria holds:

Opposing momentum of jet 50% higher than the momentum of the turbidity current

For a fictive prototype diffuser issuing at 45°over a valley width of 50 m, this would lead to a jet with a discharge per unit width of $0.15\,m^2/s$ and a momentum per unit width of approximately $0.62\,m^3/s^2$. Over the whole width this results in a total discharge of $7.5\,m^3/s$ with an exit jet velocity of approximately 4.2 m/s. This momentum could be introduced, for example, with 10 nozzles distributed every 5 m with a diameter of 0.47 m.

Bubble curtains. Only one representative experiment was made, where the buoyancy flux per unit width of the bubble curtain was 22 times larger than the buoyancy flux of the turbidity current. For the present case, this would lead to a discharge in air per unit width of 23.5 l/s or a total discharge over a width of 50 m of $1.18\,m^3/s$. The power and energy necessary to transport the air to the bottom of the reservoir depends on its depth. But it can easily be seen that an important power is necessary to inject this air down to large depths. Furthermore, due to the compressibility the buoyancy flux is significantly reduced, and even larger discharges are necessary at prototype scale.

Therefore, it can be concluded that bubble curtains cannot be recommended to stop or control turbidity currents in reservoirs. Nevertheless, they may be useful in shallow waters, such as rivers, to stop density intrusions as was reported in the literature. Another possible application of bubble curtains to maintain fine sediments in suspension to prevent their sedimentation and favor their evacuation through the intake structures will need further research.

For the final design, numerical simulations, as presented in Chapter 7, can be a useful help for the project engineers to allow further optimization of dimensions and characteristics of the considered measure.

8.2 Concluding Remarks

This work done on the effects of obstacles, screens and jets is a first step in developing new measures to control or prevent reservoir sedimentation due to turbidity currents. The results show, that turbidity currents can be efficiently blocked with such measures and that the sediments can be successfully retained.

The presented measures may be interesting in combination with other traditional methods, such as flushing or turbidity current venting, but also with new concepts of sediment management in reservoirs by jet-induced density currents (Cantero and Garcia, 2001) or by turbining the sediment-laden water (Schleiss and Oehy, 2002). The various measures might also be of interest for the design stage of a hydro project, where they could be integrated without important, additional costs.

The applications of such measures are not only restrained to turbidity currents, but can be extended to other density-currents related problems, as for example salt water intrusions in rivers. Similar measures may also be applied to problems related to pollutants in stratified surface flows, or in interflows of stratified lakes.

9 Summary and Further Work

9.1 Summary

Several investigations showed that turbidity currents largely contribute to the transport and redistribution of fine sediments inside a reservoir by entraining particles on their way and bringing them to the deeper part of the reservoir where they settle down. After some time the fine sediment deposits can cover the bottom outlets and power intakes, both of which are often located near or at the dam. Therefore, reservoir sediment due to turbidity currents not only reduces water-storage capacity, but it also increases the risks of blockage of bottom outlets and of sediment entrainment into the waterway systems of hydropower schemes.

In the present study the effects of obstacles, screens and jets on the flow and deposits of turbidity currents was analyzed to check their performance to control reservoir sedimentation and to prevent deposition in the area of the most affected structures. The investigations were carried out by means of physical experiments and numerical simulations.

Six series of experiments were carried out within a flume of 7.1 m long, 27.2 cm wide and 90.0 cm high. For each series, experiments on a horizontal bottom and with an inclined slope of 4.64% were performed. To measure the deposits a new device was developed, which recorded their spatial and temporal evolution. The method is based on the resistance measurement of the sediment layer formed by deposition. An accuracy in the order of 0.15 mm was achieved. Furthermore, vertical velocity profiles were measured by means of an ultrasonic velocity profiler (UVP) and the front velocities were determined from video recordings.

The first series consisted of continuously-fed turbidity current experiments, where the similarity collapse of the velocity profiles at different locations confirmed the self-similarity of the turbidity current runs. Constant front velocities were found and a dimensionless ratio of the front velocity to the cubic root of the initial buoyancy flux with an average value of 1.0 for the experiments having an inclined bottom and of 0.8 for a horizontal bottom was determined. The evolution of the deposits was measured and an exponential decrease with distance was observed.

The five other series consisted of experiments with possible measures to block the turbidity current, such as

- an obstacle with a height of 24 cm;
- two vertical screens made of different geotextiles;
- vertical jets issuing from a multiport diffuser;
- inclined jets issuing from a multiport diffuser at 45°upstream; and
- a bubble curtain.

The height of the obstacle was twice the average height of the approaching turbidity current in the case of the horizontal bottom and 2.5 times higher for the inclined bottom. The different geotextiles had porosities in the order of 30%, and a mesh size of 1.2 mm and 0.5 mm, respectively. The discharge ratio of the vertical jets to the turbidity current was between 1/20 and 1/10. The discharge ratio of the inclined jets to the turbidity current was ranging from 1/14 to 1/7, whereas the ratio of the momentum in the streamwise direction varied from 1.1 to 3.3. In the bubble curtain experiment, the ratios of discharge and buoyancy flux between bubble curtain and turbidity current were 1/40 and 22, respectively.

Due to the presence of an obstacle, screen or inclined jets, the flow was reduced and an internal bore travelling upstream occurred. A significant difference in the behavior depending on the approaching flow conditions was observed. For a horizontal bottom, i.e. a subcritical turbidity current, the reflected bores showed a smooth change in depth with a train of internal waves. In the case of the inclined bottom, i.e. a supercritical approaching flow, a strong bore was observed with a front or leading edge moving upstream. Constant front velocities were measured for the oncoming and outgoing turbidity current as well as for the bore in all these experiments. Upstream of the obstacle, screen and inclined jets, the flow velocities were reduced, which increased the deposition rate.

In the experiments of a turbidity current flowing across a vertical diffuser, an effect of the jets on the upstream flow could only be observed for one subcritical experiment with a ratio between the streamwise momentum of the current and the injected vertical momentum of the jet, being smaller than unity. In the other experiments this ratio varied from 1.7 to 3.3 and no effects upstream were seen in both subcritical and supercritical runs.

The experiments with a turbidity current flowing through a bubble curtain showed, that depending on the intensity of the buoyancy flux of the bubble curtain, the turbidity current is completely or partially entrained up to the surface. A recirculation cell existed, extending laterally over one water depth on both sides, within of which the suspended sediments were distributed. The deposition measurements indicated that no significant effect of the bubble curtain on the deposits occurred.

To simulate and further investigate the efficiency of the tested measures, a numerical model was developed. This model is based on the three-dimensional

flow solver CFX-4.4, which allowed implementation of user Fortran routines to adapt the standard solver to the specific flow problems. To calculate the transport of the suspended sediment particles, settling velocity was introduced in the convection term of the Reynolds-averaged sediment concentration transport equation. Three transport equations for the diameters d_{16}, d_{50} and d_{84} were solved. The pick-up and settling rate approach proposed by Parker et al. (1987) and Garcia and Parker (1993) was used for the modelling of the erosion and deposition fluxes. To simulate the obstacle only the geometry needed modification. For the modelling of the screen a porous region was defined having a certain porosity and flow resistance. The jet was modelled with a larger nozzle size than the one used in the experiments, therefore, an additional momentum source was introduced in the cells above the jet nozzle.

Generally, the comparison of the numerical simulations with the measured velocity profiles, front velocities and evolution of deposits showed good agreement. The analysis of the reflected bores due to the presence of an obstacle showed a different flow behavior of weak and strong bores similar to the observations in the physical experiments. It was observed that in the case of a subcritical turbidity current, the streamwise velocity is reduced quite uniformly over the depth in the region between the obstacle and the undular bore. Furthermore, orbital motions within the bores, as measured and described by Kneller et al. (1997) were also reproduced. For the supercritical flow, the reflected bore forms a front flowing back on top of the body of the approaching turbidity current. Upstream of the obstacle a dead zone develops, which the approaching current is overflowing in an undular motion up to the obstacle crest. These results confirmed the observations made in the deposition measurements, that, in the case of a supercritical turbidity current, a major part of its body continues flowing over the obstacle.

To measure the blocking effect of the various investigated configurations a ratio, η is defined as the proportion of the sediment flux passing the obstacle crest, screen or jet compared to the sediment flux passing at the same cross-section without these flow obstacles. It was observed that for the subcritical flow over an obstacle the simulation results are in agreement with the analytical shallow-water considerations, and almost complete blocking occurred until the waves propagating upstream returned due to the reflection from the upper end of the flume. In the case of the supercritical approach flow, the evolution of the passing sediment flux was oscillatory increasing from 50% up to 80%. This transient phenomena was also observed on the video recordings of the experiments and a possible explanation is that internal waves originating at the front of the bore are propagating downstream.

The predictions of the turbidity current flowing through a screen agreed fairly well with the measurements. In particular, the difference in the evolution of the deposits upstream and downstream of the screen is well reproduced. The simulated geotextile was quite permeable, therefore, values of η increasing

with time from 30% to 50% for the subcritical and from 40% to 70% for the supercritical flow were calculated. The linear increase of the passing sediment flux was explained by the constrained geometry of the upstream region of the flume, which slowly filled up. It was found that the oscillatory change in sediment flux found in the flow over an obstacle was smoothed by the presence of the screen. The computations also confirmed the results of the shallow-water analysis, that for a given porosity, the passing flow through a screen is only weakly depending to the approaching flow conditions.

The special treatment for the jet source showed reasonable results for the prediction of the jet flow. The simulations of the turbidity current flowing across a vertical diffuser confirmed, that in the case of a supercritical turbidity current no blocking effect on the passing sediment flux as well as no influence on the upstream flow occurs. On the other hand, the computed evolution of the deposits showed a significant effect on the deposition rate downstream of the jet, similar to the experimental measurements. Therefore, it was concluded, that due to the injection of the vertical momentum, the distribution of the sediment concentration within the turbidity current is modified, and the near-bed concentration as well as the deposition rate are reduced over a certain distance downstream of the jet.

The complicated interaction of the inclined jet with the turbidity current was simulated fairly well and the comparison of the computed and measured evolution of deposits showed good agreement. For the subcritical approaching flow only 5% of the sediment flux passed the jet until the reflected waves from the upstream wall returned. For the simulation with a supercritical approach flow, η changed with time in an oscillatory increase from 65% to 100%, as the retention volume was filled up.

The comparison of the numerical simulations with the experimental results clearly confirmed that the turbidity current flow over an obstacle, through a screen or across a jet can be modelled with good agreement. Furthermore, the numerical simulations proofed a good help to investigate the blocking effect of the various experimental configurations.

In a case study, the numerical model was then applied to Lake Grimsel, where the blocking effect of a submerged embankment dam was investigated. This "obstacle" is built of demolition and excavation materials from the heightening of the dams and has a height of approximately twice the height of the approaching turbidity current. The three-dimensional simulations over the complex topography of the reservoir showed, that the sediments are efficiently retained with the dam of 15 m high and that no deposition in the area of the intake and bottom outlet structures occurred.

Finally, some recommendations, given as rules of thumb, were presented to illustrate possible applications of the investigated measures to control reservoir sedimentation due to turbidity currents. These recommendations are summarized as follows

Obstacle. The obstacle shows efficient blocking if the approaching flow is subcritical and if the height of the obstacle is at least equal to twice the height of the approaching flow.

Screen. The blocking effect of the permeable screen or geotextile depends mainly on its porosity and is efficient to both, sub- and supercritical flows. To obtain a significant blocking effect, the screen height needs to be at least three times the height of the turbidity current with porosities smaller than 30%.

Inclined jets. A subcritical turbidity current can be efficiently blocked, if the opposing momentum of the jet is 50% higher than the momentum of the turbidity current.

Bubble curtain. A bubble curtain is not suited to block turbidity currents in deep reservoirs. Nevertheless, in shallow waters, turbidity currents can be stopped and diluted by means of bubble curtains.

9.2 Further Work

The work done on the effects of obstacles, screens and jets is a first step in developing new measures to control or prevent reservoir sedimentation due to turbidity currents.

The present experimental and numerical investigations focused on the short-term effects of obstacles, screens and jets on the turbidity current flow. To study their long-term behavior and efficiency, numerical simulations may give valuable information. At present, such three-dimensional computations, as presented in this study, are very CPU-time consuming, and simulations over long time periods are impossible. Instead, the existing two-dimensional integral models offer the advantage, that they are much faster and that they can easily handle moving beds. The long-term effect of the investigated measures should, therefore, be simulated with these models, including locally additional terms characterizing the obstacles, screens or jets.

A lack of knowledge still exists on the interaction between the particles in the flow and those on the bottom. The developed measuring device allows accurate measurement of the deposits both in space and time. Existing formulations of deposition and erosion in turbidity current flows should be checked and further developed by means of such a measuring technique. In the present work only the qualitative evolution of deposits was analyzed. With some further development, this type of measuring method could also be used to study the mechanisms of erosion and deposition in more detail. For example, the frequency analysis of the measurements could help to identify coherent structures or bursts within the flow close to the bottom.

The numerical model validated with the physical experiments allows for further analysis of the various parameters such as obstacle height, screen porosity and resistance as well as jet discharge, momentum and inclination. The influence of the constrained geometry of the flume should also be investigated. First, the effect of the relative submergence can be evaluated and secondly, the influence of the longitudinal extent of the flume on the time evolution of the passing sediment flux can be studied.

Currently, only the embankment dam in Lake Grimsel is planned for realization. With further case studies the various measures should be adapted to in-situ conditions and field tests with monitoring should be done to understand the prototype behavior.

Acknowledgements

The present study was carried out at the Laboratory of Hydraulic Constructions (LCH) at the Swiss Federal Institute of Technology in Lausanne (EPFL) under the guidance of Prof. Dr. Anton Schleiss. It is a pleasure to thank all the people who have contributed to this work, in particular

Prof. Dr. A. Schleiss for his help, guidance and support during the course of the present work;

Dr. J. Bühler and Dr. M. Altinakar for many stimulating discussions and for acting as co-examiners;

B. Hagin, A. Baumer, H. Bodenmann, Dr. N. Bretz, B. Feuz, Dr. H. Grein, Dr. W. Hauenstein, Dr. E. Parkinson and Dr. P.-B. Raboud for their collaboration as external experts;

R. Fontanellaz and E. Pantillon for their assistance in the different modifications on the experimental installation;

Dr. J. Poliak, L. Schneiter and J. Bisang for their support in the development of the deposition measuring device and other problems related to the electronic equipment; and

all my colleagues and friends from LCH for their help during the physical experiments, the many fruitful discussions and the excellent personal relations.

The author acknowledges the financial support by the PSEL foundation of the Swiss Union of Electricity Producers, grant N°175 and the Swiss Committee on Dams (SCD).

The case study was financed by the Kraftwerke Oberhasli (KWO) company in the context of the project KWO Plus.

Last but not least, I express my gratitude to my wife, Nadine, for her patience and for her continuous support and encouragement.

References

Abraham, G. and Burgh, P. V. D. (1964). Pneumatic reduction of salt intrusion through locks, *Journal of Hydraulics Division* **90**(1): 83–119. 34, 35

AEA Technology (2001). *CFX-4.4: Solver Manual*, AEA Technology, Oxfordshire, UK. 106, 114, 115, 117

Akiyama, J. and Stefan, H. G. (1984). Plunging flow into a reservoir: Theory, *Journal of Hydraulic Engineering* **110**(4): 484–499. 3

Akiyama, J. and Stefan, H. G. (1985). Turbidity current with erosion and deposition, *Journal of Hydraulic Engineering* **111**(12): 1473–1496. 16

Akiyama, J. and Stefan, H. G. (1986). Prediction of turbidity currents in reservoirs and coastal regions, *3rd Int. Symp. on River Sedimentation*, University of Mississippi, Mississippi, USA, pp. 1295–1305. 3

Alam, S. (1999). The influence and management of sediment at hydro projects, *Hydropower & Dams* **3**: 54–57. 2, 8

Alavian, V., Jirka, G. H., Denton, R. A., Johnson, M. C. and Stefan, H. G. (1992). Density currents entering lakes and reservoirs, *Journal of Hydraulic Engineering* **118**(11): 1464–1489. 3

Alexander, J. and Morris, S. (1994). Observations on experimental, nonchannelized, high-concentration turbidity currents and variations in deposits around obstacles, *Journal of Sedimentary Research* **A64**(4): 899–909. 25

Altinakar, M., Graf, W. and Hopfinger, E. (1996). Flow structure in turbidity currents, *Journal of Hydraulic Research* **34**(5): 713–718. 13, 14, 73, 74, 75

Altinakar, M. S. (1988). *Weakly depositing turbidity current on a small slope*, PhD thesis, No. 738, Swiss Federal Institute of Technology, EPFL, Lausanne, Switzerland. 12, 45, 51, 74, 101, 102

Altinakar, M. S., Graf, W. H. and Hopfinger, E. J. (1990). Weakly depositing turbidity current on a small slope, *Journal of Hydraulic Research* **28**(1): 55–80. 11, 12

Asaeda, T. and Imberger, J. (1993). Structure of bubble plumes in linearly stratified environments, *Journal of Fluid Mechanics* **249**: 35–57. 35

Atkinson, E. (1998). Looking a little flushed, *International Water Power & Dam Construction* **2**: 30–33. 7

Bagnold, R. A. (1963). *The Sea – Ideas and Observations on Progress in the Study of the Seas, Volume 3 - The Earth Beneath the Sea*, Wiley–Interscience, London, chapter Beach and Nearshore Processes. Part I. Mechanics of Marine Sedimentation, pp. 507–553. 19

Baines, P. G. (1995). *Topographic effects in stratified flows*, Cambridge University Press. 23

Baines, W. D. and Leitch, A. M. (1992). Destruction of stratification by bubble plume, *Journal of Hydraulic Engineering* **118**(4): 559–577. 34, 35

Barrett, M. E., Malina, J. F. and Charbeneau, R. J. (1998). An evaluation of geotextiles for temporary sediment control, *Water Environment Research* **70**(3): 283–290. 31

Batuca, D. G. and Jordaan, J. M. (2000). *Silting and desilting of reservoirs*, A. A. Balkema, Rotterdam. 1, 6

Bell, H. S. (1942). Density currents as agents for transporting sediments, *Journal of Geology* **L5**(50). 5

Best, J. L., Kirkbride, A. D. and Peakall, J. (2001). Mean flow and turbulence structure of sediment-laden gravity currents: new insights using ultrasonic doppler velocity profiling, *Spec. Publs. int. Ass. Sediment.* **31**: 159–172. 48

Beyer Portner, N. (1998). *Erosion des bassin versants alpins par ruissellement de surface*, PhD thesis, Communication 6, Laboratory of Hydraulic Constructions (LCH), Swiss Federal Institute of Technology, Lausanne, Switzerland. 1

Bezinge, A. and Aeschlimann, R. (1989). Eaux glaciaires, transports solides et décantation en hydro-électricité, *La Houille Blanche* **3/4**. 5

Bühler, J. and Siegenthaler, C. (1986). Self-preserving solutions for turbidity currents, *Acta Mechanica* **63**(11): 217–233. 17

Boillat, J.-L. and Delley, P. (1992). Transformation de la prise d'eau de Malvaglia - Etude sur modèle et réalisation, *wasser, energie, luft – eau, énergie, air* **7/8**: 145–151. 1

Boillat, J.-L. and Pougatsch, H. (2000). State of the art of sediment management in Switzerland, *International Workshop and Symposium on Reservoir Sedimentation Management*, Tokyo, Japan. 7

Bombardelli, F. A. and Garcia, M. H. (2001). Simulation of density currents in urban environments, *Proc. of the 2001 Int. Symp. on Env. Hydraulics*, Tempe AZ, USA. 106

Bonnecaze, R. T., Huppert, H. E. and Lister, J. R. (1993). Particle-driven gravity currents, *Journal of Fluid Mechanics* **250**: 339–369. 51, 105

Bonnecaze, R. T., Huppert, H. E. and Lister, J. R. (1996). Patterns of sedimentation from polydispersed turbidity currents, *Proc. Roy. Soc. London A* **452**: 2247–2261. 19

Bournet, P. E., Dartus, D., Tassin, B. and Vinçon-Leite, B. (1999). Numerical investigation of plunging density current, *Journal of Hydraulic Engineering* **125**(6): 584–594. 3

Bradford, S. F. and Katopodes, N. D. (1999a). Hydrodynamics of turbid underflows I: Formulation and numerical analysis, *Journal of Hydraulic Engineering* **125**(10): 1006–1015. 105

Bradford, S. F. and Katopodes, N. D. (1999b). Hydrodynamics of turbid underflows II: Aggradation, avulsion, and channelization, *Journal of Hydraulic Engineering* **125**(10): 1016–1028. 105

Britter, R. E. and Linden, P. F. (1980). The motion of the front of a gravity current travelling down an incline, *Journal of Fluid Mechanics* **99**(3): 531–543. 12, 74

Burchard, H. and Petersen, O. (1999). Models of turbulence in the marine environment – a comparative study of two-equation turbulence models, *Journal of Marine Systems* **21**: 29–53. 109, 110, 111, 159

Burchard, H., Petersen, O. and Rippeth, T. P. (1998). Comparing the performance of the Mellor–Yamada and the k-ε two-equation turbulence models, *Journal of Geophysical Research* **103**(C5): 10543–10554. 110

Bursik, M. I. and Woods, A. W. (2000). The effect of topography on sedimentation from particle-laden turbulent density currents, *Journal of Sedimentary Research* **70**(1): 53–63. 25, 26

Cantero, M. I. and Garcia, M. H. (2001). Sediment management in water reservoirs by jet-induced density currents, *Proc. of the 2001 Int. Symp. on Env. Hydraulics*, Tempe AZ, USA. 169

Cao, R. (1992). Experimental study on density current with hyperconcentration of sediment, *Int. Journal of Sediment Research* **8**(1): 51–67. 3, 12

Cebeci, T. and Bradshaw, P. (1977). *Momentum transfer in boundary layers*, Hemisphere, Washington, D. C. 116

Celik, I. and Rodi, W. (1988). Modeling suspended sediment transport in non–equilibrium situations, *Journal of Hydraulic Engineering* **114**(10): 1157–1191. 112

Chikita, K. (1990). Sedimentation by river-induced turbidity currents: Field measurements and interpretation, *Sedimentology* **37**: 891–905. 5

Chochua, G., Shyy, W., Thakur, S., Brankovic, A., Lienau, J., Porter, L. and Lischinsky, J. (2000). A computational and experimental investigation of turbulent jet and crossflow interaction, *Numerical Heat Transfer, Part A* **38**: 557–572. 122

Choi, S.-U. (1999). Layer-averaged modeling of two-dimensional turbidity currents with a dissipative-Galerkin finite element method – Part II: Sensitivity analysis and experimental verification, *Journal of Hydraulic Research* **37**(2): 257–271. 105

Choi, S.-U. and Garcia, M. H. (1995). Modeling of one-dimensional turbidity currents with a dissipative-Galerkin finite element method, *Journal of Hydraulic Research* **33**(5): 623–648. 12, 105

Choi, S.-U. and Garcia, M. H. (2002). k-ε turbulence modeling of density currents developing two dimensionally on a slope, *Journal of Hydraulic Engineering* **128**(1): 55–63. 106

Dade, W. B. and Huppert, H. E. (1995). Runout and fine-sediment deposits of axisymmetric turbidity currents, *Journal of Geophysical Research* **100**(C9): 18597–18609. 19

De Cesare, G. (1998). *Alluvionnement des retenues par courants de turbidité*, PhD thesis, No. 1820, Swiss Federal Institute of Technology, Lausanne, Switzerland. 5, 158

De Cesare, G., Schleiss, S. and Hermann, F. (2001). Impact of turbidity currents on reservoir sedimentation, *Journal of Hydraulic Engineering* **127**(1): 6–16. 5, 106

De Rooij, F., Dalziel, S. B. and Linden, P. F. (1999). Electrical measurement of sediment layer thickness under suspension flows, *Experiments in Fluids* **26**: 470–474. 52, 54

Edwards, D. A. (1993). *Turbidity Currents: Dynamics, Deposits and Reversals*, Vol. 41, Springer-Verlag, Berlin, Germany. 25, 26

Edwards, D. A., Leeder, M. R., Best, J. L. and Pantin, H. M. (1994). On experimental reflected density currents and the interpretation of certain turbidities, *Sedimentology* **41**: 437–461. 137

Einstein, H. A. (1968). Deposition of suspended particles in a gravel bed, *Journal of Hydraulic Division* **94**: 1197–1205. 112

Ellison, T. H. and Turner, J. S. (1959). Turbulent entrainment in stratified flow, *Journal of Fluid Mechanics* **6**: 423–448. 13, 14, 17

Fan, J. (1986). Turbid density currents in reservoirs, *Water International* **11**(3): 107–116. 5

Fan, J. and Morris, G. L. (1992a). Reservoir sedimentation I: Delta and density current deposits, *Journal of Hydraulic Engineering* **118**(3): 354–369. 5

Fan, J. and Morris, G. L. (1992b). Reservoir sedimentation II: Reservoir desiltation and long-term, storage capacity, *Journal of Hydraulic Engineering* **118**(3): 370–384. 8

Fanneløp, T. K., Hirschberg, S. and Küffer, J. (1991). Surface current and recirculating cells generated by bubble curtains and jets, *Journal of Fluid Mechanics* **229**: 629–657. 34

Ford, D. E. and Johnson, M. C. (1983). An assessment of reservoir density currents and inflow processes, *Technical Report E-83-7*, U.S. Army Corps of Engineers, Waterway Experiment Station, Vicksburg, USA. 3

France, P. (1981). An investigation of a jet-assisted hydraulic jump, *Journal of Hydraulic Research* **19**(4): 325–337. 32

Friedl, M. J. (1998). *Bubble plumes and their interactions with the water surface*, PhD thesis, No. 12667, Swiss Federal Institute of Technology, Zürich. 34

Galperin, B., Kantha, L. H., Hassid, S. and Rosati, A. (1988). A quasi-equilibrium turbulent energy model for geophysical flows, *Journal of the Atmospheric Sciences* **45**(1): 55–62. 110

Garcia, M. H. (1989). *Depositing and Eroding Sediment-Driven Flows: Turbidity Currents*, PhD thesis, University of Minnesota, Minneapolis, USA. 16, 73, 75, 101

Garcia, M. H. (1993). Hydraulic jumps in sediment-driven bottom currents, *Journal of Hydraulic Engineering* **119**(10): 1094–1117. 18, 22

Garcia, M. H. (1994). Depositional turbidity currents laden with poorly sorted sediment, *Journal of Hydraulic Engineering* **120**(11): 1240–1263. 51

Garcia, M. H. and Parker, G. (1993). Experiments on the entrainment of sediment into suspension by a dense bottom current, *Journal of Geophysical Research (Oceans)* **98**(C3): 4793–4807. 15, 16, 17, 113, 114, 119, 155, 173

Graf, W. H. (1971). *Hydraulics of Sediment Transport*, McGraw Hill, New York, USA. 17

Graf, W. H. (1983). The behaviour of silt-laden current, *International Water Power & Dam Construction* **35**(9): 33–38. 5, 8

Graf, W. H. (1984). Storage losses in reservoirs, *International Water Power & Dam Construction* **36**(4): 37–40. 1

Graf, W. H. and Altinakar, M. S. (1998). *Fluvial hydraulics*, John Wiley & Sons Ltd, Chichester, England. 20, 22

Gröbelbauer, H. P. (1995). *Experimental study on the dispersion of instantaneously released dense gas clouds*, PhD thesis, No. 10973, Swiss Federal Institute of Technology, Zürich, Switzerland. 138

Greenspan, H. P. and Young, R. E. (1978). Flow over a containment dyke, *Journal of Fluid Mechanics* **87**(1): 179–192. 19

Grein, H. and Krause, M. (1994). Research and prevention of hydroabrasive wear, *17th IAHR Symposium*, Bejing, China, pp. 90–101. 8

Grein, H. and Schachenmann, A. (1992). Abrasion in hydroelectric machinery, *Sulzer Technical Review* **1**: 19–29. 8

Grover, N. C. and Howard, C. L. (1938). The passage of turbid water through Lake Mead, *Trans. ASCE* **103**. 5

Hager, W. H. (1984). A simplified hydrological rainfall-runoff model, *Journal of Hydrology* **74**: 151–170. 158

Han, D., Orozco, V. and Mungal, M. G. (2000). Gross-entrainment behavior of turbulent jets injected obliquely into a uniform crossflow, *AIAA Journal* **38**(9): 1643–1649. 32

Hasselbrink, E. F. and Mungal, M. G. (2001). Transverse jets and jet flames. Part 1. Scaling laws for strong transverse jets, *Journal of Fluid Mechanics* **443**: 1–25. 32

Hauenstein, W. (1982). *Zuflussbedingte Dichteströmungen in Seen*, PhD thesis, Swiss Federal Institute of Technology, Zürich, Switzerland. 19

Hauenstein, W. and Dracos, T. (1984). Investigation of plunging density currents generated by inflows in lakes, *Journal of Hydraulic Research* **22**: 157–179. 3, 19

Hebbert, B., Imberger, J., Loh, I. and Patterson, J. (1979). Collie River underflow into the Wellington Reservoir, *Journal of the Hydraulics Division* **105**(5): 533–545. 3

Hermann, F., Issler, D. and Keller, S. (1994). Towards a numerical model of powder snow avalanches, *ECCOMAS 94*, John Wiley and Sons Ltd, Switzerland. 106

Hodgson, J. E., Rajaratnam, N. and Moawad, A. K. (1999). Circular jets in crossflow of finite depth, *Proc. of the Institution of Civil Engineers – Water, Maritime & Energy* **136**(3): 35–42. 32

Hotchkiss, R. H. and Huang, X. (1995). Hydrosuction sediment removal systems (HSRS): Principles and field test, *Journal of Hydraulic Engineering* **121**(6). 7

Howard, C. S. (1953). Density currents in Lake Mead, *5th IAHR Congress*, Minnesota, USA, pp. 335–368. 5

Hugi, C. (1993). *Modelluntersuchungen von Blasenstrahlen für die Seebelüftung*, PhD thesis, No. 10246, Swiss Federal Institute of Technology, Zürich, Switzerland. 34

Huq, P. (1997). Observations of jets in density stratified crossflows, *Atmospheric Environment* **31**(13): 2011–2022. 32

Huq, P. and Stewart, E. J. (1996). A laboratory study of buoyant plumes in laminar and turbulent crossflows, *Atmospheric Environment* **30**(7): 1125–1135. 32

Huwiler, P. (2002). Möglichkeiten zur Feststoffevakuation aus Stauseen durch die Triebwasserleitung, *Technical report*, Travail de diplôme postgrade, Cycle postgrade en aménagements hydrauliques. 8

Hwang, R. R. and Chiang, T. P. (1995). Numerical simulation fo vertical forced plume in a crossflow of stably stratified fluid, *Transactions of ASME* **117**(12): 696–705. 124

Hwang, R. R., Chiang, T. P. and Yang, W. C. (1995). Effect of ambient stratification on buoyant jets in cross-flow, *Journal of Engineering Mechanics* **121**(8): 865–872. 124

Idel'cik, I. E. (1969). *Mémento des pertes de charge*, number 13 in *Collection du centre de recherches et d'essais de Chatou*, Eyrolles, Paris, France. 122

International Comittee on Large Dams (ICOLD) (1989). *Sedimentation control of reservoirs – Guidelines*, Vol. 67. 1

International Comittee on Large Dams (ICOLD) (1996). *Dealing with reservoir sedimentation – Guidelines and case studies*, Vol. 115. 6

Jacobsen, T. (1998). New sediment removal techniques and their applications, *Hydropower & Dams*, Aix-en-Provence, France, pp. 135–146. 8

Jacobsen, T. (1999). Sustainable reservoir development: The challenge of reservoir sedimentation, *Conference Proceedings "Hydropower into the next century"*, Gmunden, Austria, pp. 719–728. 1

Jirka, G. H. and Akar, P. J. (1991). Hydrodynamic classification of submerged multiport-diffuser discharges, *Journal of Hydraulic Engineering* **117**(9): 1113–1128. 32, 91

Jirka, G. H. and Doneker, R. L. (1991). Hydrodynamic classification of submerged single-port discharges, *Journal of Hydraulic Engineering* **117**(9): 1095–1112. 32

Kalita, K., Dewan, A. and Dass, A. K. (2002). Prediction of turbulent plane jet in crossflow, *Numerical Heat Transfer, Part A* **41**: 101–111. 124

Karpik, S. R. and Raithby, G. D. (1990). Lateral averaged hydrodynamics model for reservoir predictions, *Journal of Hydraulic Engineering* **116**(6): 783–798. 105

Keimasi, M. R. and Taeibi-Rahni, M. (2001). Numerical simulation of jets in a crossflow using different turbulence models, *AIAA Journal* **39**(12): 2268–2277. 122

Kneller, B. C., Bennett, S. J. and McCaffrey, W. D. (1997). Velocity and turbulence structure of density currents and internal solitary waves: Potential sediment transport and the formation of wave ripples in deep water, *Sedimentary Geology* **112**: 235–250. 137, 155, 173

Kneller, B. C., Edwards, D., McCaffrey, W. and Moore, R. (1991). Oblique reflection of turbidity currents, *Geology* **19**: 250–252. 25

Kneller, B. and McCaffrey, W. (1999). Depositional effects of flow nonuniformity and stratification within turbidity currents approaching a bounding slope: Deflection, reflection, and facies variation, *Journal of Sedimentary Research* **69**(5): 980–991. 26

Kobus, H. E. (1972). Berechnungsmethode für Luftschleier-Strömungen zur Auslegung von Pressluft-Ölsperren, *Wasserwirtschaft* **62**(6): 159–166. 34

Kranenburg, C. (1993a). Gravity-current fronts advancing into horizontal ambient flow, *Journal of Hydraulic Engineering* **119**: 369–379. 19

Kranenburg, C. (1993b). Unsteady gravity currents advancing along a horizontal surface, *Journal of Hydraulic Research* **31**(1): 49–60. 19

Krause, M. and Grein, H. (1993). Abrasion, research and prevention, *Sulzer Technical Review* **2**: 30–36. 1

Kubasch, J. H. (2001). *Bubble hydrodynamics in large pools*, PhD thesis, Swiss Federal Institute of Technology, Zürich, Switzerland. 34

Lane, E. W. and Koelzer, V. A. (1943). Density of sediments deposited in reservoirs, *Technical Report 9*, Interagency Committee on Water Resources, University of Iowa. 5

Lane-Serff, G. F., Beal, L. M. and Hadfield, T. D. (1995). Gravity current flow over obstacles, *Journal of Fluid Mechanics* **292**: 39–53. 19, 23, 24

Lavelli, A., De Cesare, G. and Boillat, J.-L. (2002). *Modélisation des courants de turbidité dans le bassin nord du lac de Lugano*, Communication 11, Laboratory of Hydraulic Constructions (LCH), Swiss Federal Institute of Technology, Lausanne, Switzerland. 3

Lee, H.-Y. and Yu, W.-S. (1997). Experimental study of reservoir turbidity current, *Journal of Hydraulic Engineering* **123**(6): 520–528. 3

Lemckert, C. J. and Imberger, J. (1993). Energetic bubble plumes in arbitrary stratification, *Journal of Hydraulic Engineering* **119**(6): 680–703. 34, 35

Long, R. R. (1954). Some aspects of the flow of stratified fluids. II. Experiments with a two-fluid system, *Tellus* **6**: 97–115. 19, 21, 23

Long, R. R. (1970). Blocking effects in flow over obstacles, *Tellus* **22**: 471–480. 19, 23

McDougall, T. J. (1978). Bubble plumes in stratified environments, *Journal of Fluid Mechanics* **85**: 655–672. 35

Met-Flow SA (2000). *UVP Monitor - User Guide*, Lausanne, Switzerland. 46

Middleton, G. V. (1966). Experiments on density and turbidity currents: I. motion of the head, *Canadian Journal of Earth Sciences* **3**: 523–546. 11, 105

Milgram, J. H. (1983). Mean flow in round bubble plumes, *Journal of Fluid Mechanics* **85**: 345–376. 34

Moawad, A. K. and Rajaratnam, N. (1998). Dilution of multiple nonbuoyant circular jets in crossflows, *Journal of Environmental Engineering* **124**(1): 51–58. 32

Monaghan, J. J., Cas, R. A. F., Kos, A. M. and Hallworth, M. (1999). Gravity currents descending a ramp in a stratified tank, *Journal of Fluid Mechanics* **379**: 39–69. 106

Moodie, T. B., Pascal, J. P. and Bowman, J. C. (2000). Modeling sediment deposition patterns arising from suddenly released fixed-volume turbulent suspensions, *Studies in Applied Mathematics* **105**: 333–359. 19

Morris, G. L. and Fan, J. (1998). *Resevoir sedimentation handbook – Design and management of dams, reservoirs, and watersheds for sustainable use*, McGraw-Hill. 5, 6

Naaim, M. (1995). Modélisation numérique des avalanches aérosols, *La Houille Blanche* **5/6**: 56–62. 106

Nakai, M. and Arita, M. (2002). An experimental study on prevention of saline wedge intrusion by an air curtain in rivers, *Journal of Hydraulic Research* **40**(3): 333–339. 36, 37, 101

National Instruments (2000). LabVIEW^{TM}6.0 – *Measurements Manual*. 53

Nizéry, A., Braudeau, G. and Bonnin, J. (1953). La station du Sautet pour l'étude de l'alluvionnement des réservoirs, *2e journées de l'hydraulique*, pp. 180–215. 5

Oehy, C., De Cesare, G. and Schleiss, A. (2000). Parametric study on the influence of turbidity currents on the sedimentation of Alpine reservoirs, *HYDRO 2000 "Making Hydro more Competitive"*, Bern, Switzerland, pp. 137–146. 2

Oehy, C. and Schleiss, A. (2001a). Comparative study between two buoyancy-extended and the standard k-ε model for simulating turbidity currents, *Proc. of the 2001 Int. Symp. on Env. Hydraulics*, Tempe AZ, USA. 119

Oehy, C. and Schleiss, A. (2001b). Numerical modeling of a turbidity current passing over an obstacle – Practical application in the Lake Grimsel, switzerland, *Proc. of the 2001 Int. Symp. on Env. Hydraulics*, Tempe AZ, USA. 157

Oehy, C. and Schleiss, A. (2002). Einfluss von Hindernissen auf das Fliessverhalten von Trübeströmen am Beispiel des Grimselsees, *Proceedings Wasserbau Symposium "Moderne Methoden und Konzepte im Wasserbau"*, Vol. 174 of *VAW Mitteilungen*, Zürich, Switzerland, pp. 51–60. 157

Office fédéral de l'environnement, des forêts et du paysage (OFEFP) (1994). Conséquences écologiques des curages de bassins de retenue, *Cahier de l'environnement* **219**. 7

Olsen, N. R. B. and Tesaker, E. (1995). Numerical and physical modelling of a turbidity current, *26th IAHR Biennal Congress - "HYDRA 2000"*, London, UK. 106, 159

Pantin, H. M. and Leeder, M. R. (1987). Reverse flow in turbidity currents: The role of internal solutions, *Sedimentology* **34**: 1143–1156. 26

Parker, G., Fukushima, Y. and Pantin, H. M. (1986). Self-accelerating turbidity currents, *Journal of Fluid Mechanics* **171**: 145–181. 14, 15, 17, 114

Parker, G., Garcia, M., Fukushima, Y. and Yu, W. (1987). Experiments on turbidity currents over an erodable bed, *Journal of Hydraulic Research* **25**(1): 123–147. 15, 16, 106, 113, 155, 173

Pratte, B. D. and Baines, W. D. (1967). Profiles of the round turbulent jet in a cross flow, *Journal of Hydraulics Division* **92**: 53–64. 32

Prinos, P. (1999). Two-dimensional density currents over obstacles, *18th IAHR Congress*, Graz, Austria. 23, 24

Pyrkin, Y. G. and Samolyubov, B. I. (1978). Transport of suspended sediments in the Nurek Hydroelectric Station Reservoir by density current and calculation of siltation, *Translated from Gidrotekhnicheskoe Stroitel'stvo* **5**: 9–12. 5

Rajaratnam, N. (1976). *Turbulent Jets*, Vol. 5, Elsevier, Amsterdam, Netherlands. 32

Riess, I. R. and Fanneløp, T. K. (1998). Recirculating flow generated by line-source bubble plumes, *Journal of Hydraulic Engineering* **124**(9): 932–940. 34, 97

Rémini, B. (2000). "Bon"ou "mauvais"soutirage? L'exemple de quelques barrages algériens, *La Houille Blanche* **3/4**: 68–75. 8

Rodi, W. (1980). Turbulence models and their application in hydraulics: A state of the art review, *IAHR*, Delft, Netherlands. 107

Rodi, W. (1985). Calculation of stably stratified shear-layer flows with a buoyancy-extended k-ε turbulence model, *in* J. C. R. Hunt (ed.), *Turbulence and diffusion in stable environments*, The institute of mathematics and its applications conference series, Claredon Press, Oxford, pp. 111–140. 108

Rodi, W. (1987). Examples of calculation methods for flow and mixing in stratified fluids, *Journal of Geophysical Research* **92**: 5305–5328. 159

Rottman, J. W., Simpson, J. E., Hunt, J. C. R. and Britter, R. E. (1985). Unsteady gravity current flows over obstacle: Some observations and analysis related to phase II trials, *Journal of Hazardous Materials* **11**: 325–340. 19, 20, 23, 26

Schaad, F. (1979). Vorschläge zur Verminderung der Stauraumverlandung bei starker Schwebestoffzufuhr, *Wasser und Boden* **31**(12): 347–352. 8

Scheuerlein, H. (1992). L'excavation des dépôts sédimentaires dans les réservoirs par dragage, *La Revue Marocaine du Génie Civil* **38**: 60–66. 8

Schladow, S. G. (1993). Lake destratification by bubble plume systems: Design methodology, *Journal of Hydraulic Engineering* **119**(3): 350–368. 34, 35

Schläpfer, D. B. (1990). *Stationäre zwei-dimensionale Dichteströmungen bei kleinen Neigungen. Einfluss der Reibung und der Tiefe*, PhD thesis, No. 9023, Swiss Federal Institute of Technology, Zürich, Switzerland. 19

Schleiss, A., Feuz, B., Aemmer, M. and Zünd, B. (1996). Verlandungsprobleme im Stausee Mauvoisin. Ausmass, Auswirkungen und mögliche Massnahmen, *Int. Symposium "Verlandung von Stauseen"- Mitteilungen VAW*, No 141, Teil 1, Zürich, Switzerland, pp. 37–58. 1

Schleiss, A. and Oehy, C. (2002). Verlandung von Stauseen und Nachhaltigkeit, *wasser, energie, luft – eau, énergie, air* **7/8**: 227–234. 6, 169

Shen, H. W. (2000). Flushing sediment through reservoirs, *Journal of Hydraulic Research* **37**(6): 743–757. 8

Simmons, H. B. (1967). Potential benefits of pneumatic barriers in estuaries, *Journal of Hydraulics Division* **93**(3): 1–16. 34, 35

Simpson, J. E. (1997). *Gravity currents: In the environment and the laboratory*, Cambridge University Press. 3, 77

Singh, B. and Shah, C. R. (1971). Plunging phenomenon of density currents in reservoirs, *La Houille Blanche* **26**(1): 59–64. 3

Sinniger, R., De Cesare, G. and Martini, O. (1994). Apports de sédiments dans une retenue par courant de densité - Mesures in situ, *XVIIIth Congress ICOLD*, Vol. Q.69-R.7, Durban, South Africa. 5

Sinniger, R. O., De Cesare, G. and Boillat, J.-L. (1999). Propriétés des alluvions récentes dans les retenues alpines, *wasser, energie, luft – eau, énergie, air* **9/10**: 255–258. 2

Smith, S. H. and Mungal, M. G. (1998). Mixing, structure and scaling of the jet in crossflow, *Journal of Fluid Mechanics* **357**: 83–122. 32

Suter, P. (1998). Verlandung und Spülung des Rempenbeckens der AG Kraftwerk Wägital, *wasser, energie, luft – eau, énergie, air* **5/6**: 127–131. 7

Takeda, Y. (1995). Velocity profile measurement by ultrasonic doppler method, *Experimental Thermal and Fluid Science* **10**: 444–453. 46

Thévenin, M. J. (1960). La sédimentation des barrages-réservoirs en Algérie et les moyens mis en oeuvre pour préserver les capacités, *Annales de l'institut technique du bâtiment* **156**. 5

Trussel, R. R. and Chang, M. (1999). Review of flow through porous media as applied to head loss in water filters, *Journal of Hydraulic Engineering* **125**(11): 998–1006. 121

Turner, J. S. (1973). *Buoyancy effects in fluids*, Cambridge University Press, Cambridge, United Kingdom. 14, 15, 19

Van Kessel, T. and Kranenburg, C. (1996). Gravity current of fluid mud on sloping bed, *Journal of Hydraulic Engineering* **122**(12): 710–717. 13

Van Rijn, L. C. (1984a). Sediment transport: Part III – Bed forms and alluvial roughness, *Journal of Hydraulic Engineering* **110**(12): 1733–1754. 159

Van Rijn, L. C. (1984b). Sediment transport: Part II – Suspended load transport, *Journal of Hydraulic Engineering* **110**(11): 1613–1641. 112, 116

Varma, C. V. J., Naidu, B. S. K. and Rao, A. R. G. (2000). *Silting problems in hydro power plants*, A. A. Balkema, Rotterdam. 1

Wüest, A., Brooks, N. H. and Imboden, D. M. (1992). Bubble plume modeling for lake restoration, *Journal of Water Resource Research* **28**(12): 3235–3250. 34

Wilkinson, D. L. (1979). Two-dimensional bubble plumes, *Journal of Hydraulics Division* **105**: 139–154. 34

Wood, I. R. and Simpson, J. E. (1984). Jumps in layered miscible fluids, *Journal of Fluid Mechanics* **140**: 329–342. 23, 77

Wright, S. J. (1984). Buoyant jets in density-stratified crossflow, *Journal of Hydraulic Engineering* **110**(5): 643–656. 32

Wu, W., Rodi, W. and Wenka, T. (2000). 3D numerical modeling of flow and sediment transport in open channels, *Journal of Hydraulic Engineering* **126**(1): 4–15. 113, 115, 159

Yeh, H. H. and Shrestha, M. (1989). Free-surface flow through screen, *Journal of Hydraulic Engineering* **115**(10): 1371–1385. 30

A Experimental Data

A.1 Continuously-Fed Turbidity Current

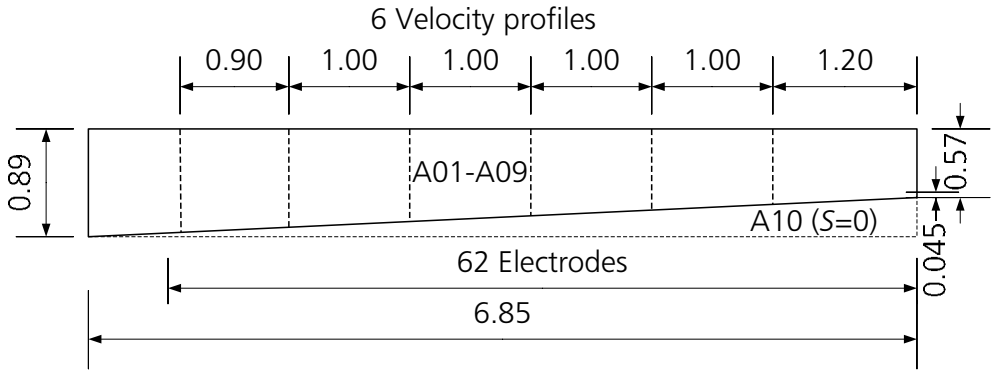

Figure A.1: Experimental set–up for series A with locations of velocity profiles.

Exp [–]	S [%]	T_a [°C]	ρ_a [g/cm^3]	T_0 [°C]	ρ_0 [g/cm^3]	C [%]	g_0' [m/s^2]	Q_0 [m^3/s]
A01	4.64	13.0	0.9993	10.8	1.0040	3.477	0.0463	0.00096
A02	4.64	10.2	0.9998	11.3	1.0031	2.382	0.0316	0.00075
A03	4.64	8.9	0.9999	10.4	1.0046	3.486	0.0462	0.00072
A04	4.64	8.8	0.9999	11.3	1.0027	2.066	0.0274	0.00085
A05	4.64	13.2	0.9994	10.3	1.0056	4.630	0.0616	0.00137
A06	4.64	9.0	0.9998	10.8	1.0033	2.610	0.0353	0.00086
A07	4.64	12.1	0.9995	11.0	1.0041	3.448	0.0459	0.00050
A08	4.64	10.3	0.9997	11.8	1.0039	3.105	0.0412	0.00063
A09	4.64	10.5	0.9995	11.0	1.0057	4.554	0.0606	0.00071
A10	-	12.9	0.9995	12.2	1.0040	3.371	0.0449	0.00073

Table A.1: Experimental parameters A series.

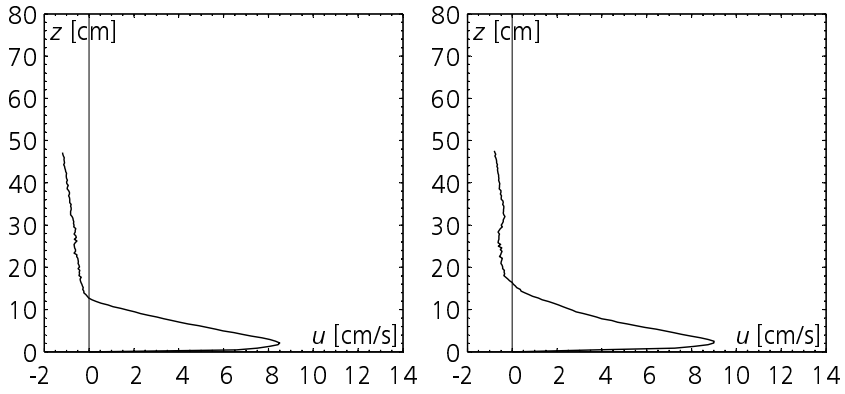

(a) x=120 cm. *(b)* x=220 cm.

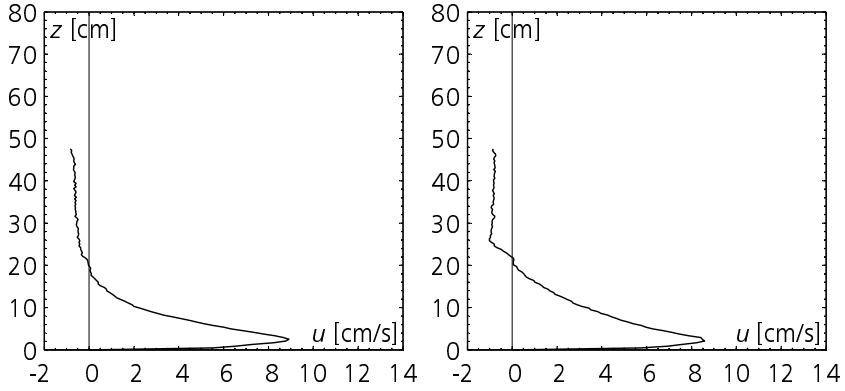

(c) x=320 cm. *(d)* x=420 cm.

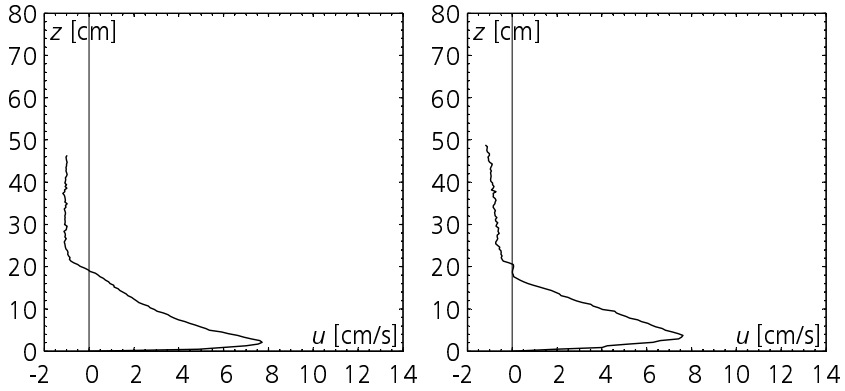

(e) x=520 cm. *(f)* x=610 cm.

Figure A.2: Vertical velocity profiles of experiment A02.

x [cm]	h [cm]	U [cm/s]	h_{max} [cm]	U_{max} [cm/s]	U_{max}/U [–]	h_{max}/h [–]
120	9.07	6.24	2.05	8.51	1.36	0.23
220	10.58	6.24	2.46	9.01	1.44	0.23
320	10.85	5.92	2.46	8.92	1.51	0.23
420	13.21	5.60	2.05	8.59	1.53	0.16
520	13.02	4.97	2.05	7.73	1.56	0.16
610	13.33	5.33	3.69	7.62	1.43	0.28

Table A.2: Integral scale and maximum values of experiment A02.

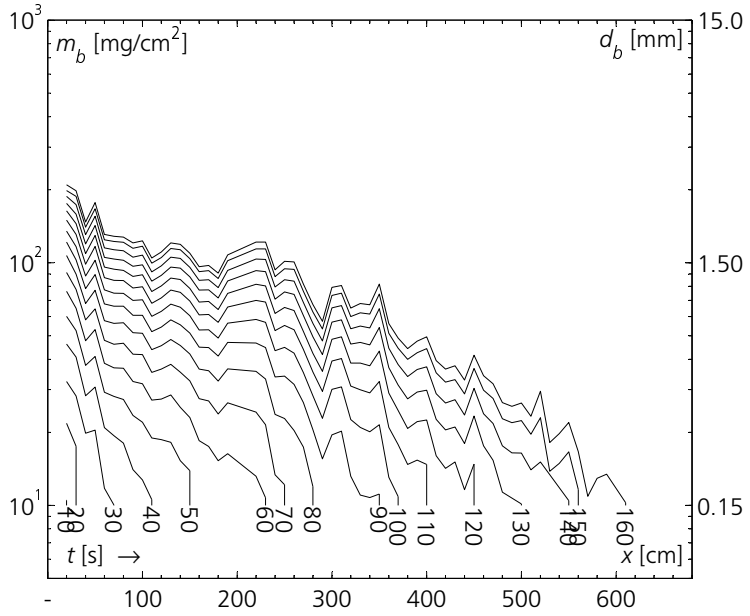

Figure A.3: Measured deposition evolution of experiment A02 along the flume axis, x with time steps of 10 s.

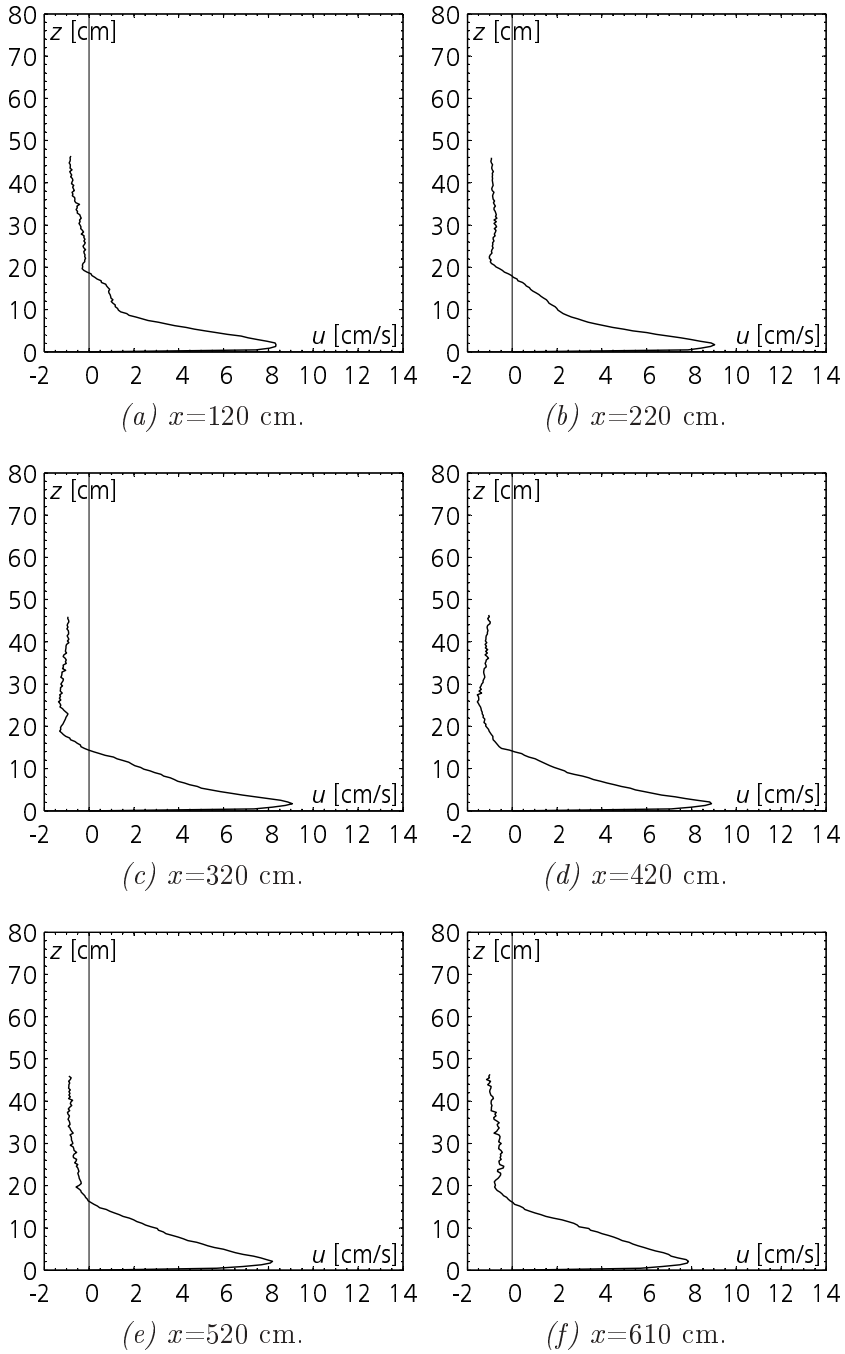

(a) x=120 cm. *(b)* x=220 cm.

(c) x=320 cm. *(d)* x=420 cm.

(e) x=520 cm. *(f)* x=610 cm.

Figure A.4: Vertical velocity profiles of experiment A03.

x [cm]	h [cm]	U [cm/s]	h_{max} [cm]	U_{max} [cm/s]	U_{max}/U [–]	h_{max}/h [–]
120	10.05	5.60	1.64	8.34	1.49	0.16
220	10.60	5.85	1.64	9.04	1.55	0.15
320	10.15	6.04	1.64	9.07	1.50	0.16
420	9.79	6.00	1.64	8.89	1.48	0.17
520	11.50	5.57	2.05	8.18	1.47	0.18
610	11.80	5.61	2.05	7.86	1.40	0.17

Table A.3: Integral scale and maximum values of experiment A03.

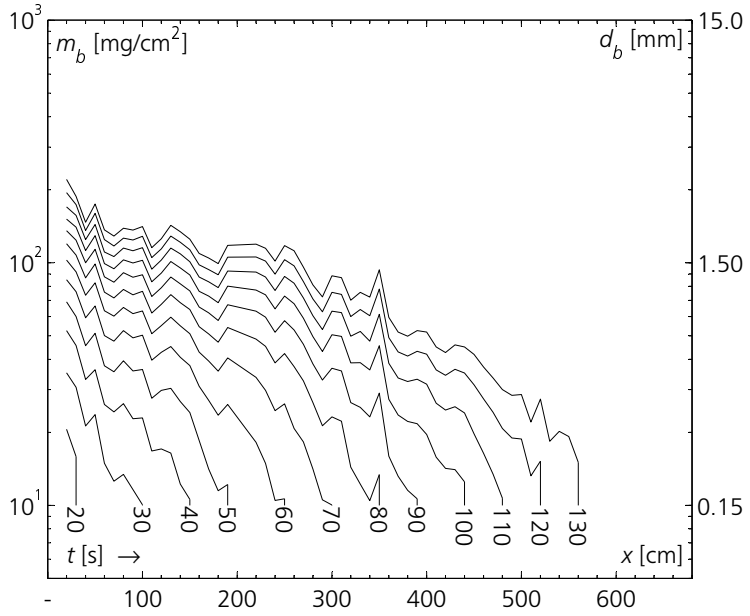

Figure A.5: Measured deposition evolution of experiment A03 along the flume axis, x with time steps of 10 s.

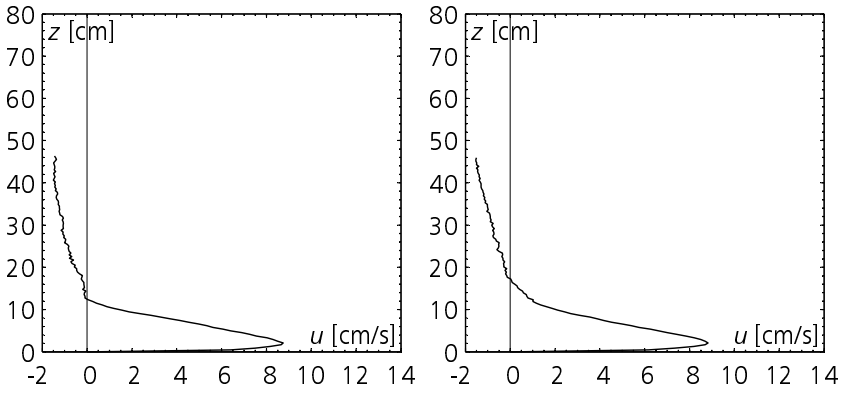

(a) x=120 cm. *(b)* x=220 cm.

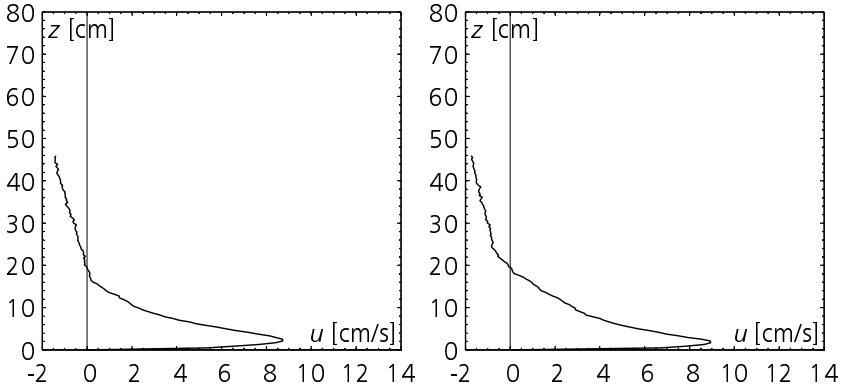

(c) x=320 cm. *(d)* x=420 cm.

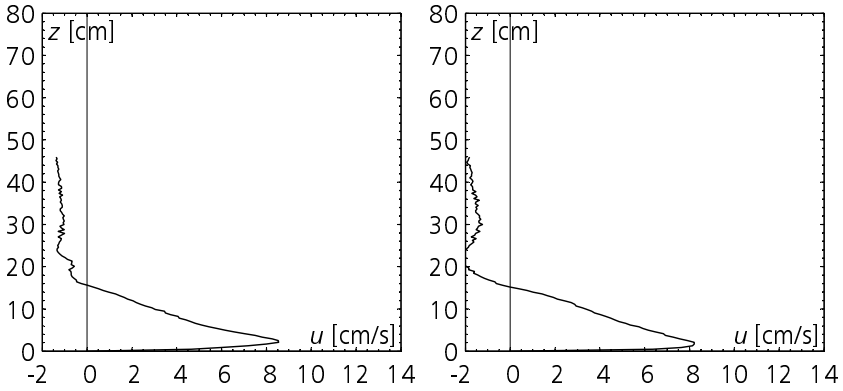

(e) x=520 cm. *(f)* x=610 cm.

Figure A.6: Vertical velocity profiles of experiment A04.

x [cm]	h [cm]	U [cm/s]	h_{max} [cm]	U_{max} [cm/s]	U_{max}/U [–]	h_{max}/h [–]
120	9.02	6.51	2.05	8.75	1.34	0.23
220	10.26	6.25	2.05	8.82	1.41	0.20
320	10.93	5.82	2.46	8.73	1.50	0.23
420	12.23	5.64	1.64	8.94	1.59	0.13
520	11.47	5.71	2.05	8.54	1.50	0.18
610	11.85	5.79	2.05	8.21	1.42	0.17

Table A.4: Integral scale and maximum values of experiment A04.

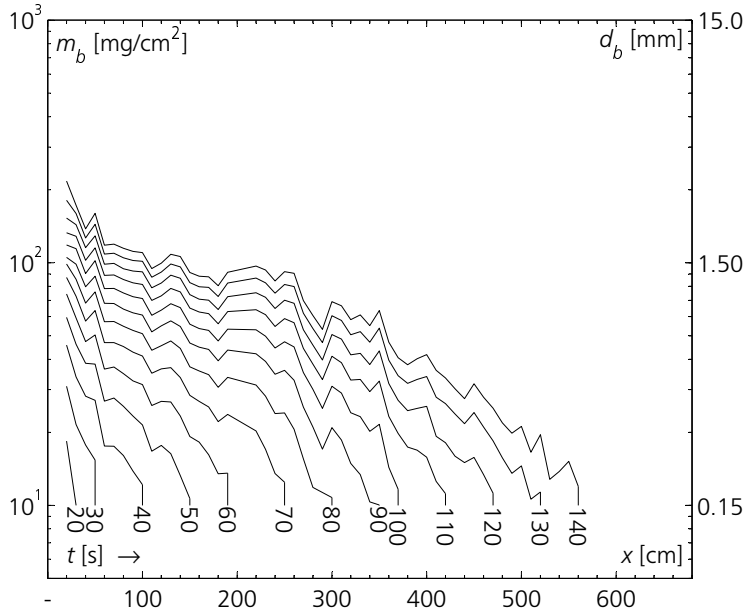

Figure A.7: Measured deposition evolution of experiment A04 along the flume axis, x with time steps of 10 s.

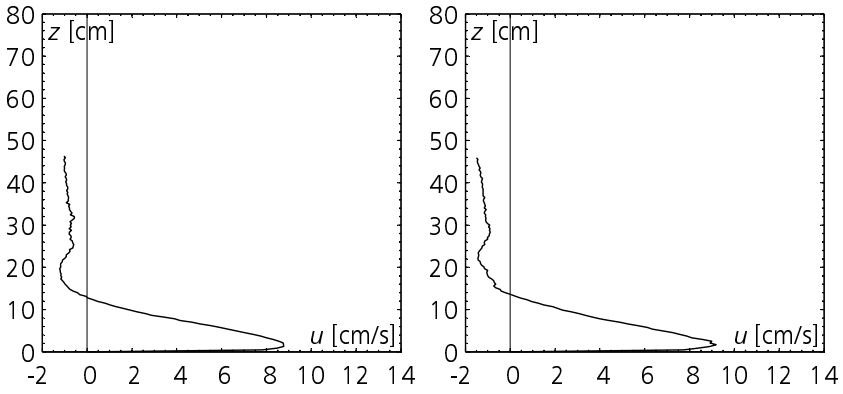

(a) x=120 cm.

(b) x=220 cm.

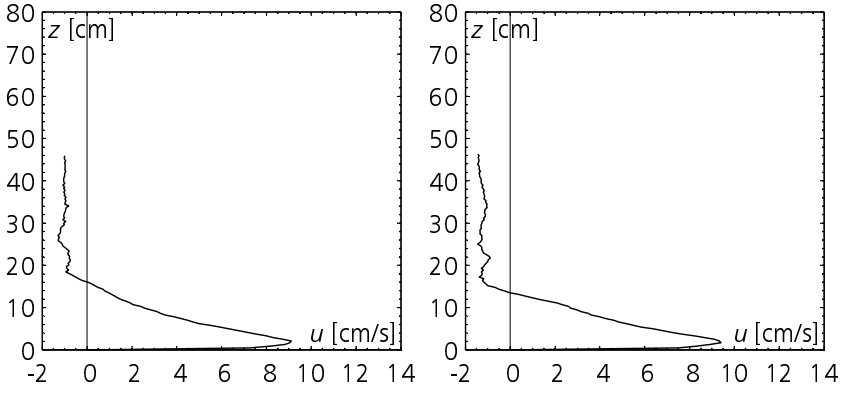

(c) x=320 cm.

(d) x=420 cm.

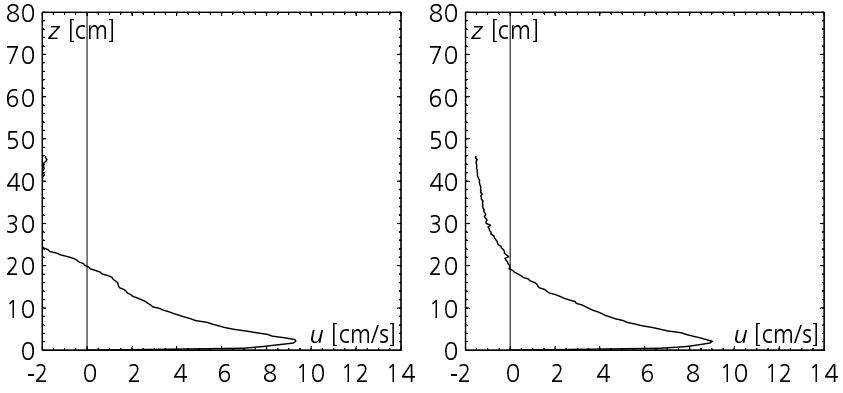

(e) x=520 cm.

(f) x=610 cm.

Figure A.8: Vertical velocity profiles of experiment A06.

x [cm]	h [cm]	U [cm/s]	h_{max} [cm]	U_{max} [cm/s]	U_{max}/U [–]	h_{max}/h [–]
120	9.30	6.69	1.23	8.78	1.31	0.13
220	9.81	6.71	1.64	9.18	1.37	0.17
320	10.67	6.24	2.05	9.11	1.46	0.19
420	10.06	6.56	1.64	9.41	1.43	0.16
520	13.00	6.01	2.05	9.32	1.55	0.16
610	12.86	5.99	2.05	9.02	1.51	0.16

Table A.5: Integral scale and maximum values of experiment A06.

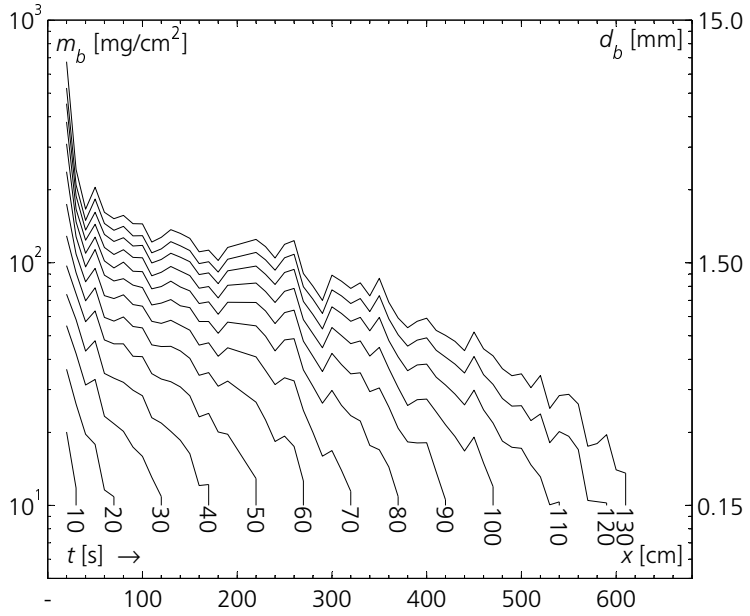

Figure A.9: Measured deposition evolution of experiment A06 along the flume axis, x with time steps of 10 s.

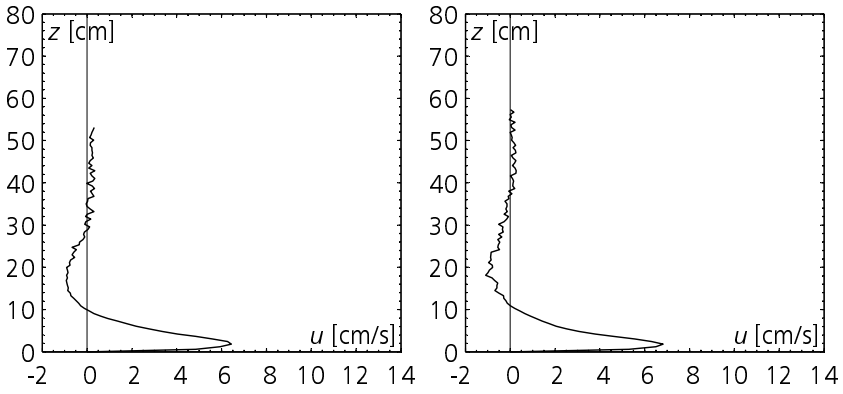

(a) x=120 cm. *(b)* x=220 cm.

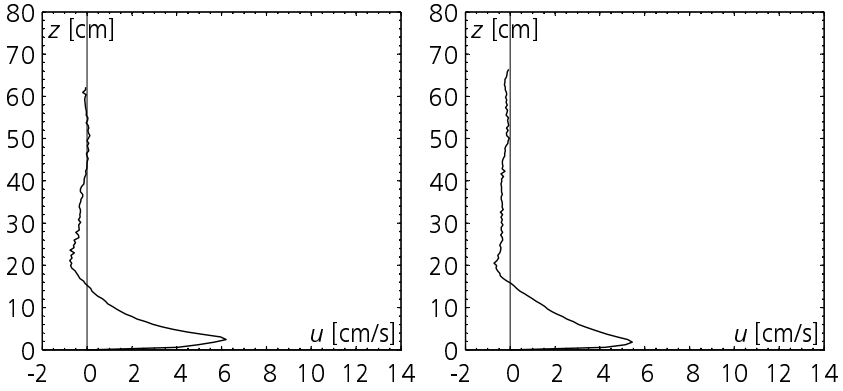

(c) x=320 cm. *(d)* x=420 cm.

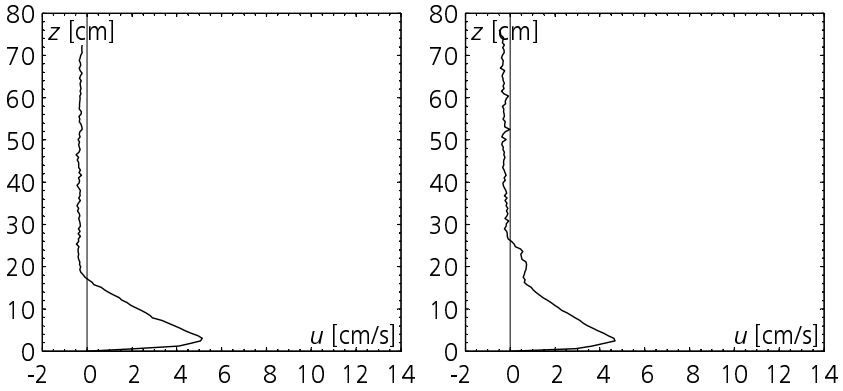

(e) x=520 cm. *(f)* x=610 cm.

Figure A.10: Vertical velocity profiles of experiment A07.

x [cm]	h [cm]	U [cm/s]	h_{max} [cm]	U_{max} [cm/s]	U_{max}/U [–]	h_{max}/h [–]
120	6.71	4.68	1.81	6.44	1.38	0.27
220	6.87	4.72	1.81	6.82	1.44	0.26
320	9.43	4.06	2.41	6.20	1.53	0.26
420	10.78	3.62	1.81	5.45	1.51	0.17
520	12.48	3.58	3.02	5.14	1.44	0.24
610	16.38	2.95	2.41	4.67	1.58	0.15

Table A.6: Integral scale and maximum values of experiment A07.

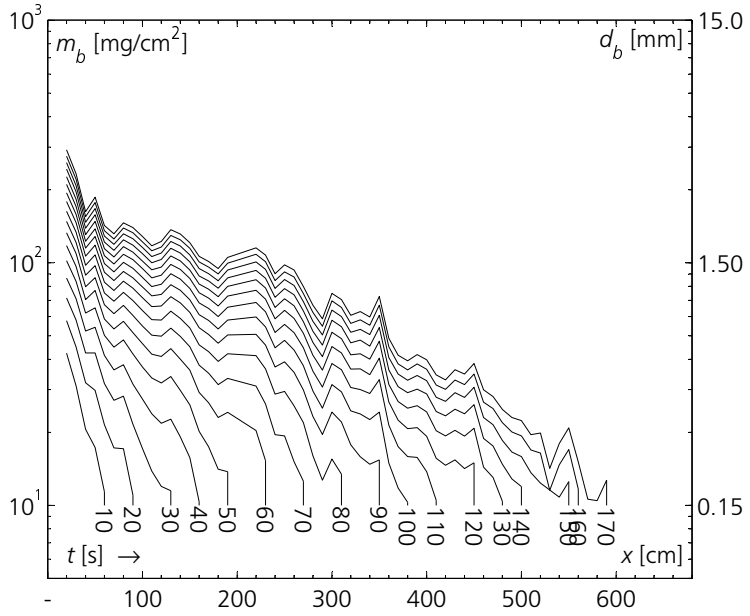

Figure A.11: Measured deposition evolution of experiment A07 along the flume axis, x with time steps of 10 s.

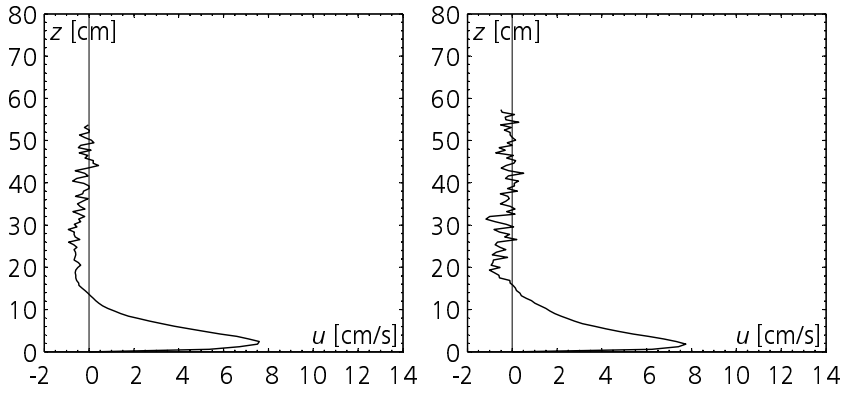

(a) x=120 cm.

(b) x=220 cm.

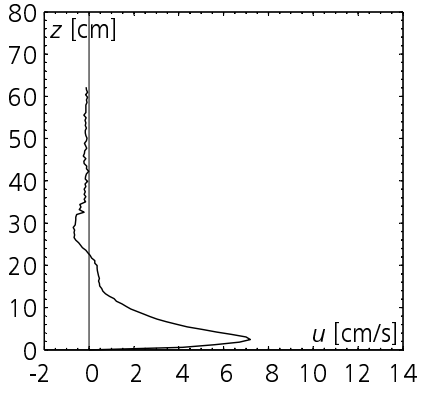

(c) x=320 cm.

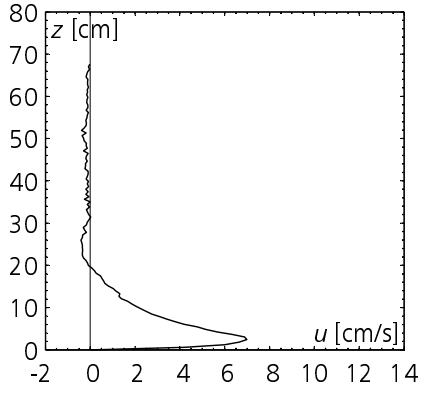

(d) x=420 cm.

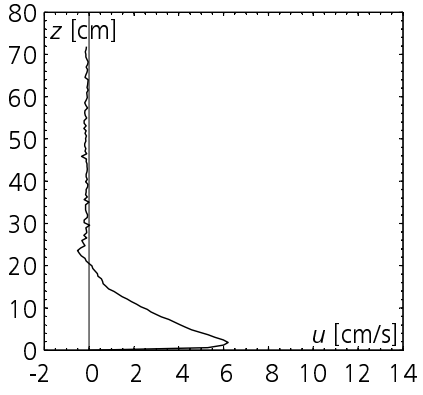

(e) x=520 cm.

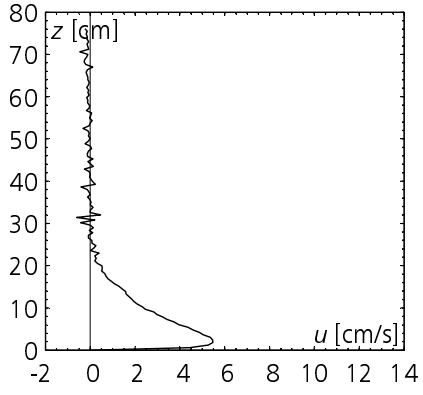

(f) x=610 cm.

Figure A.12: Vertical velocity profiles of experiment A08.

x [cm]	h [cm]	U [cm/s]	h_{max} [cm]	U_{max} [cm/s]	U_{max}/U [–]	h_{max}/h [–]
120	8.43	5.43	2.41	7.59	1.40	0.29
220	9.45	5.17	1.81	7.75	1.50	0.19
320	11.37	4.51	2.41	7.19	1.59	0.21
420	12.08	4.52	2.41	6.99	1.55	0.20
520	12.92	4.14	1.81	6.20	1.50	0.14
610	15.11	3.66	1.81	5.47	1.49	0.12

Table A.7: Integral scale and maximum values of experiment A08.

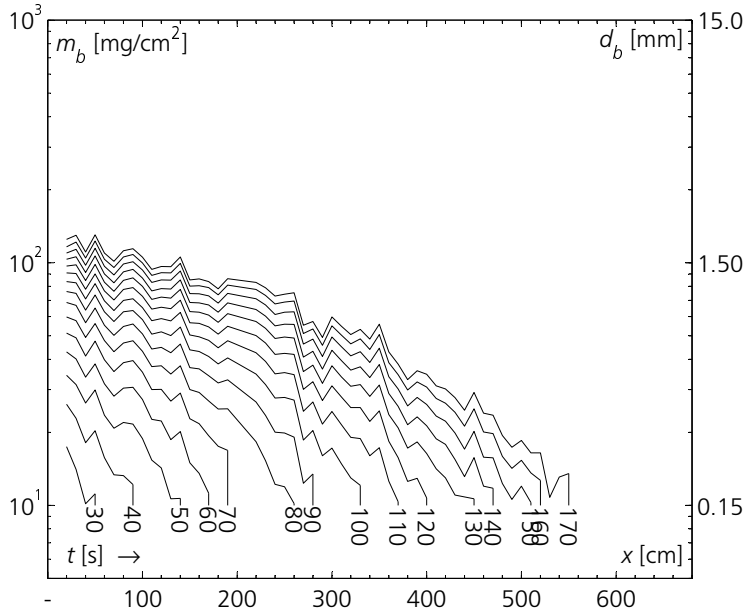

Figure A.13: Measured deposition evolution of experiment A08 along the flume axis, x with time steps of 10 s.

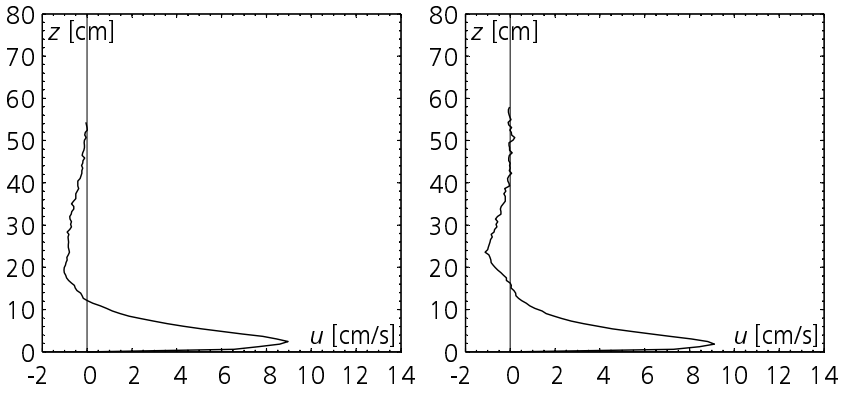

(a) x=120 cm. *(b)* x=220 cm.

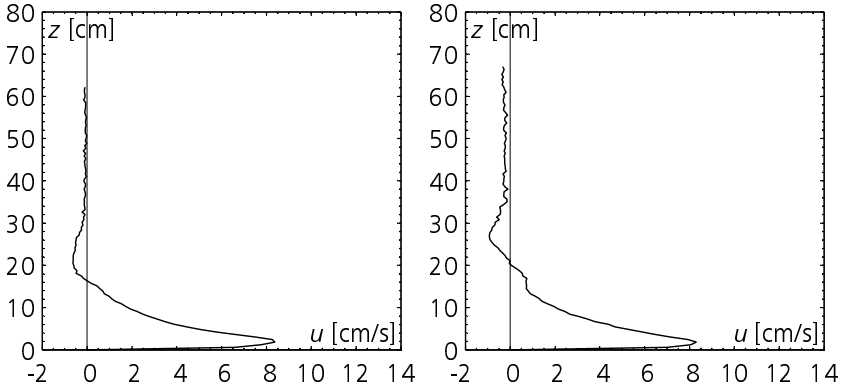

(c) x=320 cm. *(d)* x=420 cm.

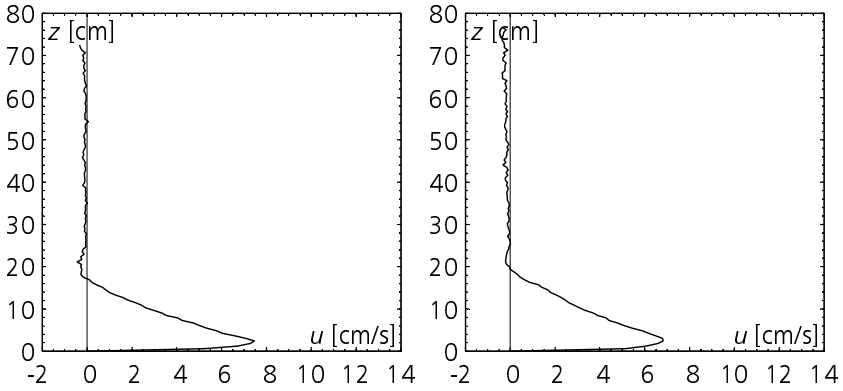

(e) x=520 cm. *(f)* x=610 cm.

Figure A.14: Vertical velocity profiles of experiment A09.

x [cm]	h [cm]	U [cm/s]	h_{max} [cm]	U_{max} [cm/s]	U_{max}/U [–]	h_{max}/h [–]
120	8.09	6.45	2.41	8.96	1.39	0.30
220	8.47	6.25	1.81	9.11	1.46	0.21
320	9.97	5.48	1.81	8.38	1.53	0.18
420	11.24	5.28	1.81	8.30	1.57	0.16
520	11.95	5.11	2.41	7.47	1.46	0.20
610	13.82	4.79	2.41	6.82	1.42	0.17

Table A.8: Integral scale and maximum values of experiment A09.

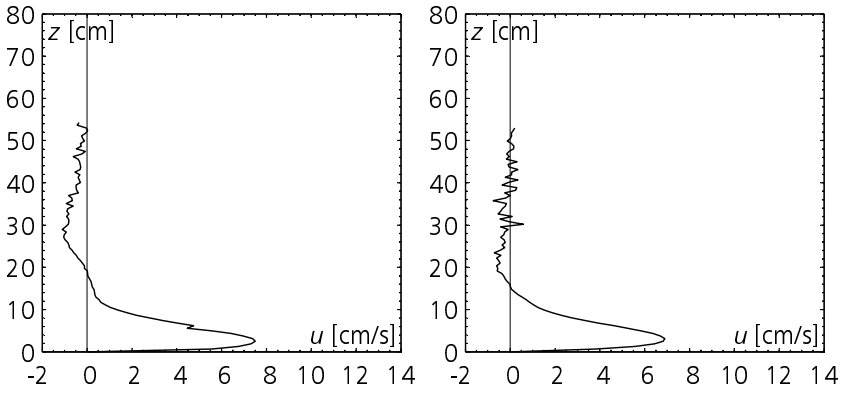

(a) x=120 cm. *(b)* x=220 cm.

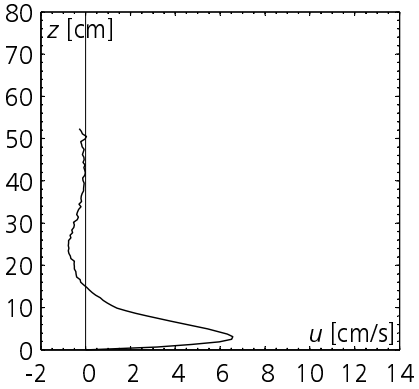

(c) x=320 cm.

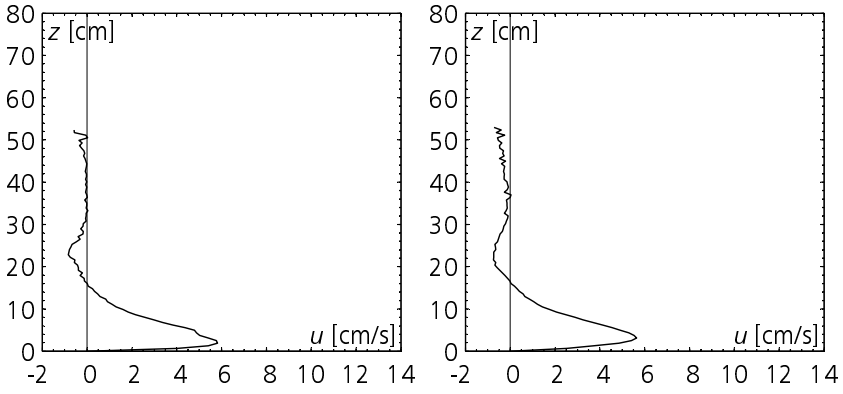

(d) x=520 cm. *(e)* x=610 cm.

Figure A.15: Vertical velocity profiles of experiment A10.

x [cm]	h [cm]	U [cm/s]	h_{max} [cm]	U_{max} [cm/s]	U_{max}/U [–]	h_{max}/h [–]
120	9.58	5.42	2.46	7.51	1.39	0.26
220	9.74	5.03	3.08	6.90	1.37	0.32
320	9.69	4.70	3.08	6.57	1.40	0.32
420	n.d.	n.d.	n.d.	n.d.	n.d.	n.d.
520	10.40	4.16	1.85	5.82	1.40	0.18
610	10.77	3.99	3.08	5.64	1.41	0.29

Table A.9: Integral scale and maximum values of experiment A10.

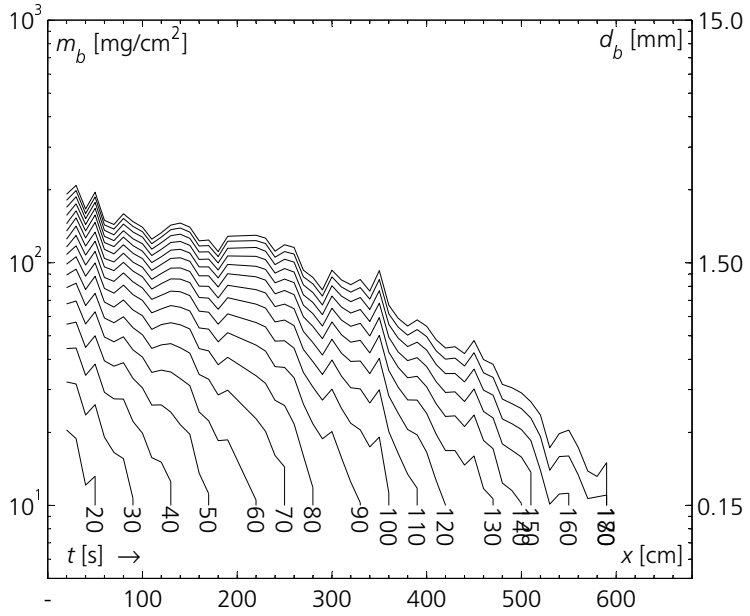

Figure A.16: Measured deposition evolution of experiment A10 along the flume axis, x with time steps of 10 s.

A.2 Flow Over an Obstacle

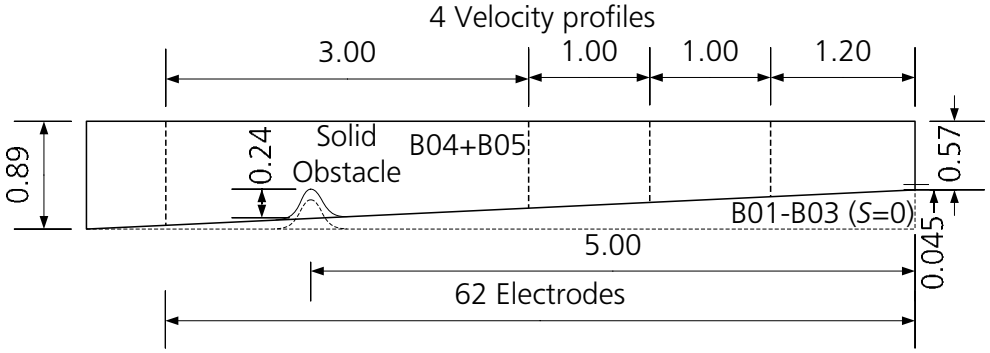

Figure A.17: Experimental set–up for series B with location of velocity profiles.

Exp	S	T_a	ρ_a	T_0	ρ_0	C	g'_0	Q_0
[–]	[%]	[°C]	[g/cm^3]	[°C]	[g/cm^3]	[%]	[m/s^2]	[m^3/s]
B01	-	13.2	0.9996	11.7	1.0031	2.570	0.0342	0.00073
B02	-	12.4	0.9996	11.4	1.0022	1.913	0.0254	0.00080
B03	-	11.9	0.9997	13.3	1.0030	2.432	0.0323	0.00071
B04	4.64	11.8	0.9996	12.0	1.0031	2.614	0.0347	0.00056
B05	4.64	11.6	0.9996	13.6	1.0032	2.637	0.0350	0.00083

Table A.10: Experimental parameters B series.

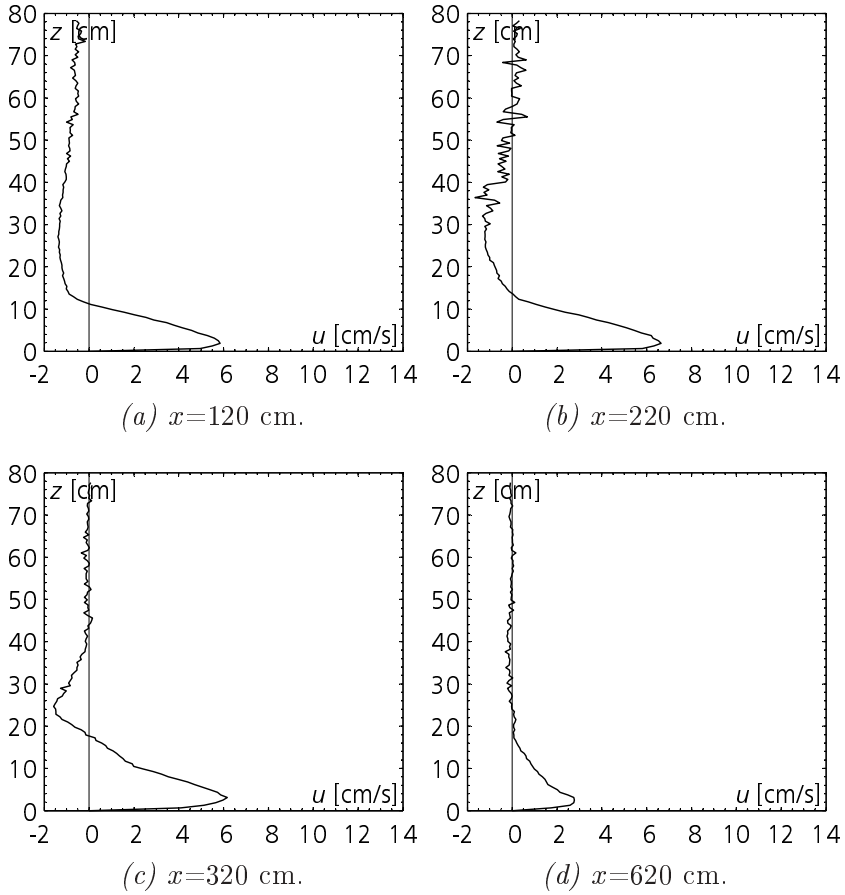

(a) x=120 cm. *(b)* x=220 cm.

(c) x=320 cm. *(d)* x=620 cm.

Figure A.18: Vertical velocity profiles of experiment B01.

x [cm]	h [cm]	U [cm/s]	h_{max} [cm]	U_{max} [cm/s]	U_{max}/U [–]	h_{max}/h [–]
120	8.86	4.53	1.85	5.84	1.29	0.21
220	9.88	5.12	1.85	6.64	1.30	0.19
320	12.40	4.38	3.08	6.17	1.41	0.25
620	12.68	1.80	2.46	2.77	1.54	0.19

Table A.11: Integral scale and maximum values of experiment B01.

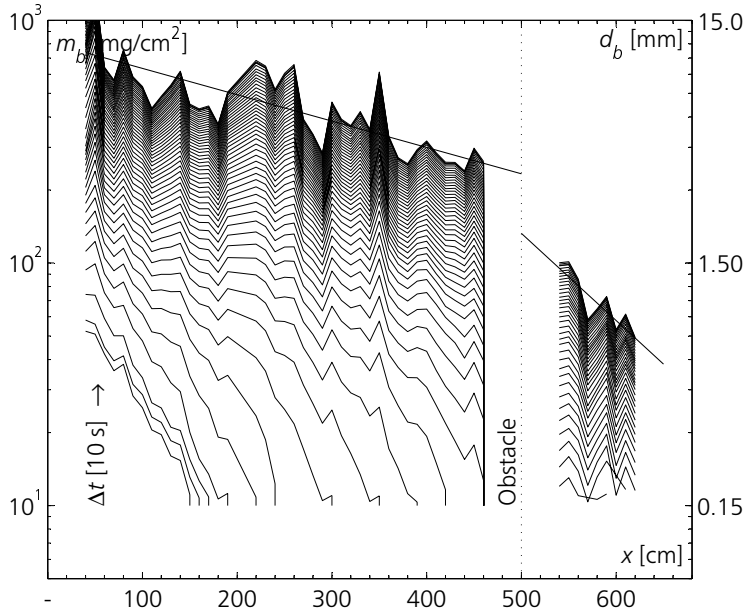

Figure A.19: Measured deposition evolution of experiment B01 along the flume axis, x with time steps of 10 s.

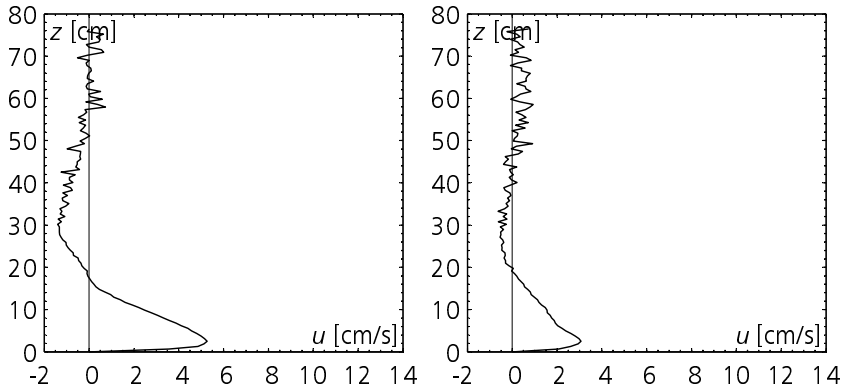

(a) x=220 cm. *(b)* x=620 cm.

Figure A.20: Vertical velocity profiles of experiment B02.

x [cm]	h [cm]	U [cm/s]	h_{max} [cm]	U_{max} [cm/s]	U_{max}/U [–]	h_{max}/h [–]
120	n.d.	n.d.	n.d.	n.d.	n.d.	n.d.
220	12.25	3.89	2.46	5.27	1.35	0.20
320	n.d.	n.d.	n.d.	n.d.	n.d.	n.d.
620	14.04	2.06	3.07	2.46	1.19	0.22

Table A.12: Integral scale and maximum values of experiment B02.

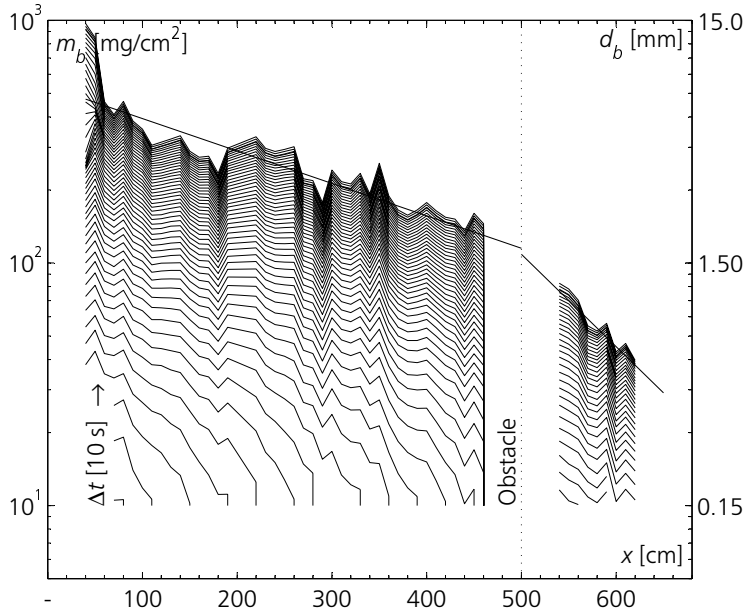

Figure A.21: Measured deposition evolution of experiment B02 along the flume axis, x with time steps of 10 s.

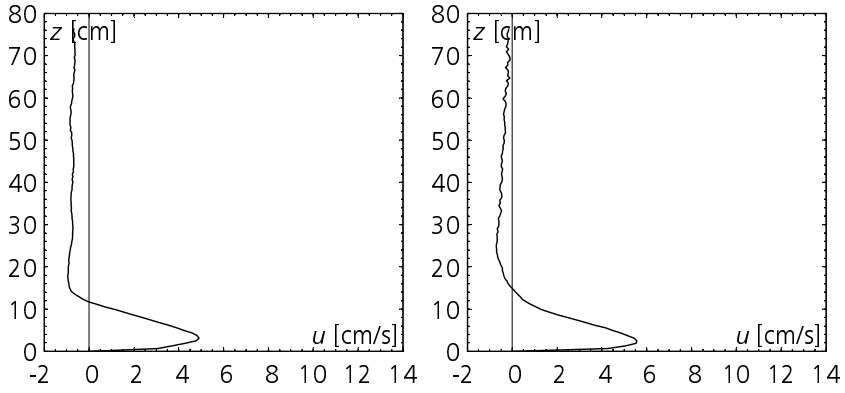

(a) x=120 cm.

(b) x=220 cm.

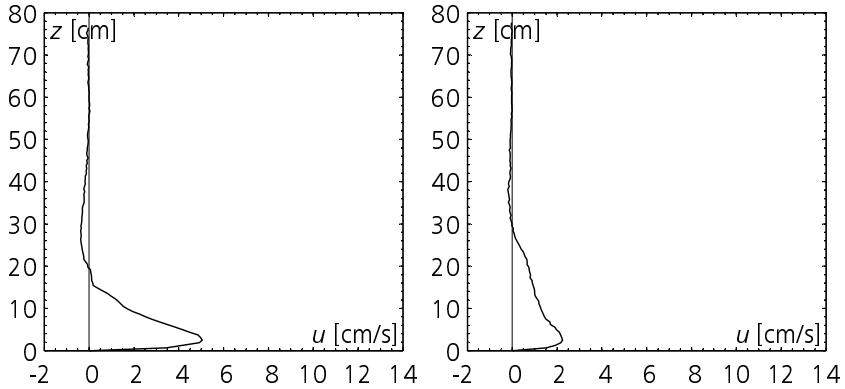

(c) x=320 cm.

(d) x=620 cm.

Figure A.22: Vertical velocity profiles of experiment B03.

x [cm]	h [cm]	U [cm/s]	h_{max} [cm]	U_{max} [cm/s]	U_{max}/U [–]	h_{max}/h [–]
120	9.27	3.74	3.08	4.91	1.31	0.33
220	9.82	4.15	2.46	5.56	1.34	0.25
320	11.68	3.55	2.46	5.05	1.42	0.21
620	21.24	1.43	2.46	2.25	1.57	0.12

Table A.13: Integral scale and maximum values of experiment B03.

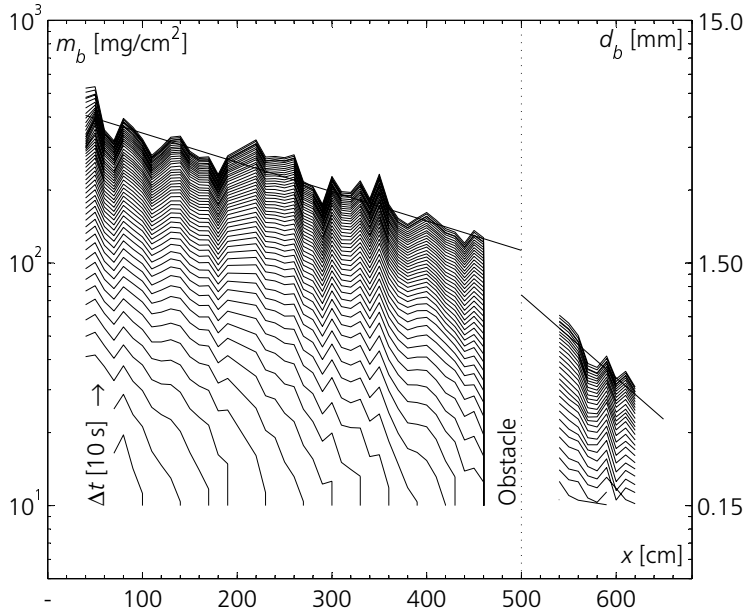

Figure A.23: Measured deposition evolution of experiment B03 along the flume axis, x with time steps of 10 s.

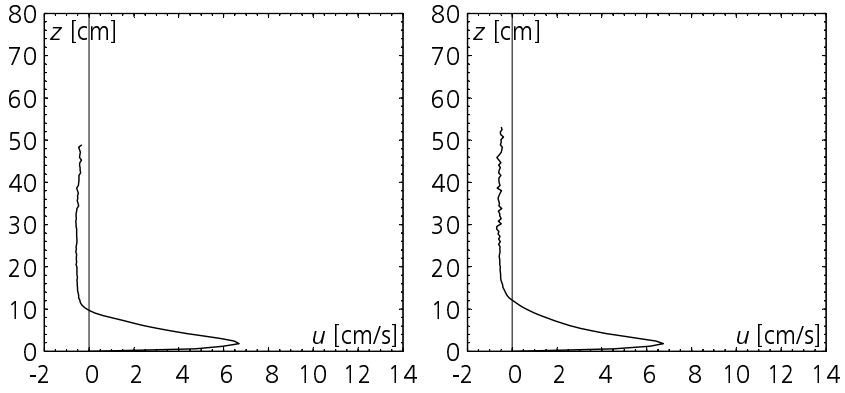

(a) x=120 cm.

(b) x=220 cm.

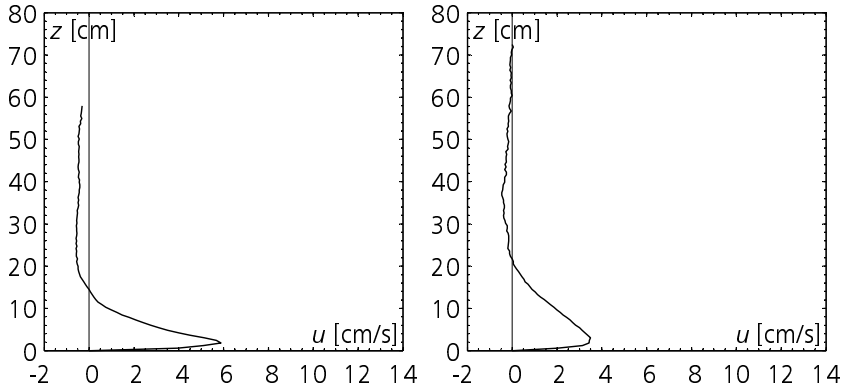

(c) x=320 cm.

(d) x=620 cm.

Figure A.24: Vertical velocity profiles of experiment B04.

x [cm]	h [cm]	U [cm/s]	h_{max} [cm]	U_{max} [cm/s]	U_{max}/U [–]	h_{max}/h [–]
120	6.82	4.83	1.81	6.69	1.39	0.27
220	7.73	4.54	1.81	6.75	1.49	0.23
320	8.72	3.92	1.81	5.89	1.50	0.21
620	14.68	2.48	3.02	3.49	1.41	0.21

Table A.14: Integral scale and maximum values of experiment B04.

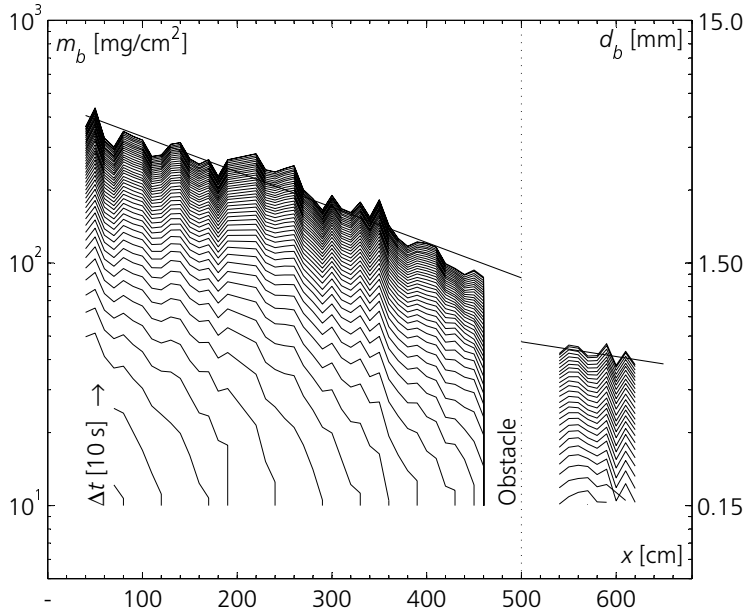

Figure A.25: Measured deposition evolution of experiment B04 along the flume axis, x with time steps of 10 s.

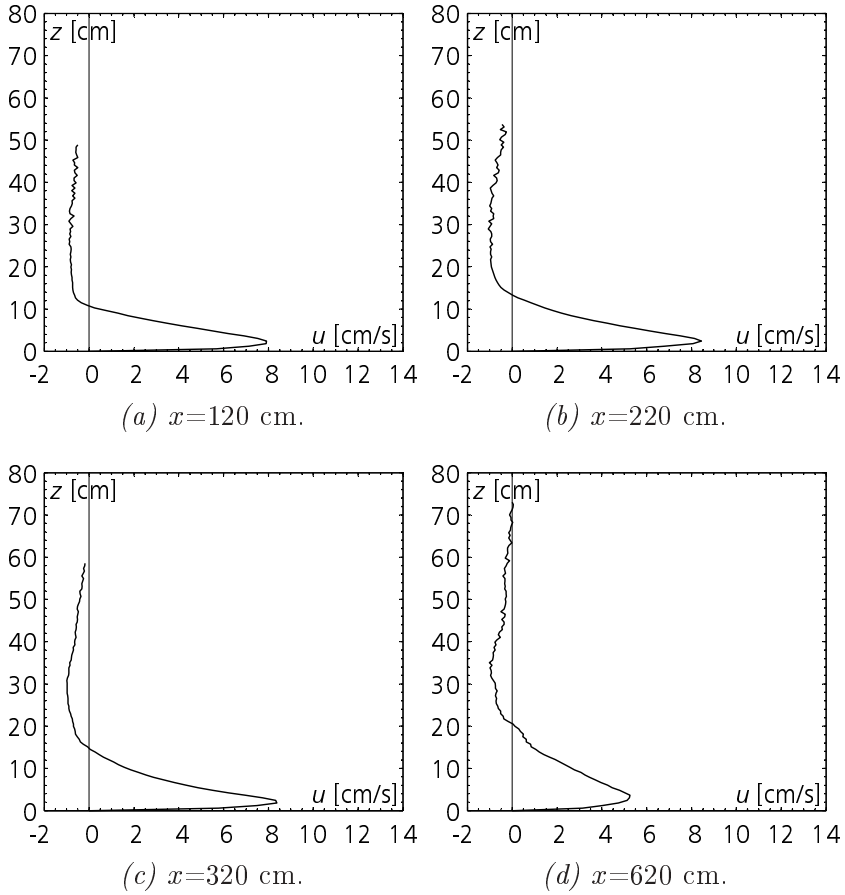

(a) x=120 cm. *(b)* x=220 cm.

(c) x=320 cm. *(d)* x=620 cm.

Figure A.26: Vertical velocity profiles of experiment B05.

x [cm]	h [cm]	U [cm/s]	h_{max} [cm]	U_{max} [cm/s]	U_{max}/U [–]	h_{max}/h [–]
120	7.86	5.92	2.41	7.92	1.34	0.31
220	9.17	5.93	2.41	8.45	1.42	0.26
320	9.47	5.69	1.81	8.38	1.47	0.19
620	14.00	3.69	3.62	5.26	1.43	0.26

Table A.15: Integral scale and maximum values of experiment B05.

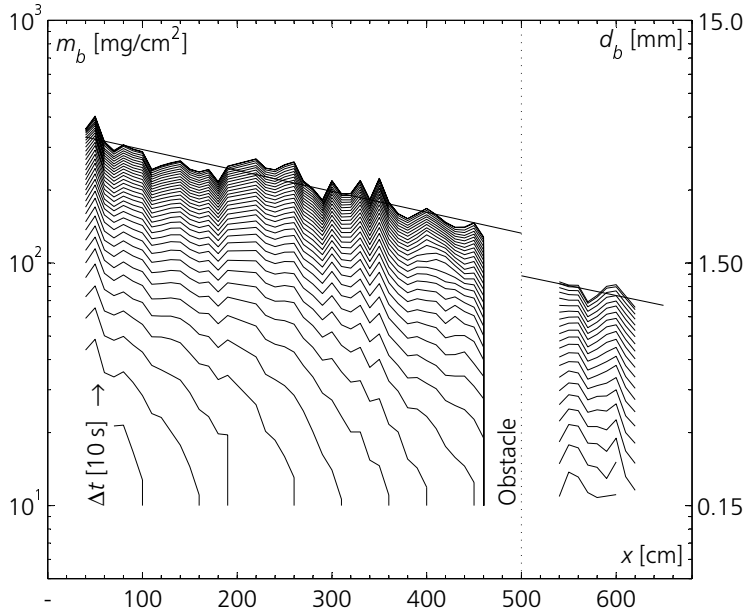

Figure A.27: Measured deposition evolution of experiment B05 along the flume axis, x with time steps of 10 s.

A.3 Flow Through a Screen

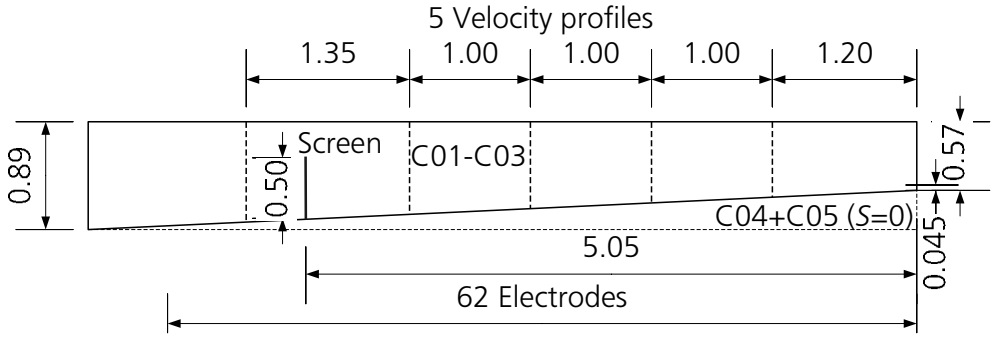

Figure A.28: Experimental set–up for series C with locations of velocity profiles.

Exp	S	T_a	ρ_a	T_0	ρ_0	C	g'_0	Q_0
[–]	[%]	[°C]	[g/cm^3]	[°C]	[g/cm^3]	[%]	[m/s^2]	[m^3/s]
C01	4.64	12.5	0.9994	11.8	1.0041	3.437	0.0457	0.00079
C02	4.64	11.2	0.9995	11.1	1.0049	3.956	0.0526	0.00070
C03	4.64	11.2	0.9995	10.5	1.0040	3.292	0.0438	0.00068
C04	-	10.9	0.9997	11.0	1.0029	2.395	0.0318	0.00063
C05	-	11.8	0.9997	11.0	1.0030	2.454	0.0326	0.00068

Table A.16: Experimental parameters C series.

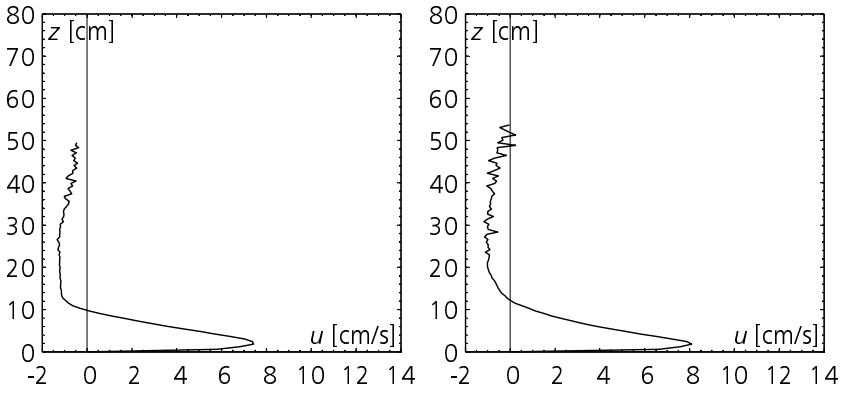

(a) x=120 cm. *(b)* x=220 cm.

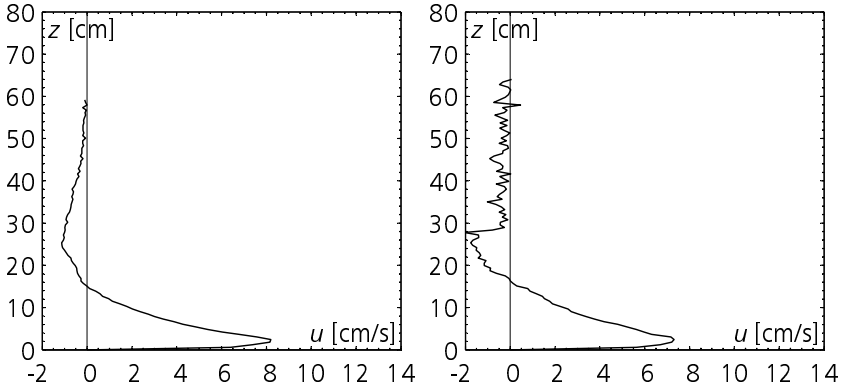

(c) x=320 cm. *(d)* x=420 cm.

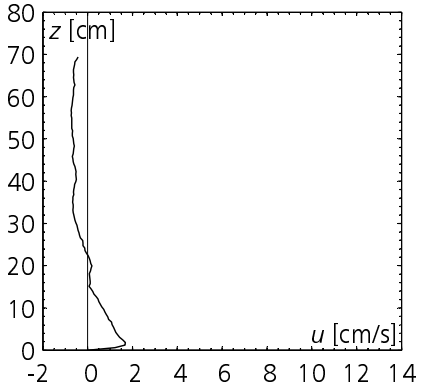

(e) x=555 cm.

Figure A.29: Vertical velocity profiles of experiment C01.

x [cm]	h [cm]	U [cm/s]	h_{max} [cm]	U_{max} [cm/s]	U_{max}/U [–]	h_{max}/h [–]
120	7.34	5.67	1.81	7.43	1.31	0.25
220	8.19	5.80	1.81	8.10	1.40	0.22
320	9.76	5.60	2.41	8.20	1.46	0.25
420	11.24	5.08	2.41	7.31	1.44	0.21
555	13.23	1.07	1.81	1.68	1.57	0.14

Table A.17: Integral scale and maximum values of experiment C01.

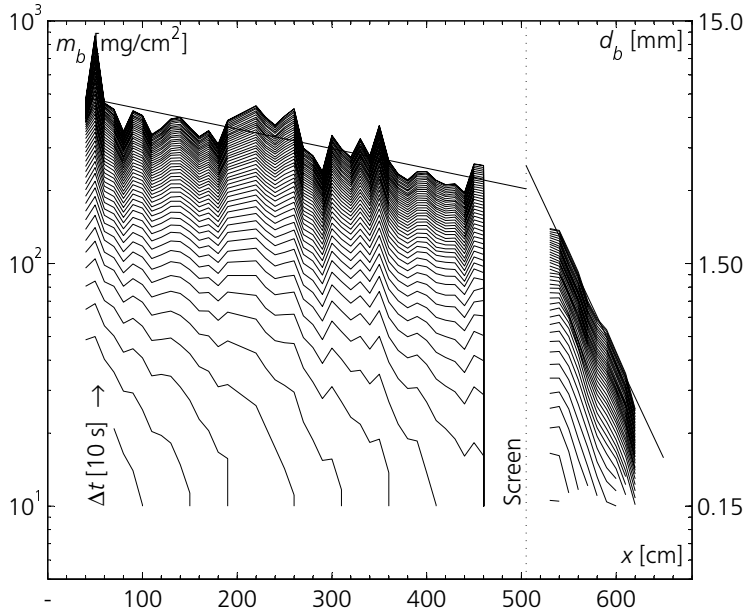

Figure A.30: Measured deposition evolution of experiment C01 along the flume axis, x with time steps of 10 s.

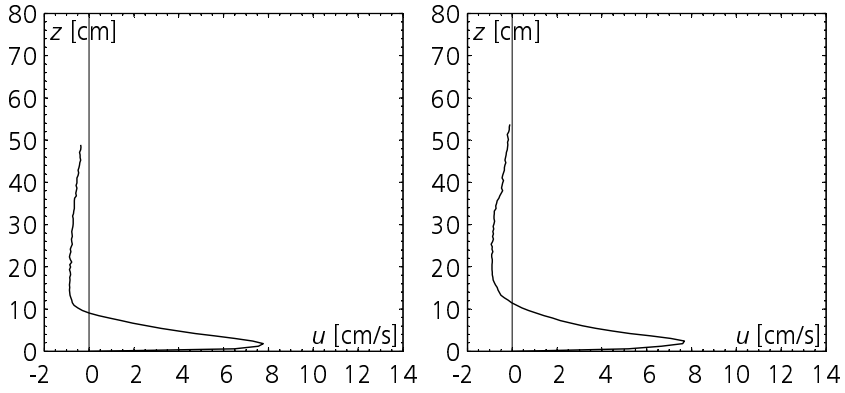

(a) x=120 cm.

(b) x=220 cm.

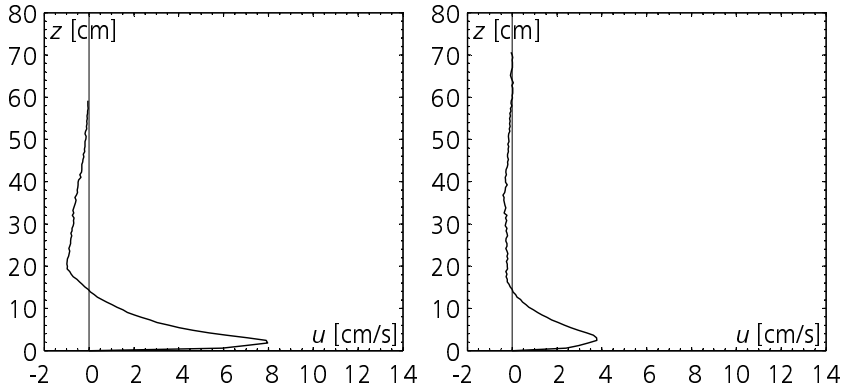

(c) x=320 cm.

(d) x=555 cm.

Figure A.31: Vertical velocity profiles of experiment C02.

x [cm]	h [cm]	U [cm/s]	h_{max} [cm]	U_{max} [cm/s]	U_{max}/U [–]	h_{max}/h [–]
120	6.43	5.76	1.81	7.78	1.35	0.28
220	7.59	5.42	2.41	7.68	1.42	0.32
320	8.82	5.33	1.81	7.97	1.50	0.21
420	n.d.	n.d.	n.d.	n.d.	n.d.	n.d.
555	9.61	2.69	2.41	3.78	1.41	0.25

Table A.18: Integral scale and maximum values of experiment C02.

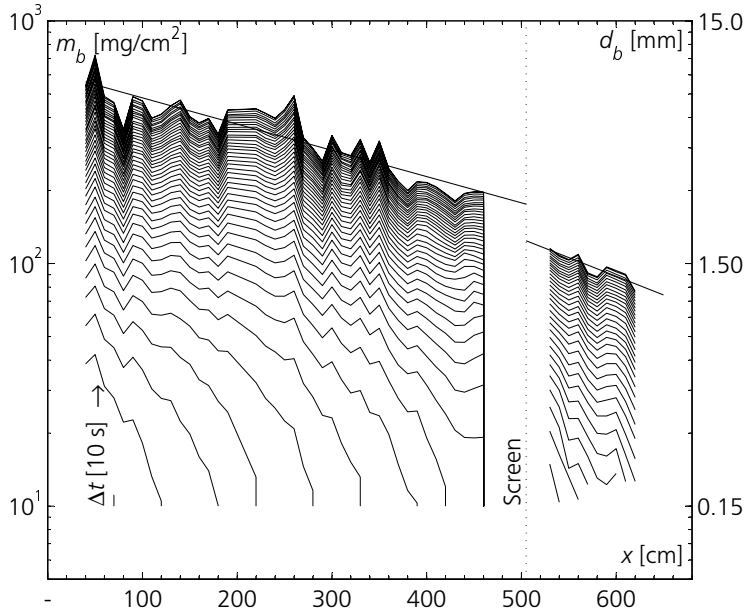

Figure A.32: Measured deposition evolution of experiment C02 along the flume axis, x with time steps of 10 s.

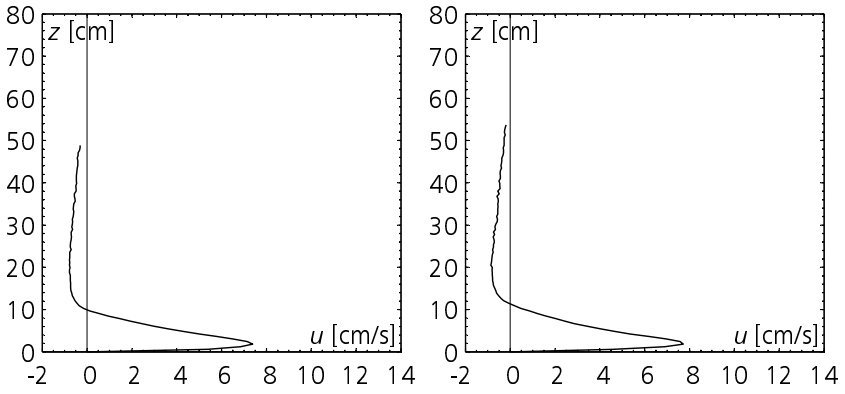

(a) x=120 cm. *(b)* x=220 cm.

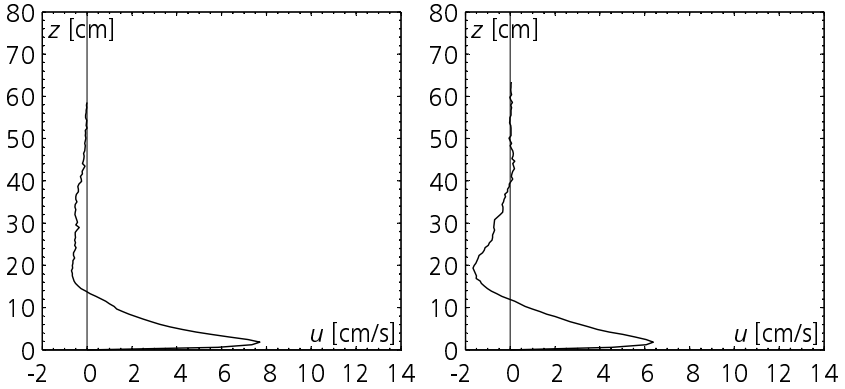

(c) x=320 cm. *(d)* x=420 cm.

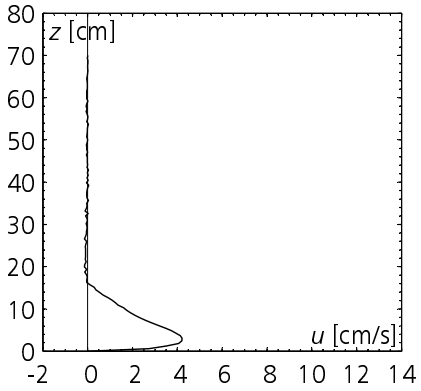

(e) x=555 cm.

Figure A.33: Vertical velocity profiles of experiment C03.

x [cm]	h [cm]	U [cm/s]	h_{max} [cm]	U_{max} [cm/s]	U_{max}/U [–]	h_{max}/h [–]
120	7.10	5.37	1.81	7.39	1.38	0.25
220	7.80	5.39	1.81	7.72	1.43	0.23
320	8.76	5.05	1.81	7.71	1.53	0.21
420	8.35	4.43	1.81	6.38	1.44	0.22
555	11.67	3.07	3.02	4.22	1.37	0.26

Table A.19: Integral scale and maximum values of experiment C03.

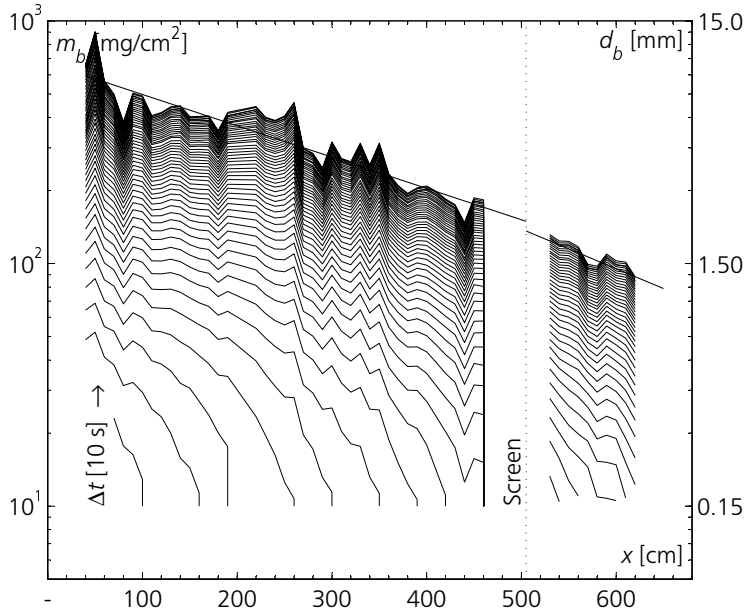

Figure A.34: Measured deposition evolution of experiment C03 along the flume axis, x with time steps of 10 s.

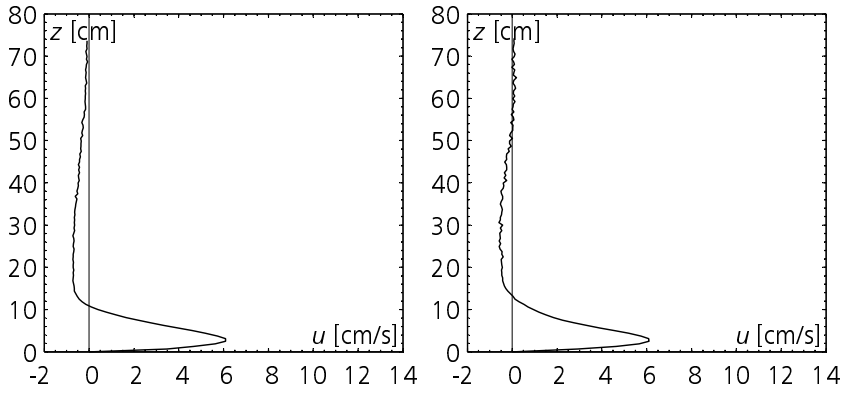

(a) x=120 cm. *(b)* x=220 cm.

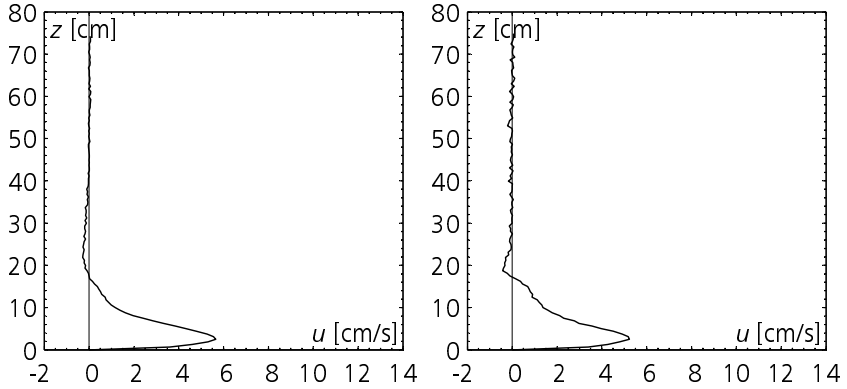

(c) x=320 cm. *(d)* x=420 cm.

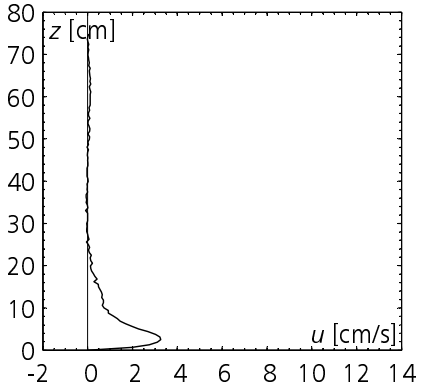

(e) x=555 cm.

Figure A.35: Vertical velocity profiles of experiment C04.

x [cm]	h [cm]	U [cm/s]	h_{max} [cm]	U_{max} [cm/s]	U_{max}/U [–]	h_{max}/h [–]
120	7.96	4.56	2.50	6.09	1.34	0.31
220	8.65	4.37	2.50	6.10	1.40	0.29
320	10.18	3.91	2.50	5.66	1.45	0.25
420	11.40	3.49	2.50	5.23	1.50	0.22
555	12.63	2.01	2.50	3.26	1.62	0.20

Table A.20: Integral scale and maximum values of experiment C04.

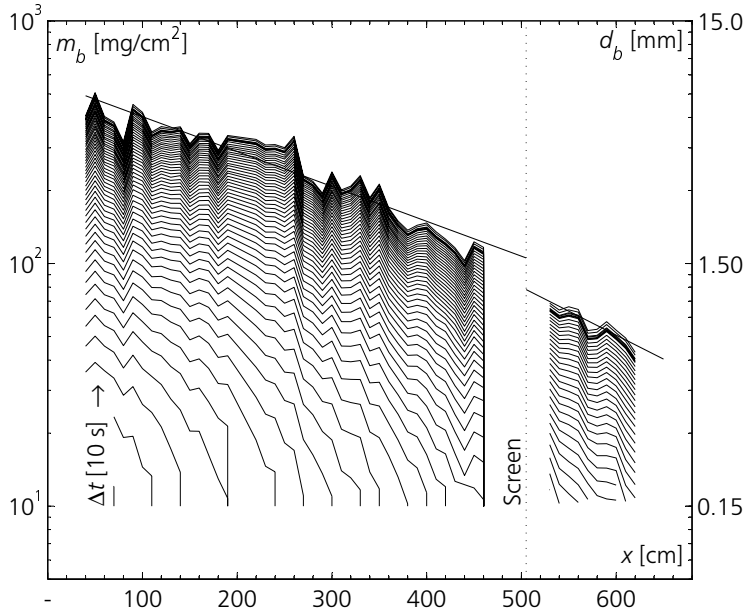

Figure A.36: Measured deposition evolution of experiment C04 along the flume axis, x with time steps of 10 s.

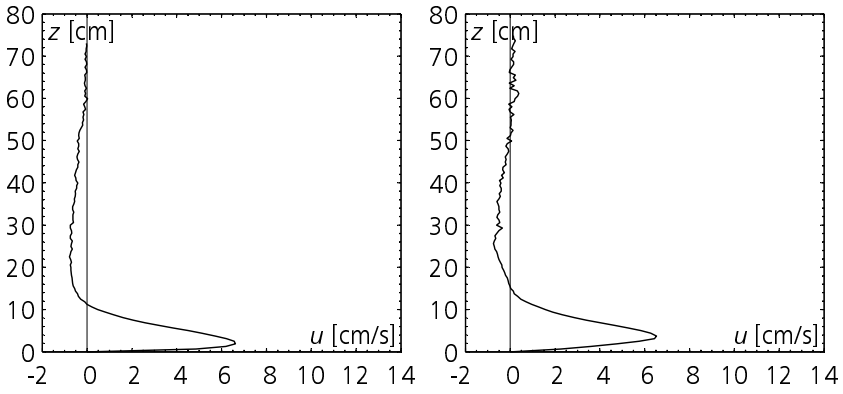

(a) x=120 cm. *(b)* x=220 cm.

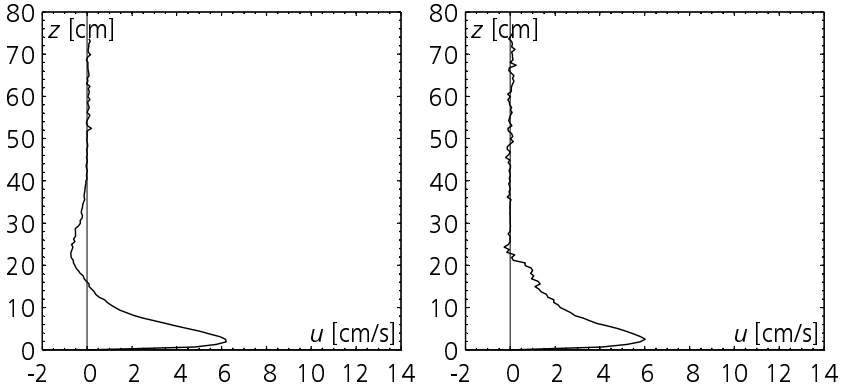

(c) x=320 cm. *(d)* x=420 cm.

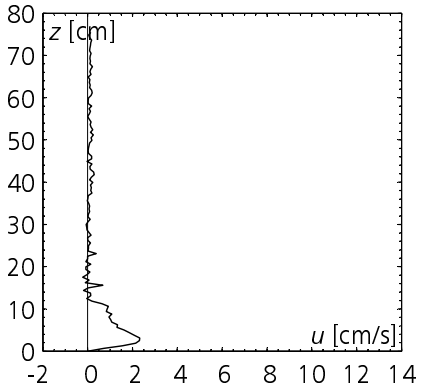

(e) x=555 cm.

Figure A.37: Vertical velocity profiles of experiment C05.

x [cm]	h [cm]	U [cm/s]	h_{max} [cm]	U_{max} [cm/s]	U_{max}/U [–]	h_{max}/h [–]
120	7.84	4.97	1.87	6.62	1.33	0.24
220	9.69	4.62	3.74	6.52	1.41	0.39
320	9.62	4.44	1.87	6.20	1.40	0.19
420	14.83	3.81	2.50	6.03	1.58	0.17
555	9.86	1.57	3.12	2.33	1.48	0.32

Table A.21: Integral scale and maximum values of experiment C05.

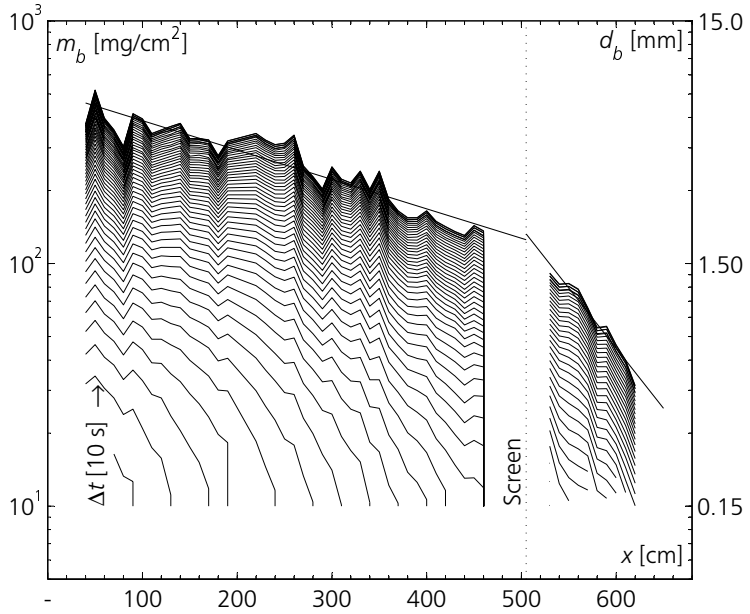

Figure A.38: Measured deposition evolution of experiment C05 along the flume axis, x with time steps of 10 s.

A.4 Flow Through Multiple Jets

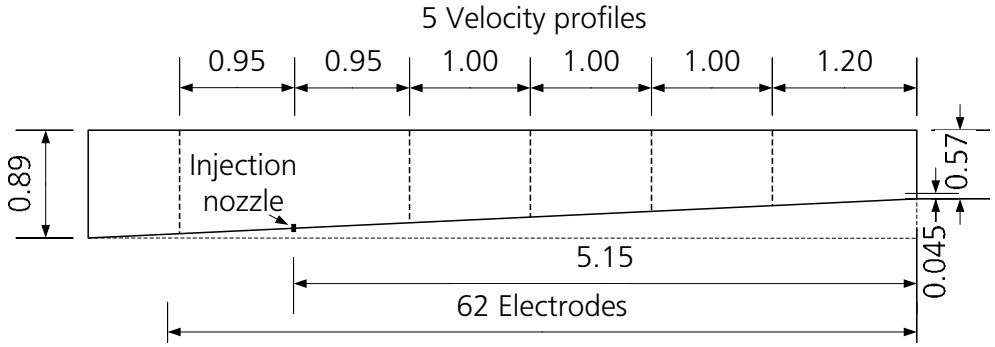

Figure A.39: Experimental set–up for series D and E with locations of velocity profiles.

Exp	S	T_a	ρ_a	T_0	ρ_0	C	g_0'	Q_0
[–]	[%]	[°C]	[g/cm^3]	[°C]	[g/cm^3]	[%]	[m/s^2]	[m^3/s]
D01	-	12.7	0.9996	12.0	1.0033	2.769	0.0368	0.00066
D02	-	12.6	0.9994	11.2	1.0032	2.765	0.0368	0.00073
D03	-	12.1	0.9995	11.2	1.0024	2.147	0.0286	0.00074
D04	4.64	12.4	0.9995	11.9	1.0033	2.818	0.0375	0.00081
E01	4.64	13.6	0.9992	12.2	1.0033	2.990	0.0399	0.00078
E02	4.64	13.2	0.9993	11.6	1.0030	2.785	0.0371	0.00066
E03	-	13.3	0.9994	12.6	1.0033	2.890	0.0385	0.00072
E04	-	10.9	0.9995	11.1	1.0033	2.790	0.0371	0.00076

Table A.22: Experimental parameters D and E series.

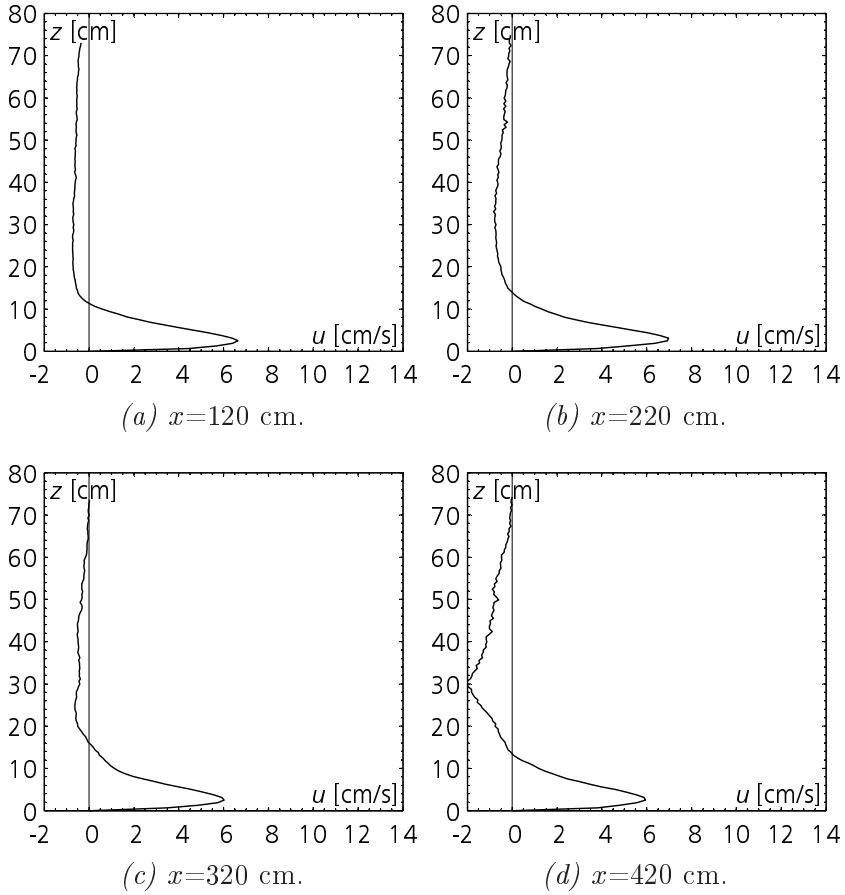

(a) x=120 cm. *(b)* x=220 cm.

(c) x=320 cm. *(d)* x=420 cm.

Figure A.40: Vertical velocity profiles of experiment D01.

x [cm]	h [cm]	U [cm/s]	h_{max} [cm]	U_{max} [cm/s]	U_{max}/U [–]	h_{max}/h [–]
120	8.03	4.91	2.50	6.64	1.35	0.31
220	9.11	4.97	3.12	6.97	1.40	0.34
320	9.64	4.20	2.50	6.03	1.44	0.26
420	9.24	4.30	2.50	5.95	1.38	0.27
610	n.d.	n.d.	n.d.	n.d.	n.d.	n.d.

Table A.23: Integral scale and maximum values of experiment D01.

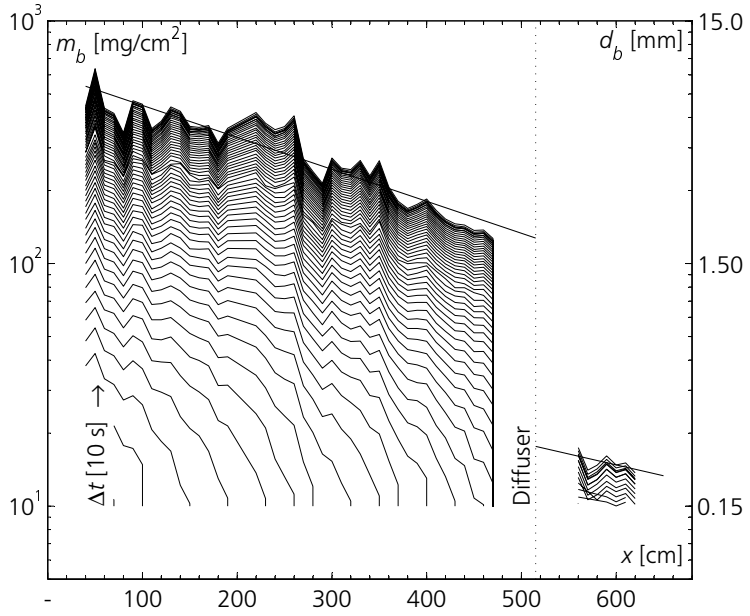

Figure A.41: Measured deposition evolution of experiment D01 along the flume axis, x with time steps of 10 s.

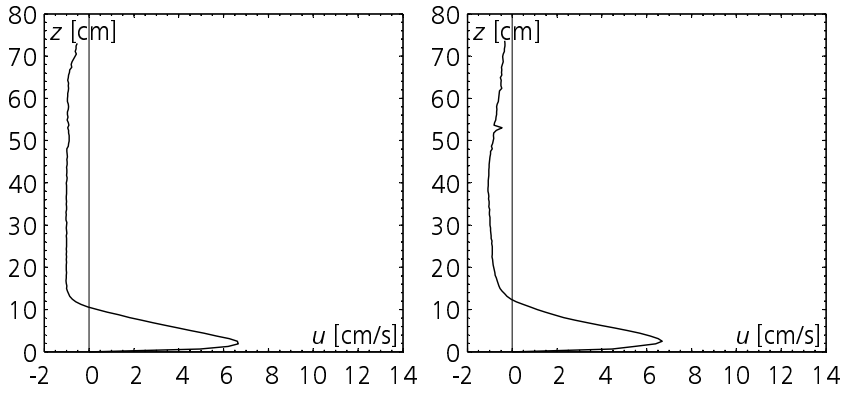

(a) x=120 cm. *(b)* x=220 cm.

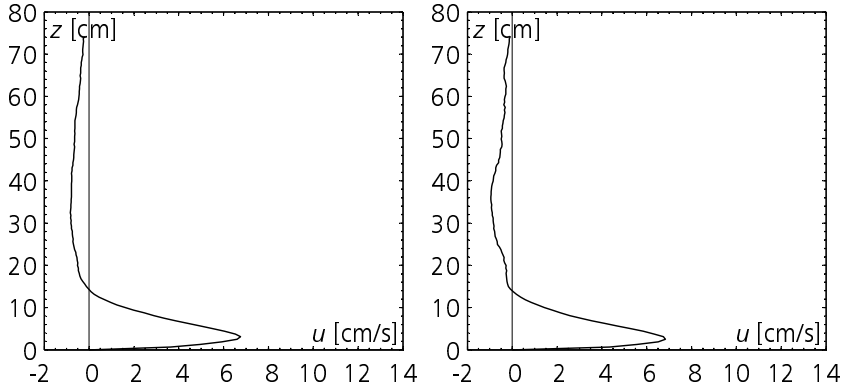

(c) x=320 cm. *(d)* x=420 cm.

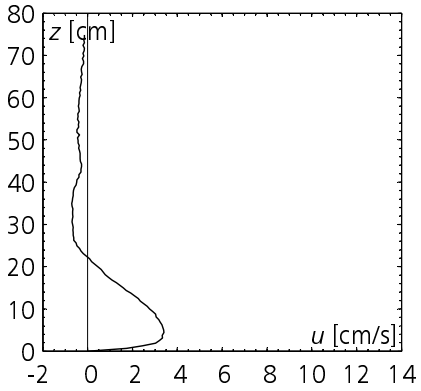

(e) x=610 cm.

Figure A.42: Vertical velocity profiles of experiment D02.

x [cm]	h [cm]	U [cm/s]	h_{max} [cm]	U_{max} [cm/s]	U_{max}/U [–]	h_{max}/h [–]
120	7.91	5.01	1.87	6.65	1.33	0.24
220	8.85	4.94	2.50	6.69	1.35	0.28
320	9.72	4.86	3.12	6.76	1.39	0.32
420	9.42	4.94	2.50	6.84	1.38	0.27
610	17.33	2.66	4.37	3.41	1.28	0.25

Table A.24: Integral scale and maximum values of experiment D02.

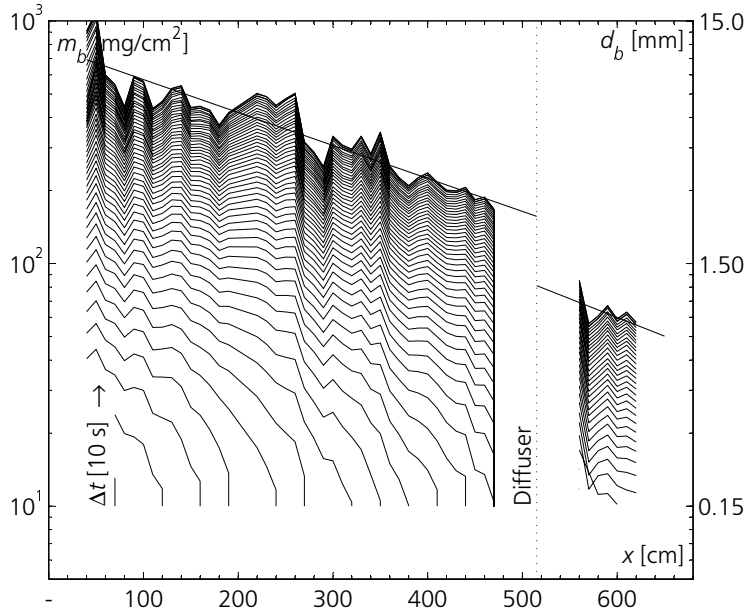

Figure A.43: Measured deposition evolution of experiment D02 along the flume axis, x with time steps of 10 s.

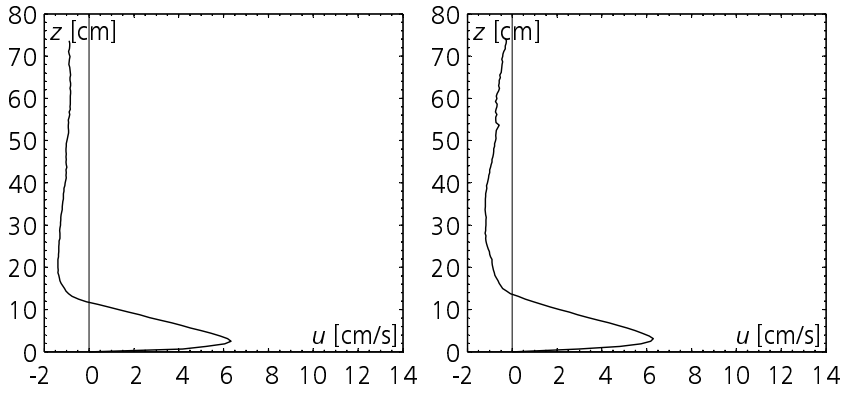

(a) x=120 cm. *(b)* x=220 cm.

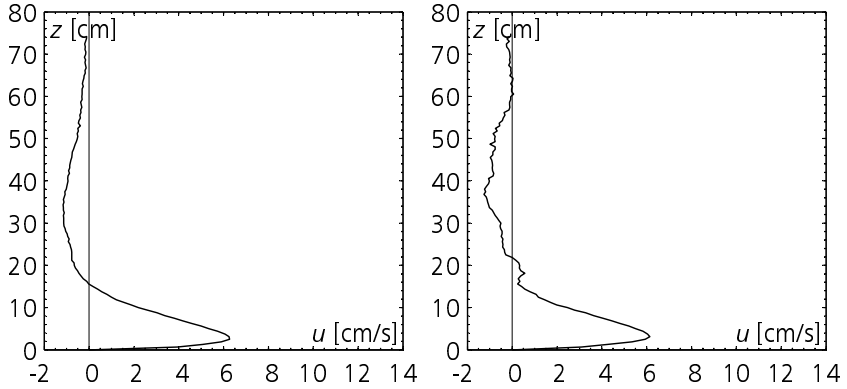

(c) x=320 cm. *(d)* x=420 cm.

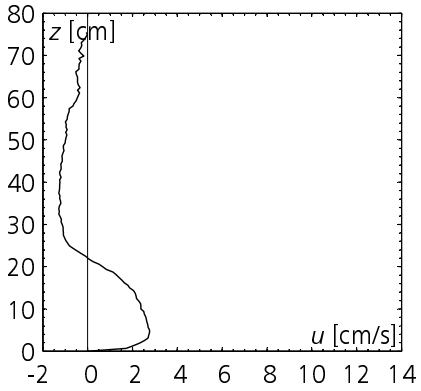

(e) x=610 cm.

Figure A.44: Vertical velocity profiles of experiment D03.

x [cm]	h [cm]	U [cm/s]	h_{max} [cm]	U_{max} [cm/s]	U_{max}/U [–]	h_{max}/h [–]
120	9.17	4.74	2.50	6.33	1.34	0.27
220	10.32	4.68	3.12	6.30	1.35	0.30
320	11.07	4.59	2.50	6.27	1.37	0.23
420	12.42	4.30	3.12	6.15	1.43	0.25
610	19.08	2.25	4.99	2.76	1.23	0.26

Table A.25: Integral scale and maximum values of experiment D03.

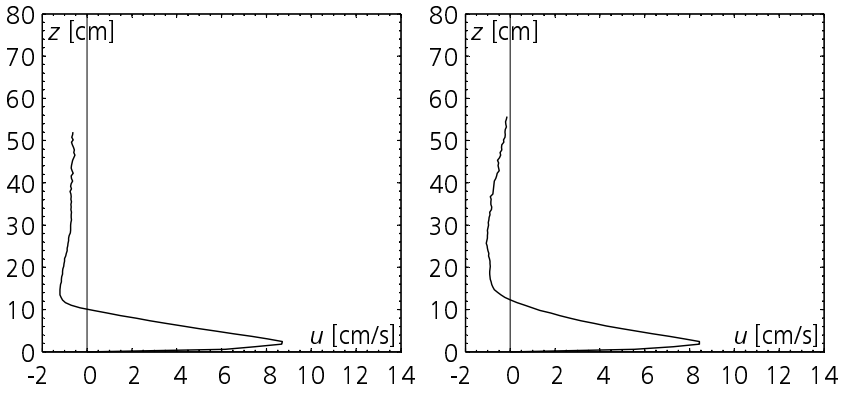

(a) x=120 cm. *(b)* x=220 cm.

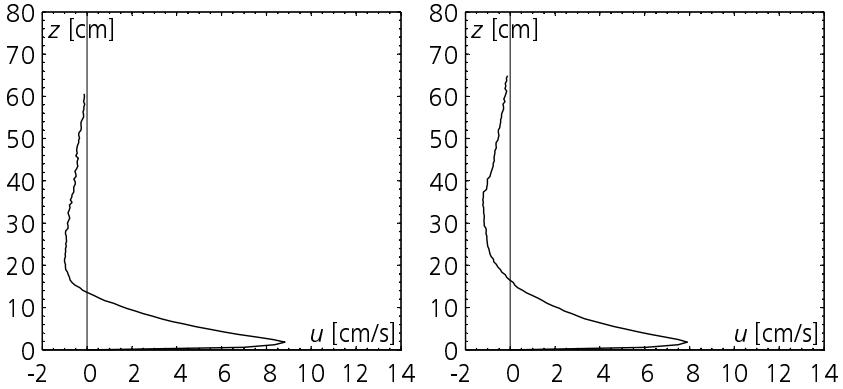

(c) x=320 cm. *(d)* x=420 cm.

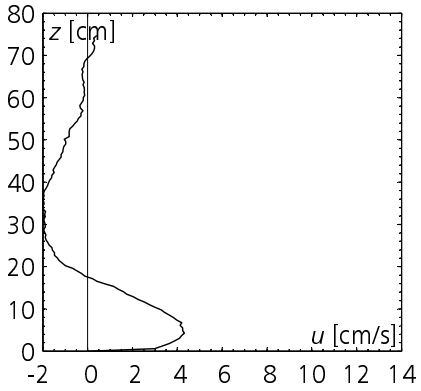

(e) x=610 cm.

Figure A.45: Vertical velocity profiles of experiment D04.

x [cm]	h [cm]	U [cm/s]	h_{max} [cm]	U_{max} [cm/s]	U_{max}/U [–]	h_{max}/h [–]
120	7.59	6.45	2.45	8.72	1.35	0.32
220	8.56	5.97	2.45	8.45	1.42	0.29
320	9.10	5.99	1.84	8.83	1.47	0.20
420	10.49	5.21	1.84	7.91	1.52	0.18
610	14.51	3.44	4.29	4.32	1.26	0.30

Table A.26: Integral scale and maximum values of experiment D04.

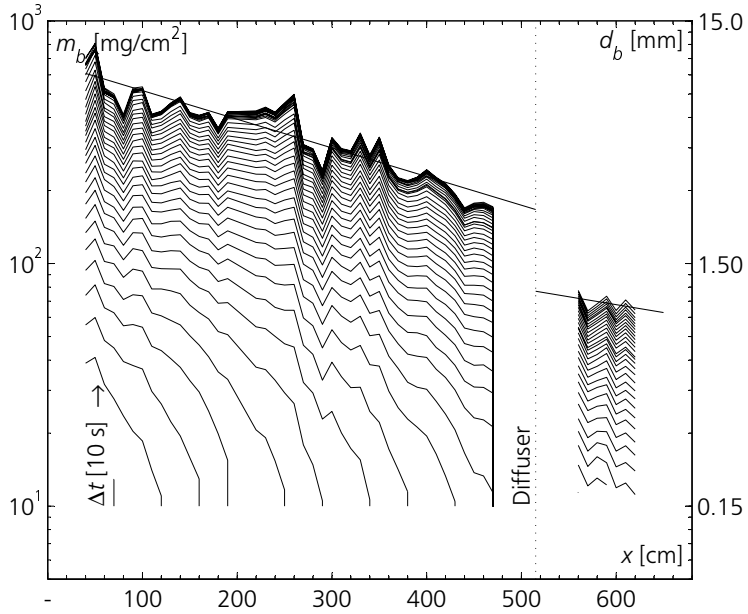

Figure A.46: Measured deposition evolution of experiment D04 along the flume axis, x with time steps of 10 s.

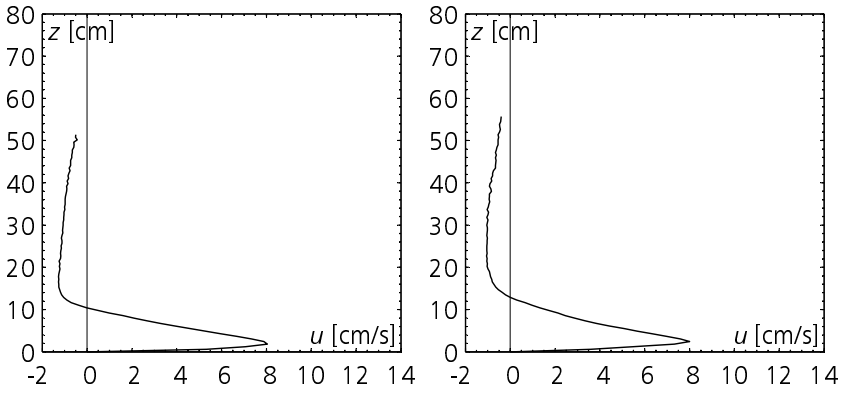

(a) x=120 cm. *(b)* x=220 cm.

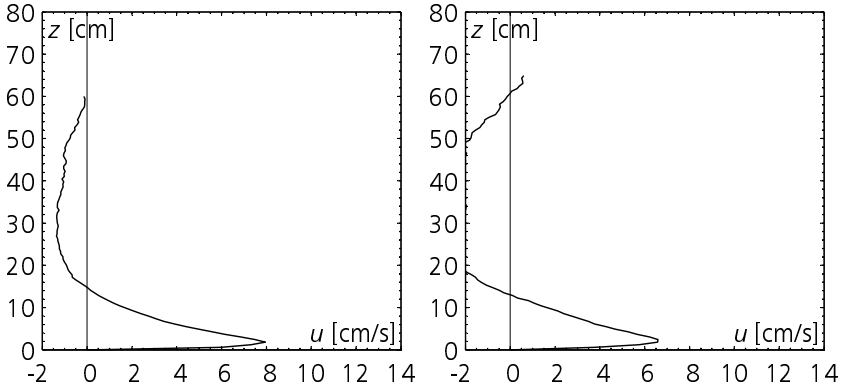

(c) x=320 cm. *(d)* x=420 cm.

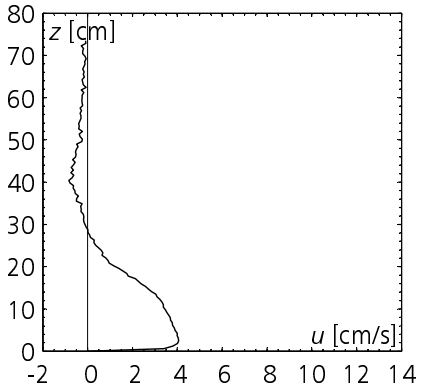

(e) x=610 cm.

Figure A.47: Vertical velocity profiles of experiment E01.

x [cm]	h [cm]	U [cm/s]	h_{max} [cm]	U_{max} [cm/s]	U_{max}/U [–]	h_{max}/h [–]
120	7.74	5.85	1.84	8.04	1.37	0.24
220	9.09	5.42	2.45	8.01	1.48	0.27
320	9.53	5.29	1.84	7.95	1.50	0.19
420	9.58	4.62	2.45	6.60	1.43	0.26
610	21.00	3.19	2.45	4.06	1.27	0.12

Table A.27: Integral scale and maximum values of experiment E01.

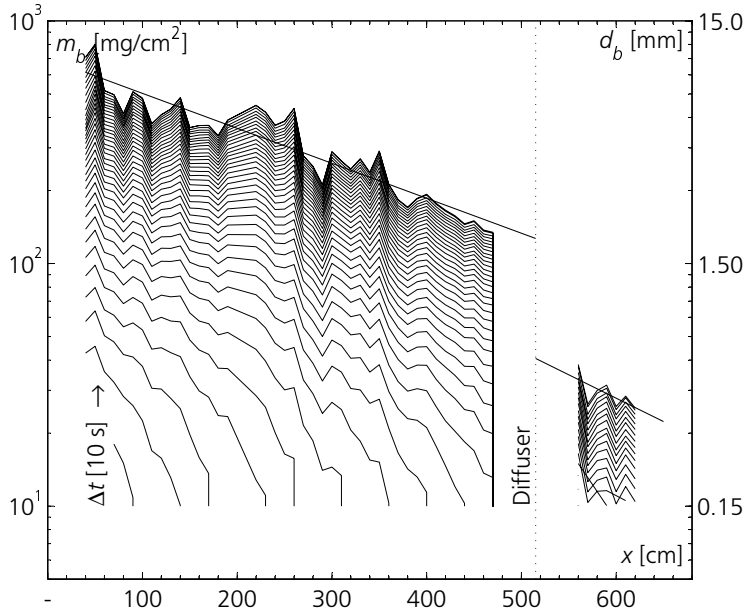

Figure A.48: Measured deposition evolution of experiment E01 along the flume axis, x with time steps of 10 s.

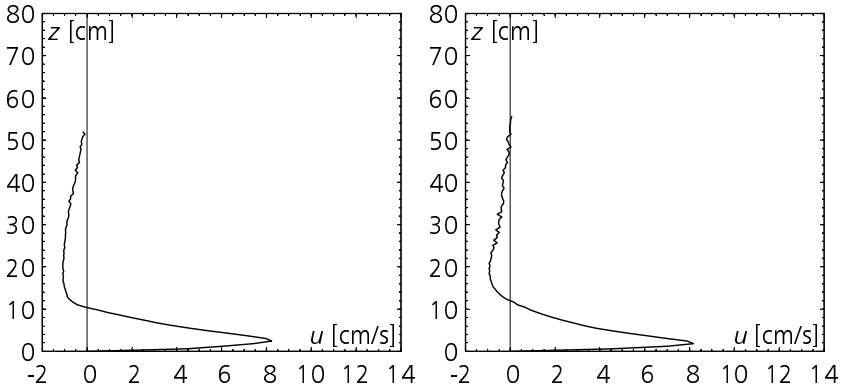

(a) x=120 cm. *(b)* x=220 cm.

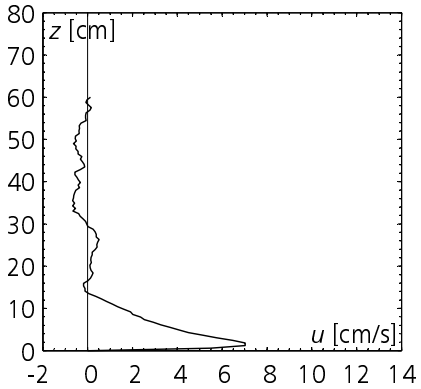

(c) x=320 cm.

Figure A.49: Vertical velocity profiles of experiment E02.

x [cm]	h [cm]	U [cm/s]	h_{max} [cm]	U_{max} [cm/s]	U_{max}/U [–]	h_{max}/h [–]
120	7.59	5.84	2.45	8.24	1.41	0.32
220	7.85	5.46	1.84	8.17	1.50	0.23
320	9.32	4.65	1.22	7.03	1.51	0.13
420	n.d.	n.d.	n.d.	n.d.	n.d.	n.d.
610	n.d.	n.d.	n.d.	n.d.	n.d.	n.d.

Table A.28: Integral scale and maximum values of experiment E02.

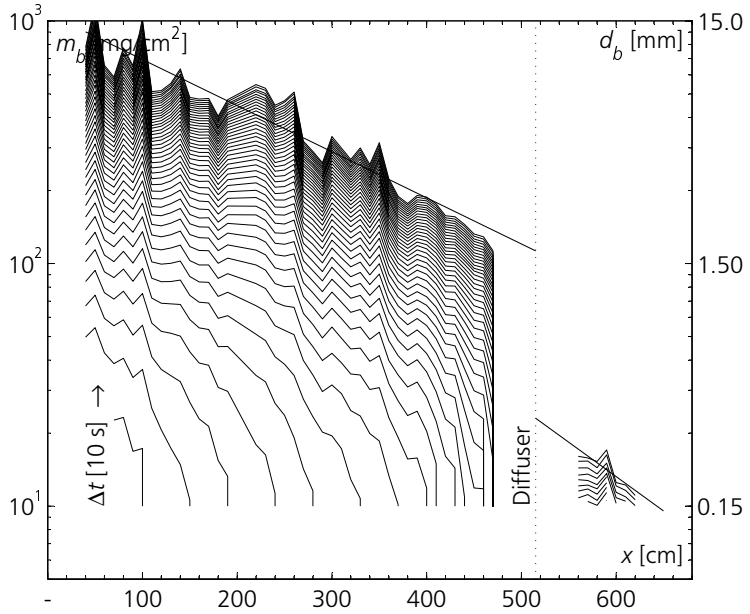

Figure A.50: Measured deposition evolution of experiment E02 along the flume axis, x with time steps of 10 s.

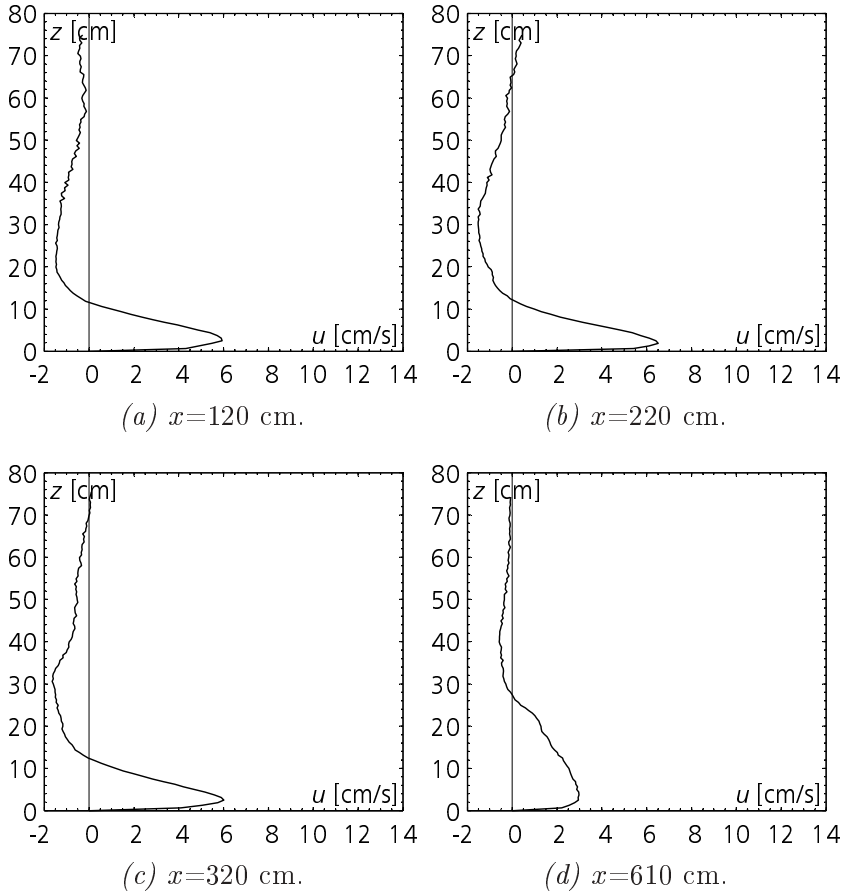

(a) x=120 cm. *(b)* x=220 cm.

(c) x=320 cm. *(d)* x=610 cm.

Figure A.51: Vertical velocity profiles of experiment E03.

x [cm]	h [cm]	U [cm/s]	h_{max} [cm]	U_{max} [cm/s]	U_{max}/U [–]	h_{max}/h [–]
120	8.88	4.57	2.50	5.94	1.30	0.28
220	8.67	4.92	1.87	6.51	1.32	0.22
320	9.17	4.47	2.50	6.01	1.34	0.27
420	n.d.	n.d.	n.d.	n.d.	n.d.	n.d.
610	21.18	2.28	3.74	2.99	1.31	0.18

Table A.29: Integral scale and maximum values of experiment E03.

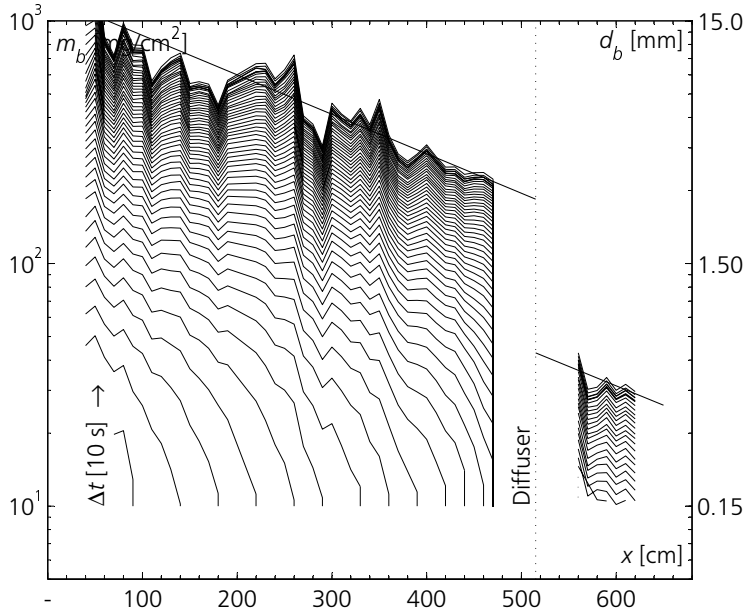

Figure A.52: Measured deposition evolution of experiment E03 along the flume axis, x with time steps of 10 s.

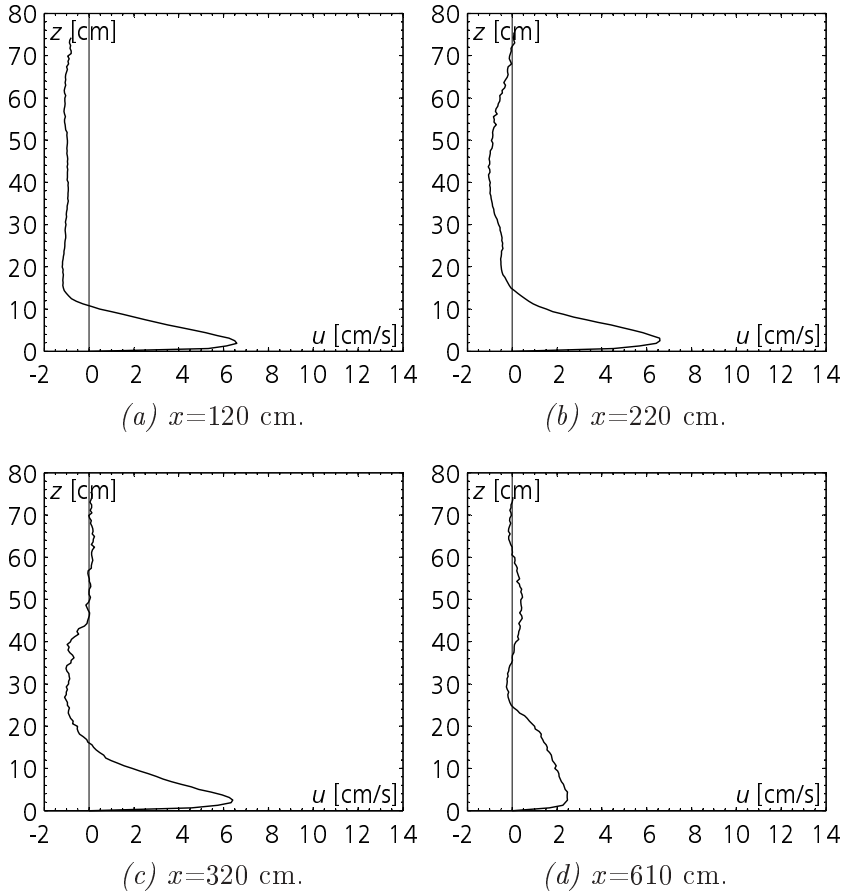

(a) x=120 cm. *(b)* x=220 cm.

(c) x=320 cm. *(d)* x=610 cm.

Figure A.53: Vertical velocity profiles of experiment E04.

x [cm]	h [cm]	U [cm/s]	h_{max} [cm]	U_{max} [cm/s]	U_{max}/U [–]	h_{max}/h [–]
120	8.13	5.01	1.87	6.60	1.32	0.23
220	9.80	4.88	2.50	6.60	1.35	0.26
320	10.59	4.60	2.50	6.42	1.40	0.24
420	n.d.	n.d.	n.d.	n.d.	n.d.	n.d.
610	20.88	1.89	2.50	2.47	1.31	0.12

Table A.30: Integral scale and maximum values of experiment E04.

A.5 Flow Through a Bubble Curtain

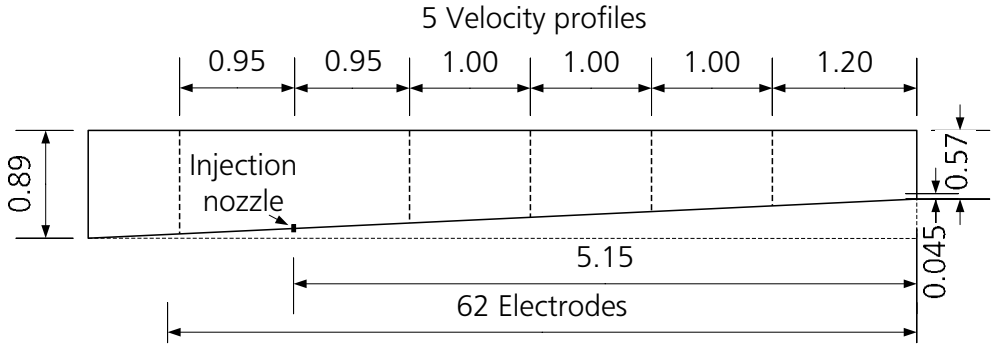

Figure A.54: Experimental set–up for series F with locations of velocity profiles.

Exp	S	T_a	ρ_a	T_0	ρ_0	C	g'_0	Q_0
[–]	[%]	[°C]	[g/cm^3]	[°C]	[g/cm^3]	[%]	[m/s^2]	[m^3/s]
F01	-	9.8	0.9995	10.8	1.0034	2.841	0.0378	0.00070
F02	-	11.8	0.9996	12.1	1.0034	2.792	0.0371	0.00080

Table A.31: Experimental parameters F series.

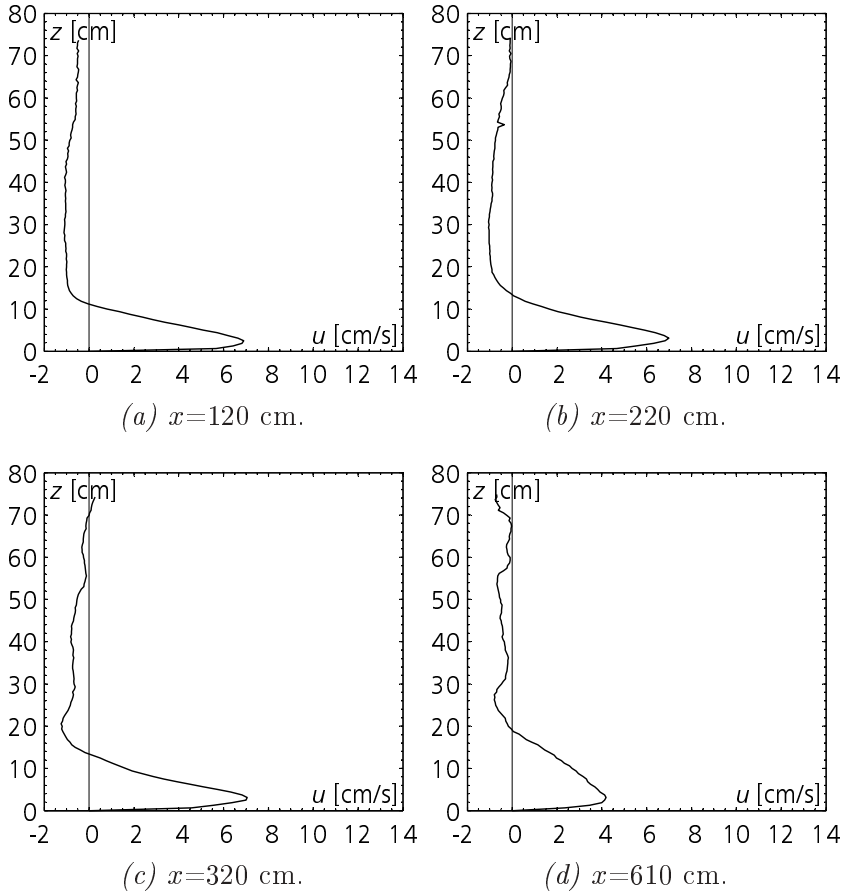

(a) x=120 cm. *(b)* x=220 cm.

(c) x=320 cm. *(d)* x=610 cm.

Figure A.55: Vertical velocity profiles of experiment F02.

x [cm]	h [cm]	U [cm/s]	h_{max} [cm]	U_{max} [cm/s]	U_{max}/U [–]	h_{max}/h [–]
120	8.45	5.30	2.50	6.90	1.30	0.30
220	9.63	5.22	3.12	6.99	1.34	0.32
320	9.61	5.15	3.11	7.05	1.37	0.32
610	15.01	3.10	3.11	4.18	1.35	0.21

Table A.32: Integral scale and maximum values of experiment F02.

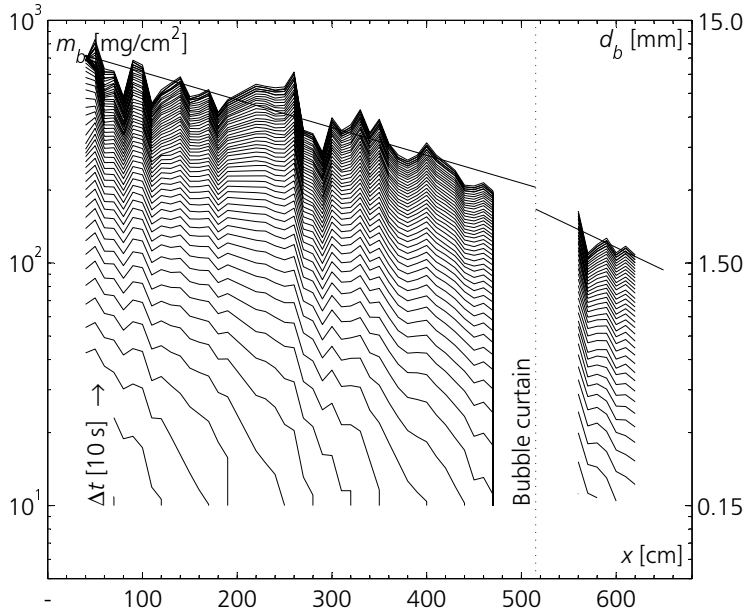

Figure A.56: Measured deposition evolution of experiment F02 along the flume axis, x with time steps of 10 s.

B Comparison of Experimental and Numerical Results

B.1 Continuously-Fed Turbidity Current

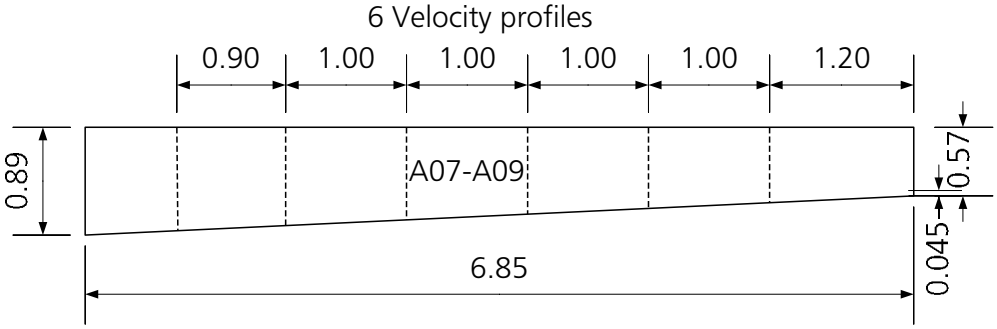

Figure B.1: Experimental set–up for series A with locations of velocity profiles.

Exp [−]	S [%]	T_a [°C]	ρ_a [g/cm^3]	T_0 [°C]	ρ_0 [g/cm^3]	C [%]	g_0' [m/s^2]	Q_0 [m^3/s]
A07	4.64	12.1	0.9995	11.0	1.0041	3.448	0.0459	0.00050
A08	4.64	10.3	0.9997	11.8	1.0039	3.105	0.0412	0.00063
A09	4.64	10.5	0.9995	11.0	1.0057	4.554	0.0606	0.00071

Table B.1: Experimental parameters A series.

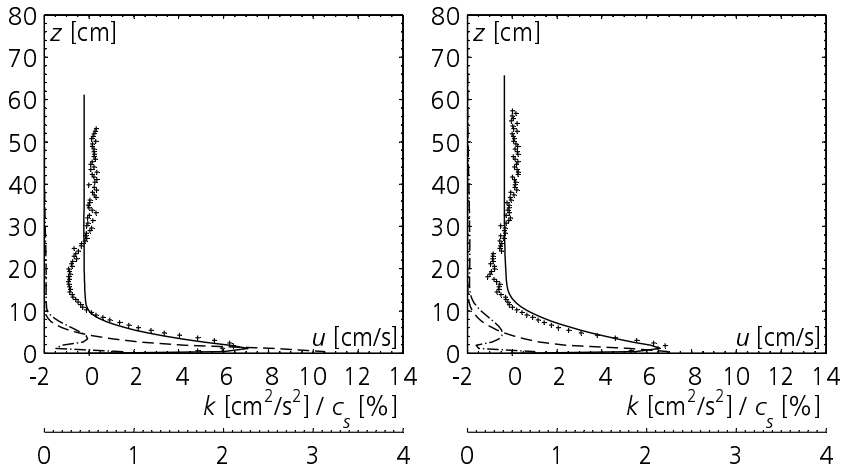

(a) x=120 cm. *(b)* x=220 cm.

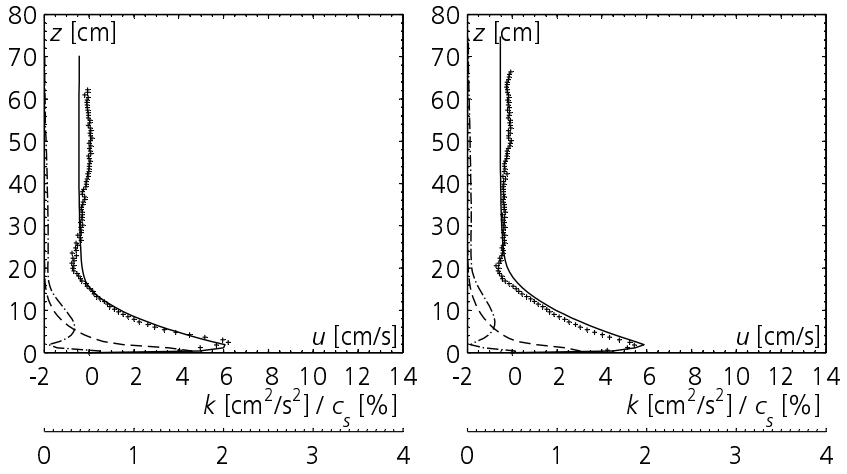

(c) x=320 cm. *(d)* x=420 cm.

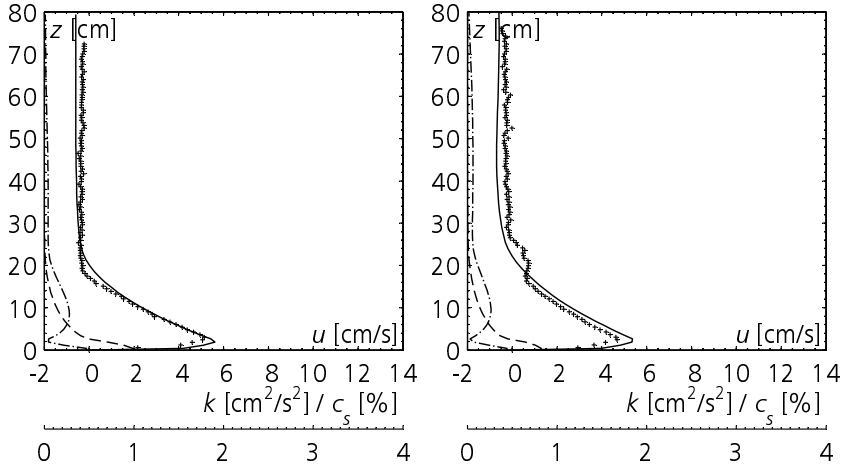

(e) x=520 cm. *(f)* x=610 cm.

Figure B.2: Vertical profiles of computed velocity, u (solid line), measured velocity (cross), computed concentration, c_s (dashed line) and turbulent kinetic energy, k (dash-dotted line) of experiment A07.

	Measured values					Computed values					
x	h	U	h_{max}	U_{max}	U_{max}/U	h	U	U_{max}	U_{max}/U	C_s	Ri
[cm]	[cm]	[cm/s]	[cm]	[cm/s]	[−]	[cm]	[cm/s]	[cm/s]	[−]	[%]	[−]
120	6.71	4.68	1.81	6.44	1.38	6.02 (−10)	4.85 (+4)	7.08 (+10)	1.46 (+6)	1.458	0.50
220	6.87	4.72	1.81	6.82	1.44	8.03 (+17)	4.44 (−6)	6.57 (−4)	1.48 (+2)	0.903	0.49
320	9.43	4.06	2.41	6.20	1.53	9.97 (+6)	4.15 (+2)	6.06 (−2)	1.46 (−4)	0.626	0.48
420	10.78	3.62	1.81	5.45	1.51	11.71 (+9)	3.94 (+9)	5.86 (+8)	1.49 (−1)	0.476	0.48
520	12.48	3.58	3.02	5.14	1.44	13.45 (+8)	3.78 (+6)	5.60 (+9)	1.48 (+3)	0.377	0.47
610	16.38	2.95	2.41	4.67	1.58	14.88 (−9)	3.67 (+24)	5.35 (+15)	1.46 (−8)	0.319	0.47

Table B.2: Comparison of measured and computed integral values for experiment A07.

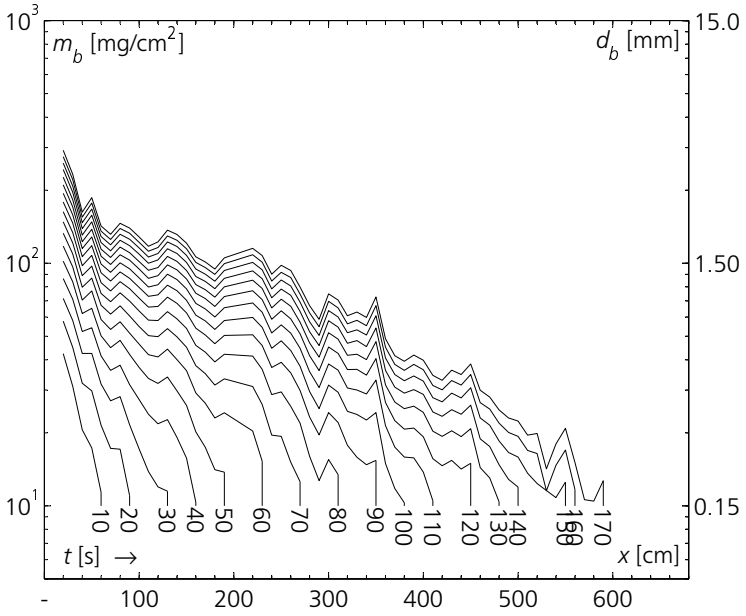

(a) Measured evolution of deposition.

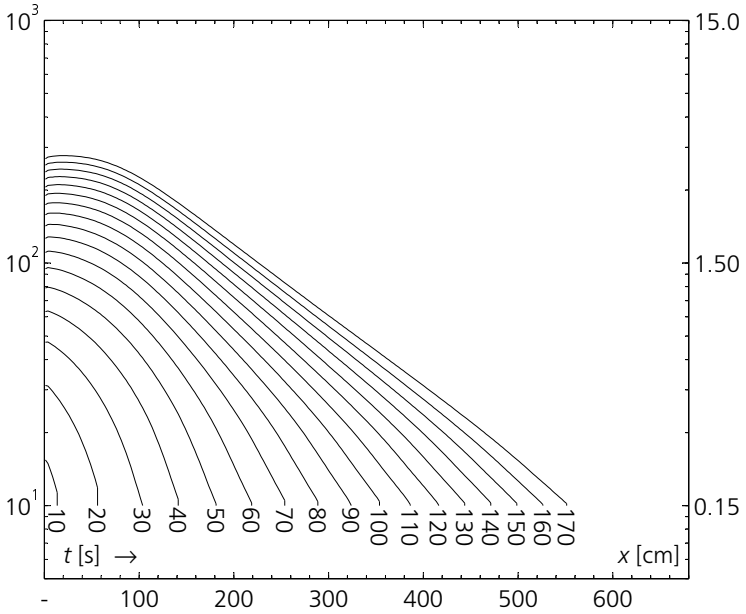

(b) Computed evolution of deposition.

Figure B.3: Comparison of measured and computed evolution of the sediment deposition in experiment A07.

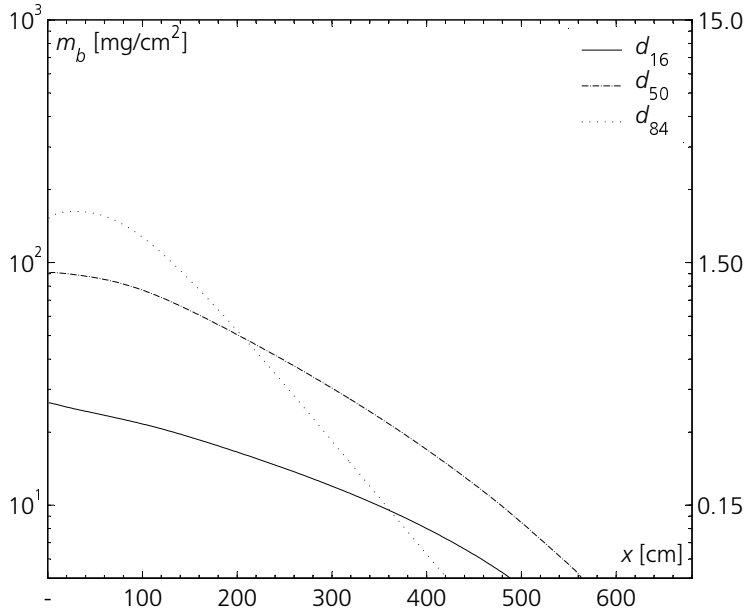

Figure B.4: Deposition thickness of three grain sizes, d_{16}, d_{50} and d_{84} at the end of experiment A07 (t=170 s).

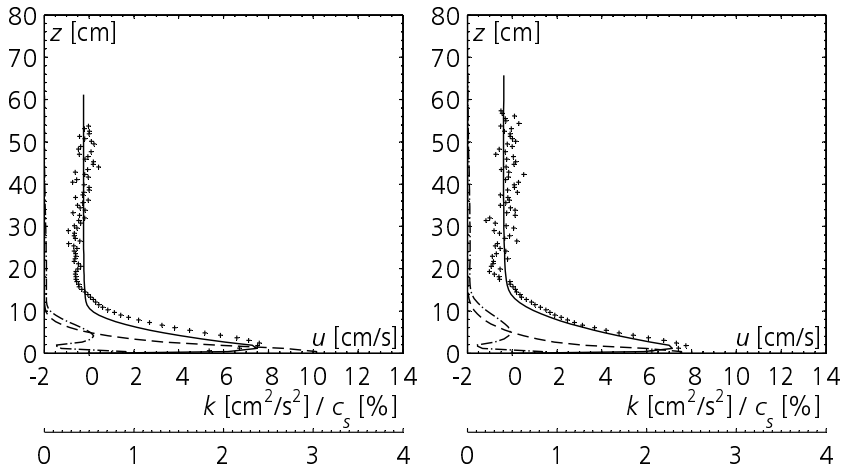

(a) x=120 cm. *(b)* x=220 cm.

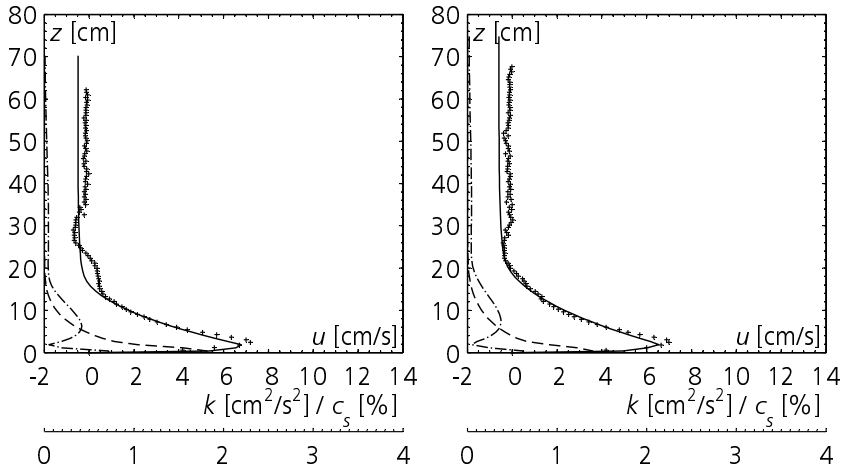

(c) x=320 cm. *(d)* x=420 cm.

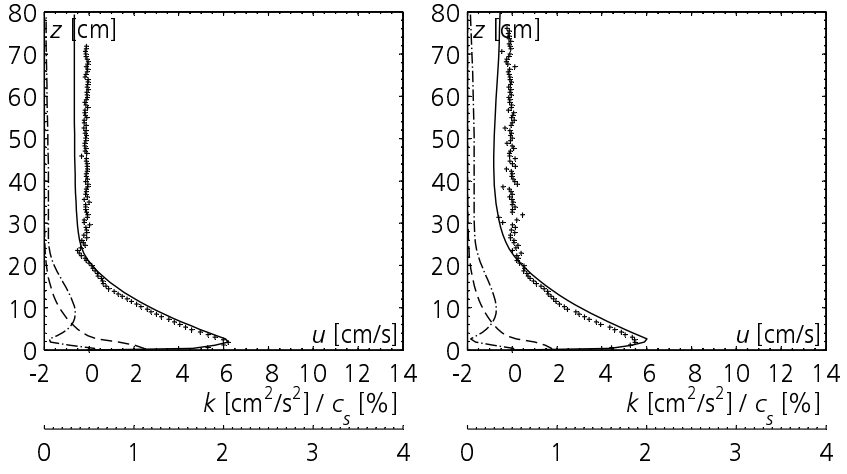

(e) x=520 cm. *(f)* x=610 cm.

Figure B.5: Vertical profiles of computed velocity, u (solid line), measured velocity (cross), computed concentration, c_s (dashed line) and turbulent kinetic energy, k (dash-dotted line) of experiment A08.

	Measured values					Computed values					
x	h	U	h_{max}	U_{max}	U_{max}/U	h	U	U_{max}	U_{max}/U	C_s	Ri
[cm]	[cm]	[cm/s]	[cm]	[cm/s]	[−]	[cm]	[cm/s]	[cm/s]	[−]	[%]	[−]
120	8.43	5.43	2.41	7.59	1.40	6.58 (−22)	5.29 (−3)	7.46 (−2)	1.41 (+1)	1.512	0.47
220	9.45	5.17	1.81	7.75	1.50	8.52 (−10)	4.91 (−5)	7.12 (−8)	1.45 (−3)	0.987	0.46
320	11.37	4.51	2.41	7.19	1.59	10.44 (−8)	4.61 (+2)	6.79 (−6)	1.47 (−8)	0.700	0.46
420	12.08	4.52	2.41	6.99	1.55	12.03 (−0)	4.39 (−3)	6.49 (−7)	1.48 (−4)	0.550	0.46
520	12.92	4.14	1.81	6.20	1.50	13.83 (+7)	4.21 (+2)	6.18 (−0)	1.47 (−2)	0.438	0.45
610	15.11	3.66	1.81	5.47	1.49	15.42 (+2)	4.08 (+11)	5.99 (+10)	1.47 (−2)	0.368	0.45

Table B.3: Comparison of measured and computed integral scale and maximum values for experiment A08.

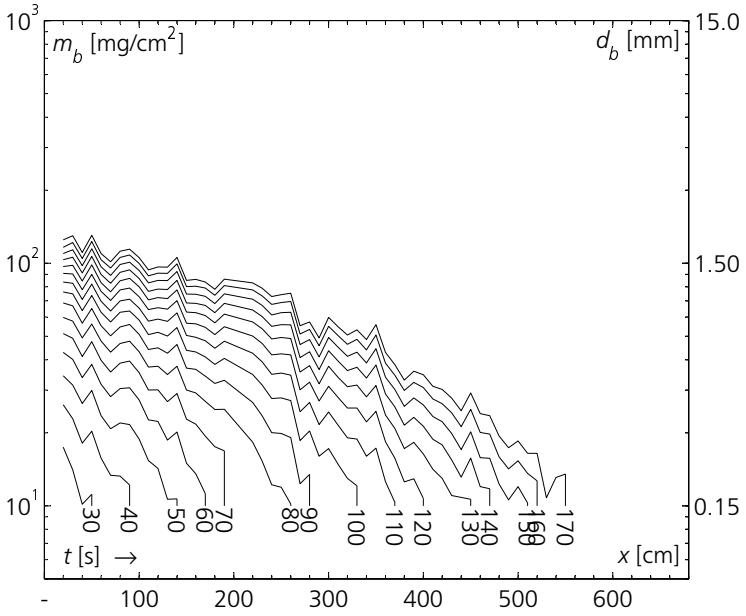

(a) Measured evolution of deposition.

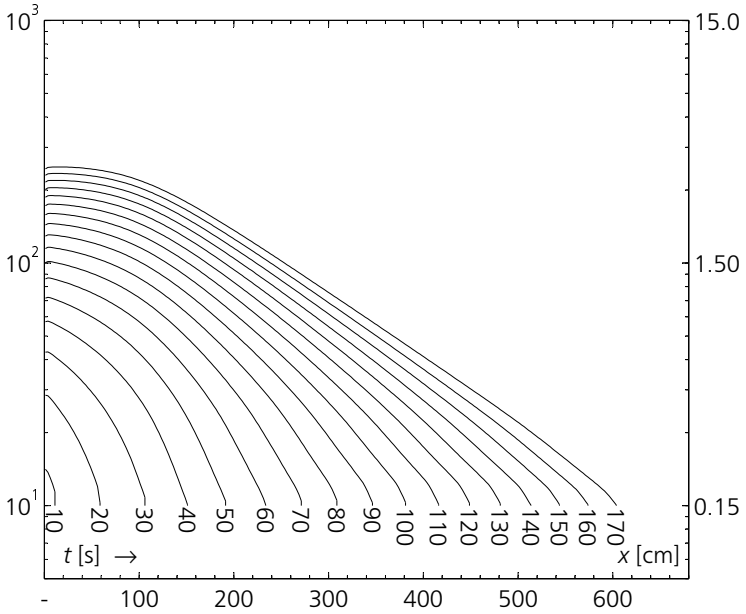

(b) Computed evolution of deposition.

Figure B.6: Comparison of measured and computed evolution of the sediment deposition in experiment A08.

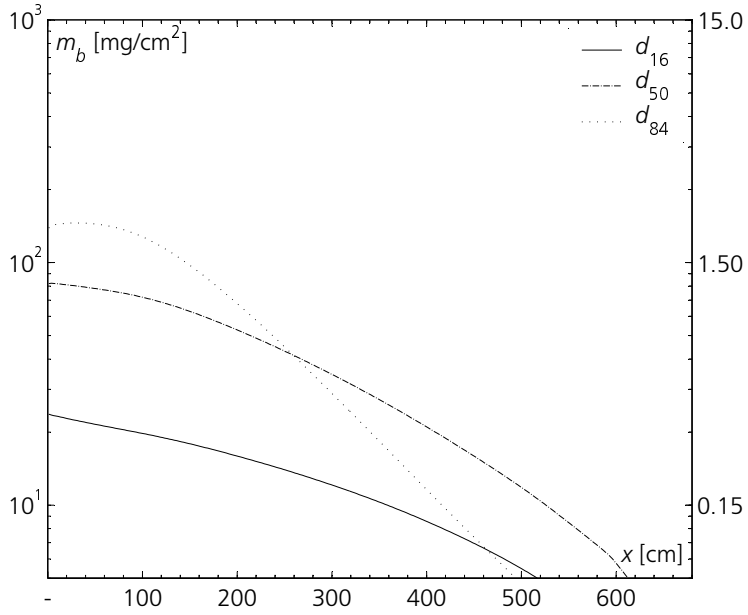

Figure B.7: Deposition thickness of three grain sizes, d_{16}, d_{50} and d_{84} at the end of experiment A08 (t=170 s).

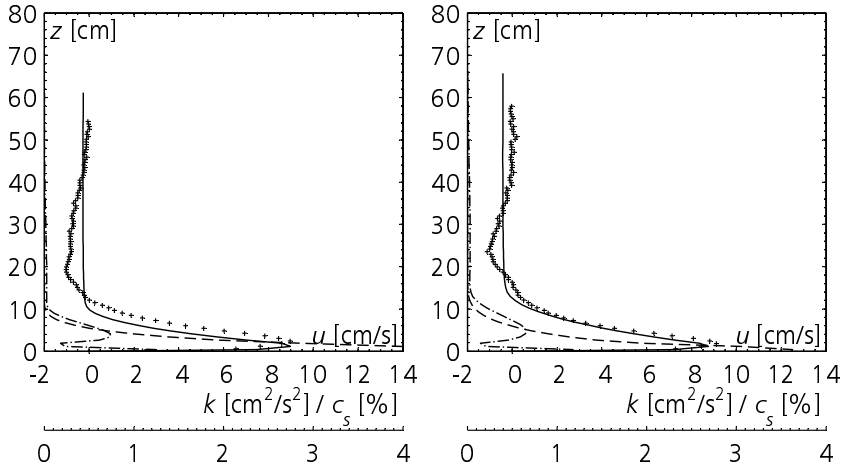

(a) x=120 cm. *(b)* x=220 cm.

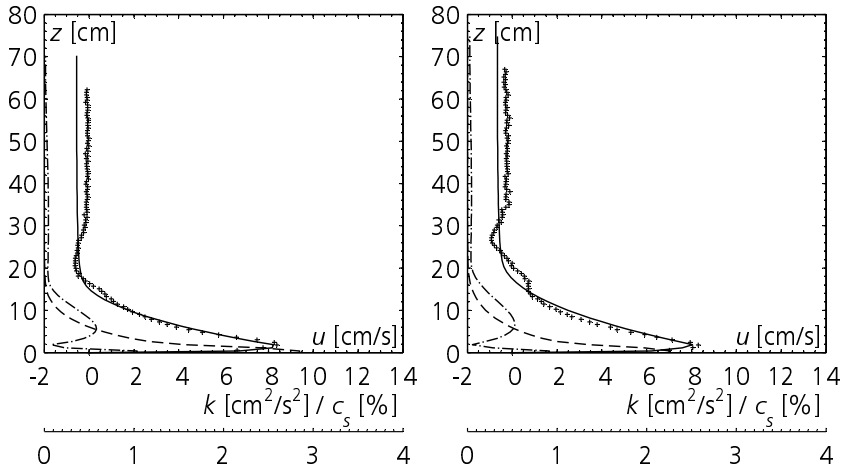

(c) x=320 m. *(d)* x=420 cm.

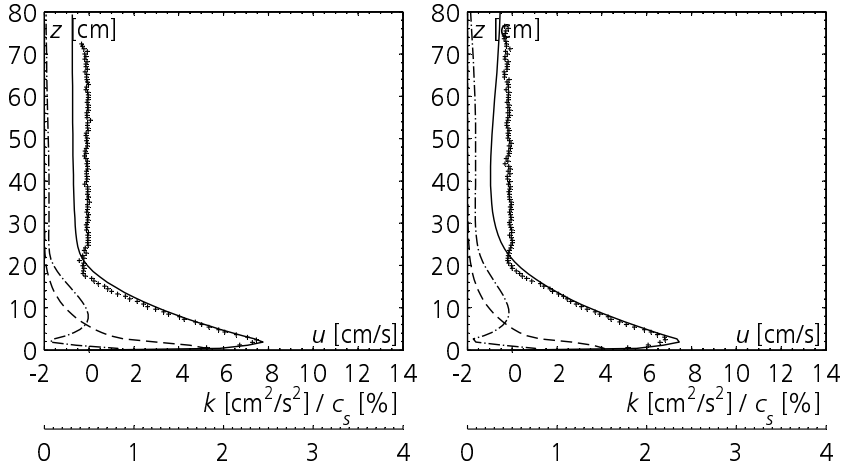

(e) x=520 cm. *(f)* x=610 cm.

Figure B.8: Vertical profiles of computed velocity, u (solid line), measured velocity (cross), computed concentration, c_s (dashed line) and turbulent kinetic energy, k (dash-dotted line) of experiment A09.

	Measured values					Computed values					
x	h	U	h_{max}	U_{max}	U_{max}/U	h	U	U_{max}	U_{max}/U	C_s	Ri
[cm]	[cm]	[cm/s]	[cm]	[cm/s]	[−]	[cm]	[cm/s]	[cm/s]	[−]	[%]	[−]
120	8.09	6.45	2.41	8.96	1.39	6.12 (−24)	6.38 (−1)	8.98 (+0)	1.41 (+1)	2.311	0.46
220	8.47	6.25	1.81	9.11	1.46	7.91 (−7)	5.97 (−4)	8.74 (−4)	1.46 (+0)	1.544	0.45
320	9.97	5.48	1.81	8.38	1.53	9.66 (−3)	5.64 (+3)	8.21 (−2)	1.46 (−5)	1.119	0.45
420	11.24	5.28	1.81	8.30	1.57	11.19 (−0)	5.39 (+2)	7.98 (−4)	1.48 (−6)	0.880	0.45
520	11.95	5.11	2.41	7.47	1.46	12.90 (+8)	5.19 (+2)	7.74 (+4)	1.49 (+2)	0.699	0.44
610	13.82	4.79	2.41	6.82	1.42	14.27 (+3)	5.04 (+5)	7.42 (+9)	1.47 (+3)	0.595	0.44

Table B.4: Comparison of measured and computed integral scale and maximum values for experiment A09.

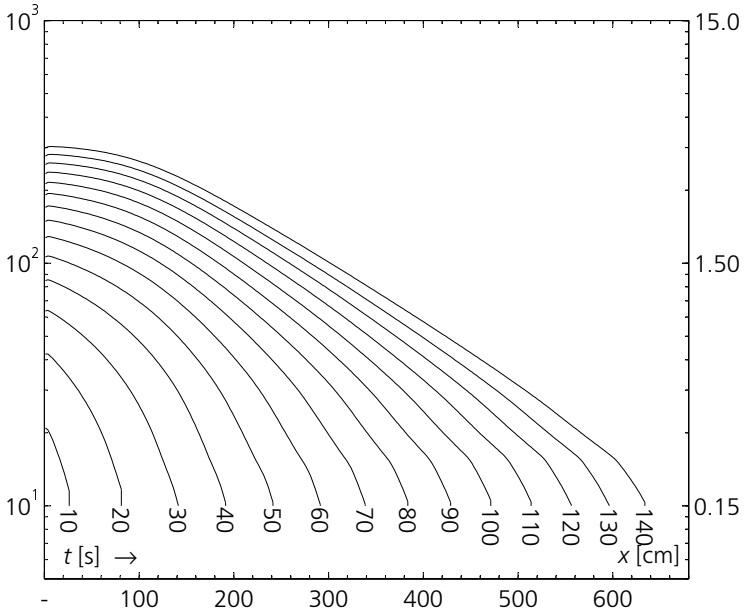

Figure B.9: Computed deposition evolution of experiment A09.

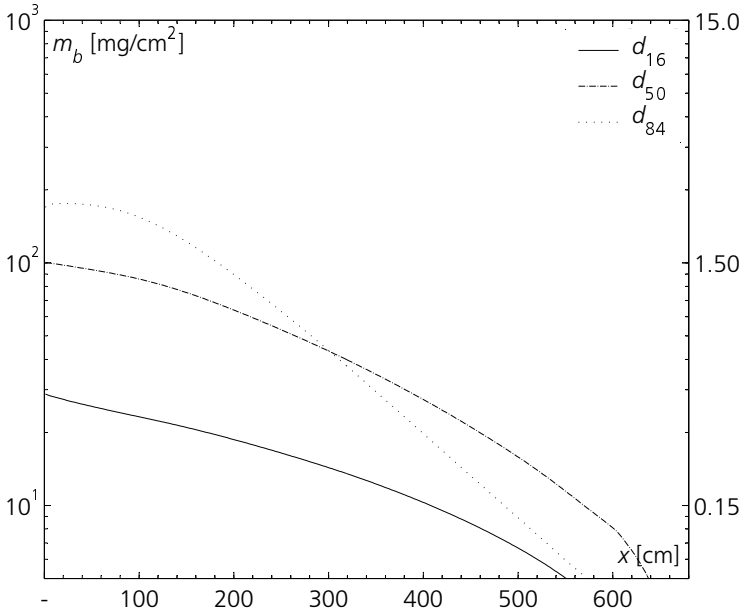

Figure B.10: Deposition thickness of three grain sizes, d_{16}, d_{50} and d_{84} at the end of experiment A09 (t=140 s).

B.2 Flow Over an Obstacle

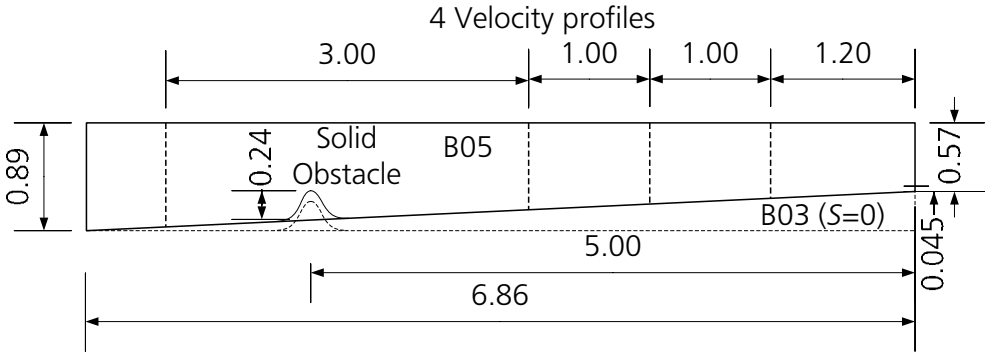

Figure B.11: Experimental set–up for series B with locations of velocity profiles.

Exp	S	T_a	ρ_a	T_0	ρ_0	C	g'_0	Q_0
[−]	[%]	[°C]	[g/cm^3]	[°C]	[g/cm^3]	[%]	[m/s^2]	[m^3/s]
B03	-	11.9	0.9997	13.3	1.0030	2.432	0.0323	0.00071
B05	4.64	11.6	0.9996	13.6	1.0032	2.637	0.0350	0.00083

Table B.5: Experimental parameters B series.

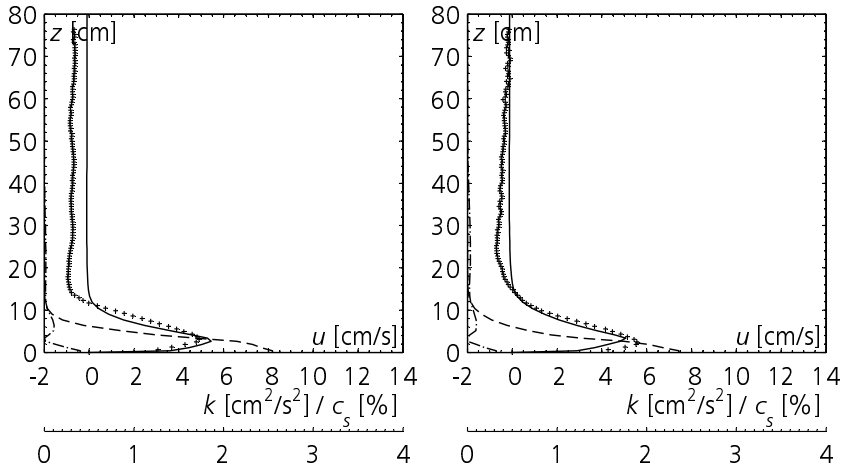

(a) x=120 cm. *(b)* x=220 cm.

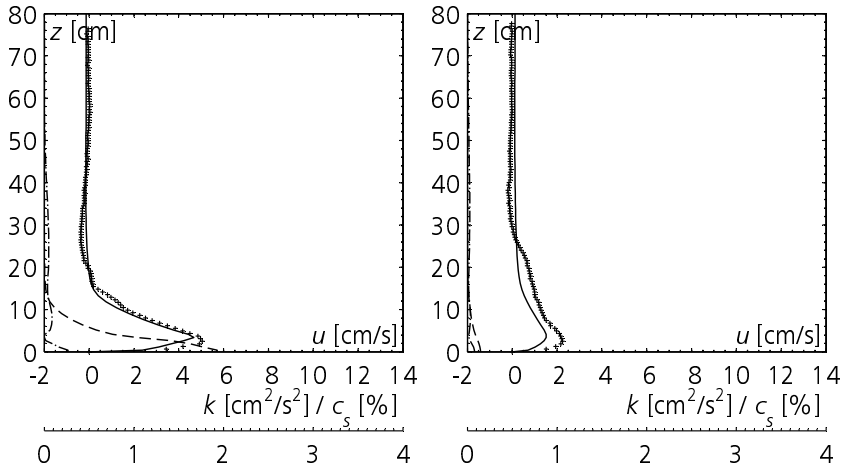

(c) x=320 cm. *(d)* x=620 cm.

Figure B.12: Vertical profiles of computed velocity, u (solid line), measured velocity (cross), computed concentration, c_s (dashed line) and turbulent kinetic energy, k (dash-dotted line) of experiment B03.

	Measured values					Computed values					
x	h	U	h_{max}	U_{max}	U_{max}/U	h	U	U_{max}	U_{max}/U	C_s	Ri
[cm]	[cm]	[cm/s]	[cm]	[cm/s]	[−]	[cm]	[cm/s]	[cm/s]	[−]	[%]	[−]
120	9.27	3.74	3.08	4.91	1.31	8.22 (−11)	3.98 (+6)	5.43 (+11)	1.36 (+4)	1.486	1.02
220	9.82	4.15	2.46	5.56	1.34	9.84 (+0)	3.50 (−16)	5.05 (−9)	1.44 (+8)	1.087	1.16
320	11.68	3.55	2.46	5.05	1.42	10.94 (−6)	3.18 (−10)	4.65 (−8)	1.46 (+3)	0.819	1.18
620	21.24	1.43	2.46	2.25	1.57	35.36 (+66)	0.73 (−49)	1.52 (−32)	2.08 (+32)	0.042	3.69

Table B.6: Comparison of measured and computed integral scale and maximum values for experiment B03.

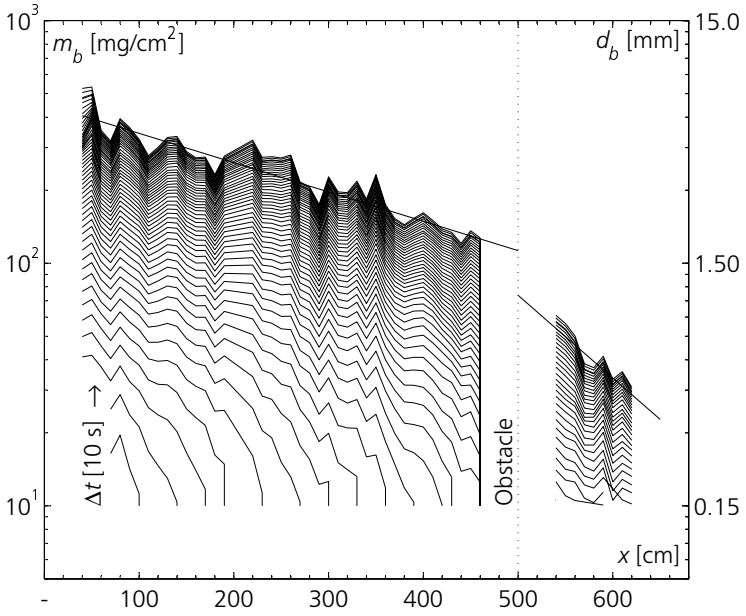

(a) Measured evolution of deposition.

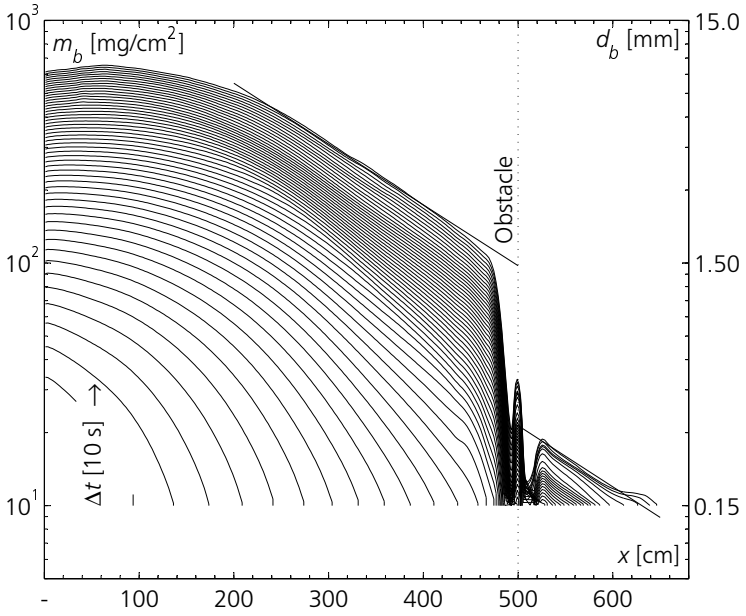

(b) Computed evolution of deposition.

Figure B.13: Comparison of measured and computed evolution of the sediment deposition in experiment B03.

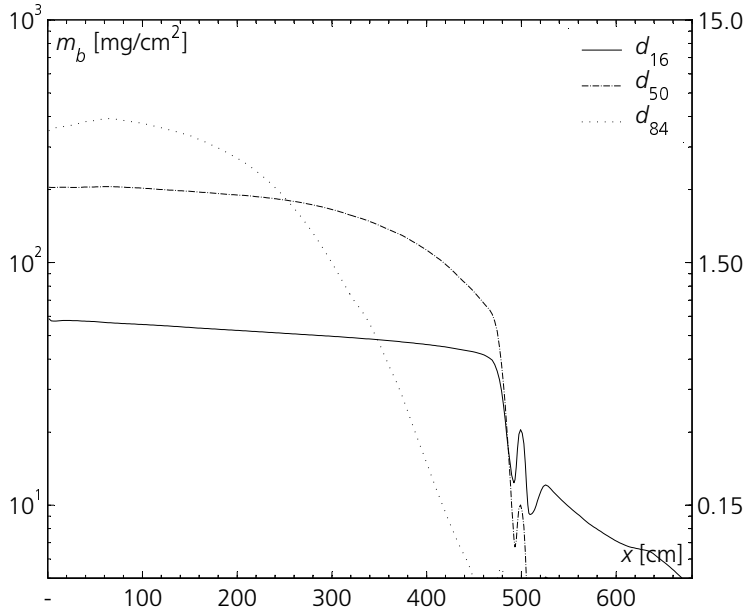

Figure B.14: Deposition thickness of three grain sizes, d_{16}, d_{50} and d_{84} at the end of experiment B03 (t=540 s).

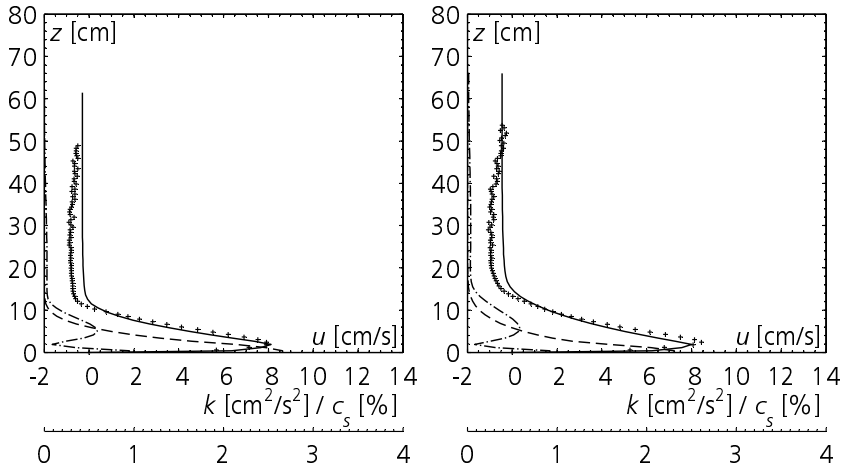

(a) x=120 cm. *(b)* x=220 cm.

(c) x=320 cm. *(d)* x=620 cm.

Figure B.15: Vertical profiles of computed velocity, u (solid line), measured velocity (cross), computed concentration, c_s (dashed line) and turbulent kinetic energy, k (dash-dotted line) of experiment B05.

	Measured values					Computed values					
x	h	U	h_{max}	U_{max}	U_{max}/U	h	U	U_{max}	U_{max}/U	C_s	Ri
[cm]	[cm]	[cm/s]	[cm]	[cm/s]	[−]	[cm]	[cm/s]	[cm/s]	[−]	[%]	[−]
120	7.86	5.92	2.41	7.92	1.34	7.69 (−2)	5.77 (−3)	8.12 (+3)	1.41 (+5)	1.444	0.44
220	9.17	5.93	2.41	8.45	1.42	9.50 (+4)	5.46 (−8)	8.00 (−5)	1.47 (+3)	1.020	0.43
320	9.47	5.69	1.81	8.38	1.47	11.33 (+20)	5.17 (−9)	7.67 (−8)	1.48 (+1)	0.765	0.43
620	14.00	3.69	3.62	5.26	1.43	13.72 (−2)	4.29 (+16)	6.36 (+21)	1.48 (+4)	0.349	0.34

Table B.7: Comparison of measured and computed integral scale and maximum values for experiment B05.

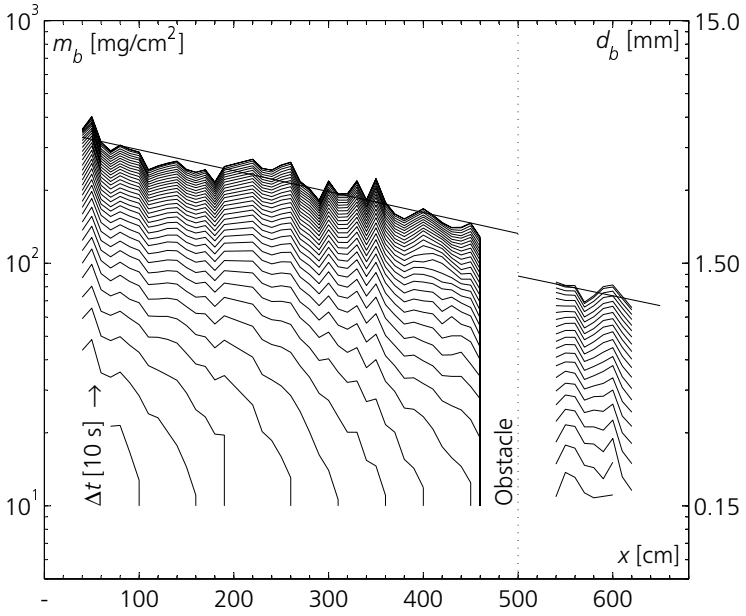

(a) Measured evolution of deposition.

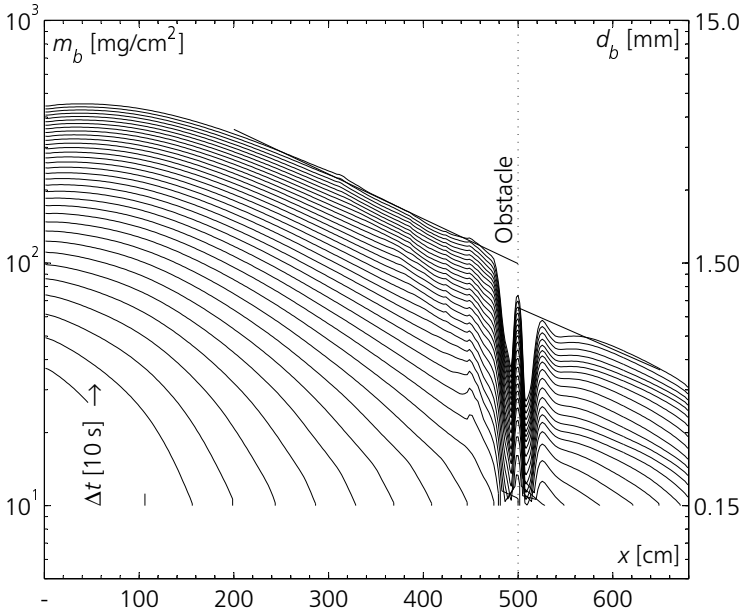

(b) Computed evolution of deposition.

Figure B.16: Comparison of measured and computed evolution of the sediment deposition in experiment B05.

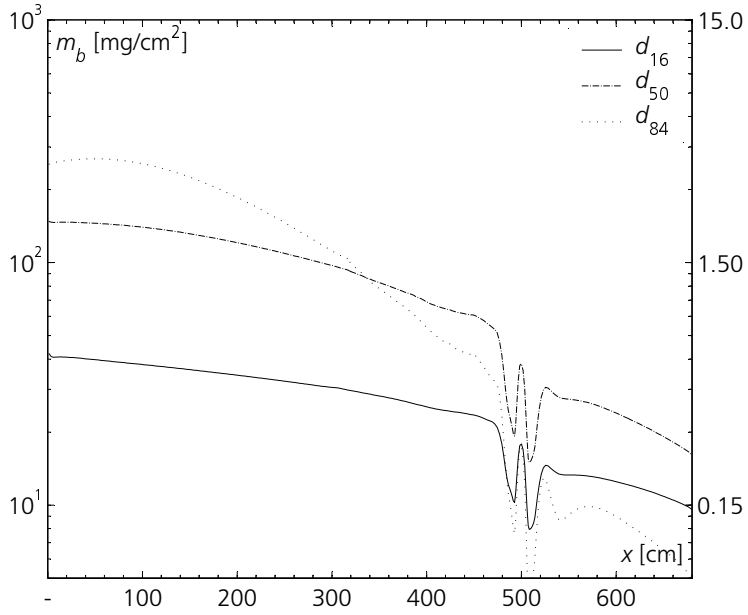

Figure B.17: Deposition thickness of three grain sizes, d_{16}, d_{50} and d_{84} at the end of experiment B05 (t=360 s).

B.3 Flow Through a Screen

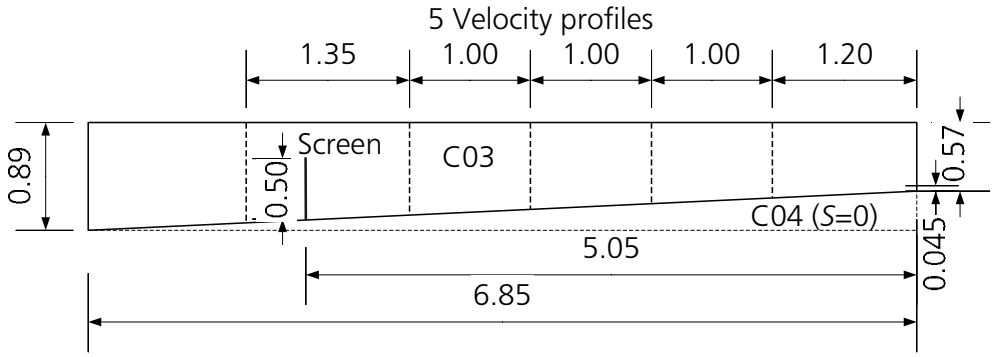

Figure B.18: Experimental set–up for series C with locations of velocity profiles.

Exp	S	T_a	ρ_a	T_0	ρ_0	C	g_0'	Q_0
[−]	[%]	[°C]	[g/cm^3]	[°C]	[g/cm^3]	[%]	[m/s^2]	[m^3/s]
C03	4.64	11.2	0.9995	10.5	1.0040	3.292	0.0438	0.00068
C04	-	10.9	0.9997	11.0	1.0033	2.668	0.0354	0.00065

Table B.8: Experimental parameters C series.

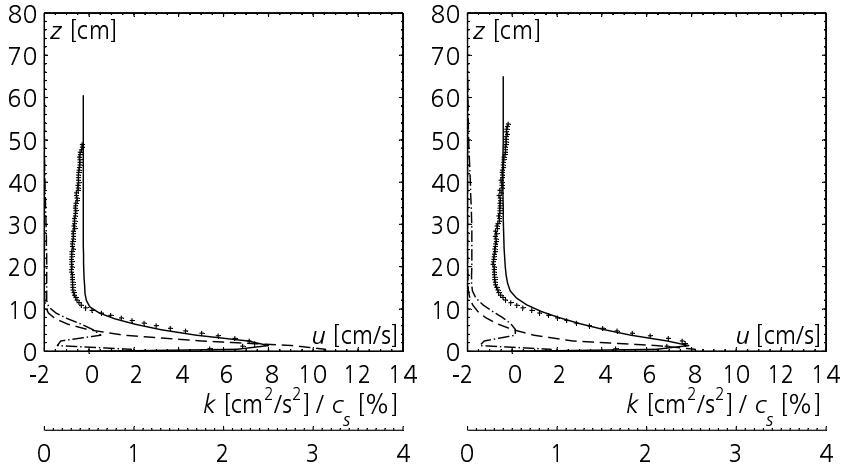

(a) x=120 cm. *(b)* x=220 cm.

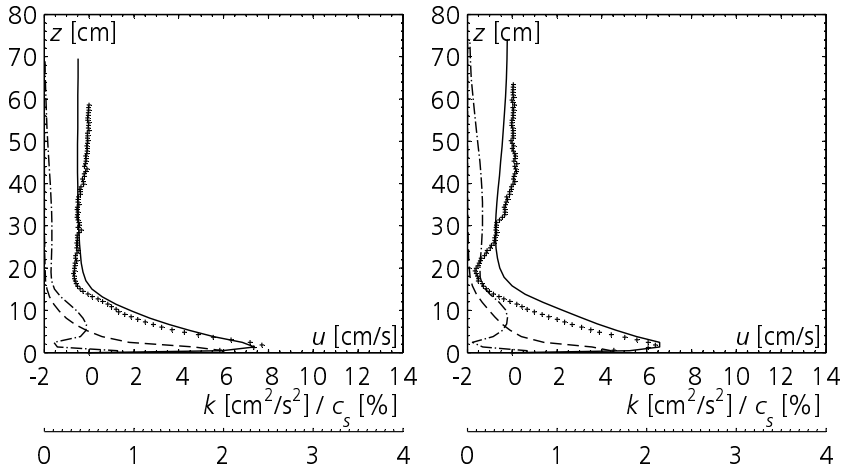

(c) x=320 cm. *(d)* x=420 cm.

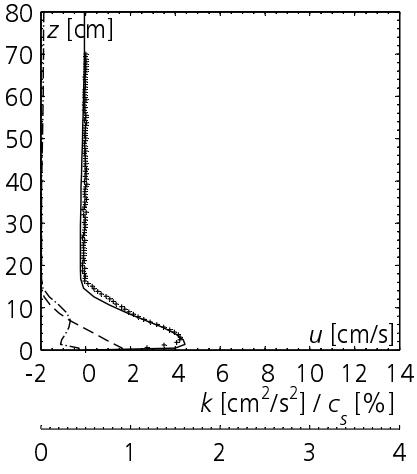

(e) x=555 cm.

Figure B.19: Vertical profiles of computed velocity, u (solid line), measured velocity (cross), computed concentration, c_s (dashed line) and turbulent kinetic energy, k (dash-dotted line) of experiment C03.

	Measured values					Computed values					
x	h	U	h_{max}	U_{max}	U_{max}/U	h	U	U_{max}	U_{max}/U	C_s	Ri
[cm]	[cm]	[cm/s]	[cm]	[cm/s]	[−]	[cm]	[cm/s]	[cm/s]	[−]	[%]	[−]
120	7.10	5.37	1.81	7.39	1.38	6.58 (−7)	5.66 (+5)	8.00 (+8)	1.41 (+3)	1.667	0.45
220	7.80	5.39	1.81	7.72	1.43	8.44 (+8)	5.28 (−2)	7.87 (+2)	1.49 (+4)	1.111	0.45
320	8.76	5.05	1.81	7.71	1.53	10.21 (+17)	4.96 (−2)	7.37 (−4)	1.49 (−3)	0.811	0.45
420	8.35	4.43	1.81	6.38	1.44	11.10 (+33)	4.70 (+6)	6.60 (+3)	1.40 (−2)	0.691	0.46
555	11.67	3.07	3.02	4.22	1.37	10.29 (−12)	3.39 (+10)	4.44 (+5)	1.31 (−5)	0.539	0.64

Table B.9: Comparison of measured and computed integral scale and maximum values for experiment C03.

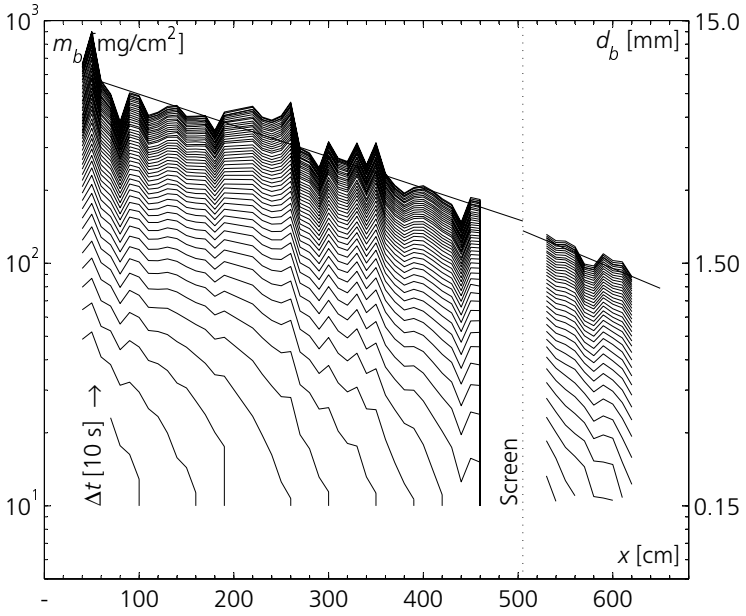

(a) Measured evolution of deposition.

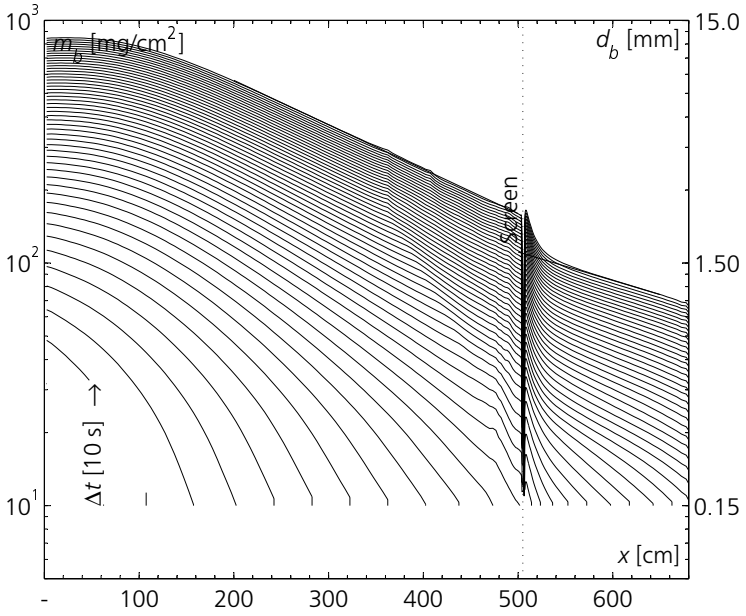

(b) Computed evolution of deposition.

Figure B.20: Comparison of measured and computed evolution of the sediment deposition in experiment C03.

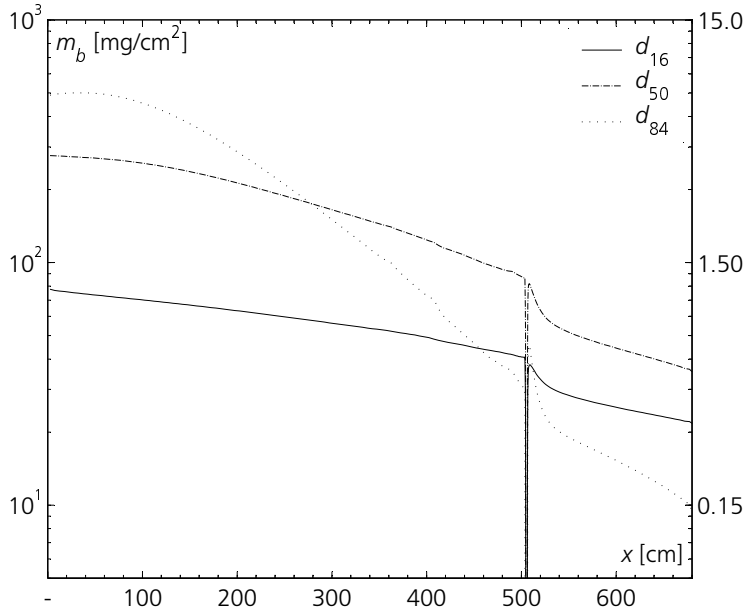

Figure B.21: Deposition thickness of three grain sizes, d_{16}, d_{50} and d_{84} at the end of experiment C03 (t=520 s).

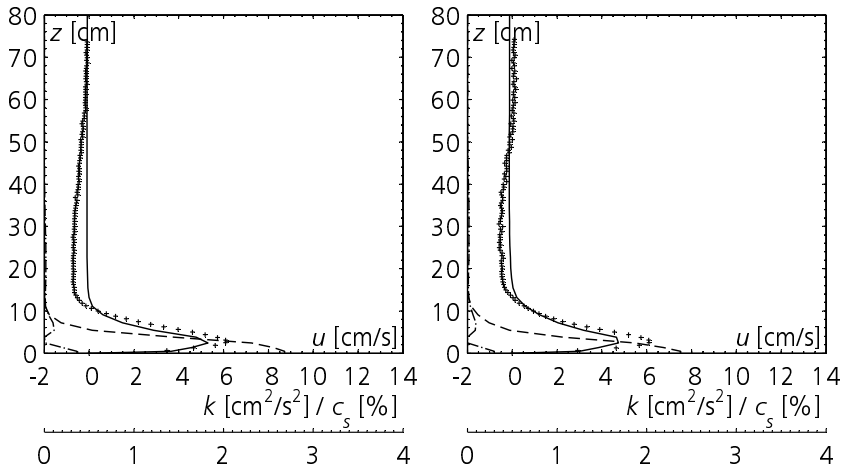

(a) x=120 cm. *(b)* x=220 cm.

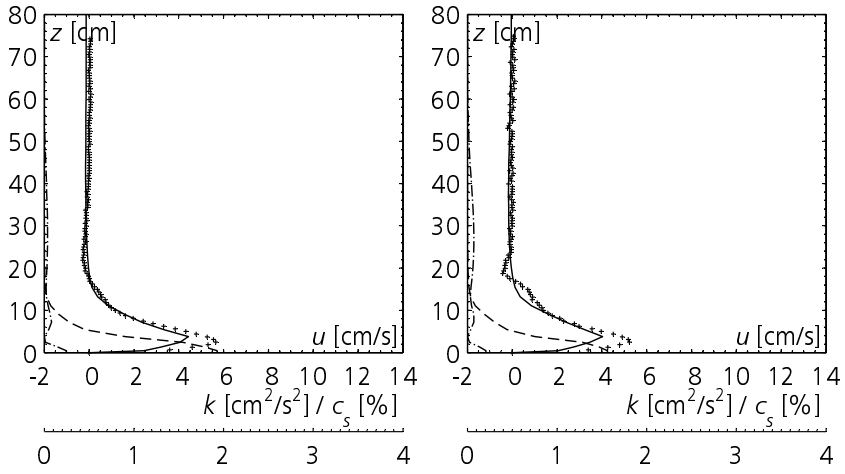

(c) x=320 cm. *(d)* x=420 cm.

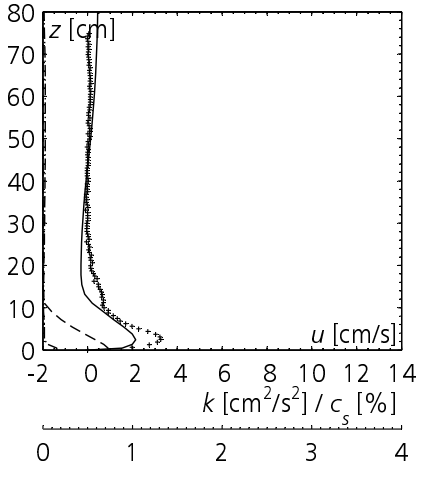

(e) x=555 cm.

Figure B.22: Vertical profiles of computed velocity, u (solid line), measured velocity (cross), computed concentration, c_s (dashed line) and turbulent kinetic energy, k (dash-dotted line) of experiment C04.

	Measured values					Computed values					
x	h	U	h_{max}	U_{max}	U_{max}/U	h	U	U_{max}	U_{max}/U	C_s	Ri
[cm]	[cm]	[cm/s]	[cm]	[cm/s]	[−]	[cm]	[cm/s]	[cm/s]	[−]	[%]	[−]
120	7.96	4.56	2.50	6.09	1.34	7.68 (−4)	3.91 (−14)	5.30 (−13)	1.36 (+1)	1.579	1.05
220	8.65	4.37	2.50	6.10	1.40	9.42 (+9)	3.41 (−22)	4.72 (−23)	1.38 (−1)	1.114	1.20
320	10.18	3.91	2.50	5.66	1.45	10.76 (+6)	3.01 (−23)	4.35 (−23)	1.45 (−0)	0.771	1.22
420	11.40	3.49	2.50	5.23	1.50	11.24 (−1)	2.73 (−22)	3.99 (−24)	1.46 (−2)	0.627	1.25
555	12.63	2.01	2.50	3.26	1.62	9.39 (−26)	1.64 (−18)	2.15 (−34)	1.31 (−19)	0.429	1.99

Table B.10: Comparison of measured and computed integral scale and maximum values for experiment C04.

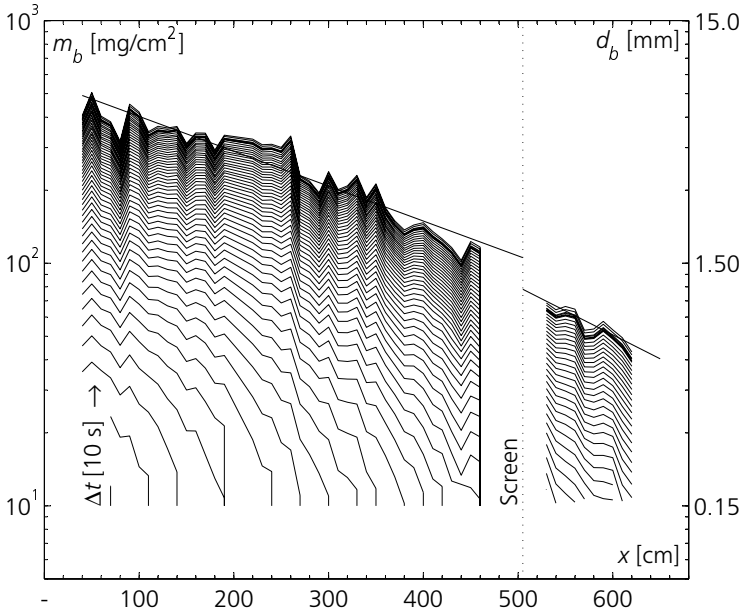

(a) Measured evolution of deposition.

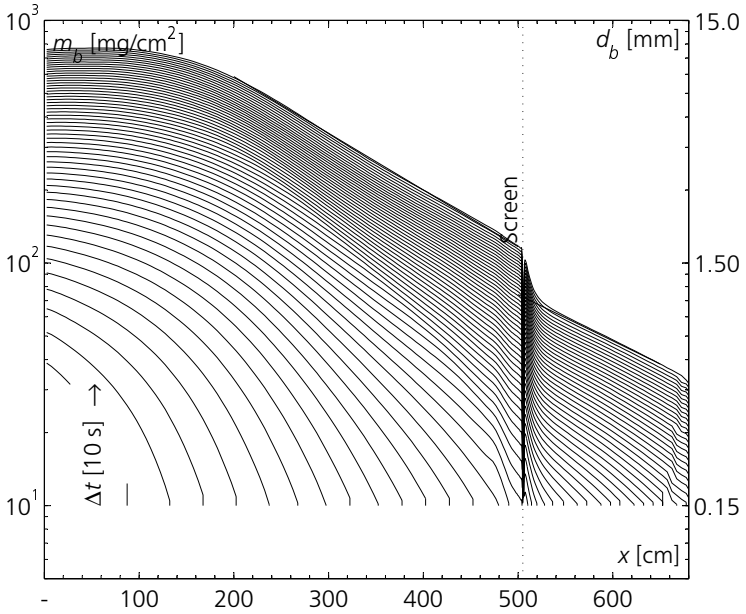

(b) Computed evolution of deposition.

Figure B.23: Comparison of measured and computed evolution of the sediment deposition in experiment C04.

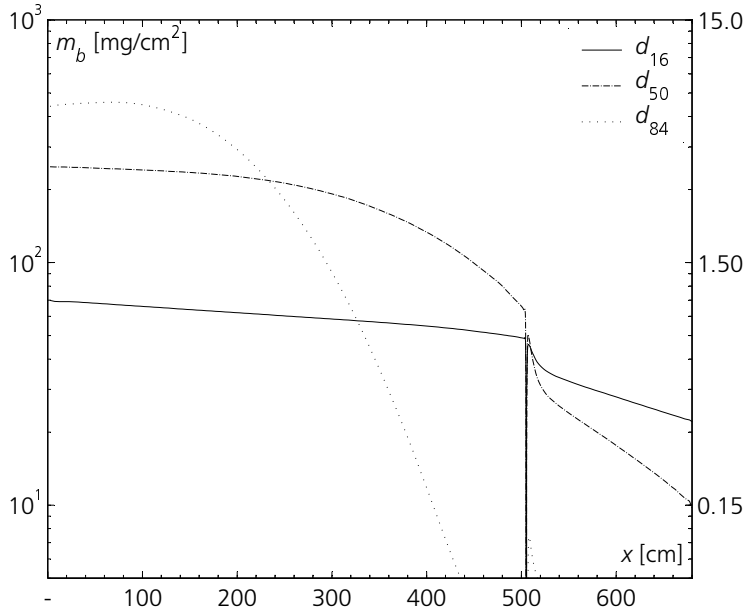

Figure B.24: Deposition thickness of three grain sizes, d_{16}, d_{50} and d_{84} at the end of experiment C04 (t=580 s).

B.4 Flow Across a Jet Diffuser

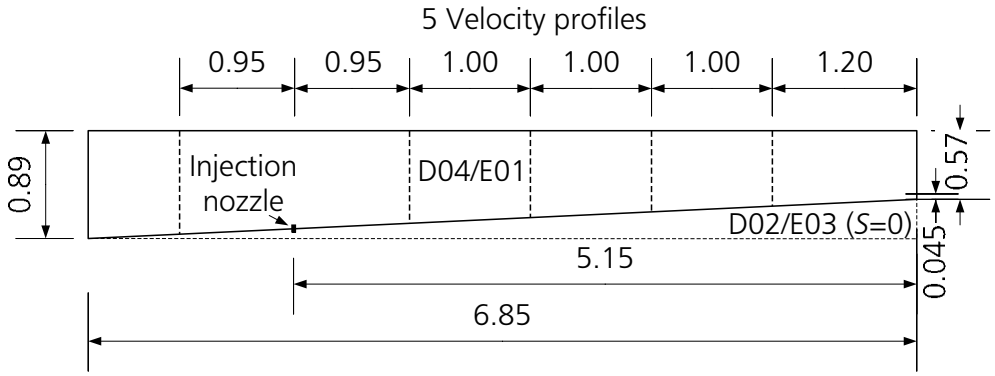

Figure B.25: Experimental set–up for series D and E with locations of velocity profiles.

Exp	S	T_a	ρ_a	T_0	ρ_0	C	g_0'	Q_0
[−]	[%]	[°C]	[g/cm^3]	[°C]	[g/cm^3]	[%]	[m/s^2]	[m^3/s]
D02	-	12.6	0.9994	11.2	1.0032	2.765	0.0368	0.00073
D04	4.64	12.4	0.9995	11.9	1.0033	2.818	0.0375	0.00081
E01	4.64	13.6	0.9992	12.2	1.0033	2.990	0.0399	0.00078
E03	-	13.3	0.9994	12.6	1.0033	2.890	0.0385	0.00072

Table B.11: Experimental parameters D and E series.

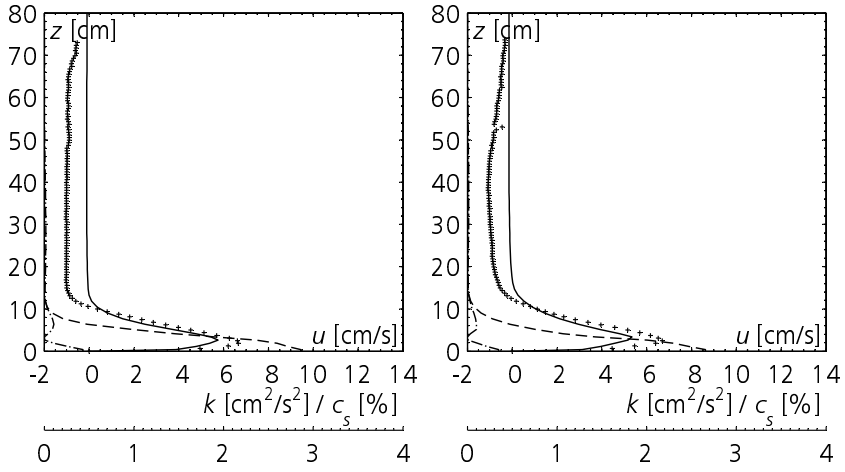

(a) x=120 cm. *(b)* x=220 cm.

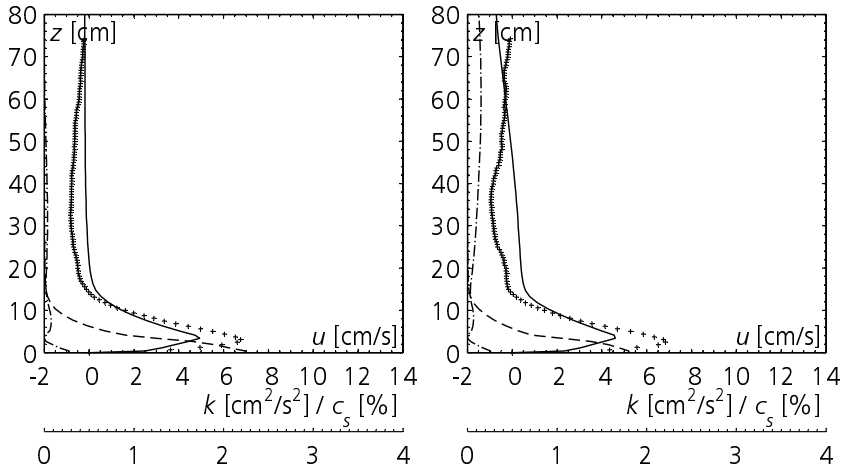

(c) x=320 cm. *(d)* x=420 cm.

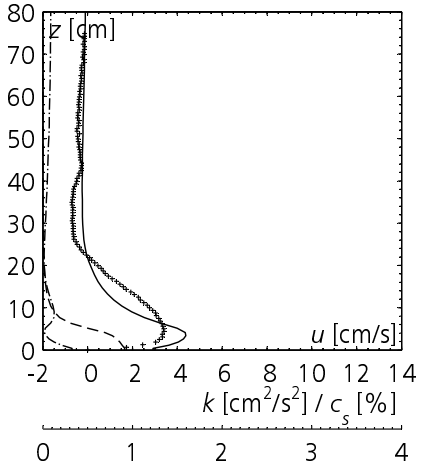

(e) x=610 cm.

Figure B.26: Vertical profiles of computed velocity, u (solid line), measured velocity (cross), computed concentration, c_s (dashed line) and turbulent kinetic energy, k (dash-dotted line) of experiment C02.

	Measured values					Computed values					
x	h	U	h_{max}	U_{max}	U_{max}/U	h	U	U_{max}	U_{max}/U	C_s	Ri
[cm]	[cm]	[cm/s]	[cm]	[cm/s]	[−]	[cm]	[cm/s]	[cm/s]	[−]	[%]	[−]
120	7.91	5.01	1.87	6.65	1.33	8.08 (+2)	4.19 (−16)	5.73 (−14)	1.37 (+3)	1.701	1.04
220	8.85	4.94	2.50	6.69	1.35	9.74 (+10)	3.69 (−25)	5.33 (−20)	1.44 (+7)	1.252	1.19
320	9.72	4.86	3.12	6.76	1.39	11.39 (+17)	3.30 (−32)	4.91 (−27)	1.49 (+7)	0.928	1.29
420	9.42	4.94	2.50	6.84	1.38	n. d.	2.69 (−46)	4.60 (−33)	1.71 (+24)	0.610	1.91
610	17.33	2.66	4.37	3.41	1.28	13.05 (−25)	3.11 (+17)	4.38 (+28)	1.41 (+10)	0.486	0.87

Table B.12: Comparison of measured and computed integral scale and maximum values for experiment D02.

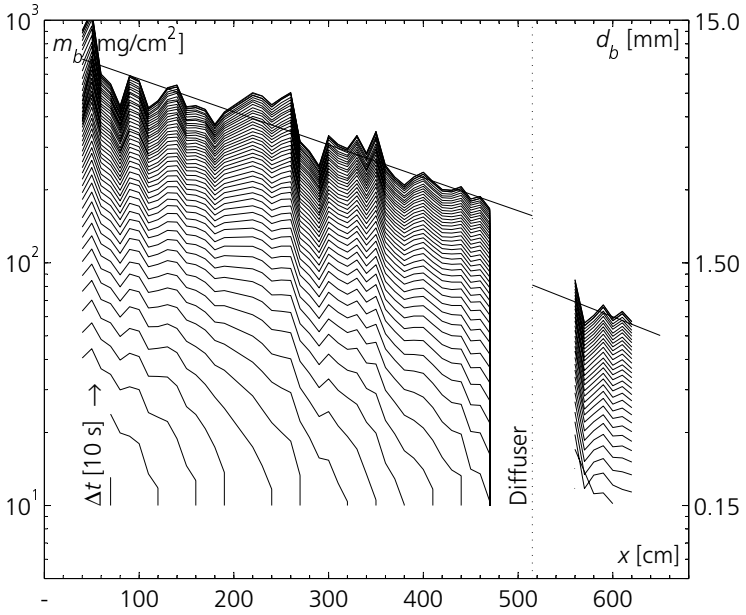

(a) Measured evolution of deposition.

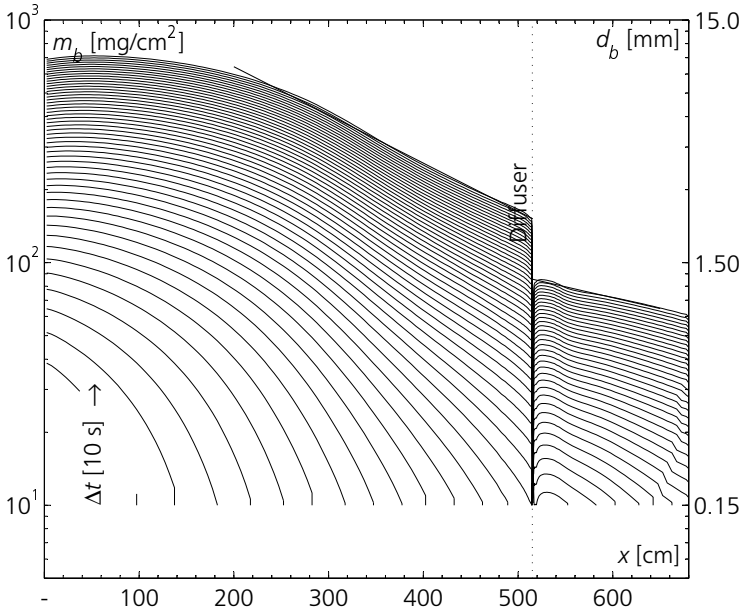

(b) Computed evolution of deposition.

Figure B.27: Comparison of measured and computed evolution of the sediment deposition in experiment D02 with flow through a screen.

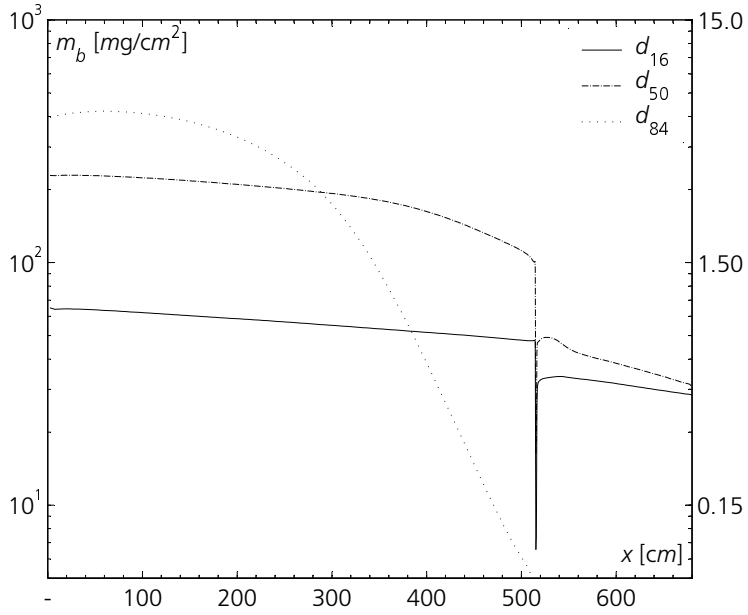

Figure B.28: Deposition thickness of three grain sizes, d_{16}, d_{50} and d_{84} at the end of experiment D02 (t=530 s).

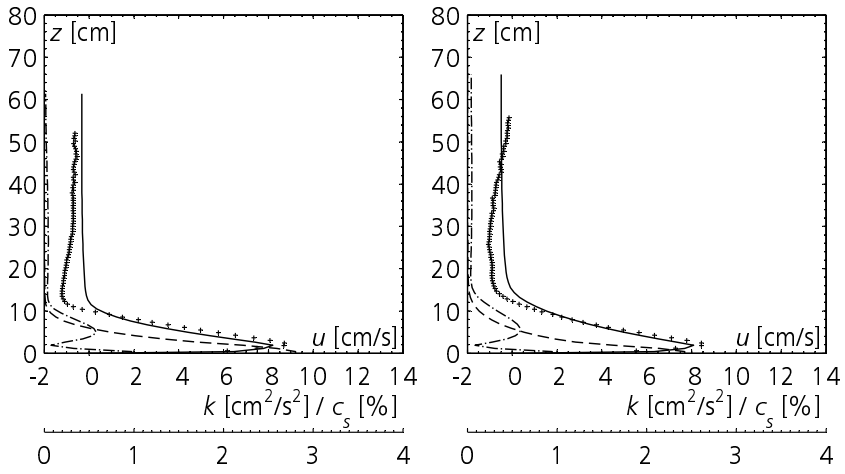

(a) x=120 cm. *(b)* x=220 cm.

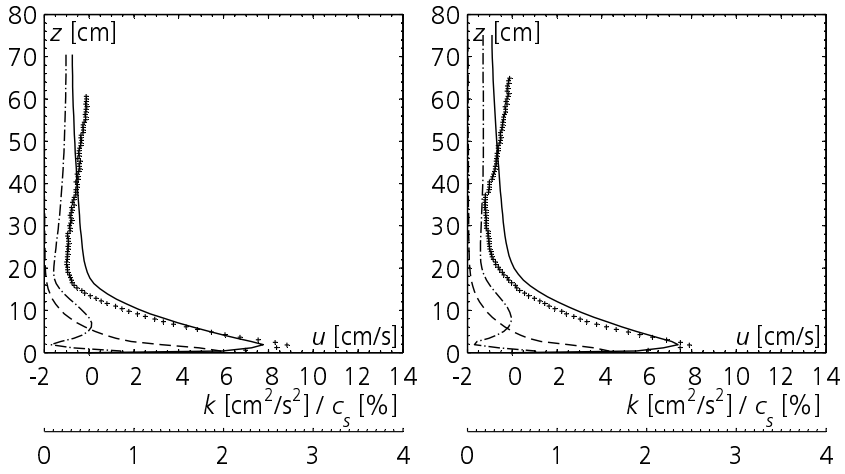

(c) x=320 cm. *(d)* x=420 cm.

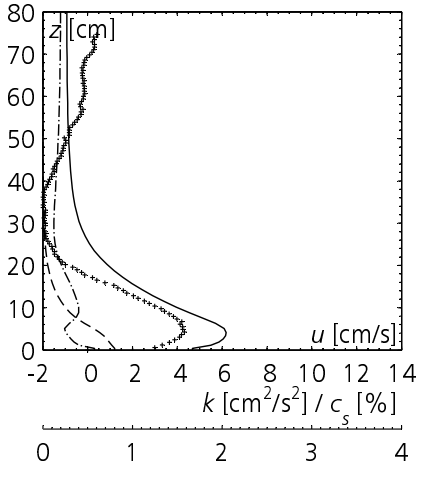

(e) x=610 cm.

Figure B.29: Vertical profiles of computed velocity, u (solid line), measured velocity (cross), computed concentration, c_s (dashed line) and turbulent kinetic energy, k (dash-dotted line) of experiment D04.

	Measured values					Computed values					
x	h	U	h_{max}	U_{max}	U_{max}/U	h	U	U_{max}	U_{max}/U	C_s	Ri
[cm]	[cm]	[cm/s]	[cm]	[cm/s]	[−]	[cm]	[cm/s]	[cm/s]	[−]	[%]	[−]
120	7.59	6.45	2.45	8.72	1.35	7.56 (−0)	5.82 (−10)	8.20 (−6)	1.41 (+4)	1.516	0.45
220	8.56	5.97	2.45	8.45	1.42	9.36 (+9)	5.52 (−8)	8.10 (−4)	1.47 (+4)	1.064	0.43
320	9.10	5.99	1.84	8.83	1.47	11.27 (+24)	5.21 (−13)	7.77 (−12)	1.49 (+1)	0.791	0.44
420	10.49	5.21	1.84	7.91	1.52	13.00 (+24)	4.96 (−5)	7.41 (−6)	1.49 (−2)	0.618	0.43
610	14.51	3.44	4.29	4.32	1.26	17.59 (+21)	4.53 (+32)	6.15 (+42)	1.36 (+8)	0.431	0.49

Table B.13: Comparison of measured and computed integral scale and maximum values for experiment D04.

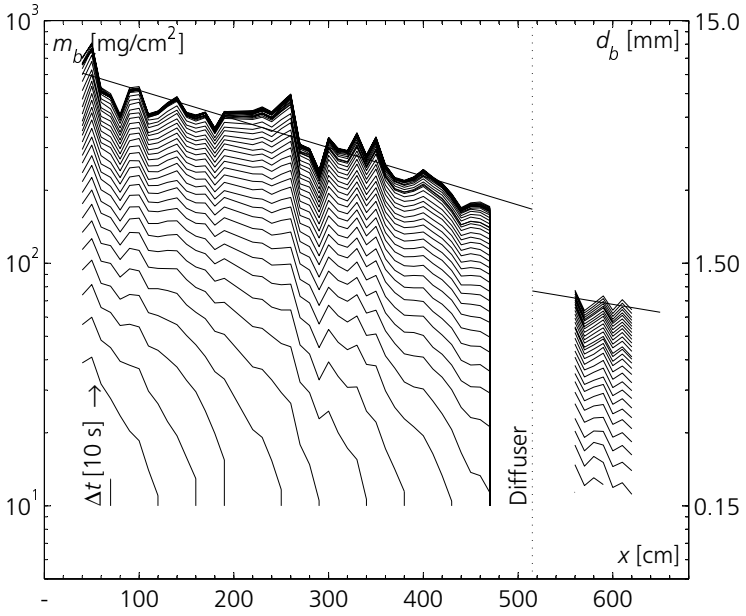

(a) Measured evolution of deposition.

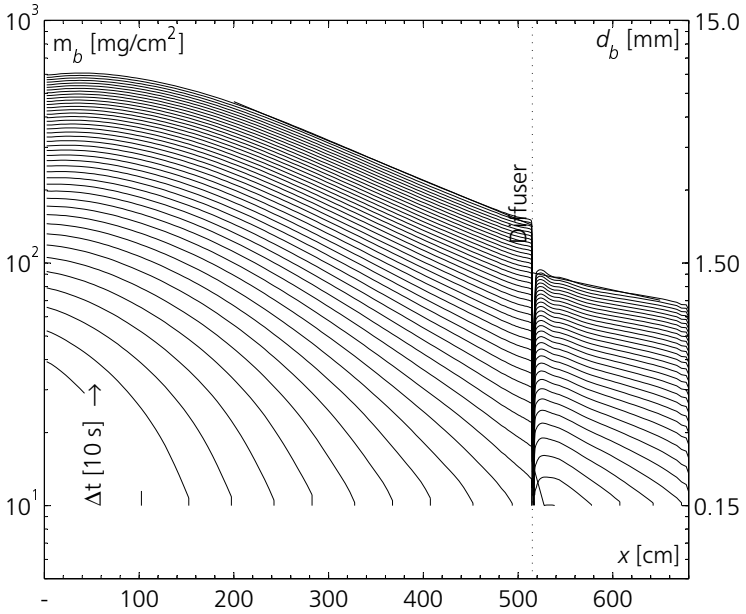

(b) Computed evolution of deposition.

Figure B.30: Comparison of measured and computed evolution of the sediment deposition in experiment D04.

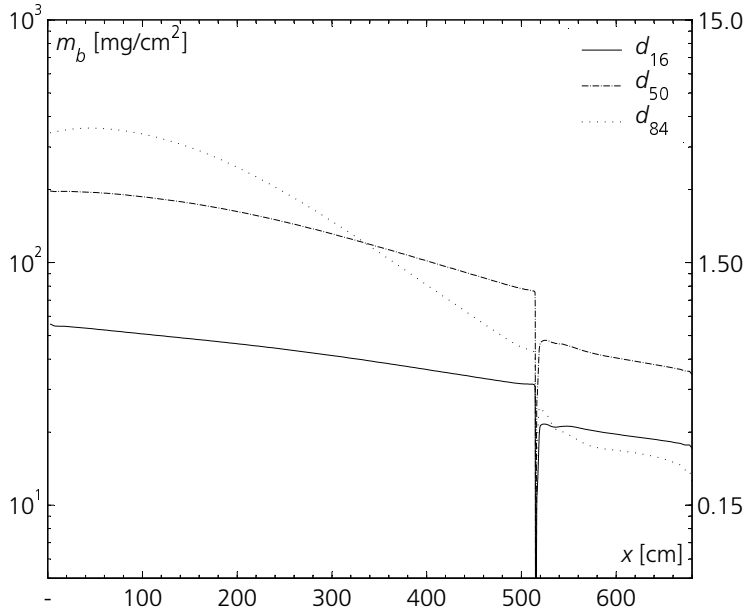

Figure B.31: Deposition thickness of three grain sizes, d_{16}, d_{50} and d_{84} at the end of experiment D04 (t=450 s).

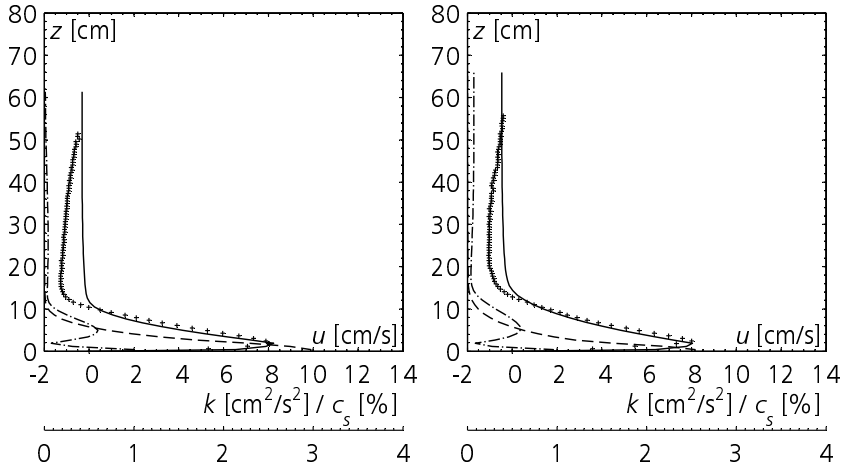

(a) x=120 cm. *(b)* x=220 cm.

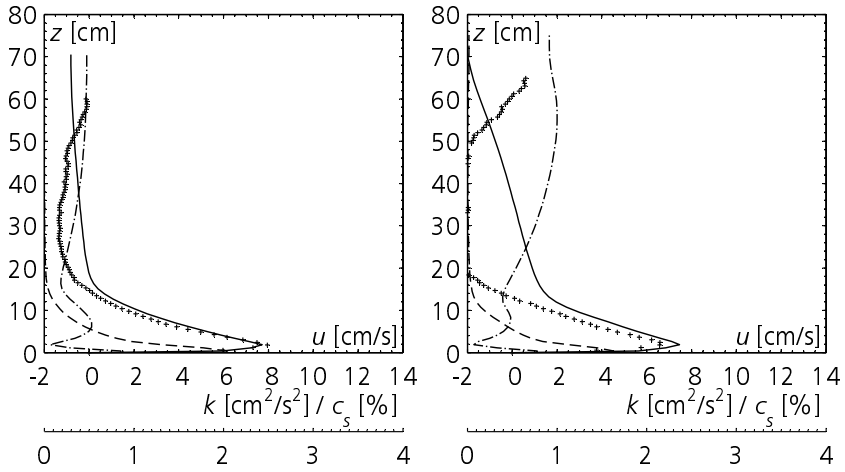

(c) x=320 cm. *(d)* x=420 cm.

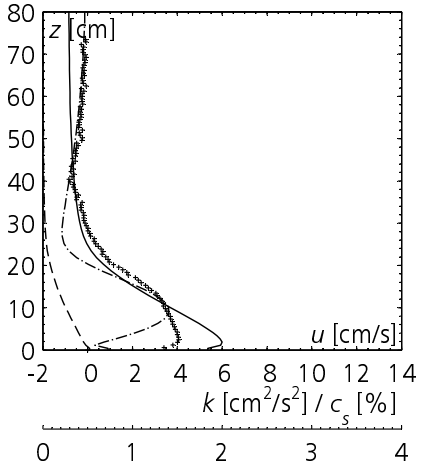

(e) x=610 cm.

Figure B.32: Vertical profiles of computed velocity, u (solid line), measured velocity (cross), computed concentration, c_s (dashed line) and turbulent kinetic energy, k (dash-dotted line) of experiment E01.

	Measured values					Computed values					
x	h	U	h_{max}	U_{max}	U_{max}/U	h	U	U_{max}	U_{max}/U	C_s	Ri
[cm]	[cm]	[cm/s]	[cm]	[cm/s]	[−]	[cm]	[cm/s]	[cm/s]	[−]	[%]	[−]
120	7.74	5.85	1.84	8.04	1.37	7.28 (−6)	5.83 (−0)	8.23 (+2)	1.41 (+3)	1.587	0.45
220	9.09	5.42	2.45	8.01	1.48	9.13 (+0)	5.50 (+1)	8.03 (+0)	1.46 (−1)	1.102	0.44
320	9.53	5.29	1.84	7.95	1.50	11.02 (+16)	5.18 (−2)	7.73 (−3)	1.49 (−1)	0.814	0.45
420	9.58	4.62	2.45	6.60	1.43	17.23 (+80)	4.40 (−5)	7.45 (+13)	1.69 (+19)	0.551	0.65
610	21.00	3.19	2.45	4.06	1.27	17.07 (−19)	4.32 (+35)	5.97 (+47)	1.38 (+9)	0.324	0.40

Table B.14: Comparison of measured and computed integral scale and maximum values for experiment E01.

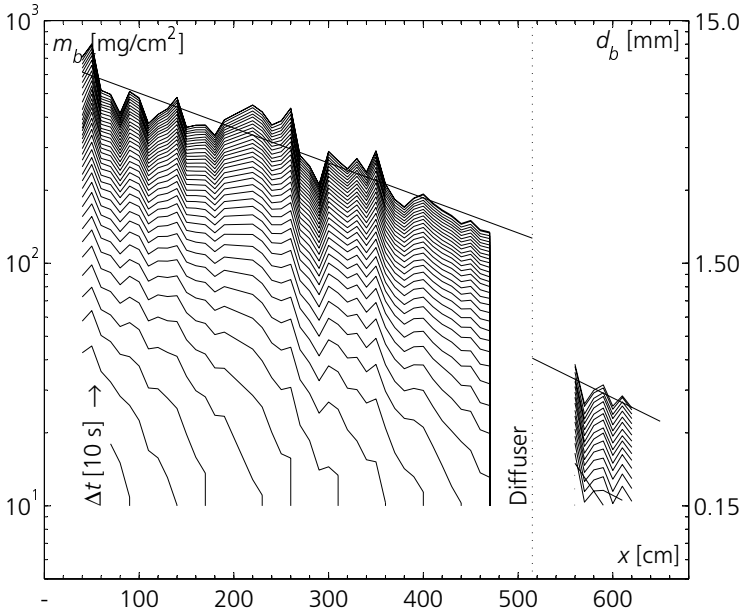

(a) Measured evolution of deposition.

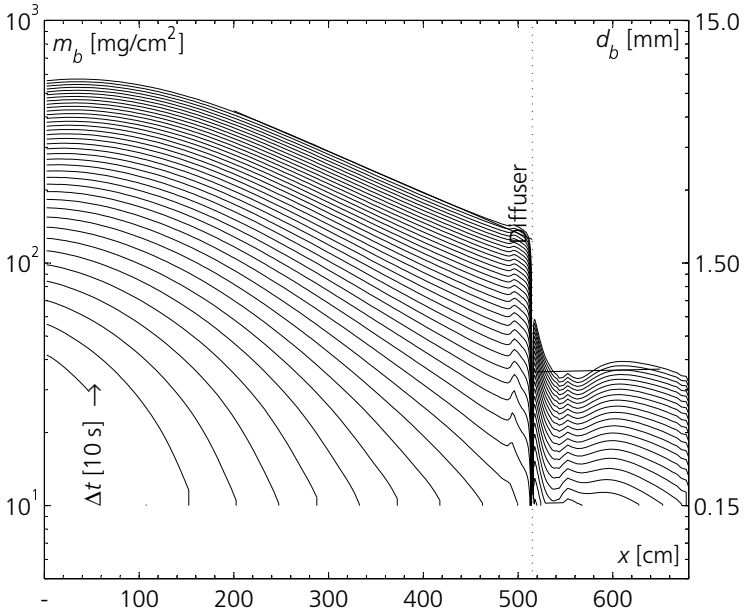

(b) Computed evolution of deposition.

Figure B.33: Comparison of measured and computed evolution of the sediment deposition in experiment E01.

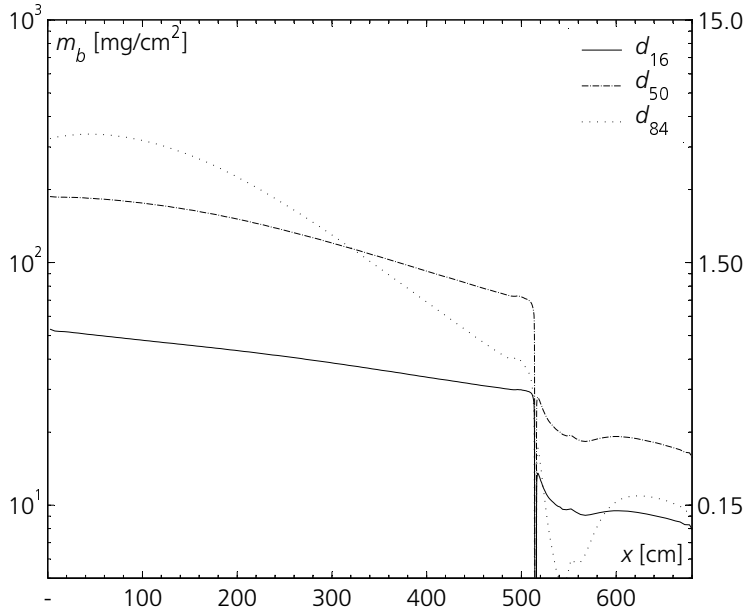

Figure B.34: Deposition thickness of three grain sizes, d_{16}, d_{50} and d_{84} at the end of experiment E01 (t=400 s).

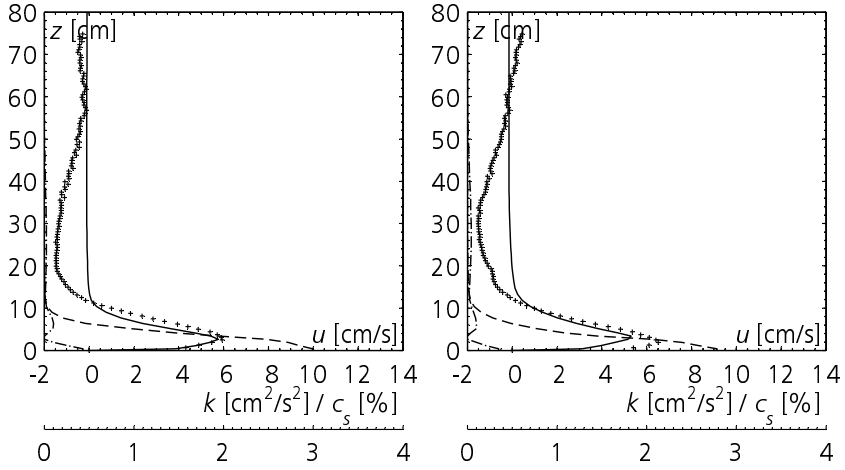

(a) x=120 cm. *(b)* x=220 cm.

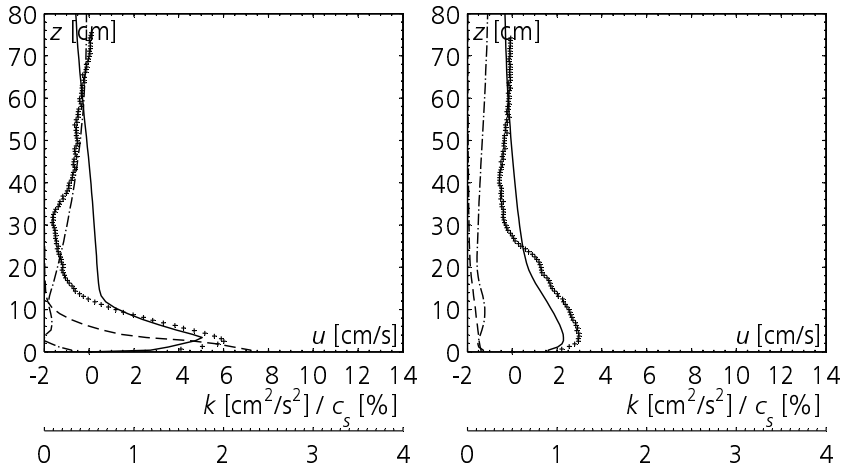

(c) x=320 cm. *(d)* x=610 cm.

Figure B.35: Vertical profiles of computed velocity, u (solid line), measured velocity (cross), computed concentration, c_s (dashed line) and turbulent kinetic energy, k (dash-dotted line) of experiment E03.

	Measured values					Computed values					
x	h	U	h_{max}	U_{max}	U_{max}/U	h	U	U_{max}	U_{max}/U	C_s	Ri
[cm]	[cm]	[cm/s]	[cm]	[cm/s]	[−]	[cm]	[cm/s]	[cm/s]	[−]	[%]	[−]
120	8.88	4.57	2.50	5.94	1.30	7.92 (−11)	4.21 (−8)	5.76 (−3)	1.37 (+5)	1.775	1.06
220	8.67	4.92	1.87	6.51	1.32	9.60 (+11)	3.69 (−25)	5.31 (−18)	1.44 (+9)	1.300	1.22
320	9.17	4.47	2.50	6.01	1.34	14.57 (+59)	2.96 (−34)	5.05 (−16)	1.71 (+27)	0.821	1.82
610	21.18	2.28	3.74	2.99	1.31	26.08 (+23)	1.53 (−33)	2.29 (−23)	1.50 (+14)	0.084	1.24

Table B.15: Comparison of measured and computed integral scale and maximum values for experiment E03.

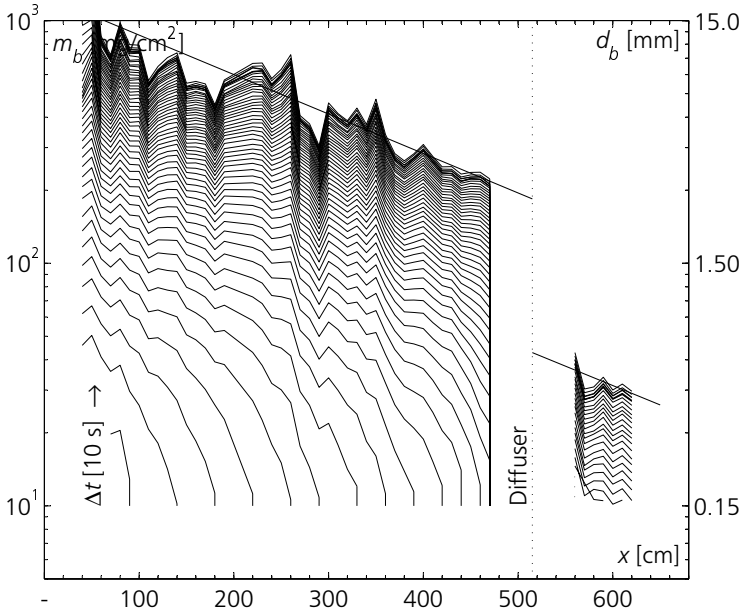

(a) Measured evolution of deposition.

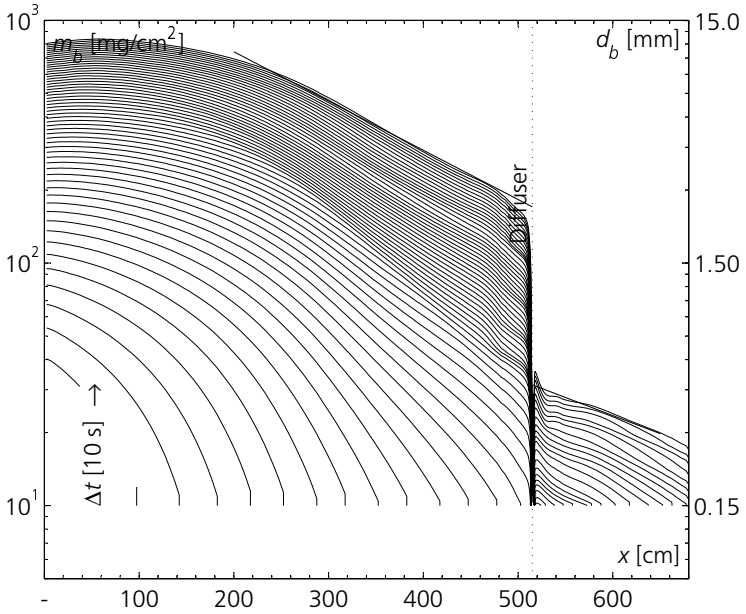

(b) Computed evolution of deposition.

Figure B.36: Comparison of measured and computed evolution of the sediment deposition in experiment E03.

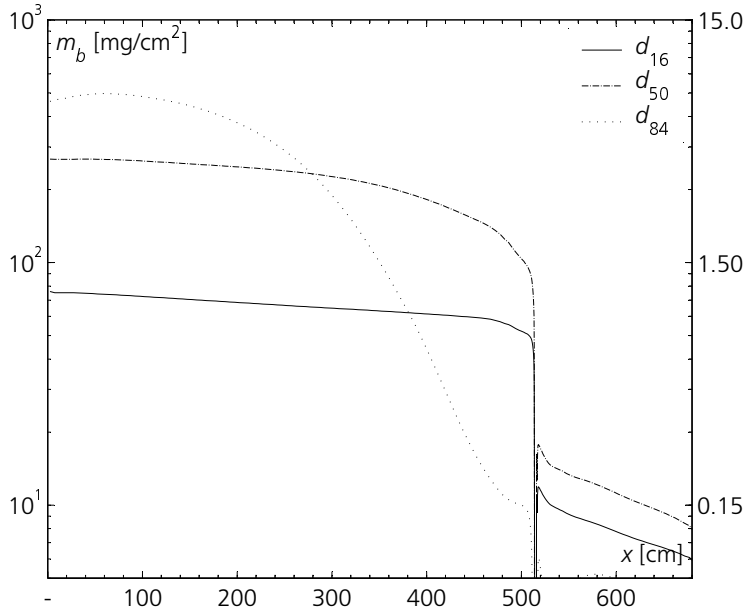

Figure B.37: Deposition thickness of three grain sizes, d_{16}, d_{50} and d_{84} at the end of experiment E03 (t=590 s).

C Turbidity Current Simulation of Flood Event in October 2000

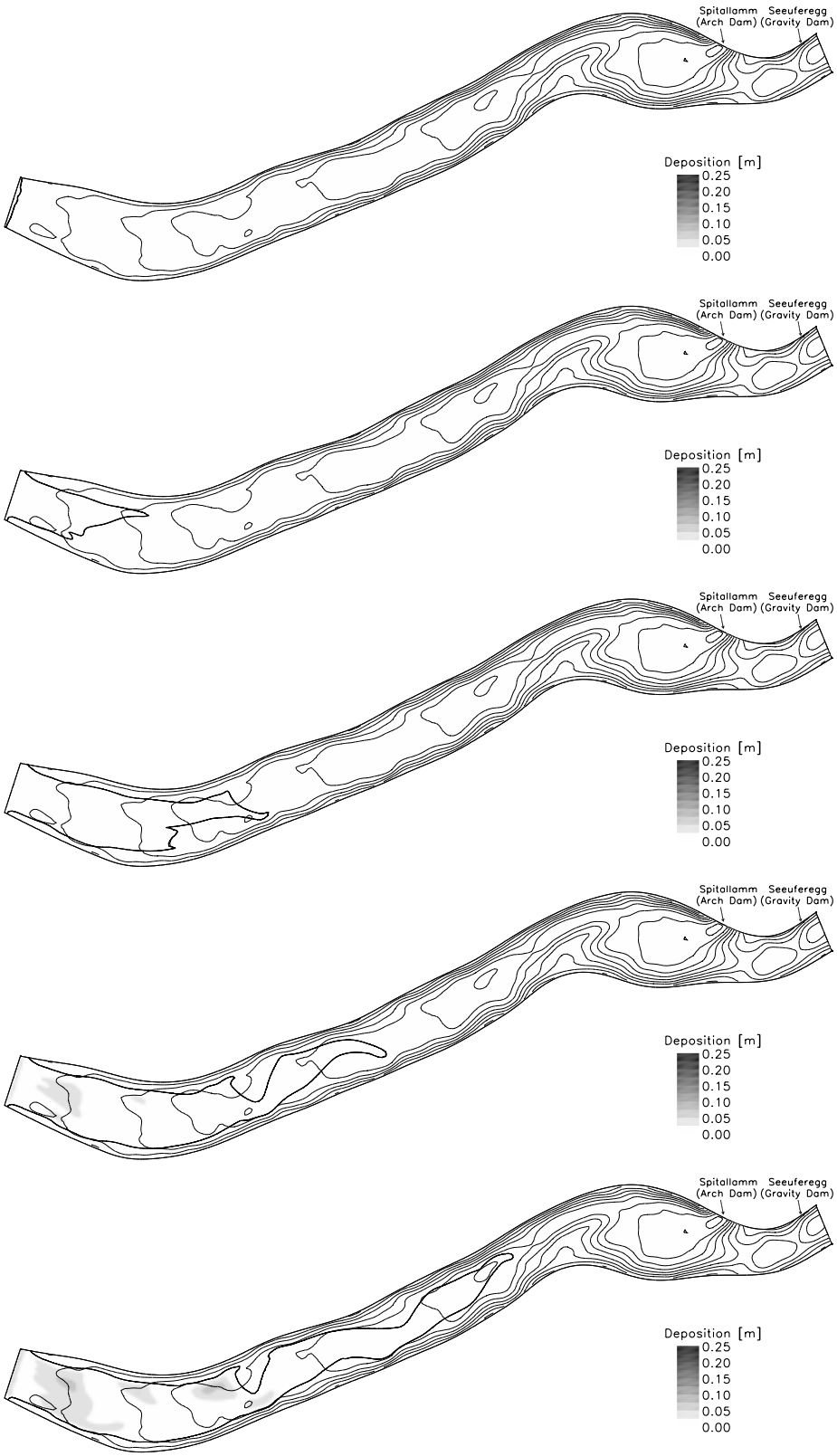

Figure C.1: Deposition with contour line of 1 g/l suspended sediment concentration after 8 to 24 hours.

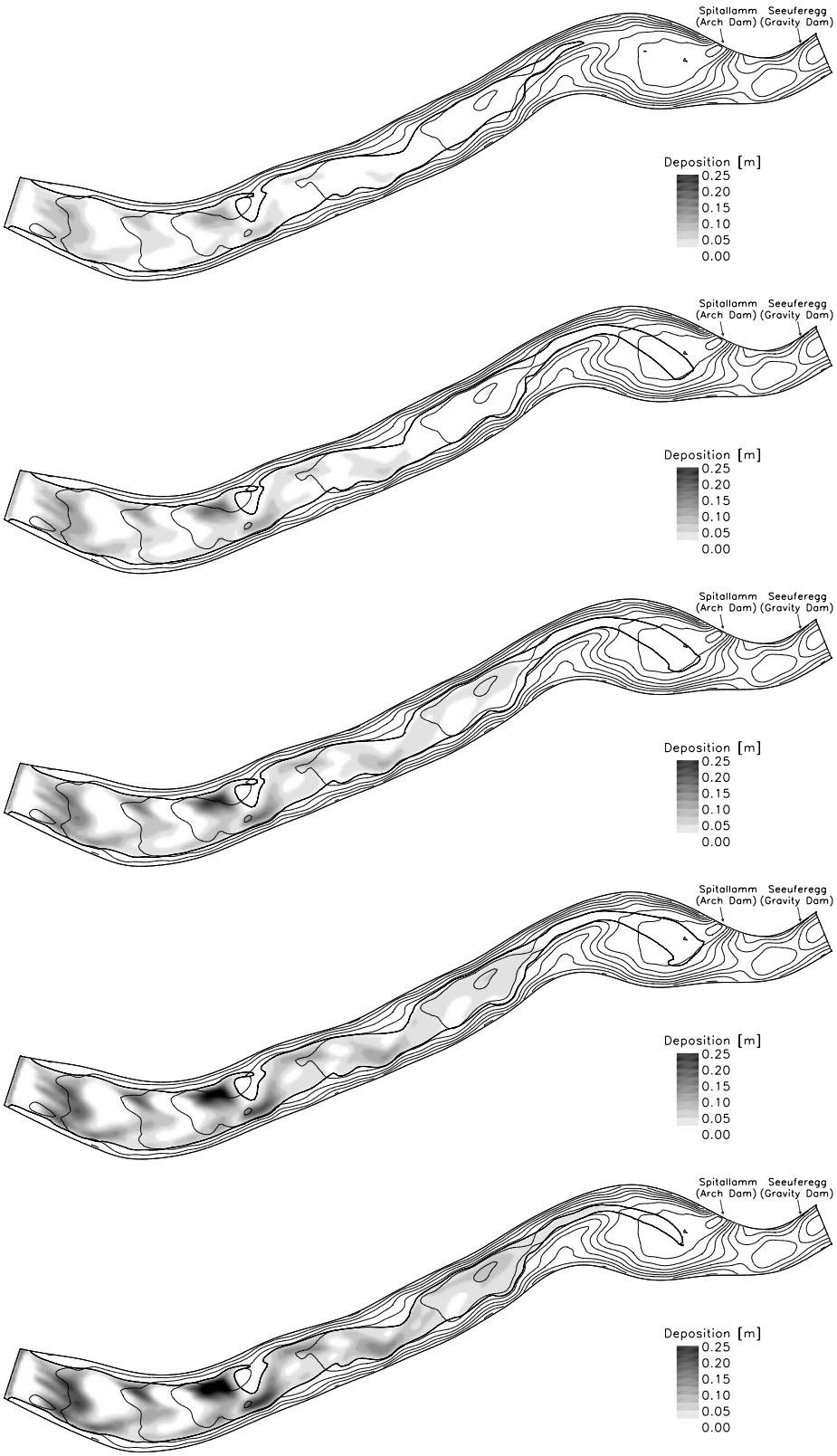

Figure C.2: Deposition with contour line of 1 g/l suspended sediment concentration after 28 to 44 hours.

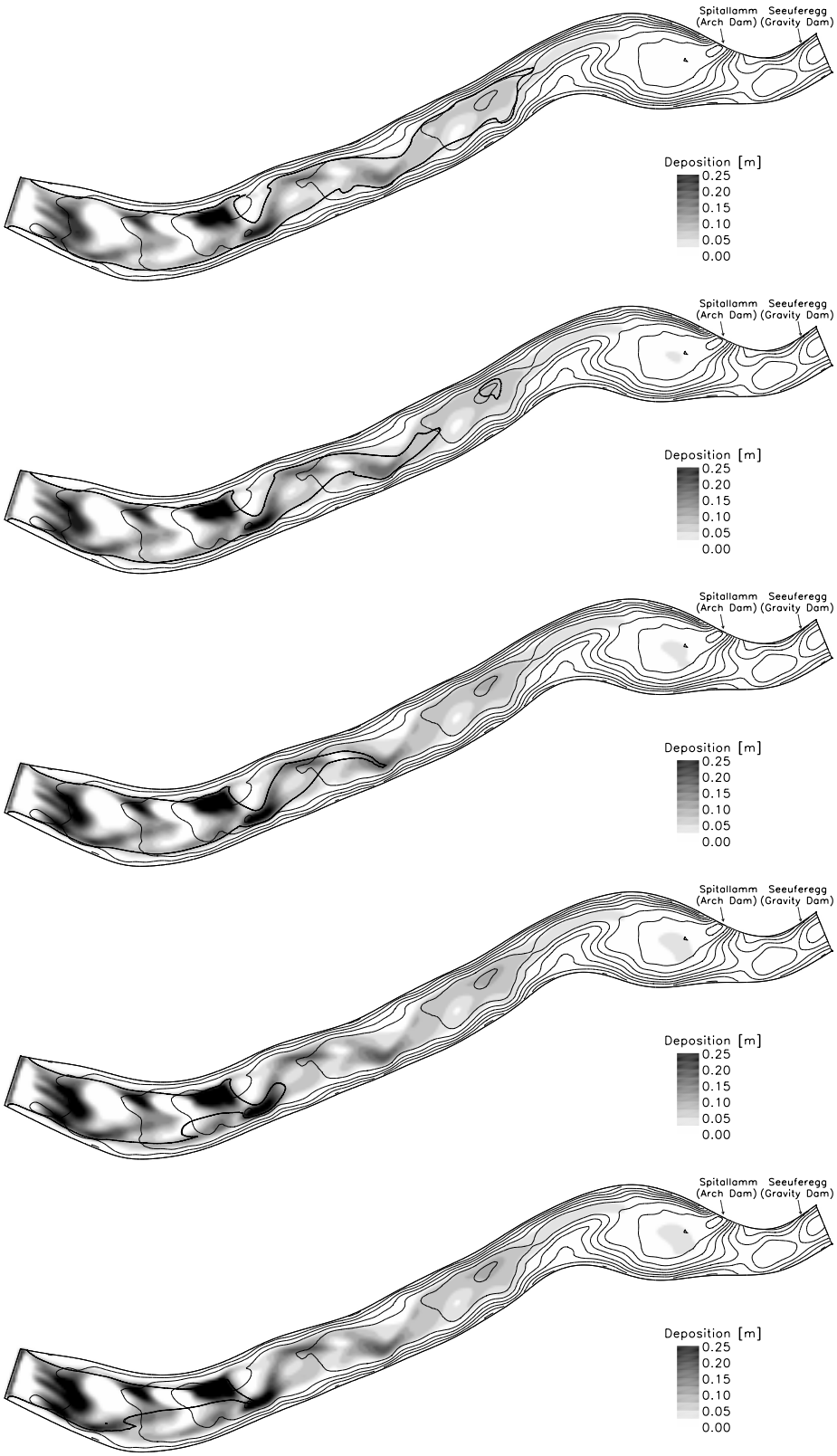

Figure C.3: Deposition with contour line of 1 g/l suspended sediment concentration after 48 to 64 hours.

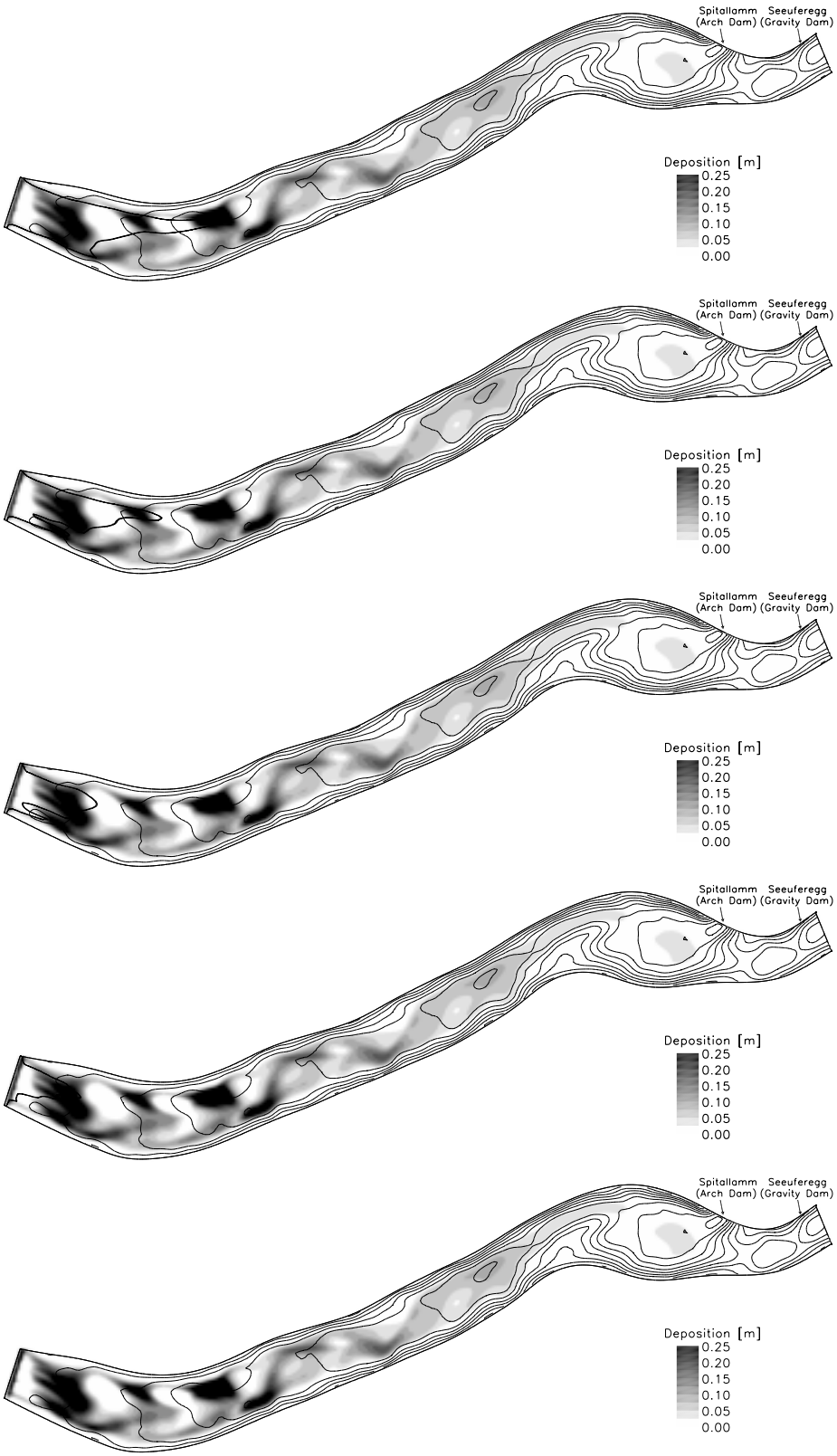

Figure C.4: Deposition with contour line of 1 g/l suspended sediment concentration after 68 to 84 hours.

D Turbidity Current Simulation with a Submerged Dam

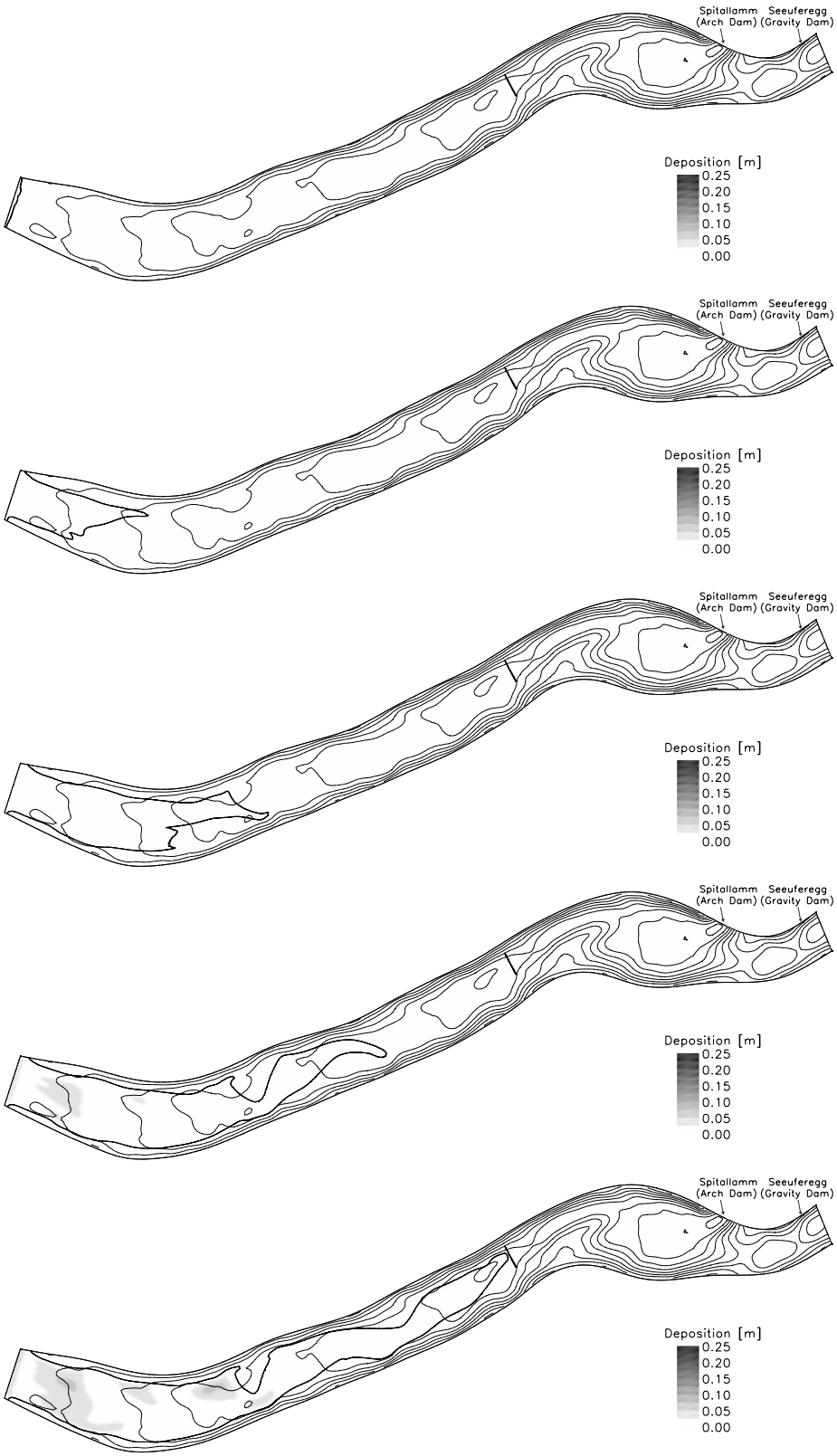

Figure D.1: Deposition with contour line of 1 g/l suspended sediment concentration and the submerged dam after 8 to 24 hours.

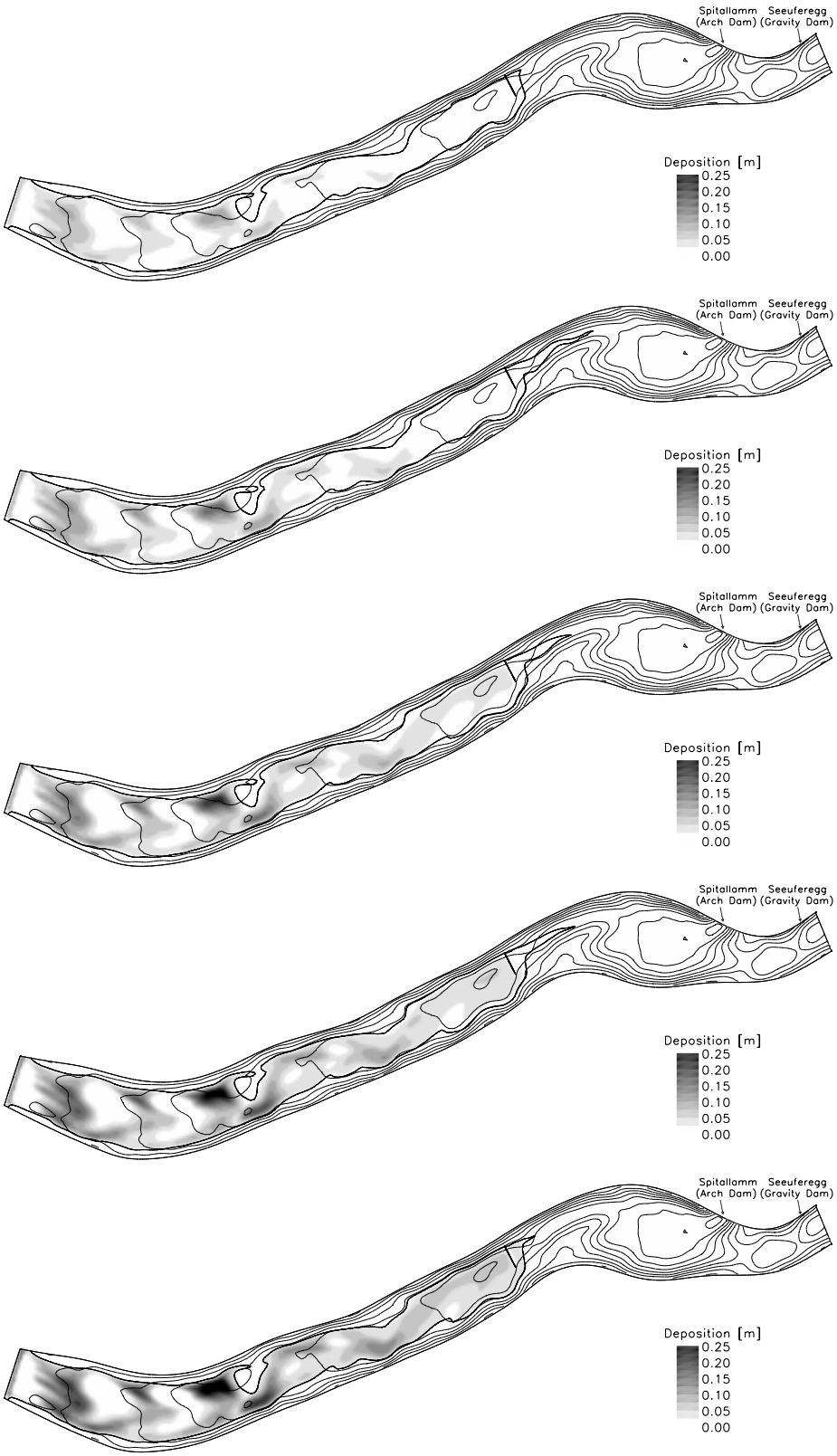

Figure D.2: Deposition with contour line of 1 g/l suspended sediment concentration and the submerged dam after 28 to 44 hours.

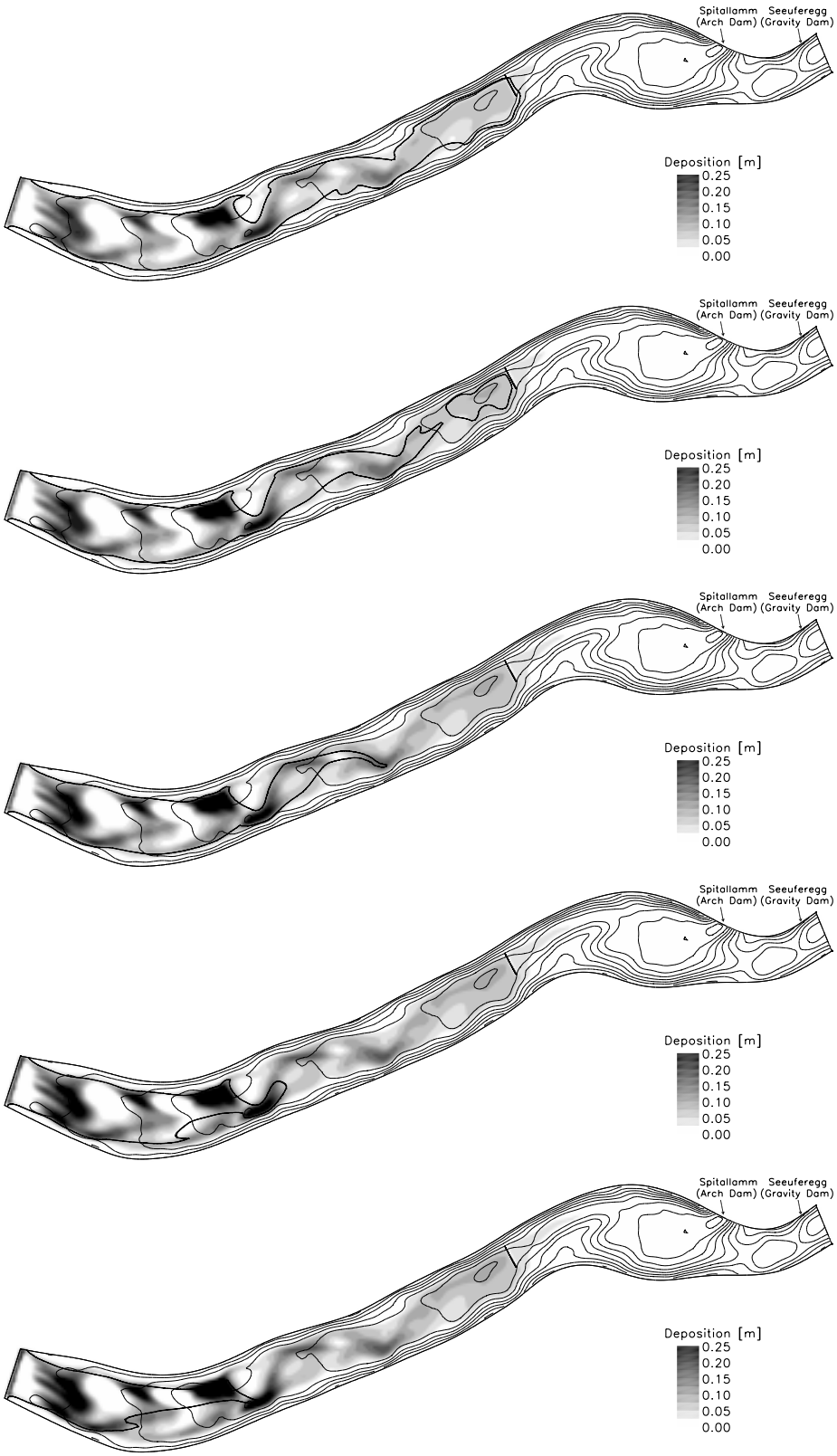

Figure D.3: Deposition with contour line of 1 g/l suspended sediment concentration and the submerged dam after 48 to 60 hours.

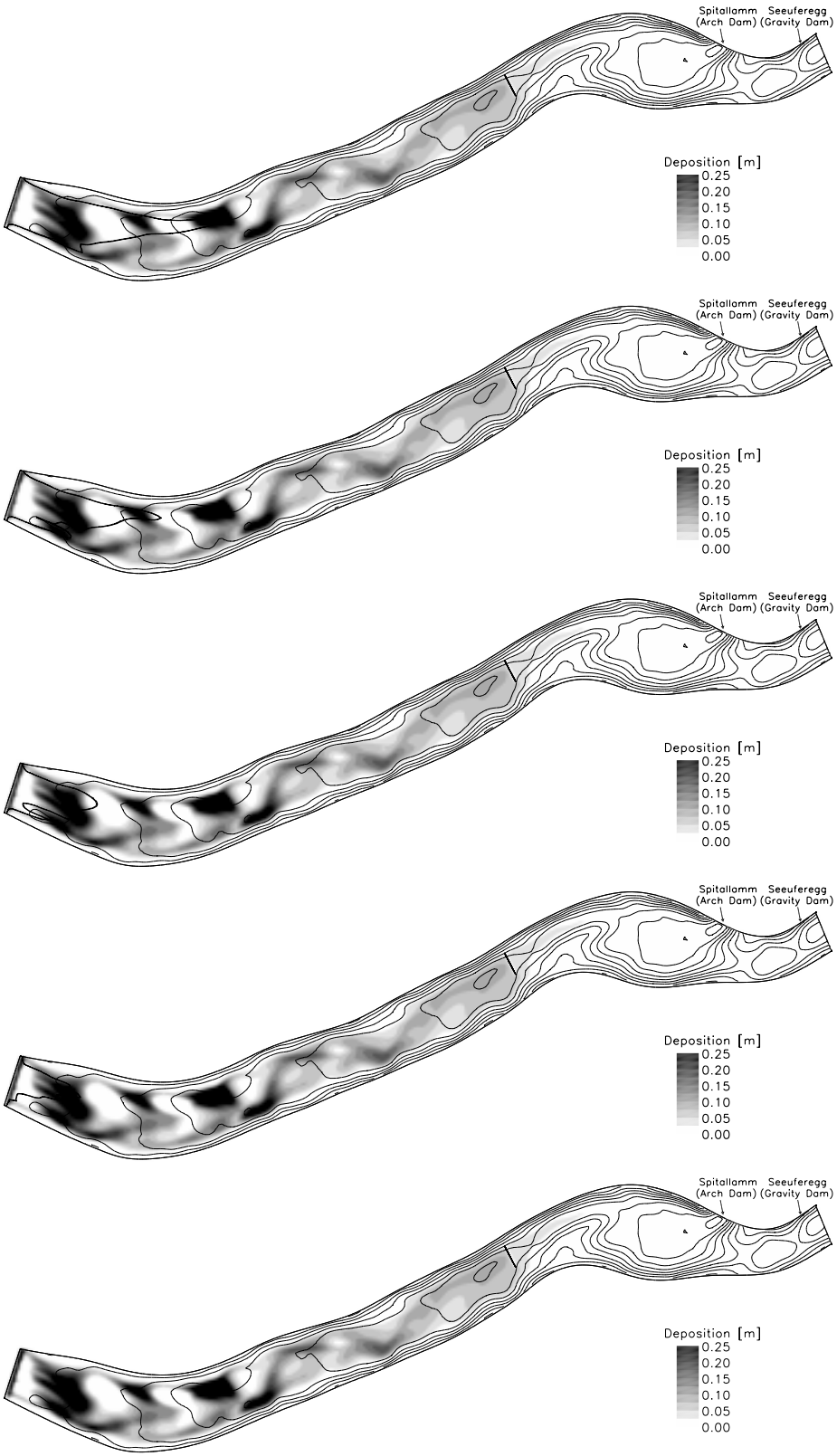

Figure D.4: Deposition with contour line of 1 g/l suspended sediment concentration and the submerged dam after 68 to 84 hours.

Communications du Laboratoire de constructions hydrauliques
Ecole Polytechnique Fédérale de Lausanne
Editeur: Prof. R. Sinniger

N° 1 1986 W. H. Hager
Discharge measurement structures

N° 2 1988 N. V. Bretz
Ressaut hydraulique forcé par seuil

N° 3 1990 R. Bremen
Expanding stilling basin

N° 4 1996 Dr R. Bremen
Ressaut hydraulique et bassins amortisseurs, aspects hydrauliques particuliers

N° 5 1997 Compte-rendu du séminaire à l'EPFL
Recherche dans le domaine des barrages, crues extrêmes

Communications du Laboratoire de constructions hydrauliques
Ecole Polytechnique Fédérale de Lausanne
Editeur: Prof. Dr A. Schleiss

N° 6 1998 et suivants, voir verso page titre

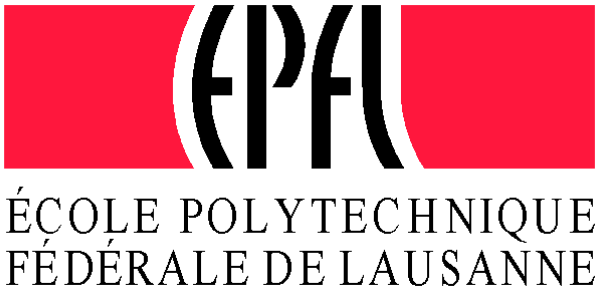

Prof. Dr A. Schleiss
Laboratoire de constructions hydrauliques - LCH
EPFL, CH-1015 Lausanne
http://lchwww.epfl.ch
e-mail: secretariat.lch@epfl.ch